Characterising Liquid Electrolytes for Lithium-Ion and Lithium Metal Batteries

Jack Fawdon

Lincoln College
University of Oxford

A thesis submitted for the degree of
Doctor of Philosophy in Materials

Trinity 2021

Abstract

Abstract

Liquid electrolytes are crucial for the continuing development of lithium-ion (LIB) and lithium metal batteries (LMB). Improving the transport and thermodynamics of the electrolyte allows for higher energy and power densities, faster charging and longer cycle life, all of which are required for furthering advanced battery technologies. Specifically, the diffusion coefficient (D_{app}) and transference number (t_{Li+}) dictate to what extent a Li^+ electrolyte concentration gradient forms across the cell, and the ionic conductivity (κ) and thermodynamic factor (χ_M) influence the ohmic, activation and concentration overpotentials.

In this work, a method for fully characterising D_{app}, t_+, κ, χ_M and the resistance of charge-transfer (R_{ct}) was described first, utilising operando Raman microspectroscopy in tandem with potentiostatic electrochemical impedance spectroscopy (PEIS). Using lithium bis(fluorosulfonylimide) in tetraglyme (LiFSI in G4) as a model system, the technique allowed for the characterisation of the electrolyte in one experimental setup. Furthermore, the study provided a method for visualising concentration gradients and a technique for correlating macroscopic transport and thermodynamic properties with microscopic intermolecular structure. Using the isolated properties, LIB and LMB simulations were conducted to understand how each property affected cell performance.

Next, tandem operando Raman microspectroscopy and PEIS were used to characterise a more complex system, namely ionic liquid electrolytes (ILEs), LiFSI in N-methyl-N-propylpyrrolidinium ($Pyr_{1,3}$) FSI. This was the first time ILE concentration gradients have been analysed along with a full ILE characterisation of transport and thermodynamic properties. The asymmetric Li^+ gradient provided evidence of large structures forming that settle to the bottom of the cell.

Finally, the plating morphology of lithium metal was studied using LiFSI in G4 and LiFSI in $Pyr_{1,3}$FSI electrolytes. Using the transport properties from previous chapters and surface analysis via X-ray photoelectron spectroscopy (XPS), reasons were presented as to how the electrolyte influenced the nucleation of non-uniform growth.

Overall, these studies provided a basis for full transport and thermodynamic electrolyte characterisation to allow for the furthering of LIB and LMB technologies.

Characterising Liquid Electrolytes for Lithium-Ion and Lithium Metal Batteries



Jack Fawdon

Lincoln College

University of Oxford

A thesis submitted for the degree of

Doctor of Philosophy in Materials

Trinity 2021

-

Copyright (©) Fawdon 2021. All rights reserved.

Abstract

Liquid electrolytes are crucial for the continuing development of lithium-ion (LIB) and lithium metal batteries (LMB). Improving the transport and thermodynamics of the electrolyte allows for higher energy and power densities, faster charging and longer cycle life, all of which are required for furthering advanced battery technologies. Specifically, the diffusion coefficient (D_{app}) and transference number (t_{Li+}) dictate to what extent a Li^+ electrolyte concentration gradient forms across the cell, and the ionic conductivity (κ) and thermodynamic factor (χ_M) influence the ohmic, activation and concentration overpotentials.

In this work, a method for fully characterising D_{app}, t_+, κ, χ_M and the resistance of charge-transfer (R_{ct}) was described first, utilising operando Raman microspectroscopy in tandem with potentiostatic electrochemical impedance spectroscopy (PEIS). Using lithium bis(fluorosulfonylimide) in tetraglyme (LiFSI in G4) as a model system, the technique allowed for the characterisation of the electrolyte in one experimental setup. Furthermore, the study provided a method for visualising concentration gradients and a technique for correlating macroscopic transport and thermodynamic properties with microscopic intermolecular structure. Using the isolated properties, LIB and LMB simulations were conducted to understand how each property affected cell performance.

Next, tandem operando Raman microspectroscopy and PEIS were used to characterise a more complex system, namely ionic liquid electrolytes (ILEs), LiFSI in N-methyl-N-propylpyrrolidinium ($Pyr_{1,3}$) FSI. This was the first time ILE concentration gradients have been analysed along with a full ILE characterisation of transport and thermodynamic properties. The asymmetric Li^+ gradient provided evidence of large structures forming that settle to the bottom of the cell.

Finally, the plating morphology of lithium metal was studied using LiFSI in G4 and LiFSI in $Pyr_{1,3}$FSI electrolytes. Using the transport properties from previous chapters and surface analysis via X-ray photoelectron spectroscopy (XPS), reasons were presented as to how the electrolyte influenced the nucleation of non-uniform growth.

Overall, these studies provided a basis for full transport and thermodynamic electrolyte characterisation to allow for the furthering of LIB and LMB technologies.

Publication List

1. Fawdon, J., Ihli, J., La Mantia, F., Pasta, M. Characterising Lithium-Ion Electrolytes via Operando Raman Microspectroscopy. *Nature Communications* **12**, 4053 (2021).

2. Fawdon, J., Rees, G. J., La Mantia, F., Pasta, M. Insights into Ionic Liquid Electrolyte Transport and Structure via Operando Raman Microspectroscopy. *Manuscript Submitted for Publication*.

3. Wang, A. W., Gunnarsdóttir, A. B., Fawdon, J., Pasta, M., Grey, C. P., Monroe, C. W., Potentiometric MRI of a Superconcentrated Lithium Electrolyte: Testing the Irreversible Thermodynamics Approach. *ACS Energy Letters* **6**, 3086-3095 (2021).

4. H. J., Lee, Brown, Z., Zhao, Y., Fawdon, J., Song, W., Lee, J. H., Pasta, M. Ordered $LiNi_{0.5}Mn_{1.5}O_4$ cathode in bis(fluorosulfonyl)imide-based ionic liquid electrolyte: importance of the cathode-electrolyte interphase. *Chemistry of Materials* **33** (4), 1238-1248 (2021).

5. Gong, C., Pu, S. D., Gao, X., Yang S., Liu, J., Ning Z., Rees, G. J., Capone, I., Pi. L., Liu. B., Hartley, G. O., Fawdon J., Luo, J., Pasta, M., Grovenor, C. R. M., Bruce, P. G., Robertson, A. W. Revealing the Role of Fluoride-Rich Battery Electrode Interphases by Operando Transmission Electron Microscopy. *Advanced Energy Materials* **11** (10), 2003118 (2021).

6. Fiore, M., Wheeler., S., Hurlbutt, K., Capone, I., Fawdon, J., Ruffo, R., Pasta, M. Paving the Way toward Highly Efficient, High-Energy Potassium-Ion Batteries with Ionic Liquid Electrolytes. *Chemistry of Materials* **32** (18), 7653-7661 (2020).

7. Xiao, A. W., Lee, H. J., Capone, I., Robertson, A., Wi, T., Fawdon, J., Wheeler, S., Lee, HW, Grobert, N., Pasta, M. Understanding the conversion mechanism and performance of monodisperse FeF_2 nanocrystal cathodes. *Nature Materials* **19**, (6) 644–654 (2020).

Acknowledgements

Firstly, I would like to thank Prof. Mauro Pasta for allowing me to join his group! Having had little prior exposure to battery science, I am immensely thankful for his trust in me: his endless enthusiasm and guidance inspired me to reach further and dig deeper into challenging questions. His time, expertise, and the opportunities he has provided, have proven invaluable.

Living in Oxford and working in the Pasta group has been a hugely enlightening experience, being surrounded by kind, thoughtful and intelligent people. I would like to thank all of the Pasta group members, past and present, for their support and help throughout the duration of the DPhil. I am especially grateful to Kevin Hurlbutt, Isaac Capone, Sam Wheeler, and Albert Xiao for their friendship and help in the lab. I couldn't have asked for a better group to begin and end this journey with! Also, I'd like to thank Shobhan Dhir and Yvonne Chart, whose probing questions and help made me a better researcher and Giulia Galatolo for help with Blender figure drawings.

I would like to thank Prof. Fabio La Mantia for the many fruitful discussions we had regarding my research and for allowing me to visit his group in my first year; it provided a wonderful basis for much of my subsequent work. Also, I would like to thank Dr. Johannes Ihli for providing initial help with the operando Raman microspectroscopy experiments and offering great feedback on the experimental detail. My sincere thanks also go to Dr. Gregory Rees, Dr. Liyu Jin, and Dr. Sudarshan Narayanan for their help in NMR and XPS measurements respectively; I hugely valued their time and patience, providing expertise that I was grateful to learn from. Many thanks go to Andy, Howard, Pete, and Steve at the mechanical workshop in PTCL for their help in making the various electrochemical cells I sent them; I truly valued their ideas and patience regarding most of my cell designs! I'd like to thank Andrew Wang for the many discussions we had about liquid electrolytes and the many challenges that come with characterising them!

I'd like to express my gratitude to the funding sources that allowed me to pursue the DPhil, namely UK Engineering and Physical Science Research Council (EPSRC) DTP Studentship, and Henry Royce Institute (through UK Engineering and Physical Science Research Council grant EP/R010145/1) for capital equipment.

Thank you to my wonderful housemates, Lewis, Chris, Anjali, and Tara, for always being present and caring, providing much-needed respite between hours in the lab!

An unending thank you to my best friends, Lizzy and Bruce, for always being there: picking up the phone no matter the situation, providing endless support in

everything I do, and affording kindness and understanding throughout my various challenges. I am in awe of both their achievements, which inspire me to be better.

Thank you to my sisters, Emily and Hannah, for their continuing and unwavering support over the years. They have been a rock in the unsteady journey that the DPhil entails! And finally, my special thanks go to my parents. I am in wonder of their hard work and dedication, affording me opportunities I otherwise could never have dreamt of. Their advice, guidance, and encouragement have been unerring, which is something I will be forever grateful for.

Contents

Publication List v

List of Abbreviations xiii

List of Key Variables xv

1 Introduction and Background 1

1.1 Electrochemical Energy Storage 1
1.2 Lithium-Ion Batteries 2
1.3 Lithium Metal Anodes 5
1.4 Electrolytes 8
1.4.1 Electrolyte Mass Transport and Thermodynamic Factor . . 8
1.5 Characterising Electrolyte Properties 16
1.5.1 Ionic Conductivity 16
1.5.2 Diffusion Coefficient 17
1.5.3 Transference Number 19
1.5.4 Thermodynamic Factor 23
1.5.5 Concentration Gradient Visualisation 25
1.5.6 Literature Electrolyte Measurements 28
1.6 Ionic Liquid Electrolytes 33
1.7 Improving Electrolyte Properties 38
1.8 Thesis Objectives 42
1.9 References 43

2 Method Fundamentals 55

2.1 Confocal Raman Microspectroscopy 55
2.1.1 Confocal Microscopy 55
2.1.2 Raman Spectroscopy Fundamentals 55
2.1.3 Raman Instrumentation 57
2.2 Electrochemical Techniques 59
2.2.1 Electrochemical Impedance Spectroscopy 59
2.2.2 Chronopotentiometry 63
2.3 References 63

3 Characterising Binary Electrolytes via Operando Raman Microspectroscopy 65
3.1 Abstract . . . 65
3.2 Introduction . . . 66
3.3 Results & Discussion . . . 69
3.3.1 Densitometry & Partial Molar Volumes . . . 69
3.3.2 Raman Calibration . . . 70
3.3.3 Cell Design & Concentration Visualisation . . . 73
3.3.4 Measuring Transport & Thermodynamic Properties . . . 77
3.3.5 Effect of Concentration . . . 86
3.3.6 Stefan-Maxwell Measurements . . . 94
3.3.7 Transport using PEIS . . . 96
3.3.8 COMSOL Modelling . . . 99
3.4 Conclusions & Future Work . . . 102
3.5 Experimental Detail . . . 105
3.6 References . . . 108

4 Insights into Ionic Liquid Electrolyte Transport and Structure 111
4.1 Abstract . . . 111
4.2 Introduction . . . 111
4.3 Results & Discussion . . . 114
4.3.1 Concentration Gradient Visualisation . . . 114
4.3.2 Asymmetry and Structural Implications . . . 118
4.3.3 Li^+ Transport Properties . . . 123
4.3.4 Dependence on Concentration . . . 131
4.3.5 Plating at Low Concentrations . . . 133
4.4 Conclusions & Future Work . . . 135
4.5 Experimental Detail . . . 137
4.6 References . . . 139

5 Effect of Electrolyte Transport and Thermodynamics on Lithium Metal Plating Morphology 143
5.1 Abstract . . . 143
5.2 Introduction . . . 143
5.3 Results & Discussion . . . 145
5.3.1 Rate of Roughening . . . 145
5.3.2 Interfacial Concentration Gradients . . . 146
5.3.3 SEI Transport . . . 147
5.4 Conclusions & Future Work . . . 161
5.5 Experimental Detail . . . 162
5.6 References . . . 163

6 Conclusion and Future Work **167**
6.1 Conclusion 167
6.2 Suggested Further Work 168

Appendices

A Python Scripts **173**
A.1 Concentration Visualisation – Binary Electrolyte 173
A.2 Symmetric Concentration Gradient Fitting 177
A.3 Concentration Visualisation – Ionic Liquid Electrolyte 181
A.4 Asymmetric Concentration Gradient Fitting 184

B Doyle-Fuller-Newman Equations **191**

C ILE Simulation Equations **193**

D Further XPS Data **195**

List of Abbreviations

1D . . . . . One-dimensional.

AGG . . . . . Aggregate.

CE . . . . . Coulombic Efficiency.

CIP . . . . . Contact Ion Pair.

CST . . . . . Concentrated Solution Theory.

DFT . . . . . Density Functional Theory.

DLS . . . . . Dynamic Light Scattering.

DMC . . . . . Dimethyl Carbonate.

EC . . . . . Ethyl Carbonate.

FLW . . . . . Finite Length Warburg.

FFKM . . . . . Perfluoroelastomer.

FSI . . . . . Bis(fluorosulfonyl)imide.

G4 . . . . . Tetraglyme.

IL(E) . . . . . Ionic Liquid (Electrolyte).

LCO . . . . . Lithium Cobalt Oxide.

LHCE . . . . . Localised High Concentrated Electrolyte.

LIB . . . . . Lithium-Ion Battery.

LMB . . . . . Lithium Metal Battery.

LMO . . . . . Lithium Manganese Oxide.

MD . . . . . Molecular Dynamics.

OCV . . . . . Open Circuit Voltage.

PC . . . . . Propylene Carbonate.

PEEK . . . . . Polyetheretherketone.

(P)EIS . . . . . (Potentiostatic) Electrochemical Impedance Spectroscopy.

PEO . . . . . Poly(ethylene oxide).

pfg-NMR . . . . Pulsed Field Gradient Nuclear Magnetic Resonance Spectroscopy.

SEI . . . . . Solid Electrolyte Interphase.

TFSI . . . . . Bis(Trifluorosulfonyl)imide.

VLF . . . . . Very Low Frequency.

XPS . . . . . X-ray Photoelectron Spectroscopy.

List of Key Variables

a	Thermodynamic activity
A	Electrode area
c_i	Concentration of species i
c_s	Concentration of salt
c_T	Total concentration
C	Capacitance
D_{app}	"Apparent", Fickian diffusion coefficient
$\mathfrak{D}_{ij}$	Thermodynamic diffusion coefficient between species i and j (anion = -, cation = +, solvent = 0)
$f_{\pm}$	Molar activity coefficient
F	Faraday constant
I	Ionicity
J	Current density
K_{ij}	Stefan-Maxwell drag coefficient between species i and j
l	Interelectode distance
m	Molality
M	Molarity
Q	Constant phase element
R	Universal gas constant
R^i	Initial resistance (0) or resistance at steady state (s)
R_{bulk}	Ohmic resistance
R_{ct}	Resistance of charge-transfer
t	Time
t_+^0	Transference number referenced against the solvent velocity
T	Temperature
V_i	Partial molar volume of salt (s) or solvent (0)
V_{cell}	Voltage of a cell
v	Velocity
W_d	Warburg diffusion resistance

z . . . . . Position of the cell in the z-direction (vertical)

α . . . . . Polarisability

ε . . . . . Dielectric constant

η_c . . . . . Concentration overpotential

$\gamma_{\pm}$ . . . . . Mean activity coefficient

κ . . . . . Ionic conductivity

μ_i . . . . . Mobility of species, i

ν . . . . . Wavenumber

ω . . . . . Frequency

Φ . . . . . Electric potential

ρ . . . . . Density

τ_0 . . . . . Time constant

τ_s . . . . . Sand's time

χ_M . . . . . Molar thermodynamic factor

$\frac{dc_s}{dz}$ . . . . . Salt concentration gradient wrt to direction z

$\frac{dc_s}{dz}|_{z=0,L}$ . . . . Interfacial salt concentration gradient wrt to direction z

$1-\frac{\partial \ln c_0}{\partial \ln c_s}$ . . . . Solvent velocity factor

1 Introduction and Background

Contents

1.1 Electrochemical Energy Storage 1
1.2 Lithium-Ion Batteries 2
1.3 Lithium Metal Anodes 5
1.4 Electrolytes 8
1.4.1 Electrolyte Mass Transport and Thermodynamic Factor 8
1.5 Characterising Electrolyte Properties 16
1.5.1 Ionic Conductivity 16
1.5.2 Diffusion Coefficient 17
1.5.3 Transference Number 19
1.5.4 Thermodynamic Factor 23
1.5.5 Concentration Gradient Visualisation 25
1.5.6 Literature Electrolyte Measurements 28
1.6 Ionic Liquid Electrolytes 33
1.7 Improving Electrolyte Properties 38
1.8 Thesis Objectives 42
1.9 References 43

1.1 Electrochemical Energy Storage

The need for advanced energy storage solutions is becoming increasingly important in modern society. Although there are multiple energy storage technologies, it is electrochemical energy storage (EES) that is becoming the primary system of choice.[1] Electrochemical cells, popularly referred to as batteries, have become a critical component of our personal lives, through portable electronics such as smartphones, and are progressively more important for many industries including manufacturing, transport and renewable energy grid storage.[2, 3] As countries pledge to become carbon neutral in the coming decades, the mentioned industries require a total transition from using fossil fuel-based energy to cleaner solutions, like batteries. This is especially true for the electric vehicle (EV) market, with some countries phasing out the sales of fossil fuel vehicles altogether;[4, 5] the UK will end the sale of these vehicles in 2030, for example.[6] In 2019, world electric car sales were 7.2 million, up from 17,000 in 2010. This growth is projected to

continue, reaching 245 million by 2030, illustrating the fundamental importance of continued battery development.[7]

1.2 Lithium-Ion Batteries

The growth of the battery market has almost exclusively been a result of lithium-ion batteries (LIBs), a type of secondary (or rechargeable) battery.[8, 9] Developed in the 1980s by Goodenough and his co-authors and subsequently commercialised by SONY in 1991,[10, 11] the current LIB market value is USD 36.7 billion. Due to increased LIB demand, highlighted above by the expanding EV market, the LIB market is projected to hit USD 129.3 billion by 2027. This equates to a Compound Annual Growth Rate (CAGR) of 18%.[12]

Goodenough's breakthrough came from the development of a high capacity cathode (positive electrode), namely lithium cobalt oxide (LCO), which can intercalate lithium ions at high potentials.[11] Along with the graphite anode (negative electrode), developed by SONY, and the inclusion of an electrochemically stable, organic electrolyte, the first-generation LIB was made.[13] Its invention and ingenuity was highlighted by the Nobel Prize Committee for Chemistry, with Goodenough, Whittingham and Yoshino winning the Nobel Prize for Chemistry in 2019.

Batteries transform energy induced by chemical reactions into electrical energy, which then does work on a system. They are composed of two electrodes, negative and positive, with an electrolyte in between, and an external e^- conducting circuit.[14] Due to the electrochemical potential difference between the electrodes, a spontaneous electrochemical reaction occurs on discharge, with reduction occurring at cathode (positive electrode) and oxidation at the anode (negative electrode). The physical separation of the negative and positive electrodes, and their connection to an external circuit, allows the system to do work. To maintain electroneutrality, positive ions are transported in the electrolyte, which then react at the respective electrode.[15] See Figure 1.1 for an illustration of an LIB.

As mentioned above, LIBs use graphite as the negative electrode. With graphite being a layered structure, during charge, lithium ions (Li^+) intercalate between each layer, as shown in equation 1.1 below:[16, 17]

$$C_6 + xLi^+ + xe^- \rightarrow Li_xC_6 \tag{1.1}$$

The transition metal oxide, LCO, acts as the positive electrode. Also layered in structure, during charge, Li^+ deintercalates from each layer, with Co^{3+} being oxidised to Co^{4+}[11].

$$LiCoO_2 \rightarrow Li_{1-y}CoO_2 + yLi^+ + ye^- \tag{1.2}$$

To avoid short-circuiting, a polymer-based separator is placed between the electrodes and soaked in the chosen liquid electrolyte. A variety of separators are used commercially, but nearly always are polyolefin based. One intriguing example is the so-called trilayer microporous film made by Celgard.[18] The outer layers are polypropylene (PP) and the central layer is polyethylene (PE); the trilayer architecture is used as a thermal shutdown mechanism, whereby the PE layer melts before PP, blocking ion conduction at elevated temperatures (=130 °C).[19] The electrolyte typically used in LIBs is 1 M lithium hexafluorophosphate ($LiPF_6$), in an organic solvent, 1:1 v/v ethylene carbonate (EC): dimethyl carbonate (DMC).[20, 21]

An important metric in determining battery performance is specific energy (W h kg^{-1}) or energy density (W h L^{-1}), which is a product of a battery's operating voltage and the electrodes' specific capacities (mA h g^{-1}), shown in the equation below:[14]

$$Energy_{cell} = \int_0^Q V_{Cell}\,dq \tag{1.3}$$

Where V_{cell} is the operating voltage and Q the capacity of the cell. Important to note, when judging the practical energy values of new theoretical battery innovations, one needs to include additional weights and/or volumes to the battery including excess electrolyte, the separator, conductive carbon, binder and

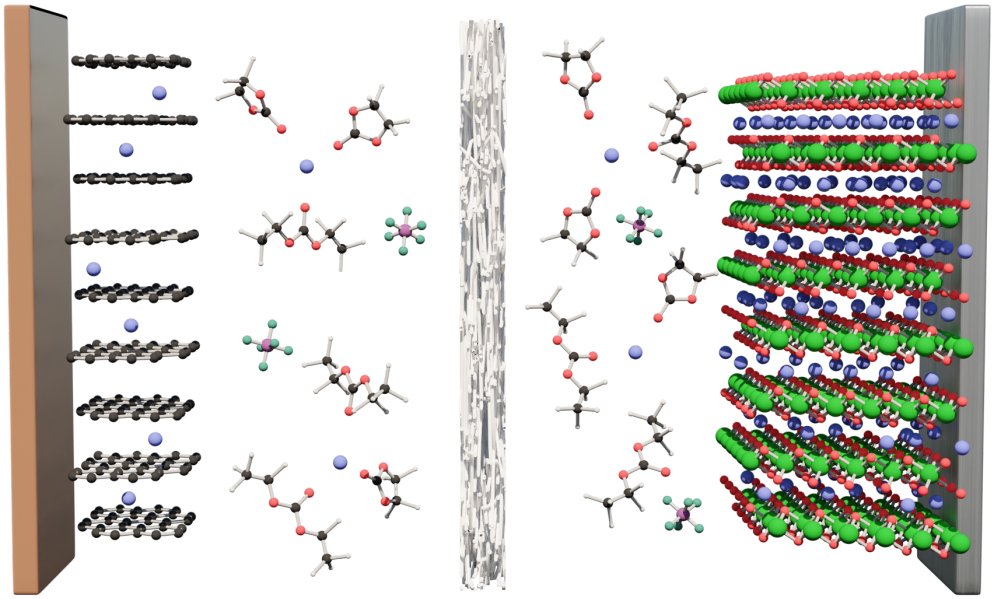


Figure 1.1: Schematic of Lithium-Ion Cell: On discharge, lithium ions deintercalate from graphite (negative electrode), traverse across the interelectrode space, through the polyolefin separator soaked in a $LiPF_6$ carbonate-based electrolyte and intercalate into the layer-oxide, traditionally $LiCoO_2$ (positive electrode). Aluminium is the current collector on the cathode side, and copper is on the anode side. During discharge, electrons flow from the anode to the cathode in an external circuit doing work. Illustration by Dr. Isaac Capone.

current collectors. This level of transparency in the battery field would help for fully understanding a proposed battery chemistry's potential.[22]

Other key parameters to consider include cost, cycle life and power density. Depending on the application, one prioritises some criteria over others; for instance, in grid-scale storage, cycle life and cost are very important, but energy-density less-so,[23] whereas for EVs, specific energy, cost per unit energy ($ per kW h) and power are firm requirements and cycle life is arguably less important.[4]

Specific energy is directly linked to the driving range of EVs, and for EVs to be competitive with fossil-fuel vehicles an increase in specific energy and decrease in $ per kW h is imperative. Furthermore, for aviation to become battery-powered, significant improvement in specific energy is required. Current LIBs are approaching their theoretical specific energy limit (270 W h kg^{-1}), and although there have been recent anode capacity improvements, with Tesla and others researching the addition of silicon to graphite, a more desirable

alternative involves a step-change improvement in capacity by utilising a lithium metal anode.[24]

1.3 Lithium Metal Anodes

With a theoretical specific capacity of 3860 mA h g^{-1} (vs. graphite's 372 mA h g^{-1}), and the lowest reduction potential of any element (-3.04 V vs. SHE (standard hydrogen electrode)) lithium metal is often heralded as the "Holy Grail" of battery anode materials.[25–27] If placed with an equally high specific capacity cathode, one could reach the theoretical specific energy limit of any battery system.[28] This is seen in so-called Li-O_2 batteries and Li-S batteries, resulting in theoretical specific energies of 3505 W h kg^{-1} and 2600 W h kg^{-1} respectively.[29] However, by critically analysing the specific energy calculation, attainable energies for Li-O_2 and Li-S batteries are likely to be 1000 W h kg^{-1} and 600 W h kg^{-1}, respectively.[30, 31] These calculations are highly dependent on cathode loadings, and the amount of additive and electrolyte one uses. Nevertheless, these technologies promise higher specific energies and therefore higher driving ranges for EVs than current state-of-the-art LIB technologies.

Although the systems described above could be seen as the ultimate goal, the use of lithium metal as an anode material, with commercially available transition metal oxide cathodes, would ensure a significant improvement on current specific energies. But for their use to become widely available, there is a considerable hurdle to be overcome: namely, the non-uniformity of Li plating and stripping during cycling.[32, 33] Lithium's inherently low reduction potential and high chemical reactivity means that at the lithium-electrolyte interface, the electrolyte reacts with lithium metal, spontaneously forming an interphase called the solid electrolyte interphase (SEI).[34] The SEI regulates the electrodeposition of Li^+, influencing the current density where stable Li^+ electrodeposition transitions to unstable, non-uniform electrodeposition (the critical current density).[35] If Li continuously electrodeposits non-uniformly during cycling, the SEI expands and contracts, revealing fresh lithium to react with the electrolyte. The constant

reaction with lithium metal reduces the coulombic efficiency (CE) as the electrolyte is reduced to irreversible SEI products. Zheng et al. notes that the CE will need to be at least 99.7% for LMBs to reach commercialisation, but preferably >99.9%, aiming to increase the overall cycle life of the battery. A CE of 99.7% will retain only 22% of its capacity after 500 cycles.[36]

The continuous reaction of the electrolyte with lithium metal means the SEI is in a constant state of repair, with an increasing amount of "active" lithium being transformed into "inactive" lithium (from the formation of SEI) or "dead" lithium, which has been isolated from the electrode surface.[37] Fang et al. demonstrated that the amount of inactive, active and dead lithium in the system after cell cycling was highly dependent on the electrolyte composition.[38] The reductive stability of the electrolyte influences its electrochemical stability against lithium metal, and therefore affects the composition and thickness of the resulting SEI. The passivation of lithium by the SEI will then influence whether active lithium is removed from the surface, transforming into dead lithium.

Classically, the non-uniformity of metal electrodeposition has been studied with metals that deposit at higher potentials (zinc or copper); within the respective electrolyte's so-called electrochemical stability window (ESW).[39] Consequently there was no decomposition of the electrolyte, and subsequently no SEI influence on the electrodeposition behaviour. The pioneering work, primarily led by Chazalviel and co-workers, described how and why metallic electrodeposits would initiate and propagate.[40] When a cell is polarised, a concentration gradient is induced in the electrolyte, and at sufficiently high current densities the concentration at the interface can drop to zero. The time it takes for the concentration to reach zero is the so-called "Sand's time",[41] τ_s, which is influenced by interelectrode distance, current density and inherent electrolyte properties, as will be described later. At τ_s, Chazalviel explains, anions are depleted at the electrode surface leading to an excess of positive charge at the lithium electrode, resulting in a local space charge, with a large electric field.[42] He predicted this will lead to fractal electrodeposits, popularly termed *dendrites*,

which propagate at a velocity proportional to the electric field E and anionic mobility μ_a (see Figure 1.2). Their theory was initially proven experimentally by Chazaviel and co-workers on copper.[42] However, if one uses lithium metal, unstable electrodeposition has been shown to occur prior to τ_s.[43, 44]

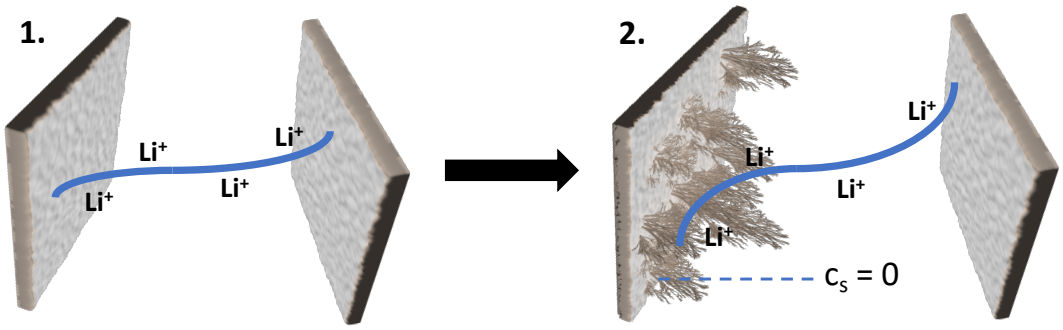


Figure 1.2: Sand's Time 1) Low current regime where a shallow Li^+ concentration gradient forms. This can cause surface roughening, and growth of mossy lithium from non-uniform electrodeposition 2) High current regime where large Li^+ concentration gradient form, leading to growth of needle or fractal dendrites, penetrating the separator and short-circuiting the battery. The time when c_s drops to zero is termed Sand's Time, τ_s.

The ramified growth that occurs before τ_s is primarily influenced by SEI composition, and has been characterised as "reaction-limited", where the electrodeposits have a moss-like morphology.[45] Depending on the electrolyte, these deposits have been observed at current densities as low as 10 μA cm^{-2}, with growth occurring at the base of the filaments. Conversely, dendrite growth as described by Chazalviel is described as diffusion-limited growth, with electrodeposition occurring at the tips of fragments.[43] The fractal dendrite is of especial safety concern, as it has the potential to traverse across the interelectrode space, penetrate the separator and short circuit the cell. With organic electrolyte mixtures being flammable, this could lead to thermal runaway and catastrophic cell failure. Bai et al. tracked the growth of lithium plating using optical microscopy and were able to distinguish the point at which the mechanism shifted from reaction-limited to diffusion-limited.[45] Crowther and West also noticed the transition between the two growth mechanisms, concluding the proportions of salt and solvent dictated

the time at which dendrites formed.[46] It is necessary to prevent both growth mechanisms if lithium metal batteries (LMBs) are to be commercially realised. The mitigation of non-uniform plating is likely to be dictated by the development of electrolytes that promote homogeneous electrodeposition.

1.4 Electrolytes

The electrolyte is the ionically conductive but electronically insulating medium between the anode and cathode.[47] In LIBs and LMBs, it is critical in determining their performance. Classically, an electrolyte solution in lithium-based batteries is composed of a lithium salt and a solvent. Over time, additional salts and co-solvents have been included in electrolyte mixtures to enhance the performance of the respective battery choice.[48] For each battery type, key requirements include: excellent mass-transport properties; the facilitation of fast charge-transfer at each electrode surface; electrochemical stability against each electrode; an ability to provide suitable decomposition products for stable SEI formation; thermal stability; safety and low cost.[49] In LMBs in particular the electrolyte heavily influences the morphology of the dendrites that form.[25] It is therefore of paramount importance to understand how each property influences overall battery performance. For LIBs, as mentioned above, $LiPF_6$ with a mixture of cyclic and linear carbonates (EC and DMC respectively) is popular; while in LMBs, LiFSI or lithium bis(trifluoromethanesulfonyl)imide (LiTFSI) in an ether solvent is commonly proposed, see Figure 1.3. While the required electrolyte properties will be briefly mentioned, the primary topics in the coming sections will be the improvement of electrolyte *mass-transport* and *charge-transfer* properties.

1.4.1 Electrolyte Mass Transport and Thermodynamic Factor

Since the 1960s, Newman and co-workers developed a theory to fully understand binary electrolyte behaviour, called concentrated solution theory (CST).[50] CST accounts for electrolyte flux in non-ideal conditions. Moreover, by combining CST with their developed porous electrode theory,[51] which describes

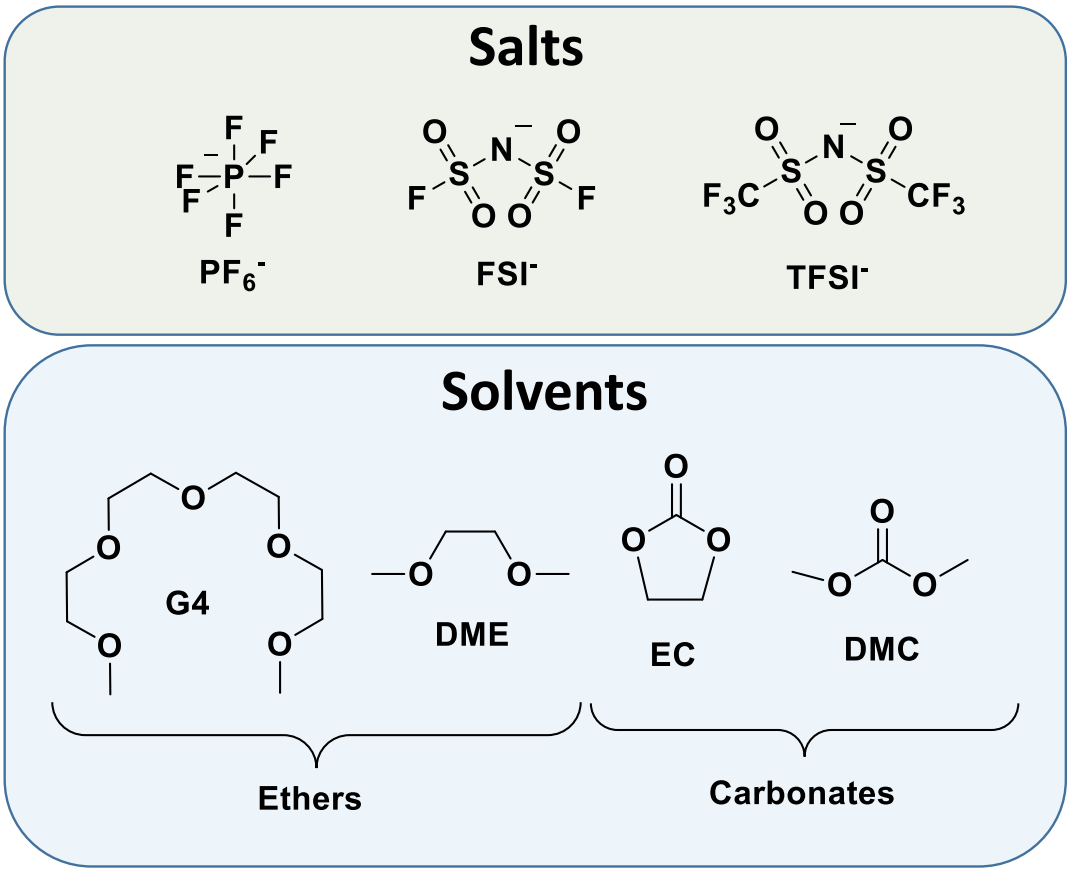


Figure 1.3: Common Salts and Solvents in LIBs and LMBs Salts include $LiPF_6$, LiFSI and LiTFSI. Fluorinated salt promote desirable SEI composition. Solvents include cyclic and linear carbonates, commonly used in commercial LIBs, and ethers, often used to demonstrate LMB capability.

electrolyte behaviour in porous microstructures, Newman developed the most established LIB model used today. The so-called "Doyle-Fuller-Newman model" (DFN)[52] is being utilised in such programs as COMSOL Multiphysics and PyBaMM. To model each battery system various properties of the electrolyte and electrodes are required.

Based on Stefan-Maxwell theory of multi-component diffusion, CST describes the diffusive fluxes of the cation, anion and solvent, and their respective interaction with each other. The standard theory used in PyBaMM and COMSOL Multiphysics is only valid for binary electrolytes; defined as electrolytes that are composed of salts that have one cation type and one anion type. Using these electrolytes, CST concludes there are four main properties that dictate its performance: namely, the

ionic conductivity (κ), the transference number (t_+^0), the salt diffusion coefficient (D_{app}) and the molar thermodynamic factor (χ_M). Understanding CST allows one to fundamentally grasp electrolytes' influence on LIB performance.

Prior to the development of the DFN model, various theories of diffusion had been theorised. First, Fick described a theory of diffusion in 1855 (see Equation 1.4),[53] providing a simple view of diffusion in a binary, "ideal" system. It described the flux of a species from a high to low concentration:

$$N_i = -D_i \nabla c_i \tag{1.4}$$

Where N_i is the flux density of species i, ∇c_i is the concentration gradient of species i and D_i is the proportionality constant named the Fickian diffusion coefficient.

This is included in the most simple equation of ionic flux, shown in Equation 1.5. Most simply, ionic flux is influenced by the electric field, through *migration*, by concentration gradients through *diffusion* and by bulk fluid motion, called *convection*. Overall this leads to the mass-transport equation:[15]

$$N_i = z_i u_i F c_i \nabla \Phi - D_i \nabla c_i + c_i v \tag{1.5}$$

Where u_i is the mobility coefficient of ion i, F is the Faraday constant, $\nabla \Phi$ is the potential gradient, and v is the velocity of the salt. This allows for a good base conceptually on how different components in a multi-component system are influenced by separate forces. The problem is equation 1.5 is invalid in ternary solutions (cation, anion and solvent) as there are two independent concentration gradients, and each species is influenced by both. To address this, Newman turned to using the diffusion model first described by Stefan and Maxwell in 1871 and 1860 respectively.

Stefan and Maxwell derived an equation for diffusion in a multicomponent system:[15]

$$\nabla x_i = -\sum_{j=1}^{N} \frac{x_i x_j}{\mathfrak{D}_{\mathrm{ij}}} (v_j - v_i) \tag{1.6}$$

$$i = 1, 2, 3...N \tag{1.7}$$

Where x_i and x_j are the mole fractions of species i and j respectively, $\mathfrak{D}_{ij}$ is the binary thermodynamic diffusion coefficient as influenced by the frictional interaction between species i and j (Newman often terms this the Onsager-Stefan-Maxwell coefficient), which is a proportionality constant that is influenced by the mole fraction gradient (∇x_i); and v_j and v_i are the velocities of species i and j.

In 1932, Onsager generalised all irreversible transport processes including diffusion, heat conduction and electrical conduction, by forming a theory of microscopic reversibility, describing when two or more irreversible transport processes take place in a thermodynamic system.[54] His discovery of reciprocal relations led to him being awarded the Nobel Prize in Chemistry in 1968. Within his work he provided an equation of diffusion that was equivalent to Stefan-Maxwell's:

$$-\nabla \mu_i = \sum_{j=1}^{M} \mathfrak{D}_{ij} N_j \tag{1.8}$$

$$i = 1, 2, 3...M \tag{1.9}$$

Where $\mathfrak{D}_{ij}$ is proportional to the chemical potential gradient, $\nabla \mu_i$.

In 1965, Newman et al. presented a similar equation to Stefan-Maxwell's (Equation 1.6) and equivalent to Onsager's (Equation 1.8), providing the basis of CST.[55] As noted above, Stefan-Maxwell provided an equation using the mole fraction gradient as the thermodynamic driving force, whereas Newman put it in terms of chemical potential gradient like Onsager (Equation 1.8):

$$c_i \nabla \mu_i = RT \sum_j \frac{c_i c_j}{c_T \mathfrak{D}_{ij}} (v_j - v_i) \tag{1.10}$$

$c_i \nabla \mu_i$ is the driving force per unit volume that is acting on species i and c_T is the total concentration ($c_T = c_0 + c_- + c_+$). The term on the right side of the equation describes the force per unit volume exerted by species j on species i due to its movement with respect to i. Overall, the equation describes a balance between driving force from the chemical potential gradient of the salt and total drag between species i and j.

If one inverts Equation 1.10, introduces current density and uses the solvent as a reference species (v_0 = 0), we can revert back to the diffusion and migration terms described in Equation 1.5, describing the two ions in solution:[15]

$$N_+ = \frac{-\nu_+ \mathfrak{D}}{\nu RT} c_i \nabla \mu_i + \frac{i_i t_+^0}{z_+ F} \tag{1.11}$$

$$N_- = \frac{-\nu_- \mathfrak{D}}{\nu RT} c_i \nabla \mu_i + \frac{i_i t_-^0}{z_- F} \tag{1.12}$$

Where t_+^0 is the cationic transference number, referenced against the solvent velocity, and describes the proportion of current carried by the cation. The chemical potential gradient can be converted into a salt concentration gradient through:

$$\frac{\mathfrak{D}}{\nu RT} \frac{c_T}{c_0} c_i \nabla \mu_i = D \left(1 - \frac{d(\ln c_0)}{d(\ln c)}\right) \nabla c \tag{1.13}$$

D is the diffusion coefficient. D is often labelled as D_{app}, as it is technically the "apparent" diffusion coefficient, as seen by monitoring the flux of species due to salt concentration gradient. The term in brackets describes how the solvent concentration is changing with respect to the salt concentration.

This allows equations 1.14 and 1.15 to be converted to fluxes based on concentration gradients:

$$N_+ = -\nu_+ D_{app} \nabla c_i + \frac{i_i t_+^0}{z_+ F} \tag{1.14}$$

$$N_- = -\nu_- D_{app} \nabla c_i + \frac{i_i t_-^0}{z_- F} \tag{1.15}$$

Equations 1.14 and 1.15 are fundamental equations used in CST to describe mass-transport, with both t_+^0 and D_{app} experimentally measurable quantities. They are fundamental mass-transport properties that describe ion movement and concentration gradient formation (see Figure 1.4). In CST specifically, the overall salt material-balance equation when assuming no convection is:[52]

$$\frac{\partial c}{\partial t} = \nabla . \left(D_{app} \left(1 - \frac{d(\ln c_0)}{d(\ln c)}\right) \nabla c \right) - \frac{i . \nabla t_+^0}{z_+ \nu_+ F} \tag{1.16}$$

Where c_0 is the concentration of the solvent. To understand how concentration of the electrolyte varies in solution, one is ultimately required to solve equation 1.16.

Also required for a full understanding of the electrolyte's influence on battery performance, one needs to know the influence the electrolyte has on the electrochemical potential of the cell. Indeed, current is not only affected by the chemical potential of the salt, but also by the electrical state of the electrolyte. Newman achieves this by first presenting the general equation for a reference electrode:[52]

$$\nabla\Phi = -\frac{i}{\kappa} - \frac{RT}{nF}\sum_i s_i \nabla \ln c_i f_{i,n} - \frac{RT}{F}\sum_j \frac{t_j^0}{z_j}\nabla \ln c_j f_{j,n} \tag{1.17}$$

Where $f_{i,n}$ is the molar activity coefficient, which relates salt concentration with thermodynamic activity, a. By including $f_{i,n}$ one accounts for non-ideality in electrolyte solutions. Activity, sometimes referred to as "effective concentration" is highly influenced by the intermolecular structures present in electrolyte solutions. It is sometimes described as a salt's escaping tendency.[56] κ is the ionic conductivity, which is the reciprocal of the ohmic resistance of an electrolyte. As a binary electrolyte, the reference electrode reaction is:

$$\mathrm{Li(s)} \rightleftharpoons \mathrm{Li^+ + e^-}$$

One can then simplify use Equation 1.17 to describe the potential gradient:

$$\nabla\Phi = -\frac{i}{\kappa} + \frac{2RT}{nF}\left(1 + \frac{d\ln f_{\pm}}{d\ln c}\right)(1 - t_+^0)\nabla \ln c \tag{1.18}$$

The first part of the equation describes the potential gradient due to current flow and ohmic resistances, and the second part describes potential differences as a result of concentration gradient formation. $\left(1 + \frac{d\ln f_{\pm}}{d\ln c}\right)$ is often described in the literature as "The Thermodynamic Factor" or χ_M.[57–59]

Fundamentally, CST is described by equations 1.16 and 1.18 to understand how salt concentration and potential varies in electrolytes.

In summary, Newman utilised diffusion theories from Stefan-Maxwell and Onsager to describe the diffusion of binary, non-ideal electrolytes, and provided a

novel equation to describe the electrochemical potential in electrolytes specifically, which was required to fully simulate battery performance. CST was combined with porous electrode theory to fully describe battery performance, and was named the Doyle-Fuller-Newman model after their seminal paper that presents it.

To reiterate, from the CST equation one should note that concentration-dependent mass-transport properties including the transference number (t_+^0) and the "apparent" Fickian diffusion coefficient (D_{app}), and electrolyte thermodynamic properties including ionic conductivity (κ) and the molar thermodynamic factor (χ_M) are required to solve them.

Going further, Newman noted that by measuring each of these properties one can calculate the specific Onsager-Stefan-Maxwell diffusion coefficients ($\mathfrak{D}_{ij}$) to understand the frictional interactions between each species in the solution.[15, 59]

$$\mathfrak{D} = \frac{2D_{0+}D_{0-}}{z_+D_{0+} - z_-D_{0-}} \tag{1.19}$$

$\mathfrak{D}_{0+}$ and $\mathfrak{D}_{0-}$ are the Onsager-Stefan-Maxwell intermolecular diffusion coefficients of the cation (+) and anion (-) respectively, and their interaction with the solvent. One can also relate $\mathfrak{D}$ to the Fickian D_{app} [15, 59] by equation 1.20.

$$D_{app} = \mathfrak{D}\frac{c_T}{c_0}\chi_M(1 - c_sV_s) \tag{1.20}$$

Where V_s is the partial molar volume of the salt. Newman derived individual Stefan-Maxwell diffusion coefficients based on ion-ion and ion-solvent interactions:

$$\mathfrak{D}_{0+} = \frac{-z_-}{z_+ - z_-}\frac{\mathfrak{D}}{1 - t_+^0} \tag{1.21}$$

$$\mathfrak{D}_{0-} = \frac{z_+}{z_+ - z_-}\frac{\mathfrak{D}}{t_+^0} \tag{1.22}$$

$$\mathfrak{D}_{+-} = \left(\frac{z_+z_-c_TF^2}{\kappa RT} - \frac{z_+ - z_-}{z_+v_+}\frac{c_0t_+^0(1 - t_+^0)}{c\mathfrak{D}}\right)^{-1} \tag{1.23}$$

Indeed, to calculate $\mathfrak{D}$ from D_{app} one needs to know the partial molar volumes of the salt and solvent in solution. This can be calculated from electrolyte density and its dependence on concentration. Using the derived equations:[15]

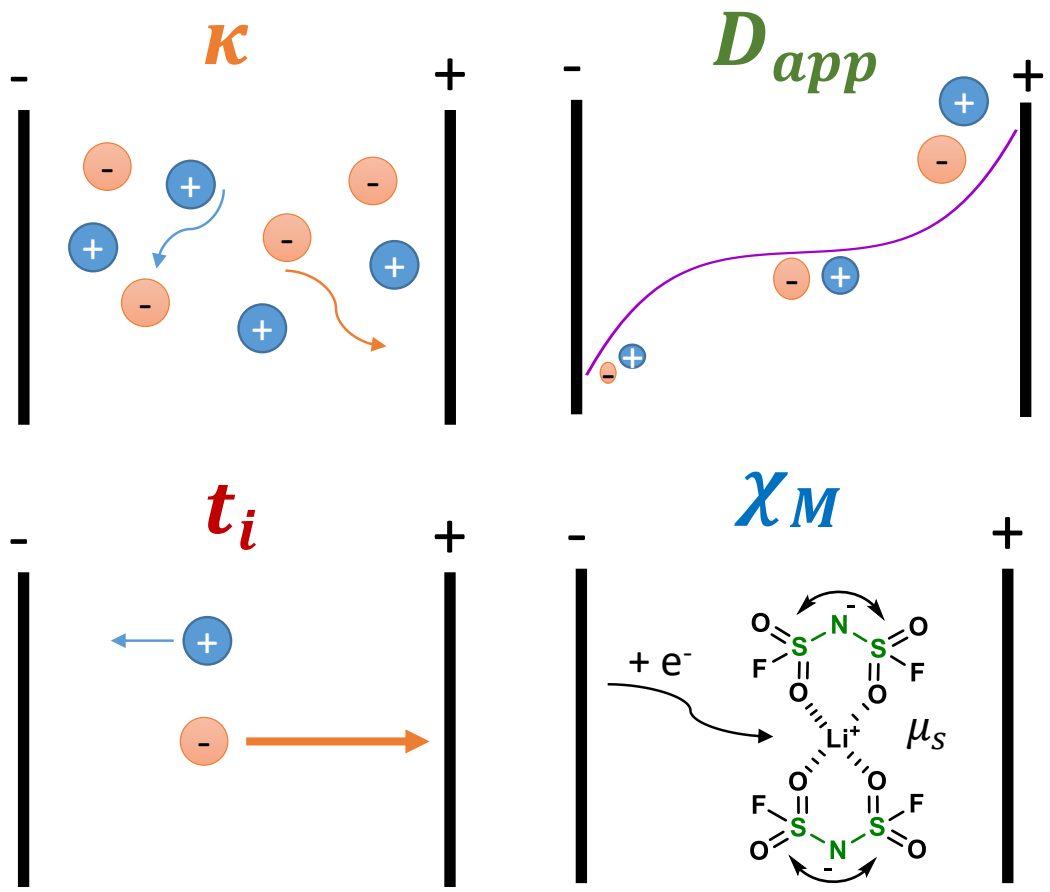


Figure 1.4: Transport and Thermodynamic Properties of Electrolytes: Ionic Conductivity, κ, describes the ease of movement of ions; Diffusion Coefficient, D_{app}, is the proportionality constant in Fick's law of diffusion, describing how well the salt moves in response to a concentration gradient; Transference Number, t_i, is the fraction of current carried by ion i, and Molar Thermodynamic Factor, χ_M, relates concentration to thermodynamic activity (related to chemical potential, μ_s), influenced by electrolyte intermolecular structure.

$$V_s = \frac{M_s - \frac{d\rho}{dc}}{\rho - c\frac{d\rho}{dc}} \tag{1.24}$$

$$V_0 = \frac{M_0}{\rho - c\frac{d\rho}{dc}} \tag{1.25}$$

By calculating each of the Stefan-Maxwell intermolecular diffusion coefficients, one can build a clear picture of the frictional interactions between salt and solvent.

Measuring D_{app}, t_+^0, κ and χ_M of electrolytes is by no-means trivial and will be a significant part of this project. Indeed, by obtaining each of these, one can

implement them into the DFN model to accurately simulate battery performance. Considering the importance of electrolyte development in the progression of next-generation battery technologies, the understanding and implementation of the described properties is paramount.

1.5 Characterising Electrolyte Properties

1.5.1 Ionic Conductivity

κ is the most frequently characterised electrolyte property due to its comparatively straightforward setup. Furthermore, it is often used as a proxy for understanding diffusional behaviour with κ being linked to ionic diffusion coefficients through the Nernst-Einstein equation:[60]

$$\kappa = \frac{F^2}{RT}(cD_+ + cD_-) \tag{1.26}$$

Where D_+ and D_- are the ionic self-diffusion coefficients of the cation and anion respectively. However, the equation assumes that ions do not interact with each other, and so is only valid in infinitely dilute solutions.[60]

As was noted above, κ is the reciprocal of the ohmic resistance. Most simply, by eliminating the possibility for concentration variations, equation 1.18 simplifies to Ohm's law:

$$\Delta\Phi = \frac{I}{\kappa} \tag{1.27}$$

κ can therefore be calculated by measuring the current response after an applied voltage if no potential accumulates due to charge-transfer kinetics or concentration gradient formation. This is achieved by using "blocking" electrodes, defined as electrodes where no chemical reactions occur. Due to polarisation errors occurring from a 2-electrode measurement, it is often recommended to measure κ via a 4-electrode measurement, where one set of electrodes applies a voltage and the other set measures the resulting current.[61] Current is a function of interelectrode distance and electrode area, so an accurate knowledge

of these values is necessary; if using a specially designed conductivity cell this is included as the "cell constant".

Although the measurement can be performed using a standard chronoamperometry (CA) experiment, it is most frequently performed via Electrochemical Impedance Spectroscopy (EIS).[62] See the Method Fundamentals section for further details on EIS theory. By analysing the resulting Nyquist Plot the ohmic resistance can be extracted and using the cell constant, κ can be calculated.

In binary electrolytes, κ increases with concentration until the viscosity increase outweighs this effect, and then κ drops, see Figure 1.5.

1.5.2 Diffusion Coefficient

D_{app} is characterised most readily via the restricted-diffusion method.[57–59, 63] Using a 2-electrode cell of known interelectrode distance (L), and following the relaxation from an arbitrarily formed concentration gradient, the semi-log of the open circuit voltage (OCV) decay can be followed with time. The ln(OCV) curve eventually becomes linear after enough time has elapsed, and the resulting slope is proportional to D_{app}. It is then calculated using equation 1.28 below:

$$\lim_{t\to\infty} \frac{d\ln(OCV)}{dt} = -\frac{\pi^2 D_{app}}{L^2} \tag{1.28}$$

Many researchers studying electrolyte properties turn to using pulsed-field gradient nuclear magnetic resonance spectroscopy (pfg-NMR) to study self-diffusion coefficients of individual ions (D_i).[64–67] Self-diffusion coefficients describe ionic movement in the absence of a chemical potential gradient. Unlike calculating D_{app} however, one can obtain an idea of how individual ions move in solution. There is a general consensus that calculating the harmonic-mean of D_i provides a good estimation of D_{app}:

$$H = \frac{n}{\sum_{i=1}^{n} \frac{1}{D_i}} \tag{1.29}$$

Where H is the harmonic mean and n is the number of ions present. Also by collecting information on individual D_i values, an ionic conductivity can be

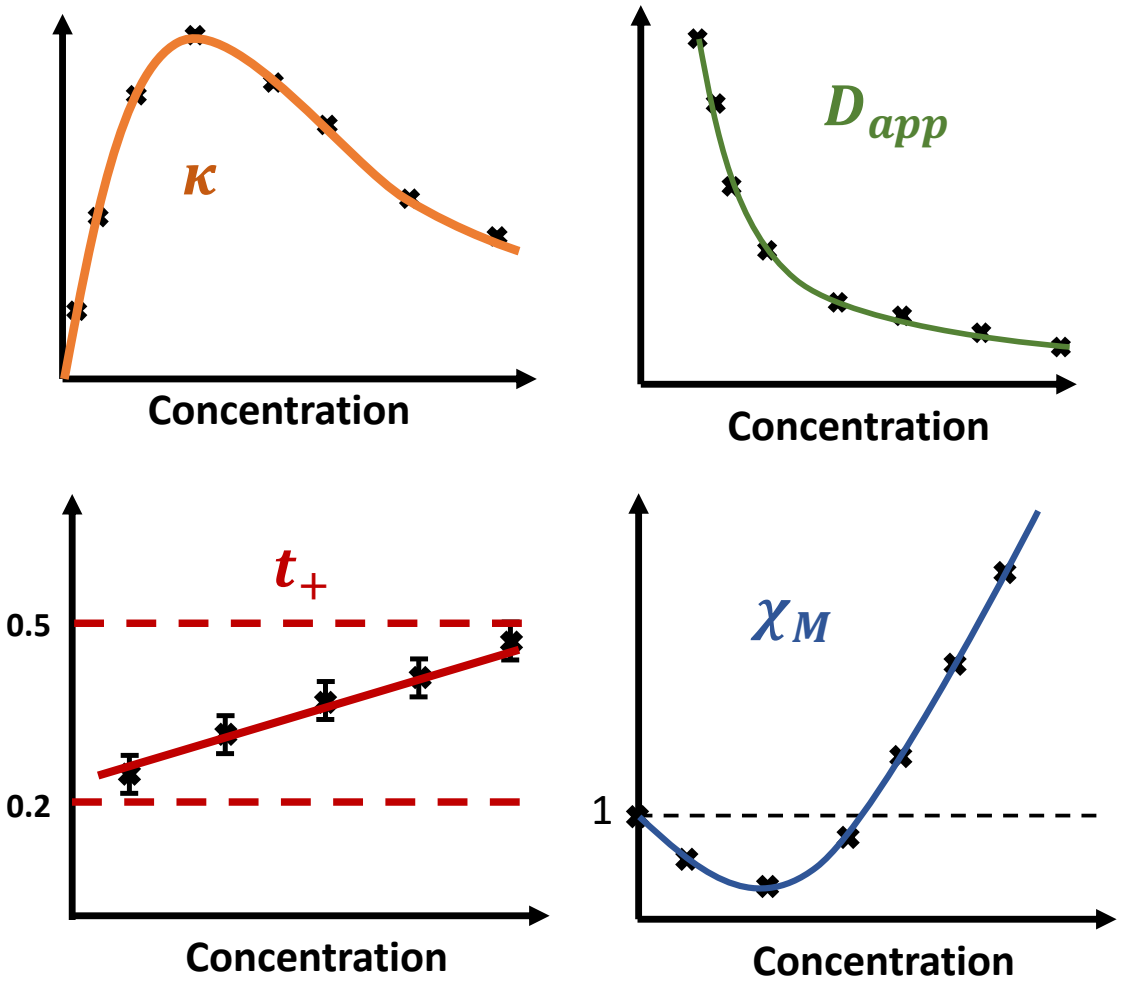


Figure 1.5: Concentration Dependency on Electrolyte Properties: κ an initial increase due to increased concentration of ions, then decrease because of large viscosity increase; D_{app}, decrease due to increase viscosity at high concentrations; t_+, usually positioned between ~0.2 and 0.5, with an example trend of increase with concentration, but other trends have been measured too[58]; χ_M is 1 at infinitely dilute concentrations and decreases due to association between cation and anion, but begins to increase because of depleting free solvent to solvate

estimated using equation 1.26. By calculating the ratio between conductivities calculated by pfg-NMR and by electrochemical means, one can estimate the extent of ion association in solution. The ratio is termed the Haven ratio.[68]

In binary electrolytes, D_{app} decreases with concentration as the solution becomes more viscous, see Figure 1.5.

1.5.3 Transference Number

As alluded to earlier, the transference number (t_i) is defined as the fraction of current carried by a specific ion (i) in solution:[15]

$$t_i = \frac{z_i F N_i}{i} \tag{1.30}$$

The flux is a combination of both diffusion and migration, as stated by equation 1.5. In a binary electrolyte, the anion is driven by both diffusion and migration, but these oppose each other until steady-state is reached, when they are exactly equal to one another. The cation, however, experiences migration and diffusion in the same direction as it is continuously consumed at the electrode. t_+ can also be related to mobilities through:[15]

$$t_+ = \frac{z_+ \mu_+}{z_+ \mu_+ + z_- \mu_-} \tag{1.31}$$

Historically, the most popular method for measuring t_+ is termed "the Hittorf method", developed by Hittorf in the 19th century.[56] The method involves measuring the change in concentration between two compartments after an amount of charge is passed. The concentration change in each compartment is proportional to t_+:

$$t_+ = 1 - \frac{\Delta n_{cell}}{n_{charge}} = \frac{F(\Delta c_s)A}{Q} \tag{1.32}$$

$$\Delta c_s = c_s^i - c_s^f \tag{1.33}$$

Where n_{charge} is the number of moles of e^- passed, n_{cell} is the molar difference between the two sides of the cell before and after time, t, Q is the charge passed over time, A is the area of the electrode and c_s^i and c_s^f are the initial and final concentrations of each compartment, respectively. Note the use of t_+ as opposed to t_+^0, with the latter being reserved for CST when ionic movement is referenced to the solvent's movement. Hou and Monroe derived an equation to include the solvent reference velocity, allowing the Hittorf method to be used in conjunction with CST:[58]

$$t_+^0 = 1 - \frac{\Delta n_{cell}}{n_{charge}} = \frac{F(\Delta c_s)A}{Q(1 - c_s V_e)} \tag{1.34}$$

Although the Hittorf method is regarded as the most rigorous and accurate method for measuring t_+^0, few researchers perform it, perhaps due to the large electrolyte volume required; difficulty in measuring the concentration in each compartment; impractical battery conditions (large interelectrode distance and lack of separator), and the specialised experimental setup. Indeed, Lewis even mentioned this in 1910[69]:

"In spite of the very important role that the transference numbers of electrolytes have played in chemical theory, since Hittorf developed sixty years ago, the method of determining these quantities by analysis of the electrode solutions, few really accurate transference numbers have been obtained. This is doubtless due to the very great patience and experimental skill demanded by the Hittorf method."

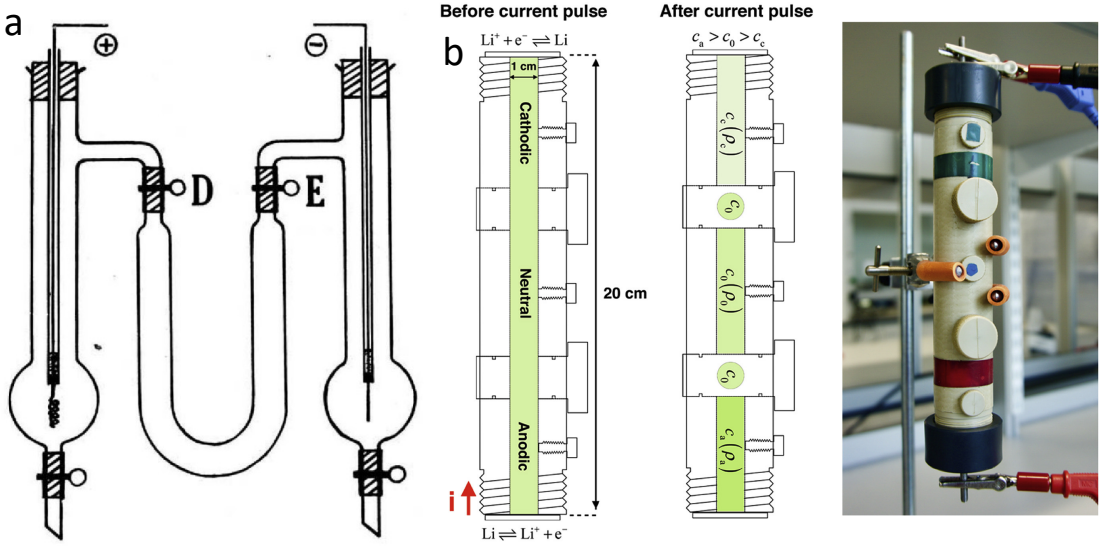


Figure 1.6: Comparison between Hittorf method apparatus designed by: a) Hallam in 1954 using glass flasks and connectors an a large volume of electrolyte. Reprinted (adapted) with permission from Ref. [70]. Copyright 1954 American Chemical Society. b) Hou in 2020 using a linear design made of plastic polyether ether ketone (PEEK) and less electrolyte ($\sim$ 15 mL). Adapted with permission under the Creative Commons Attribution 4.0 International License from Ref. [58].

Two alternative methods were developed to address the shortcomings of the Hittorf method that have subsequently become increasingly popular, namely the "steady-state methods." Here, they define t_+ as:

$$t_+ = \frac{D_+}{D_+ + D_-} \tag{1.35}$$

Which is a good approximate for the rigorously defined transference number described above. One procedure, termed the Bruce-Vincent (BV) method,[71] induces a concentration gradient in a 2-electrode setup, until the gradient reaches steady-state. Initially they proved:

$$t_+ = \frac{I_s}{I_0} \tag{1.36}$$

Where I_0 is the initial current that includes the ohmic resistance, and I_s is the steady-state current, which they assume only includes the effect of ohmic and concentration gradient resistance. To include the interfacial resistance in the steady-state current, they formulated another equation that required an EIS measurement before and after the measurement:[72]

$$t_+ = \frac{I^s(\Delta V - I^0 R^0)}{I^0(\Delta V - I^s R^s)} \tag{1.37}$$

Where ΔV is the applied voltage, R^0 is the initial ohmic and charge-transfer sum before polarisation and R^s is the resistance after polarisation. Rarely mentioned however is the difficulty in defining each process (as illustrated in a Nyquist plot semi-circle) as a purely diffusive process or an interfacial one. Mistakes are easily made if processes are not so well defined, leading to overlapping semi-circles due to similar time-constants – this means incorrect R^s and R^0 are used.

Using the same theory of steady-state concentration gradients, Sørenson and Jacobsen formulated a method for measuring t_+ purely by EIS.[73] When using this method, it requires the isolation of the finite-length Warburg diffusion element, which describes the resistance resulting from the concentration gradient formation. This means the measurement has to achieve very low frequencies, depending on the interelectrode distance of the cell.[74] The formula to calculate t_+ is:

$$t_+ = \frac{R_{bulk}}{R_{bulk} + W_d} \tag{1.38}$$

It is easier here to state whether the diffusive and interfacial processes are separated because frequencies are scanned low enough (unlike BV). W_d has a characteristic 45° angle in the Nyquist plot, so one can know confidently if W_d is present.

Both steady-state methods require a two electrode setup (simply a coin-cell, for example), with small interelectrode distances and small polarisation voltages. The popularity of the BV method would seemingly be due to the small amount of electrolyte required, the more realistic cell conditions and the quick data acquisition. However, the steady-state methods have critical assumptions that make them incompatible with CST. Both methods assume the electrolyte to be infinitely dilute, or perfectly thermodynamically ideal, in other words. This can lead to misleading conclusions, as illustrated by Doyle and Newman.[75] They measured t_+^0 of 2.58 M $NaCF_3SO_3$ in poly(ethyleneoxide) at 85 °C to be -4.38. Using their rigorously measured values for D_{app}, κ and χ_M, they concluded that t_+ measured using BV would be 0.37. The stark difference between values obtained rigorously using Hittorf, and by BV illustrates the importance of accurate transference number measurement. The same is true for the EIS method. Also, there is a requirement for reasonable chemical stability of the electrodes when using steady-state methods, as one needs to distinguish between interfacial and diffusive processes. This is especially difficult when characterising sodium or potassium-based electrolytes, with poor chemical stability against sodium and potassium metal electrodes.[76]

Another popular method for understanding t_+ is using pfg-NMR, by utilising data from measuring D_i (see equation 1.35). Although it is a popular method, there is a specific problem associated with it. Namely, the measurement is not taken in the presence of an electric field, which can lead to misleading values. This has been addressed by the recent popularisation of a technique termed "electrophoretic" pfg-NMR (eNMR). Although Holz introduced the theory

in 1994,[77] it was only Schönhoff and co-workers who utilised it to full-effect in 2015.[78] Multiple revelations have been described since its widespread use, for example the negative transference of Li^+ in ionic liquid solvents, as described below.[79] The application of an electric field is critical for a full understanding of electrolyte transport. To measure t_+ using pfg-NMR requires a probe for analysis of specific active nuclei. Although it is quite common to have access to probes for ^{7}Li analysis, it is much less common to have access to other probes for ^{23}Na and ^{39}K if one were to analyse Na-ion or K-ion electrolytes.

In Li-ion electrolytes, t_{Li^+} is often measured to be lower than t_-. Due to it being charge-dense, it can be heavily solvated, reducing its movement and lowering the t_{Li^+} value compared to t_-. The trend with concentration is dependent on the electrolyte system one uses. Figure 1.5) shows a common trend, where t_+ is increasing with concentration as anions become involved in complexation and solvation. However, the opposite trend can be measured as illustrated by Hou et al., who measured a decrease of t_+ with concentration using a $LiPF_6$ in PC electrolyte.

1.5.4 Thermodynamic Factor

χ_M is a measure of electrolyte ideality, providing a link between observed concentration and thermodynamic activity.[52]

$$\chi_M = 1 + \frac{dlnf_\pm}{dlnc} = \frac{dln\frac{cf_\pm}{c_0 f_\pm}}{dln\frac{c}{c_0}} = \frac{dln\frac{a}{a_0}}{dln\frac{c}{c_0}} \tag{1.39}$$

Where a_0 and c_0 are reference activities and concentrations respectively. By explicitly expanding this factor, one can more easily note what it is fundamentally describing. It shows how the thermodynamic activity (measured by potential differences) is changing with respect to measured concentration. χ_M is influenced by ion association, with the formation of solvent-separated ion pairs (SSIPs), contact ion pairs (CIPs) and aggregates (AGGs), and the extent and orientation of solvation.[56] Classically, Debye-Hückel theory describes electrostatics between ions in solution; these ionic movements are not random and Debye and Hückel

formulated a quantitative theory to describe the ionic distribution. Debye-Hückel theory predicts that χ_M decreases with increasing salt concentration; a higher ionic concentration leads to greater association and therefore a lower "effective concentration".[80]

$$log\gamma_{\pm} = -Az_{+}z_{-}\sqrt{I} \tag{1.40}$$

Where $\gamma_{\pm}$ is the activity coefficient. The term on the right-hand side is from classical Debye-Hückel theory, where I is the molar ionic strength, A is a temperature dependent coefficient informing the extent of association. Since then, there have been multiple extensions to this theory as experimentalists noticed deviations from it. Koryta proposed the equation:[80]

$$log\gamma_{\pm} = -\frac{Az_{+}z_{-}\sqrt{I}}{1+Ba\sqrt{I}} + CI \tag{1.41}$$

Where B is an additional coefficient describing association, a is an adjustable parameter found experimentally and CI is a linear term that generally describes an increase in $log\gamma_{\pm}$ as free solvent depletes. Additionally, the orientation of the solvent molecules in solution weaken the associated ionic interaction, so the activity increases. Therefore, with concentration, χ_M is often seen to decrease initially from 1, then increase as the associated interaction begins to weaken (see Figure 1.5). Guggenheim derived an extended Debye-Hückel equation,[81] which utilises an $x^{1/2}$ power series. This has been the most popular fitting method in recent years.[58, 59] Hou and Wang illustrate this in Figure 1.8: due to the high dielectric constant of PC, χ_M does not reduce to below 1 with very little association taking place. However, with EMC as a solvent, association is much more likely to occur (Figure 1.8b). Both were fitted with an $x^{1/2}$ power series.

χ_M of electrolytes is classically measured potentiometrically by defining the liquid-junction potential of a concentration cell.[58, 59, 82, 83] This consists of a cell with two chambers to house different electrolyte concentrations, separated by a glass-frit membrane, measuring the open circuit voltage (OCV) of the cell. As noted in equation 1.42, if there is no current, χ_M is defined as:

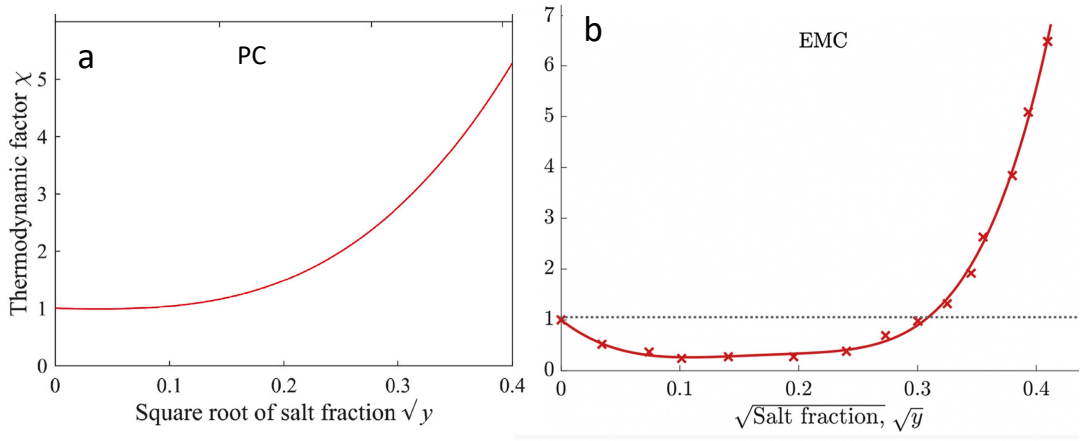


Figure 1.7: χ_M **dependence on concentration of LiPF$_6$ in** a) PC. Adapted with permission under the Creative Commons Attribution 4.0 International License from Ref. [58]. b) EMC. Reprinted (adapted) with permission from Ref. [63]. Copyright 2020 Elsevier.

$$\chi_M = \frac{nF}{2RT(1-t_+^0)} \frac{\nabla \Phi}{\nabla \ln \frac{c_2}{c_1}} \tag{1.42}$$

Where c_2 and c_1 are the electrolyte concentrations in each cell chamber. Important to note is the requirement of t_+^0 for accurate determination of χ_M. With the multiple problems associated with determining t_+^0, this has made χ_M equally difficult to measure. χ_M or any relevant activity-dependent property is very rarely measured for novel LIB or LMB electrolytes, but its importance should not be underestimated for a full thermodynamic understanding of the system.

1.5.5 Concentration Gradient Visualisation

Each of the four transport and thermodynamic properties described provide information to ultimately characterise the concentration and potential gradients present in batteries. Therefore, inversely, by visualising concentration gradients one can extract the two transport properties. Using magnetic resonance imaging (MRI), X-ray spectroscopy and Raman techniques, a few researchers have directly measured the concentration profiles and extracted D_{app} and t_+^0 values.

In 2012, Klett et al. first demonstrated the use of ^{7}Li NMR imaging (MRI) to obtain temporally and spatially resolved electrolyte concentration profiles, isolating D_{app} and t_+.[84] By utilising NMR to visualise an electrolyte concentration

gradient and then accurately measure two of its transport properties allowed Klett to characterise the electrolyte without employing conventional techniques such as Hittorf and Restricted-Diffusion. Subsequently, Goward, Krachkovskiy and co-workers have conducted a series of studies utilising pfg-NMR and MRI to visualise concentration gradients and deduce values of D_i (self-diffusion coefficients), D_{app} and t_+ for various electrolytes. Initially, in 2013, they performed "slice-selective" NMR measurements by initiating a concentration gradient and conducting a pfg-NMR measurement within a 2 mm slice.[85] Measuring D_{Li+} of 1 M LiTFSI in PC at the extremes of the cell showed D_{Li+} of 9.2 $\pm$ 0.3 m^2 s^{-1} at the negative electrode ($\sim$1.16 M) and 7.1 $\pm$ 0.2 m^2 s^{-1} at the positive electrode ($\sim$0.80 M). Then, they performed multiple studies that combined in-situ MRI experiments and pfg-NMR with inverse mathematical modelling to extract spatially resolved D_{app} and t_+ values; in 2015 with 1M LiTFSI in PC in non-steady state conditions;[86] in 2016 with $LiPF_6$ in EC:DMC 1:1 v/v (LP30) in steady-state conditions;[87] in 2017 with LP30 in steady-state and temperature-dependent;[88] in 2018 and 2019 with LP30 with an aim to understand aggregates and dendrite growth respectively,[89, 90] and finally in 2020 where Bazak et al. presented a comprehensive study of their established technique on 1 M $LiPF_6$ in EC:PC:DMC 5:2:3 v/v at different current densities and temperatures.[91] Bazak explicitly mentioned the difficulty in measuring t_+^0 as a very accurate measurement of concentration gradient was necessary when using high current densities (large polarisation). Additionally they estimated D_{app} with the harmonic mean (equation 1.29) of the self-diffusivities, D_{Li^+} and $D_{PF_6^-}$. Although this estimation has been shown to be a good approximate, it would be more valid to identify the Fickian diffusivity by monitoring the diffusion length prior to steady-state conditions having been reached. Indeed, the main advantage of the described technique using MRI concentration visualisation is its compatibility with pfg-NMR to estimate spatially resolved diffusivities. This is unique to NMR techniques for measuring transport. However, there are some inherent problems associated with using NMR imaging; namely, when measuring close to conductive electrodes (Li-metal,

current collectors etc.) there can be signal attenuation due to distortions of the static and radiofrequency magnetic fields. This is especially important if one is hoping to measure interfacial concentration gradients for t_+^0 calculations.

Takamatsu et al. in 2018 demonstrated the use of operando X-ray phase imaging to visualise concentration distributions for the first time, where they isolated D_{app} of 1 M $LiClO_4$ in EC/EMC 1:2. Experimentally they used a two-crystal X-ray interferometer with synchotron radiation.[92] Recently, in 2020, Steinrück et al. used operando X-ray techniques with continuum modelling and molecular dynamics (MD) to experimentally measure and simulate electrolyte concentration gradients.[93] Specifically by using a LiTFSI in PEO electrolyte, they measured local electrolyte velocities with synchotron X-ray Photon Correlation Spectroscopy (XPCS) and full concentration gradients via X-ray Absorption Microscopy (XAM). Additional insight was gained using MD. This was the first time the velocity of species was measured in an electrochemical system. The authors also isolated t_{Li+} in their electrolyte system. Although the primary aim of both studies was not to isolate all the transport and thermodynamic properties of the electrolyte, the techniques' capabilities could allow for a full electrolyte characterisation. However, the availability of the instruments, especially synchotron XPCS, limits the usage of this technique for electrolyte characterisation moving forward.

The availability issues of MRI and X-ray techniques have led to investigations into other experimental methods. Another analytical technique that can provide information on intermolecular structure and therefore monitor electrolyte concentration differences is Raman Spectroscopy. In 1998, Rey et al. first used confocal Raman microspectroscopy to monitor concentration differences in a Li|LiTFSI in PEO|Li symmetric cell at 80 °C, consequently determining D_{app} and t_+.[94] Importantly, according to the authors, this was the first time salt concentration gradients were measured using any technique. Georén et al. used the technique to verify a transport model and parameters they gathered from conventional methods.[95] Using LiTFSI in a PEO/PPO copolymer, they found their transport model agreed well with the in-situ Raman data. However, they did not perform

accurate line-scans, nor did they attempt to isolate transport and thermodynamic parameters for their Raman data. 12 years later, Forster et al. first used confocal Raman Spectroscopy to monitor Li^+ concentrations in liquid electrolytes.[96] They specifically used two different concentrations of lithium perchlorate ($LiClO_4$) in DMC (0.8 M and 1 M) and measured the diffusion coefficient in a microfluidic device. They created concentration gradients within the Y-shaped device, so were not passing current to create gradients, as in a conventional electrochemical cell setup. More recently Cheng and co-workers used stimulated Raman scattering (SRS) microscopy for three-dimensional visualisation of Li^+ concentration near the surface of lithium electrodes, further proving the value of in-situ Raman techniques.[97] Finally, in 2020, Wei et al. probed Li^+ concentration in an EC:DMC based solvent at the surface of LFP cathode particles.[98] Each of the above examples illustrates the capability of Raman spectroscopy in monitoring Li^+ concentration in electrolytes. However, only Rey et al. determined the transport properties, albeit at limited resolution and of polymer electrolytes. A large proportion of this thesis looks at furthering the work of Rey et al. by using operando Raman microspectroscopy to visualise liquid electrolyte concentration gradients to measure fundamental properties.

1.5.6 Literature Electrolyte Measurements

This section will describe the main electrolytes used in LIBs and LMBs, with examples of measurements of the previously described electrolyte properties.

Prior to the development of LIBs, electrolytes were primarily aqueous due to their high κ, safety and low cost.[99] However, due to the very narrow ESW of water, at 1.23 V, aqueous electrolytes were deemed unfit for use in high-energy LIBs. SONY therefore opted for an electrochemically stable, organic-based liquid electrolyte system; namely, 1 M lithium hexafluorophosphate ($LiPF_6$) in ethylene carbonate (EC): dimethylcarbonate (DMC) (1:1) (LP30).[100] EC is cyclic and DMC is linear, with EC exhibiting a higher dielectric constant than DMC; EC is therefore more viscous and preferentially solvates Li^+, while DMC lowers the

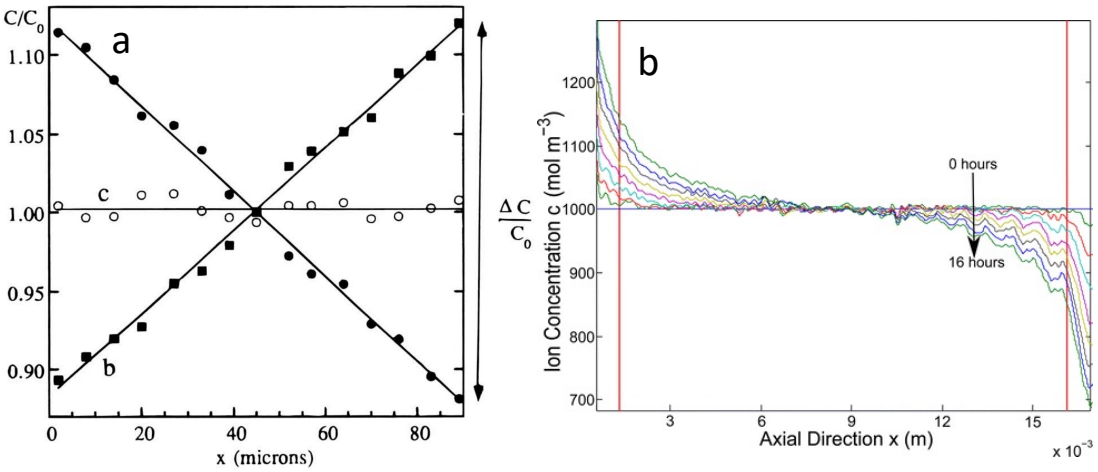


Figure 1.8: Concentration Gradient Visualisation: a) First to achieve this was Rey et al., using Raman Spectroscopy, using LiTFSI in PEO. Reprinted (adapted) with permission from Ref. [94]. Copyright 2015 IOPscience. b) Operando measurements allowed for the monitoring of gradient formation, illustrated by Sethurajan et al., using MRI and a LiTFSI in PC electrolyte. Reprinted (adapted) with permission from Ref. [86]. Copyright 2015 American Chemical Society.

viscosity to increase the overall ionic conductivity. LP30 has an ESW of 4 V, with oxidation occurring at 4.2 V as EC polymerises into polycarbonate species.[101] Although a variety of fluorinated and non-fluorinated salts were tested for use in LIBs, $LiPF_6$ has become the most widespread.[100] Xu notes that this was due to a well-balanced set of properties, as opposed to any high performing single property.[99] As mentioned above, classical CST is technically only valid for binary electrolytes, with one solvent (3 components). In principle, Onsager stated the number of independent phenomenological transport properties is given by $n(n-1)/2$ (κ, t_+^0 and D_{app}), where n is the number of species present.[59] And with most commercial electrolytes containing more than one solvent, this leads to increasing complexity and is an additional hurdle for full electrolyte characterisation. Newman has mentioned that if the multi-component solvent is treated as one species it does not appear to introduce significant error into the calculation, so most researchers use this assumption.[15, 57] Landesfeind and Gasteiger provided a full concentration and temperature-dependent analysis of $LiPF_6$ in EC:DMC (1:1) and EC:EMC(3:7), and an EC-free alternative EMC:FEC(19:1).[82] At 20

Table 1.1: Selected Carbonate Electrolyte Transport and Thermodynamic Properties at 20^oC

Electrolyte	κ / mS cm^{-1}	D_{app} / $\times 10^{-11}$ m^2 s^{-1}	t_+^0	χ_M	Ref
1M $LiPF_6$ in EC:DMC (1:1)	11 [a]	30 [c]	0.25 [c e]	2 [c e]	[62]
1M $LiPF_6$ in EC:EMC (3:7)	8 [a]	25 [c]	0.25 [c e]	1.5 [c e]	[62]
1M $LiPF_6$ in EMC:FEC (19:1)	5 [a]	35 [c]	0.15 [c e]	1 [c e]	[62]
3M $LiPF_6$ in EC:DMC (1:1)	4 [a]	15 [c]	0 [c e]	2 [c e]	[62]
3M $LiPF_6$ in EC:EMC (3:7)	3 [a]	10 [c]	0.2 [c e]	2 [c e]	[62]
3M $LiPF_6$ in EMC:FEC (19:1)	2.5 [a]	10 [c]	0.1 [c e]	2 [c e]	[62]
3M $LiPF_6$ in EMC:FEC (19:1)	2.5 [a]	10 [c]	0.1 [c e]	2 [c e]	[62]
1M $LiPF_6$ in PC:EC:DMC (0.1:0.27:0.63)	11 [b]	35 [d]	0.38 [f]	2 [e]	[62]
1M $LiPF_6$ in PC	5.5 [b]	20 [d]	0.22 [f]	2.5 [e]	[58]
1M $LiPF_6$ in EMC	5 [b]	75 [d]	0.3 [f]	0.8 [e]	[63]
1M $LiPF_6$ in EC:EMC (3:7)	9.5 [b]	35 [d]	0.25 [d]	2[e]	[59]

Method
[a] EIS
[b] Conductivity Meter
[c] Pulse Experiment Coin Cell
[d] Restricted Diffusion
[e] Concentration Cell
[f] Hittorf

°C, κ was calculated as 11 mS cm^{-1}, D_{app} = 3×10^{-10} m^2 s^{-1}, χ_M = 2 and t_+^0 = 0.25. They performed these calculations from -10 to 60 °C and 0.1-3 M. They repeatedly compared their results to the popular study by Valøen and Reimers who also measured each transport and thermodynamic property of $LiPF_6$, but in a PC(propylene carbonate)(10 vol%):EC(27 vol%):DMC(63 vol%) solvent mixture.[57] At 20 °C, by using the Hittorf method, t_+^0 = 0.38; using a conductivity meter, κ = 11 mS cm^{-1}; using a restricted diffusion cell, D_{app} = 3.5×10^{-10} m^2 s^{-1} and using a concentration cell, χ_M = 2. Most full characterisations have been focused on carbonate-based electrolytes, especially in reference to LIBs, with some choosing to use other salts such as $LiClO_4$.[102] Table 1.3 shows the extent of full characterisations of carbonate-based electrolytes from the studies mentioned, plus experiments from Nyman et al. and Monroe et al. [58, 59]

Although carbonates are popular for use in LIBs they are unsuitable for use in LMBs, due to their inherent chemical instability against lithium metal. Hence, there is increasing interest in developing electrolytes that are stable against lithium metal and are therefore good candidates for LMBs.[49] A promising alternative

is based on using an ether-based solvent and using an imide-based salt. Ether-based solvents such as glymes, like dimethoxyethane (DME) and tetraglyme (G4), have high reductive stability so are resistant to (electro)chemical breakdown from lithium.[103] Although $LiPF_6$ has been proposed as a salt for LMB electrolytes, the imide-salt LiFSI is preferable due to $LiPF_6$'s tendency to form HF in trace amounts of water. This can be detrimental to LMB cyclability and leads to major safety concerns. Indeed, LiFSI has become increasingly popular due to its propensity to form fluorine-rich stable SEI layer.[104] This is especially true at high electrolyte concentrations, as the Li^+ solvation structure changes from a solvent-based inner solvation sphere to an anion-based one. Due to its proximity, the species that is present within the inner solvation sphere is more likely to react, with its decomposition products being present in the SEI.[105]

Full characterisation of ether-based electrolytes have rarely been performed. Balsara and co-workers published two pieces of work characterising an ether-type electrolyte, namely LiFSI in C8-DMC (a fluorinated ether) and LiTFSI in tetraglyme (G4).[106, 107] Using long-chained solvents increases the viscosity of the electrolyte, which reduces κ and D_{app} values. Therefore, the 1 molal(m) LiFSI in C8-DMC had κ = 0.8 mS cm^{-1}; $D_{app} = 8 \times 10^{-12}$ m^2 s^{-1}; $t_+^0 = -0.4$ and χ_m = 0.4. Interesting to note, t_+^0 was measured as negative but t_+ (transference measured by the Bruce-Vincent "steady-state method")= 0.7. This highlights again the importance of rigorous electrolyte characterisation and explicit use of reference velocities. As noted in Table 1.2, Grundy et al. measured 1.44 m LiTFSI in G4, which showed higher κ and D_{app} values than the longer-chained C8-DMC-based electrolyte.[108] The difference between each electrolyte here is almost exclusively a result of the solvent used, with the longer-chained C8-DMC solvent leading to particularly poor transport properties. However, there are advantages to using this solvent, namely its enhanced electrochemical stability, favourable SEI formation and its decreased flammability, hence improved safety.

Solid-state electrolytes, including polymer electrolytes, have been suggested for use in LMBs for their potential in suppressing dendrite growth due to their

Table 1.2: Selected Ether Electrolyte Transport and Thermodynamic Properties at $20^{o}C$

Electrolyte	κ / **mS cm**$^{-1}$	D_{app} / $\times 10^{-11}$ m^2 s^{-1}	t_+^0	χ_M	**Ref**
1.44m LiTFSI in G4	4 [b]	3.5 [d]	0.8 [g e]	11 [e]	[108]
1m LiFSI in C8-DMC	0.8 [b]	0.8 [d]	-0.4 [g e]	0.4 [e]	[106]

Method
[b] Conductivity Meter
[d] Restricted Diffusion
[e] Concentration Cell
[g] Bruce-Vincent

favourable mechanical properties.[109, 110] Transport and thermodynamic properties in polymer electrolytes are comparable to the described liquid binary electrolytes above. In fact, Newman, Bruce and Vincent, and Sørenson and Jacobsen first highlighted their electrolyte transport theories by utilising polymer-based electrolytes.[52, 71, 73] Doyle, Fuller and Newman's seminal study in 1993 describing the DFN model utilised LiTFSI in polyethylene oxide (PEO), referencing data collected from Armand et al.[111] Ma et al. then went on to experimentally measure the full set of transport and thermodynamic electrolyte properties of 0.1-2.6 M NaTFSI in PEO in 1995.[112] This provided a clear method for comprehensively measuring the four electrolyte properties required to model electrolytes in LIB/LMBs. However, it also highlighted the problem with using polymer-based electrolytes; namely their poor D_{app} and κ: Bouridah measured D_{app} and κ in 1 M LiTFSI in PEO as 7.5×10^{-12} m^2 s^{-1} and 0.15 mS cm^{-1} respectively.[111] Also, Ma measured t_+^0 to be negative at concentrations greater than 0.5 M. Although the transport properties of polymer-based electrolytes is poor, their flexibility, stability against lithium metal and potential to inhibit dendrite growth still warrants further research as potential LMB electrolytes.

As mentioned in the previous section, for LMBs to become commercially successful, one needs to address the problem of non-uniform Li electrodeposition. Many of the reported strategies to suppress dendrite growth centre on designing high-performing electrolytes with good mass-transport properties and excellent

Table 1.3: Selected Polymer Electrolyte Transport and Thermodynamic Properties

Electrolyte	κ / **mS cm**$^{-1}$	D_{app} / $\times$ 10^{-11} m^2 s^{-1}	t_+^0	χ_M	Temperature / ^oC	**Ref**
1M LiTFSI in PEO	0.15 [a]	0.75 [c]	0.7 [c e]	0.16 [c e]	90^oC	[111]
1M NaOTf in PEO	3 [a]	6 [c]	-0.75 [e]	1.8 [e]	85^oC	[112]

Method
[a] EIS
[c] Restricted Diffusion
[e] Concentration Cell
[f] Hittorf

SEI formation. But for one to understand the potential correlative behaviour of lithium deposition morphology with electrolyte transport and thermodynamic properties, a critical and rigorous characterisation is required.

1.6 Ionic Liquid Electrolytes

Salts that are liquid at room temperature are termed "ionic liquids" (IL), and have been proposed for battery applications for numerous reasons, including their non-volatility and thermal stability, resulting in a battery that is especially safe, and operative at high temperatures. By dissolving an alkali-salt in ILs, the solution can be used as an electrolyte for alkali-ion batteries (Ionic Liquid Electrolyte – ILE).[113–115]

ILs are liquid at room temperature due to the intricate structure of the cation and anion. The cations used are often bulky with alkyl groups surrounding the charge centre. Popular examples include the imidazolium, pyrrolidinium, piperidinium, tetraalkyl ammonium and phosphonium cations (see Figure 1.9).[116–120] Each have their respective advantages and disadvantages for use as electrolytes, with differences in their conductivities, decomposition products (and therefore SEI composition) and cathodic/anodic stabilities (ESW). Common anions are charge delocalised leading to many resonance structures. This delocalisation of charge results in a weak interaction with the bulky cation. The main anions used for ILs in battery applications include dicyanamide (DCA^-), bis(fluorosulfonyl)imide (FSI^-) and bis(trifluorosulfonyl)imide ($TFSI^-$).[121–124] The FSI^- anion has become especially prevalent due to its low viscosity (and

therefore higher conductivity) and inhibition of aluminium current collector corrosion.[125]

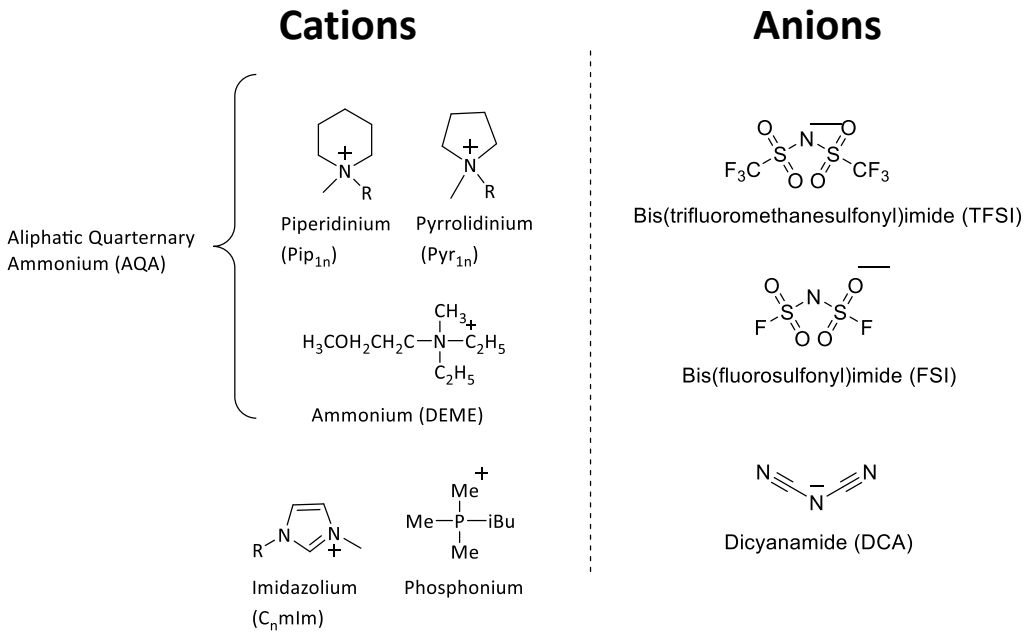


Figure 1.9: Popular Ionic Liquids: Cations: aliphatic quarternary cations include cyclic, pyrrolidinium and piperdinium, and quartenary ammonium; aromatic imidazolium and phosphonium. Anions: imides like FSI and $TFSI^-$ and nitrile, such as DCA^-.

With no neutrally-charged solvent present in the electrolyte, Li^+ ions are coordinated by anions in solution. Umebayashi et al. showed using Raman spectroscopy and density functional theory (DFT) that for LiTFSI in 1-ethyl-3-methylimidazolium (EMI) TFSI, Li^+ was coordinated by two bidentate TFSI anions via oxygens.[126] The electrode interphase has also proven to be a product of anion-based decomposition.[127] In some systems this has shown improved battery cycling over the conventional carbonate-based electrolyte described above.[128]

Although ILEs are non-volatile and have shown favourable interphase properties,[127, 129] they exhibit poor transport compared to organic-based electrolytes with carbonate and ether solvents. This is primarily the result of having inferior diffusivity and Li^+ transference compared to the organic-based electrolytes.[130] The increased ionic interaction between species present in the ionic liquid increases the viscosity of the electrolyte, resulting in low diffusion coefficients.

Most of the literature judges the diffusivity of ILs indirectly through measuring κ, comparing it favourably to conventional electrolyte mixtures. However, because κ is also a product of ionic concentration, it may overestimate the favourable diffusivity due to increased ionic concentration compared to organic-based electrolytes. Equation 4.11 shows that t_+ is related to both the mobility and concentration of each ion in solution. The Li^+ transference number (t_{Li^+}) is especially poor due Li^+ often being the species with the lowest mobility coefficient and lowest ionic concentration in solution. The combination of low D_{app} and t_{Li^+} leads to large concentration gradients forming in the bulk of the electrolyte. This results in large concentration overpotentials, reducing the energy of the battery. Furthermore, as mentioned previously, the drop in electrolyte concentration at the interface during charge has been suggested to promote the growth of dendrites in LMBs. D_{app} increases with temperature, so ILEs have more frequently been proposed as high-temperature electrolytes for LMBs.

Unfortunately, classical Newman CST is not compatible with ILEs because it is not binary with a neutral solvent, which is a requirement of CST. However, Pollard and Newman extended CST in 1979 by providing a framework theory for a mixture of two molten salts with a common anion.[131, 132] Prior to the discovery of room-temperature ILEs for battery applications, molten salts had been studied for applications such as materials processing.[133] Similar to the previously described CST, there are still three species, only now the additional species is charged. κ, t_+ and D_{app}, with a salt chemical potential, were still used to describe the electrolyte system. In 2021, Li et al. pushed this theory further, accounting for non-neutrality due to space charging.[134]

Although there has been some development in using CST for ILEs, few studies have been conducted to measure promising battery ILE transport properties electrochemically. Those that have used the steady-state method, which, as mentioned previously, assumes infinite dilution. This is especially problematic when using ILEs as it is solely composed of ions. Using PEIS and scanning to very low frequencies, Wohde et al. measured t_{Li^+} of 1.49 M LiTFSI in $Pyr_{1,4}$TFSI

at 60 °C, calculating a value of 0.055. Indeed for this value to be valid χ_M would need to be included, to understand if this value has been under- or overestimated. However, this estimate still illustrates how small t_{Li+} is likely to be in ILEs. Huang et al. used the Bruce-Vincent method to measure t_{Li+} of 0.5 M LiFSI in $Pyr_{1,3}FSI$ at 25°C.[135] They concluded it had a value of 0.15, which again is lower than the rigorously measured t_{Li+} values of carbonate and ether-based electrolytes described above.

A few decades ago there were a flurry of studies that measured t_+ using the Hittorf method, but of molten salts, not room-temperature ILEs.[136–139] Many of the studied salts had high melting points (∼300 °C), so evidently were unsuitable for battery applications. Nevertheless they provide a useful study for how potential battery-applicable electrolytes may behave. In 1972, Richter et al. measured various properties of $NaNO_3$ in $AgNO_3$, including t_{Na+} via Hittorf, showing very clearly that increasing $NaNO_3$ concentration leads to increasing t_{Na+}.[138] A later study by Hussey used an EMI-based electrolyte, namely $AlCl_3$ in EMI^+Cl^-.[139] Primarily thought of as a useful solvent for spectroscopy, the molten mixture had a melting point of ∼20 °C depending on the $AlCl_3$ concentration. Importantly, in these studies, they explicitly describe transference numbers either as external or internal. As was mentioned for binary electrolytes in a neutral solvent, t_+ requires a reference velocity for completeness; as a reminder, in the binary electrolyte, t_+ was referenced against the solvent. If t_+ is referenced against an internal component (i.e. a constituent species), this is the internal transference number. If it is referenced against an external component (i.e. laboratory reference frame) it is termed the external transference number. Haase highlighted the importance of how one reports t_+ values in ionic melts, as others report active ions moving in a direction opposite to their individual polarity.[140] Hussey indeed noted a negative external t_{Al^+} value, which they hypothesised was due to the presence of $AlCl_4^-$ species; it therefore moved in the "wrong direction". Unfortunately no Hittorf t_+ values of promising Li-ion ILEs have been reported.

pfg-NMR has been a popular technique for measuring self-diffusion coefficients of separate ions in promising Li-ion ILEs. For example, Kunze et al. measured self-diffusion coefficient values of each ion in $(Pyr_{1,4}TFSI)_{0.85}(LiTFSI)_{0.15}$, showing $D_{Pyr} = 7.20 \times 10^{-12}$ m^2 s^{-1}, $D_{TFSI} = 5.44 \times 10^{-12}$ m^2 s^{-1} and $D_{Li} = 4.03 \times 10^{-12}$ m^2 s^{-1}. D_{Li} had the lowest value here, which is often the case when analysing self-diffusion coefficients of ILEs.[141] This is likely due to Li^+'s high charge density and its tendancy to form $Li(TFSI)_2^-$ complexes, and even extended aggregates or clusters. Computational studies using molecular dynamics (MD) and experimental studies using small angle X-ray scattering (SAXS) have hypothesised ordered micro- or mesosopic domains could form in ILEs and concentrated electrolytes.[142, 143] This will likely hinder Li^+ if it moves as part of a larger cluster. But others have suggested the transport mechanism is likely to occur via ion-hopping as Li^+ moves within an ordered domain. With eNMR, Gouverneur et al. first measured the D_+ and D_- of pure ionic liquids in 2015, and subsequently calculated t_+, without the inclusion of an active salt like LiTFSI.[78] In 2018 however, they included LiTFSI to understand how a Li-ion relevant electrolyte would behave under polarisation.[79] They noted the drift direction of Li^+ was opposite than expected – it was moving toward the positive electrode, similar to $AlCl_4^-$. It was therefore concluded that t_{Li+} was negative, which was suggested to be due to $Li(TFSI)_2^-$ formation. It was a comment by Harris that motivated Schönhoff to define t_{Li+} externally or internally, with Schönhoff concluding that using internal t_{Li+} led to a loss of information. They therefore recommended to measure t_{Li+} externally when using eNMR.[144, 145]

Again, perhaps due to the ease of measurement, most researchers look at the ionic conductivity and viscosity of ILEs.[146–149] EMI-based ILEs are known for their high κ, but lower oxidative stability, whereas Pyr-based have a higher ESW but have lower κ.[116] As described above, FSI^- ILEs have a distinctly lower viscosity than $TFSI^-$.[150] For example, 1 M LiFSI in $Pyr_{1,3}FSI$, a popular ILE, has a reasonable κ of $\sim$3 mS cm^{-1} at 25 °C.[151]

Much less work has looked at the thermodynamics of ILE systems. There was a study, again by Richter et al. in 1972, that used a concentration cell to measure potential differences between concentrations of $NaNO_3$ and $LiNO_3$ in $AgNO_3$ molten salts.[152] Their plot of activity coefficient ($f_{\pm}$) vs. concentration was a very similar shape to binary electrolytes, where there was an initial drop to below 1 and then an increase as the electrolyte reached saturation. Although it is likely the thermodynamics of popular Li-ion ILEs will be similar to the described ionic melt, it is yet to be characterised.

In summary, there has been limited characterisation of fundamental transport and thermodynamics of promising ILE for Li-ion and Li metal batteries. Chapter 4 will look at a full transport and thermodynamic characterisation of a popular ILE, LiFSI in $Pyr_{1,3}FSI$.

1.7 Improving Electrolyte Properties

Improving on each of the described properties benefit both LIBs and LMBs in different ways. By increasing D_{app} and t^0_{Li+}, the concentration gradient that forms across the cell will be reduced. This reduces the concentration over-potential across the cell, increasing the rate capability and therefore power density. Furthermore, for LMBs, reducing concentration gradient formation has been shown to inhibit dendrite growth.[42] Improving t^0_{Li+} requires either increasing the transport of Li^+ or decreasing the transport of the other ions in solution. Most research thrusts look at either creating a single-ion conductor (SIC) membrane,[153] so only allows Li^+ to move, which is effectively a solid-state electrolytes, or in liquid electrolyte systems, chemically or physically tethering the inactive ions either on a molecular scale (zwitterion) or to a nanoparticle (see Figure 1.10).[154] For SIC membranes, a particularly interesting class looks at so-called ionomer membranes. Ionomers are charged polymers formulated with a liquid electrolyte and porous separator membrane; this results in a SIC conductor, with $t^0_+ = 1$.[155] The main challenge of using this electrolyte type is encouraging dissociation between Li^+ and the anionic polymer backbone. Typical

high dielectric solvents that promote ionic dissociation, like PC and DMSO, have been tested, but are known to co-intercalate with Li^+ into graphite. This suggests their use in LMBs would be more applicable. Song et al. showed a thin layer of Nafion, a well known ionomer, on the lithium metal surface, improves the average t_+^0 and cyclability in LMBs.[155] More studies are required with different polymer/solvent/salt combinations to see if cyclability of full cells can be improved further. To improve transference in solution, Archer and co-workers proposed tethering anionic species to nanoparticles.[156, 157] By covalently bonding an ammonium-type cation to zirconia nanoparticles, they showed a reduction in anionic motion, improving t_{Li+}.[158] t_{Li+} of the ILE improved from 0.05 to 0.35, but they used the Bruce-Vincent method to measure it, so further detailed studies of mass-transport are required to validate their claims. As stated previously, a promising solution-based strategy for improving t_{Li+} is to use zwitterions as an ion conductive matrix for lithium salts.[159–161] By designing a zwitterion that exhibits more dissociation on the anionic side leads to increased Li^+ movement. Narita et al. showed this with a novel organoborate zwitterionic design with LiTFSI, illustrating an improved t_{Li+} value of 0.69.[162] The low κ value of 3×10^{-2} mS cm^{-1} is a compromise that is made by decreasing the movement of the anion.

Increasing κ will decrease the ohmic overpotential, increasing the rate capability of the battery. D_{app} directly influences κ and reduces the concentration overpotential in the battery. Improving D_{app} and κ involves analysing the intermolecular structures that are forming in solution. Most studies look to improve these values by mixing low viscosity co-solvents. Low viscosity co-solvents are usually characterised by low dielectric constants, binding weakly to the salt, and therefore reducing drag.[163–165] The most relevant and popular example is by introducing the linear carbonate DMC with EC when designing LP30. Logan and Dahn suggested using aliphatic esters like methyl acetate (MA) and ethyl acetate (EA), especially at temperatures as low as -40 °C.[166, 167] However, using esters has shown to have unfavourable SEI properties on graphite. If these low molecular weight co-solvents lead to poor SEI properties, additives such as FEC and vinyl

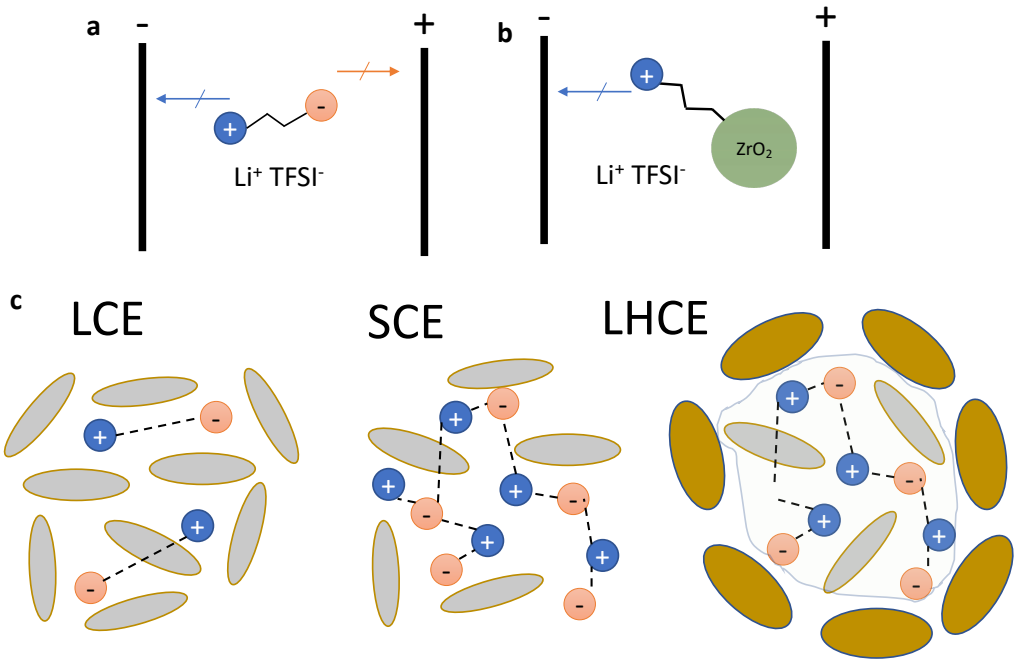


Figure 1.10: Strategies to Improve Electrolyte Properties: a) Zwitterionic electrolyte allows for favourable interfacial properties without suffering from poor t_+ that ILEs usually experience, because the bonding of two ions doesn't allow for opposite movement b) Grafting ionic species to a nanoparticle, slowing its movement, therefore increasing t_{Li+}, as seen by Archer and co-workers [156] c) Difference between concentration strategies, where low concentrated electrolytes from solvent separated ion pairs (SSIPs), but primarily solvated by the solvent; superconcentrated electrolyte form contact ion pairs (CIPs) and aggregates (AGGs), so Li^+ is primarily "solvated" by the anion, finally locally high concentrated electrolytes (LHCE) include an inert diluent (yellow), which does not get involved in solvation but reduces the viscosity, preserving the favourable solvation structure seen in SCEs.

carbonate (VC) have been added, in amounts as low as 5 vol%. Cho et al. have suggested using nitriles such as acetonitrile to improve ion transport. Here, they achieved a cycling rate of 3C at -20 °C for NCA|Graphite full cells. Other more conventional electrolyte compositions would fail at this temperature.[168]

A class of electrolytes introduced in 2013 looked to improve the ESW of non-aqueous electrolytes even further, especially their oxidative stability.[169] These were termed "solvent-in-salt" electrolytes or "superconcentrated" electrolytes (SCEs), named because of the increased salt content, [salt] $>$ [solvent].[170, 171] Structural characterisation techniques like NMR and Raman spectroscopy studies showed that Li^+ solvation changed from primarily solvent-based to anion-

based. The change in solvation resulted in changes in electrode interphases (referred to as SEI for anode and cathode electrolyte interphase (CEI)).[172] Indeed, with a similar solvent structure as ILEs, they appeared to show similar electrochemical stability but without the poor t_+ that limits ILE performance. Steady-state t_+ measurements even showed higher t_+ values than conventional dilute electrolytes.[169] Caution should be taken here however, with SCEs having high χ_M values and the authors not referencing against the solvent velocity, it's likely t_+^0 was overestimated. With increasing salt content comes decreasing κ, inhibiting SCE performance. Also as fluorinated salts are expensive, a higher salt content increases the overall cost of the battery, lessening their viability long-term. To solve this problem, a recent development has looked at adding non-solvating diluents to SCEs, which lowers the electrolytes' viscosity, increasing κ, but also keeping the favourable solvation structure. This class of electrolytes has been named localised high concentration electrolytes (LHCEs) (see Figure 1.10c).[173–175] The diluents that have been used so far are fluorinated ethers, with each ether exhibiting differing performance. Although initially it was thought the diluents did not participate in lithium metal SEI formation, it has since been proven this is not the case.[176] Fluorinated salts and solvents reduce to form LiF, which has been proposed as a favourable component of lithium metal SEIs.[177]

There is much less data on how χ_M influences LIB and LMB performance. Depending on the concentration dependency of χ_M, the activity gradient present in the electrolyte bulk may be steeper than the concentration gradient, increasing the overall concentration overpotential. Furthermore, activity affects the surface reaction kinetics, with exchange current density (i_0) in interfacial kinetics, and the reorganisation energy from Marcus theory being proportional to activity.[178] An increasing thermodynamic activity can lead to an increased rate of reaction at interfaces. Liu et al. looked at how i_0 affected the plating morphology of lithium metal, and reported a lower i_0 value promoted uniform plating.[179] This indirectly suggests a lower χ_M value could lead to more homogeneous plating. Another study looking at electrolyte thermodynamics compared the potentials between

various electrolytes including carbonate-based, ether-based and LHCEs.[180] Using 1 M LiFSI in DEC as a reference electrolyte, Kim et al. did a comparative study, measuring the potential differences between electrolytes. They concluded electrolytes with low chemical potentials (high activities) lead to better plating morphology and higher CEs. However no quantitative value was measured, like χ_M. Kim and Liu appeared to contradict each other however, with Kim stating an increasingly low potential electrolyte leading to higher i_0 values. While Liu's study suggested low i_0 values lead to higher CE. Further work is required if one is to unanimously correlate χ_M and chemical potential with Li^+ deposition morphology and ultimately LMB performance.

The design of novel electrolytes is required for step-change progression in LIB and LMBs.[181] Development will be achieved by measuring each property accurately; understanding their influence on LIB and LMB performance and therefore making informed decisions on electrolyte advancement.

1.8 Thesis Objectives

Transport and thermodynamic properties of electrolytes have been shown to influence LIB performance and deposition morphology in LMBs. However, few electrolyte compositions have been fully characterised, seemingly due to the multiple experimental setups required for a full understanding. To continue to correlate electrolyte properties with battery performance, it is imperative that more properties of electrolytes are measured and analysed.

The objectives of this thesis centre on the accurate measurement of fundamental binary electrolyte and ILE properties for use in LIBs and LMBs, utilising a novel method of characterisation. Finally, there is a comparison between binary and ILE systems on the plating morphology of Li^+.

A more detailed outline of this thesis is:

Part 1 (Chapter 3): *Characterising binary electrolytes via operando Raman microspectroscopy*.

- Use **operando Raman microspectroscopy** to visualise electrolyte **concentration gradients** with time.
- Calculate $\kappa, D_{app}, t_+, \chi_M$ and R_{ct} using concentration profiles in tandem with PEIS.
- **Simulate symmetric and full cell performance** using the measured electrolyte properties.

Part 2 (Chapter 4): *Insights into Ionic Liquid Electrolyte Transport and Thermodynamics*.

- Visualisation of **ILE concentration gradients** for the first time.
- Provide information on the **transport, thermodynamics and structure** of ILEs.
- Discuss the **mechanism of Li^+ plating** in ILEs.

Part 3 (Chapter 5): *Electrolyte Transport and Thermodynamics' Influence on LMB Plating Morphology*.

- Understand how electrolyte **concentration affects deposition morphology** on lithium metal.
- Correlate **electrolyte transport, thermodynamics and influence on SEI formation** with filament growth.

1.9 References

1. Ibrahim, H. *et al.* Energy storage systems-Characteristics and comparisons. *Renew. Sustain. Energy Rev.* **12,** 1221–1250 (2008).
2. Abraham, K. M. Prospects and limits of energy storage in batteries. *J. Phys. Chem. Lett.* **6,** 830–844 (2015).

3. Luo, X. *et al.* Overview of current development in electrical energy storage technologies and the application potential in power system operation. *Appl. Energy* **137,** 511–536 (2015).
4. Zeng, X. *et al.* Commercialization of Lithium Battery Technologies for Electric Vehicles. *Adv. Energy Mater.* **1900161,** 1900161 (2019).
5. Turcheniuk, K. *et al.* Battery materials for low-cost electric transportation. *Mater. Today,* 2020 (2020).
6. *Government takes historic step towards net-zero with end of sale of new petrol and diesel cars by 2030* `https://www.gov.uk/government/news/government-takes-historic-step-towards-net-zero-with-end-of-sale-of-new-petrol-and-diesel-cars-by-2030`. [Online; accessed 18-January-2021].
7. Whittingham, M. S. History, Evolution, and Future Status of Energy Storage. *Proc. IEEE* **100,** 1518–1534 (2012).
8. Blomgren, G. E. The Development and Future of Lithium Ion Batteries. *J. Electrochem. Soc.* **164,** A5019–A5025 (2017).
9. Scrosati, B. *et al.* Lithium batteries: Status, prospects and future. *J. Power Sources* **195,** 2419–2430 (2010).
10. Goodenough, J. B. *et al.* Challenges for Rechargeable Li Batteries. *Chem. Mater.* **22,** 587–603 (2010).
11. Mizushima, K. *et al.* LixCoO 2 (0<x
l): A NEW CATHODE MATERIAL FOR BATTERIES OF HIGH ENERGY DENSITY. *Mat Res Bull* **42,** 6131–6134 (1981).
12. *Lithium-ion Battery Market Size USD 129.3 Billion By 2027 At A CAGR of 18.0% | Valuates Reports* `https://www.prnewswire.co.uk/news-releases/lithium-ion-battery-market-size-usd-129-3-billion-by-2027-at-a-cagr-of-18-0-valuates-reports-896863595.html`. [Online; accessed 18-January-2021].
13. Whittingham, M. S. Lithium batteries and cathode materials. *Chem. Rev.* **104,** 4271–4301. arXiv: `arXiv:1011.1669v3` (2004).
14. Huggins, R. A. *Advanced Batteries* (2009).
15. Newman, J. *et al. Electrochemical Systems* 3rd (Wiley & Sons, 2004).
16. Winter, M. *et al.* Electrode materials for rechargeable lithium batteries. *Adv. Mater.* **10,** 725 (1998).
17. Lu, J. *et al.* High-Performance Anode Materials for Rechargeable Lithium-Ion Batteries. *Electrochem. Energy Rev.* **1,** 35–53 (2018).
18. Arora, P. *et al.* Battery separators. *Chem. Rev.* **104,** 4419–4462 (2004).
19. Lee, H. *et al.* A review of recent developments in membrane separators for rechargeable lithium-ion batteries. *Energy Environ. Sci.* **7,** 3857–3886 (2014).
20. Quartarone, E. *et al.* Review—Emerging Trends in the Design of Electrolytes for Lithium and Post-Lithium Batteries. *J. Electrochem. Soc.* **167,** 050508 (2020).
21. Marcinek, M. *et al.* Electrolytes for Li-ion transport - Review. *Solid State Ionics* **276,** 107–126 (2015).

22. Betz, J. *et al.* Theoretical versus Practical Energy: A Plea for More Transparency in the Energy Calculation of Different Rechargeable Battery Systems. *Adv. Energy Mater.* **9,** 1–18 (2019).

23. Yang, Z. *et al.* Electrochemical energy storage for green grid. *Chem. Rev.* **111,** 3577–3613 (2011).

24. Hwang, J.-Y. *et al.* Customizing a Li–metal battery that survives practical operating conditions for electric vehicle applications. *Energy Environ. Sci.* (2019).

25. Cheng, X. B. *et al.* Toward Safe Lithium Metal Anode in Rechargeable Batteries: A Review. *Chem. Rev.* **117,** 10403–10473 (2017).

26. Kim, H. *et al.* Metallic anodes for next generation secondary batteries. *Chem. Soc. Rev.* **42,** 9011 (2013).

27. Li, B. *et al.* A Material Perspective of Rechargeable Metallic Lithium Anodes. *Adv. Energy Mater.* **1702296,** 1–16 (2018).

28. Xu, W. *et al.* Lithium metal anodes for rechargeable batteries. *Energy Environ. Sci.* **7,** 513–537 (2014).

29. Bruce, P. G. *et al.* Li-O2 and Li-S batteries with high energy storage. *Nat. Mater.* **11,** 19–29 (2012).

30. Christensen, J. *et al.* A Critical Review of Li/Air Batteries. *J. Electrochem. Soc.* **159,** R1–R30 (2012).

31. Fotouhi, A. *et al.* Lithium-sulfur battery technology readiness and applications - A review. *Energies* **10** (2017).

32. Steiger, J. *et al.* Mechanisms of dendritic growth investigated by in situ light microscopy during electrodeposition and dissolution of lithium. *J. Power Sources* **261,** 112–119 (2014).

33. Wood, K. N. *et al.* Dendrites and pits: Untangling the complex behavior of lithium metal anodes through operando video microscopy. *ACS Cent. Sci.* **2,** 790–801 (2016).

34. Peled, E. *et al.* Review—SEI: Past, Present and Future. *J. Electrochem. Soc.* **164,** A1703–A1719 (2017).

35. Meyerson, M. L. *et al.* The Effect of Local Lithium Surface Chemistry and Topography on Solid Electrolyte Interphase Composition and Dendrite Nucleation. *J. Mater. Chem. A* **7,** 14882–14894 (2019).

36. Zheng, J. *et al.* Regulating electrodeposition morphology of lithium: towards commercially relevant secondary Li metal batteries. *Chem. Soc. Rev.* **49,** 2701–2750 (2020).

37. Zheng, J. *et al.* Physical Orphaning versus Chemical Instability: Is Dendritic Electrodeposition of Li Fatal? *ACS Energy Lett.* **4,** 1349–1355 (2019).

38. Fang, C. *et al.* Quantifying inactive lithium in lithium metal batteries. *Nature* **572,** 511–515. arXiv: 1811.01029 (2019).

39. Chazalviel, J. N. Electrochemical aspects of the generation of ramified metallic electrodeposits. *Phys. Rev. A* **42,** 7355–7367 (1990).

40. Fleury, V. *et al.* Coupling of drift, diffusion, and electroconvection, in the vicinity of growing electrodeposits. *Phys. Rev. E* **48,** 1279–1295 (1993).
41. Sand, H. S. J. S. On the concentration at the electrodes in a solution, with special reference to the liberation of hydrogen by electrolysis of a mixture of copper sulphate and sulphuric acid. *Proc. Phys. Soc. London* **17,** 496–534 (1899).
42. Rosso, M. *et al.* Experimental Evidence for Gravity Induced Motion in the Vicinity of Ramified Electrodeposits. *Electrochim. Acta* **39,** 507–515 (1994).
43. Brissot, C. *et al.* Dendritic growth mechanisms in lithium/polymer cells. *J. Power Sources* **81,** 925–929 (1999).
44. Rosso, M. *et al.* Onset of dendritic growth in lithium/polymer cells. *J. Power Sources* **97-98,** 804–806 (2001).
45. Bai, P. *et al.* Transition of lithium growth mechanisms in liquid electrolytes. *Energy Environ. Sci.* **9,** 3221–3229 (2016).
46. Crowther, O. *et al.* Effect of Electrolyte Composition on Lithium Dendrite Growth. *J. Electrochem. Soc.* **155,** A806 (2008).
47. Li, M. *et al.* New Concepts in Electrolytes. *Chem. Rev.* **120,** 6783–6819 (2020).
48. Xu, G. *et al.* Key Scientific Issues in Formulating Blended Lithium Salts Electrolyte for Lithium Batteries. *Angew. Chemie Int. Ed.* (2019).
49. Tikekar, M. D. *et al.* Design principles for electrolytes and interfaces for stable lithium-metal batteries. *Nat. Energy* **1,** 16114 (2016).
50. Newman, J. *et al.* Restricted diffusion in binary solutions. *AIChE J.* **19,** 343–348 (1973).
51. Newman, J. *et al.* Porous-electrode theory with battery applications. *AIChE J.* **21,** 25–41 (1975).
52. Doyle, M. Modeling of Galvanostatic Charge and Discharge of the Lithium/Polymer/Insertion Cell. *J. Electrochem. Soc.* **140,** 1526 (1993).
53. Byron Bird, R. *et al. Transport Phenomena* **2** (2002).
54. Monroe, C. W. *et al.* An introduction to the onsager reciprocal relations. *Chem. Eng. Educ.* **41,** 233–238 (2007).
55. Newman, J. *et al.* Mass Transfer in Concentrated Binary Electrolytes. *Berichte der Bunsengesellschaft für Phys. Chemie* **69,** 608–612 (1965).
56. Bockris, J. O. *et al. Modern Electrochemistry Volume 1 Ionics* 2nd (Kluwer Academic Publishers, 2002).
57. Valoen, L. O. *et al.* Transport Properties of LiPF₆-Based Li-Ion Battery Electrolytes. *J. Electrochem. Soc.* **152,** A882 (2005).
58. Hou, T. *et al.* Composition-dependent thermodynamic and mass-transport characterization of lithium hexafluorophosphate in propylene carbonate. *Electrochim. Acta* **332,** 135085 (2020).
59. Nyman, A. *et al.* Electrochemical characterisation and modelling of the mass transport phenomena in LiPF₆ -EC-EMC electrolyte. *Electrochim. Acta* **53,** 6356–6365 (2008).

60. Shao, Y. *et al.* Role of Viscosity in Deviations from the Nernst-Einstein Relation. *J. Phys. Chem. B* **124,** 4774–4780 (2020).

61. *Two, Three and Four Electrode Experiments* `https://www.gamry.com/application-notes/instrumentation/two-three-four-electrode-experiments/`. [Online; accessed 12-April-2021].

62. Landesfeind, J. *et al.* Temperature and Concentration Dependence of the Ionic Transport Properties of Lithium-Ion Battery Electrolytes. *J. Electrochem. Soc.* **166,** A3079–A3097 (2019).

63. Wang, A. A. *et al.* Shifting-reference concentration cells to refine composition-dependent transport characterization of binary lithium-ion electrolytes. *Electrochim. Acta* **358,** 136688 (2020).

64. Stejskal, E. O. *et al.* Spin diffusion measurements: Spin echoes in the presence of a time-dependent field gradient. *J. Chem. Phys.* **42,** 288–292. arXiv: `1011.1669v3` (1965).

65. Bolimowska, E. *et al.* Investigation of Li+ Cation Coordination and Transportation, by Molecular Modeling and NMR Studies, in a LiNTf2-Doped Ionic Liquid-Vinylene Carbonate Mixture. *J. Phys. Chem. B* **122,** 8560–8569 (2018).

66. Saunier, J. *et al.* NMR study of cation, anion, and solvent mobilities in macroporous poly(vinylidene fluoride). *J. Phys. Chem. B* **109,** 2487–2492 (2005).

67. Zhao, J. *et al.* Determination of Lithium-Ion Transference Numbers in LiPF6–PC Solutions Based on Electrochemical Polarization and NMR Measurements. *J. Electrochem. Soc.* **155,** A292 (2008).

68. Murch, G. E. THE HAVEN RATIO IN FAST IONIC CONDUCTORS < X2 > E = 0Eq < X > E # 02kT. *Solid State Ionics* **7,** 177–198 (1982).

69. Lewis, G. N. The Theory of the Determination of Transference Numbers by the Method of Moving Boundaries. *J. Am. Chem. Soc.* **86,** 862–869 (1910).

70. Hallam, H. E. A student transference number apparatus. *J. Chem. Educ.* **31,** 306–307 (1954).

71. Evans, J. *et al.* Electrochemical measurement of transference numbers in polymer electrolytes. *Polymer (Guildf).* **28,** 2324–2328 (1987).

72. Bruce, P. G. *et al.* Steady state current flow in solid binary electrolyte cells. *J. Electroanal. Chem.* **225,** 1–17 (1987).

73. Ravn Sørensen, P. *et al.* Conductivity, charge transfer and transport number-an ac-investigation of the polymer electrolyte LiSCN-poly(ethyleneoxide). *Electrochim. Acta* **27,** 1671–1675 (1982).

74. Wohde, F. *et al.* Li ⁺ Transference Numbers in Liquid Electrolytes Obtained by Very-Low-Frequency Impedance Spectroscopy at Variable Electrode Distances. *J. Electrochem. Soc.* **163,** A714–A721 (2016).

75. Doyle, M. *et al.* Analysis of Transference Number Measurements Based on the Potentiostatic Polarization of Solid Polymer Electrolytes. *J. Electrochem. Soc.* **142,** 3465 (1995).

76. Dhir, S. *et al.* Outlook on K-ion Batteries. *Chem* **6,** 1–19 (2020).

77. Holz, M. Electrophoretic NMR. *Chem. Soc. Rev.* **23,** 165–174 (1994).

78. Gouverneur, M. *et al.* Direct determination of ionic transference numbers in ionic liquids by electrophoretic NMR. *Phys. Chem. Chem. Phys.* **17,** 30680–30686 (2015).

79. Gouverneur, M. *et al.* Negative effective Li transference numbers in Li salt/ionic liquid mixtures: does Li drift in the "Wrong" direction? *Phys. Chem. Chem. Phys.* **20,** 7470–7478 (2018).

80. Koryta, J. *et al. Principles of Electrochemistry* 2nd (Wiley & Sons, 1987).

81. Guggenheim, E. *Thermodynamics: An Advanced Treatment for Chemists and Physicists* 5th (North-Holland Publishing Company, 1950).

82. Landesfeind, J. *et al.* Direct Electrochemical Determination of Thermodynamic Factors in Aprotic Binary Electrolytes. *J. Electrochem. Soc.* **163,** A1254–A1264 (2016).

83. Ehrl, A. *et al.* Determination of Transport Parameters in Liquid Binary Lithium Ion Battery Electrolytes: Part I. Diffusion Coefficient. *J. Electrochem. Soc.* **164,** A826–A836 (2017).

84. Klett, M. *et al.* Quantifying mass transport during polarization in a Li Ion battery electrolyte by in situ 7Li NMR imaging. *J. Am. Chem. Soc.* **134,** 14654–14657 (2012).

85. Krachkovskiy, S. A. *et al.* Slice-selective NMR diffusion measurements: A robust and reliable tool for in situ characterization of ion-transport properties in Lithium-ion battery electrolytes. *J. Phys. Chem. Lett.* **4,** 3940–3944 (2013).

86. Sethurajan, A. K. *et al.* Accurate Characterization of Ion Transport Properties in Binary Symmetric Electrolytes Using In Situ NMR Imaging and Inverse Modeling. *J. Phys. Chem. B* **119,** 12238–12248 (2015).

87. Krachkovskiy, S. A. *et al.* Visualization of Steady-State Ionic Concentration Profiles Formed in Electrolytes during Li-Ion Battery Operation and Determination of Mass-Transport Properties by in Situ Magnetic Resonance Imaging. *J. Am. Chem. Soc.* **138,** 7992–7999 (2016).

88. Bazak, J. D. *et al.* Multi-Temperature in Situ Magnetic Resonance Imaging of Polarization and Salt Precipitation in Lithium-Ion Battery Electrolytes. *J. Phys. Chem. C* **121,** 20704–20713 (2017).

89. Richardson, G. *et al.* The Effect of Ionic Aggregates on the Transport of Charged Species in Lithium Electrolyte Solutions. *J. Electrochem. Soc.* **165,** H561–H567 (2018).

90. Sethurajan, A. K. *et al.* Incorporating Dendrite Growth into Continuum Models of Electrolytes: Insights from NMR Measurements and Inverse Modeling. *J. Electrochem. Soc.* **166,** A1591–A1602 (2019).

91. Bazak, J. D. *et al.* Mapping of Lithium-Ion Battery Electrolyte Transport Properties and Limiting Currents with In Situ MRI Mapping of Lithium-Ion Battery Electrolyte Transport Properties and Limiting Currents with In Situ MRI. *J. Electrochem. Soc.* **167,** 140518 (2020).

92. Takamatsu, D. *et al.* Quantitative visualization of salt concentration distributions in lithium-ion battery electrolytes during battery operation using X-ray Phase Imaging. *J. Am. Chem. Soc.* **140,** 1608–1611 (2018).

93. Steinrück, H.-G. *et al.* Concentration and Velocity Profiles in a Polymeric Lithium-ion Battery Electrolyte. *Energy Environ. Sci.* **13,** 4312 (2020).

94. Rey, I. *et al.* Raman Spectroelectrochemistry of a Lithium/Polymer Electrolyte Symmetric Cell. *J. Electrochem. Soc.* **145,** 3034 (1998).

95. Georén, P. *et al.* Concentration Polarization of a Polymer Electrolyte. *J. Electrochem. Soc.* **149,** A1015 (2002).

96. Forster, J. D. *et al.* Mapping Li+ concentration and transport via in situ confocal Raman microscopy. *J. Phys. Chem. Lett.* **5,** 2007–2011 (2014).

97. Cheng, Q. *et al.* Operando and three-dimensional visualization of anion depletion and lithium growth by stimulated Raman scattering microscopy. *Nat. Commun.* **9,** 1–10 (2018).

98. Wei, Z. *et al.* Probing Li-ion concentration in an operating lithium ion battery using in situ Raman spectroscopy. *J. Power Sources* **449,** 227361 (2020).

99. Xu, K. Nonaqueous Liquid Electrolytes for Lithium-Based Rechargeable Batteries. *Chem. Rev.* **104,** 4303–4418 (2004).

100. Winter, M. *et al.* Before Li Ion Batteries. *Chem. Rev.* **118,** 11433–11456 (2018).

101. Guyomard, D. *et al.* Rechargeable Li1 + x Mn2 O 4 / Carbon Cells with a New Electrolyte Composition: Potentiostatic Studies and Application to Practical Cells. *J. Electrochem. Soc.* **140,** 3071–3081 (1993).

102. Georén, P. *et al.* Characterisation and modelling of the transport properties in lithium battery gel electrolytes: Part I. The binary electrolyte PC/LiClO4. *Electrochim. Acta* **49,** 3497–3505 (2004).

103. Zhang, Y. *et al.* Towards better Li metal anodes : Challenges and strategies. *Mater. Today* **xxx** (2019).

104. Shkrob, I. A. *et al.* Why bis(fluorosulfonyl)imide is a "magic anion" for electrochemistry. *J. Phys. Chem. C* **118,** 19661–19671 (2014).

105. Cao, R. *et al.* Effect of the Anion Activity on the Stability of Li Metal Anodes in Lithium-Sulfur Batteries. *Adv. Funct. Mater.* **26,** 3059–3066 (2016).

106. Shah, D. B. *et al.* Difference between approximate and rigorously measured transference numbers in fluorinated electrolytes. *Phys. Chem. Chem. Phys.* **21,** 7857–7866 (2019).

107. Shah, D. B. *et al.* Comparing Measurements of Limiting Current of Electrolytes with Theoretical Predictions up to the Solubility Limit. *J. Phys. Chem. C* **123,** 23872–23881 (2019).

108. Grundy, L. S. *et al.* Impact of Frictional Interactions on Conductivity , Diffusion , and Transference Number in Ether- and Perfluoroether-Based Electrolytes. *J. Electrochem. Soc.* **167,** 120540 (2020).

109. Janek, J. *et al.* A solid future for battery development. *Nat. Energy* **1,** 16141 (2016).

110. Quartarone, E. *et al.* Electrolytes for solid-state lithium rechargeable batteries: Recent advances and perspectives. *Chem. Soc. Rev.* **40,** 2525–2540 (2011).

111. Bouridah, A. *et al.* Potentiometric measurements of ionic transport parameters in poly(ethylene oxide)-LiX electrolytes. *J. Appl. Electrochem.* **17,** 625–634 (1987).

112. Ma, Y. *et al.* The Measurement of a Complete Set of Transport Properties for a Concentrated Solid Polymer Electrolyte Solution. *J. Electrochem. Soc.* **142,** 1859–1868 (1995).

113. Macfarlane, D. R. *et al.* Energy applications of ionic liquids. *Energy Environ. Sci.* **7,** 232–250 (2014).

114. Watanabe, M. *et al.* Application of Ionic Liquids to Energy Storage and Conversion Materials and Devices. *Chem. Rev.* **117,** 7190–7239 (2017).

115. Navarra, M. A. Ionic liquids as safe electrolyte components for Li-metal and Li-ion batteries. *MRS Bull.* **38,** 548–553 (2013).

116. Matsumoto, H. *et al.* Fast cycling of Li/LiCoO2 cell with low-viscosity ionic liquids based on bis(fluorosulfonyl)imide [FSI]-. *J. Power Sources* **160,** 1308–1313 (2006).

117. Castiglione, F. *et al.* Pyrrolidinium-based ionic liquids doped with lithium salts: How does Li+ coordination affect its diffusivity? *J. Phys. Chem. B* **118,** 13679–13688 (2014).

118. Lewandowski, A. *et al.* Ionic liquids as electrolytes for Li-ion batteries-An overview of electrochemical studies. *J. Power Sources* **194,** 601–609 (2009).

119. Seki, S. *et al.* Quaternary Ammonium Room-Temperature Ionic Liquid/Lithium Salt Binary Electrolytes: Electrochemical Study. *J. Electrochem. Soc.* **155,** A421 (2008).

120. Fraser, K. J. *et al.* Phosphonium-based ionic liquids: An overview. *Aust. J. Chem.* **62,** 309–321 (2009).

121. Shkrob, I. A. *et al.* Why Bis(fluorosulfonyl)imide is a “Magic Anion” for Electrochemistry? *J. Phys. Chem. C* **118,** 19661–19671 (2014).

122. Yoon, H. *et al.* Lithium electrochemistry and cycling behaviour of ionic liquids using cyano based anions. *Energy Environ. Sci.* **6,** 979–986 (2013).

123. Sakaebe, H. *et al.* N-methyl-N-propylpiperidinium bis(trifluoromethanesulfonyl)imide (PP13-TFSI) - Novel electrolyte base for Li battery. *Electrochem. commun.* **5,** 594–598 (2003).

124. Henderson, W. A. *et al.* Phase Behavior of Ionic Liquid-LiX Mixtures: Pyrrolidinium Cations and TFSI -Anions. *Chem. Mater.* **16,** 2881–2885 (2004).

125. Cho, E. *et al.* Corrosion/passivation of aluminum current collector in bis(fluorosulfonyl) imide-based ionic liquid for lithium-ion batteries. *Electrochem. commun.* **22,** 1–3 (2012).

126. Umebayashi, Y. *et al.* Liquid structure of and Li+ ion solvation in bis(trifluoromethanesulfonyl)amide based ionic liquids composed of 1-ethyl-3-methylimidazolium and N -methyl- N -propylpyrrolidinium cations. *J. Phys. Chem. B* **115,** 12179–12191 (2011).

127. Basile, A. *et al.* Stabilizing lithium metal using ionic liquids for long-lived batteries. *Nat. Commun.* **7,** 11794 (2016).

128. Yamagata, M. *et al.* The First Lithium-ion Battery with Ionic Liquid Electrolyte Demonstrated in Extreme Environment of Space. *Electrochemistry* **83,** 918–924 (2015).

129. Grande, L. *et al.* Homogeneous Lithium Electrodeposition with Pyrrolidinium-Based Ionic Liquid Electrolytes. *ACS Appl. Mater. Interfaces* **7,** 5950–5958 (2015).

130. Giffin, G. A. Ionic liquid-based electrolytes for "beyond lithium" battery technologies. *J. Mater. Chem. A* **4,** 13378–13389 (2016).

131. Pollard, R. *et al.* Transport Equations for a Mixture of Two Binary Molten Salts in a Porous Electrode. *J. Electrochem. Soc.* **126,** 1713–1717 (1979).

132. Pollard, R. *et al.* Mathematical Modeling of the Lithium-Aluminum, Iron Sulfide Battery: II . The Influence of Relaxation Time on the Charging Characteristics. *J. Electrochem. Soc.* **128,** 503–507 (1981).

133. Samaan Ladkany *et al.* Molten Salts and Applications I: Molten Salt History, Types, Thermodynamic and Physical Properties, and Cost. *J. Energy Power Eng.* **12,** 507–516 (2018).

134. Li, G. *et al.* Modeling Lithium Transport and Electrodeposition in Ionic-Liquid Based Electrolytes. *Front. Energy Res.* **9,** 1–10 (2021).

135. Huang, Q. *et al.* Pyrrolidinium Ionic Liquid Electrolyte with Bis(trifluoromethylsulfonyl)imide and Bis(fluorosulfonyl)imide Anions: Lithium Solvation and Mobility, and Performance in Lithium Metal-Lithium Iron Phosphate Batteries. *Ind. Eng. Chem. Res.* **58,** 22587–22597 (2019).

136. Dymek, C. J. *et al.* Transport Numbers in Molten Aluminum Chloride-1-Methyl-3-Ethylimidazolium Chloride Mixtures. *J. Electrochem. Soc.* **132,** 1375–1380 (1985).

137. Hussey, C. L. *et al.* Aluminum Bromide-1-Methyl-3-Ethylimidazolium Bromide Ionic Liquids: *J. Electrochem. Soc.* **134,** 1977 (1987).

138. Richter, J. *et al.* On the Migration of Ions in Alkali Nitrate-Silver Nitrate Melts. *Zeitschrift fur Naturforsch. - Sect. A J. Phys. Sci.* **27,** 280–287 (1972).

139. Hussey, C. L. *et al.* Transport Numbers in Molten Acidic Aluminum Chloride-1-Methyl-3-Ethylimidazolium Chloride: Their Relationship to EMF Measurements in Chloroaluminate Melts. *J. Electrochem. Soc.* **131,** 1621–1625 (1984).

140. Haase, R. Internal and External Transport Numbers in Ionic Melts. *Zeitschrift fur Phys. Chemie* **87,** 77–87 (1991).

141. Kunze, M. *et al.* New insights to self-aggregation in ionic liquid electrolytes for high-energy electrochemical devices. *Adv. Energy Mater.* **1,** 274–281 (2011).

142. Hayes, R. *et al.* Structure and Nanostructure in Ionic Liquids. *Chem. Rev.* **115,** 6357–6426 (2015).

143. Russina, O. *et al.* Mesoscopic structural organization in triphilic room temperature ionic liquids. *Faraday Discuss.* **167,** 499–513 (2013).

144. Harris, K. R. Comment on "negative effective Li transference numbers in Li salt/ionic liquid mixtures: Does Li drift in the "wrong" direction?" by M. Gouverneur, F. Schmidt and M. Schönhoff,: Phys. Chem. Chem. Phys., 2018, 20, 7470. *Phys. Chem. Chem. Phys.* **20,** 30041–30045 (2018).

145. Schönhoff, M. *et al.* Reply to the 'Comment on "negative effective Li transference numbers in Li salt/ionic liquid mixtures: Does Li drift in the "wrong" direction?"' by M. Gouverneur, F. Schmidt and M. Schönhoff,: Phys. Chem. Chem. Phys., 2018, 20, 7470. *Phys. Chem. Chem. Phys.* **20,** 30041–30045 (2018).

146. Garcia, B. *et al.* Room temperature molten salts as lithium battery electrolyte. *Electrochim. Acta* **49,** 4583–4588 (2004).

147. Fang, S. *et al.* New functionalized ionic liquids based on pyrrolidinium and piperidinium cations with two ether groups as electrolytes for lithium battery. *J. Power Sources* **196,** 5637–5644 (2011).

148. Tsunashima, K. *et al.* Physical and electrochemical properties of low-viscosity phosphonium ionic liquids as potential electrolytes. *Electrochem. commun.* **9,** 2353–2358 (2007).

149. Yoon, H. *et al.* Physical properties of high Li-ion content N-propyl-N-methylpyrrolidinium bis(fluorosulfonyl)imide based ionic liquid electrolytes. *Phys. Chem. Chem. Phys.* **17,** 4656–4663 (2015).

150. Bayley, P. M. *et al.* Transport properties and phase behaviour in binary and ternary ionic liquid electrolyte systems of interest in lithium batteries. *ChemPhysChem* **12,** 823–827 (2011).

151. Fawdon, J. *et al.* Characterising lithium-ion electrolytes via operando Raman microspectroscopy. *Nat. Commun.,* 13–15 (2021).

152. Richter, J. *et al.* Thermodynamic properties of Alkali Nitrate-Silver Nitrate Melts. *J. Phys. F Met. Phys.* **2,** 833–841 (1972).

153. Pan, Q. *et al.* A dense transparent polymeric single ion conductor for lithium ion batteries with remarkable long-term stability. *J. Power Sources* **336,** 75–82 (2016).

154. Diederichsen, K. M. *et al.* The Most Promising Routes to a High Li + Transference Number Electrolyte for Lithium Ion Batteries. *ACS Energy Lett.* **2,** 2563–2575 (2017).

155. Song, J. *et al.* Ionomer-Liquid Electrolyte Hybrid Ionic Conductor for High Cycling Stability of Lithium Metal Electrodes. *Sci. Rep.* **5,** 1–9 (2015).

156. Choudhury, S. *et al.* A highly reversible room-temperature lithium metal battery based on crosslinked hairy nanoparticles. *Nat. Commun.* **6,** 1–9 (2015).

157. Choudhury, S. *et al.* Hybrid Hairy Nanoparticle Electrolytes Stabilizing Lithium Metal Batteries. *Chem. Mater.* **28,** 2147–2157 (2016).

158. Moganty, S. S. *et al.* Ionic-liquid-tethered nanoparticles: Hybrid electrolytes. *Angew. Chemie - Int. Ed.* **49,** 9158–9161 (2010).

159. Byrne, N. *et al.* The zwitterion effect in ionic liquids: Towards practical rechargeable lithium-metal batteries. *Adv. Mater.* **17,** 2497–2501 (2005).

160. Byrne, N. *et al.* Effect of zwitterion on the lithium solid electrolyte interphase in ionic liquid electrolytes. *J. Power Sources* **184,** 288–296 (2008).

161. Ohno, H. *et al.* Design and properties of functional zwitterions derived from ionic liquids. *Phys. Chem. Chem. Phys.* **20,** 10978–10991 (2018).

162. Narita, A. *et al.* Lithium ion conduction in an organoborate zwitterion–LiTFSI mixture. *Chem. Commun.,* 1926–1928 (2006).

163. Lane, G. H. *et al.* The electrochemistry of lithium in ionic liquid/organic diluent mixtures. *Electrochim. Acta* **55,** 8947–8952 (2010).

164. Bayley, P. M. *et al.* Transport properties of ionic liquid electrolytes with organic diluents. *Phys. Chem. Chem. Phys.* **11,** 7202–7208 (2009).

165. Lombardo, L. *et al.* Mixtures of ionic liquid-Alkylcarbonates as electrolytes for safe lithium-ion batteries. *J. Power Sources* **227,** 8–14 (2013).

166. Logan, E. R. *et al.* Electrolyte Design for Fast-Charging Li-Ion Batteries. *Trends Chem.* **2,** 354–366 (2020).

167. Logan, E. R. *et al.* Ester-Based Electrolytes for Fast Charging of Energy Dense Lithium-Ion Batteries. *J. Phys. Chem. C* **124,** 12269–12280 (2020).

168. Cho, Y. G. *et al.* Nitrile-assistant eutectic electrolytes for cryogenic operation of lithium ion batteries at fast charges and discharges. *Energy Environ. Sci.* **7,** 1737–1743 (2014).

169. Suo, L. *et al.* A new class of Solvent-in-Salt electrolyte for high-energy rechargeable metallic lithium batteries. *Nat. Commun.* **4,** 1481 (2013).

170. Yamada, Y. *et al.* Review—Superconcentrated Electrolytes for Lithium Batteries. *J. Electrochem. Soc.* **162,** A2406–A2423 (2015).

171. Wang, J. *et al.* Superconcentrated electrolytes for a high-voltage lithium-ion battery. *Nat. Commun.* **7,** 1–9. arXiv: `arXiv:1011.1669v3` (2016).

172. Borodin, O. *et al.* Uncharted Waters: Super-Concentrated Electrolytes. *Joule* **4,** 69–100 (2020).

173. Ren, X. *et al.* Localized High-Concentration Sulfone Electrolytes for High-Efficiency Lithium-Metal Batteries. *Chem* **4,** 1877–1892 (2018).

174. Niu, C. *et al.* High-energy lithium metal pouch cells with limited anode swelling and long stable cycles. *Nat. Energy* **4,** 551–559 (2019).

175. Niu, C. *et al.* Balancing interfacial reactions to achieve long cycle life in high-energy lithium metal batteries. *Nat. Energy* (2021).

176. Cao, X. *et al.* Effects of fluorinated solvents on electrolyte solvation structures and electrode/electrolyte interphases for lithium metal batteries. *Proc. Natl. Acad. Sci. U. S. A.* **118,** 1–9 (2021).

177. Ko, J. *et al.* Recent progress in LiF materials for safe lithium metal anode of rechargeable batteries: Is LiF the key to commercializing Li metal batteries? *Ceram. Int.* **45,** 30–49 (2019).

178. Boyle, D. T. *et al.* Transient Voltammetry with Ultramicroelectrodes Reveals the Electron Transfer Kinetics of Lithium Metal Anodes. *ACS Energy Lett.* **5,** 701–709 (2020).

179. Liu, Y. *et al.* Insight into the Critical Role of Exchange Current Density on Electrodeposition Behavior of Lithium Metal. *Adv. Sci.* **8,** 1–11 (2021).

180. Kim, S. C. *et al.* Potentiometric Measurement to Probe Solvation Energy and Its Correlation to Lithium Battery Cyclability. *J. Am. Chem. Soc.* (2021).

181. Amanchukwu, C. V. The Electrolyte Frontier: A Manifesto. *Joule* **4,** 281–285 (2020).

2 | Method Fundamentals

Contents

2.1 Confocal Raman Microspectroscopy 55
2.1.1 Confocal Microscopy 55
2.1.2 Raman Spectroscopy Fundamentals 55
2.1.3 Raman Instrumentation 57
2.2 Electrochemical Techniques 59
2.2.1 Electrochemical Impedance Spectroscopy 59
2.2.2 Chronopotentiometry 63
2.3 References 63

2.1 Confocal Raman Microspectroscopy

2.1.1 Confocal Microscopy

Originally patented by Marvin Minksey in 1957, confocal microscopy uses a point-like light source (a laser, for example), focuses it onto the sample and uses a pinhole aperture in front of the detector to block out-of-focus light. This allows spectra to be measured in a precise plane of focus. Performing confocal microscopy eliminates the limitations of wide-field microscopy, with the latter using a detector that picks up all out-of-focus light too. Although using a pinhole aperture leads to 95% loss of light, the optical resolution of the sample is much improved over wide-field microscopy; however, the decreased signal intensity can mean sample exposure times need to be increased.[1]

2.1.2 Raman Spectroscopy Fundamentals

Raman Spectroscopy is a non-destructive analytical technique that identifies vibrational modes of molecules to further understand their intra- and intermolecular structure. Conventionally, a sample is illuminated by monochromatic light, such as a laser, leading to vibrational excitations.[2] The absorption of a photon results in a vibrational unstable "virtual" state, so relaxes and immediately re-emits the photon as scattered light. The vast majority of light relaxes back to its original vibrational energy state, which is called elastic scattering, or often termed

"Rayleigh scattering". In the minority of cases (roughly 1 in 10 million photons) "inelastic scattering" occurs, as photons relax to a different vibrational energy states. This scattering type is termed "Raman scattering" and is fundamental in Raman spectroscopy for elucidating structural information. If relaxation leads to a net-increase in molecular vibrational energy, lower energy scattered light is detected, which is called Stokes Raman scattering. If relaxation results in a net-decrease in energy, it is termed Anti-Stokes Raman scattering. Due to statistically more molecules being in their ground vibrational state, Stokes scattering is a more likely process and therefore results in more intense Raman spectral peaks compared to Anti-Stokes scattering.[3]

The number of vibrational modes in a non-linear molecule is $3N-6$, where $3N$ is the number of degrees of freedom in a molecule. Due to there being 3 translational and 3 rotational degrees of freedom, 6 is subtracted from the total. For linear molecules there are $3N-5$ vibrational modes. Raman spectroscopy is characterised by its gross selection rule; namely a Raman active molecules must have *anisotropic polarisability* i.e. when excited from the light, Raman scattering requires a change in polarisability between the initial and final state. Its polarisability is directly related to the intensity of the Raman peak through equation:

$$I = C_i K I \alpha_1^2 \omega^4 \tag{2.1}$$

Where I is peak intensity, C_i is the concentration of species i, K is a constant composed of the speed of light, I is the laser power and ω is the incident radiation frequency. α_1 is the polarisability of the molecule described by the equation below:

$$\alpha_1 = \alpha_0 \cdot \frac{n^2-1}{n^2+1} \tag{2.2}$$

Where α_0 is the polarisability of an individual molecule in a vacuum and n is the refractive index of the solution.

When reporting Raman shift, it is usually converted to wavenumber with:[4]

$$\Delta\overline{\nu}(cm^{-1}) = \frac{1}{\lambda_0(nm)} - \frac{1}{\lambda_1(nm)} \times \frac{10^7(nm)}{cm} \tag{2.3}$$

Where $\Delta\overline{\nu}$ is the wavenumber, and λ_0 and λ_1 are the excitation laser and scattered light wavelength respectively. Reporting Raman shift in wavenumbers allows for a comparison of data independent of the laser wavelength one uses. There are a variety of laser wavelengths one can use in Raman spectroscopy, generally ranging from near-IR to visible to UV wavelengths. Raman scattering is inversely proportional to λ^4, so decreasing wavelength is preferable to increase Raman signal. However, with decreasing λ, there is an increase in fluorescence emission in many materials, which can lead to poor resolution of the Raman peaks. Within the Raman spectrometer setup that was accessed in this work, there were three common laser wavelengths, namely 785 nm, 633 nm and 532 nm. For the measurements of all studies in this project, the 785 nm laser was used because it balanced good spectral resolution (or scattering efficiency), detector efficiency and lack of fluorescence emission. When testing smaller wavelength lasers, there was a noticeable increase in fluorescence emission. Raman spectroscopy lends itself well to microscopic analysis. By coupling a spectrometer with a microscope, one can sample very small volumes depending on the microscope objective one uses.

2.1.3 Raman Instrumentation

Typically a Raman spectrometer consists of three main components: the light source (laser), monochromator to isolate one scattered wavelength of light and a detector. Figure 2.1 shows a schematic of a common Raman microscope spectrometer setup. [3] The monochromator is often in the form of a diffraction grating, which disperses the scattered signal onto the detector. Each grating has a groove density (gr/mm), with more grooves equating to a higher spectral resolution. The grating disperses the signal over a larger number of pixels when using a CCD (Charge Coupled Device) detector, within a defined spectral range. CCD detectors have an array of light-sensitive silicon diodes connected to a capacitor. A typical detector size is 1024 x 127 pixels. CCD detectors are the most popular detectors in modern Raman spectrometers due to their

high sensitivity to light and their multichannel operatation (ability to measure a spectrum in one acquisition).[5]

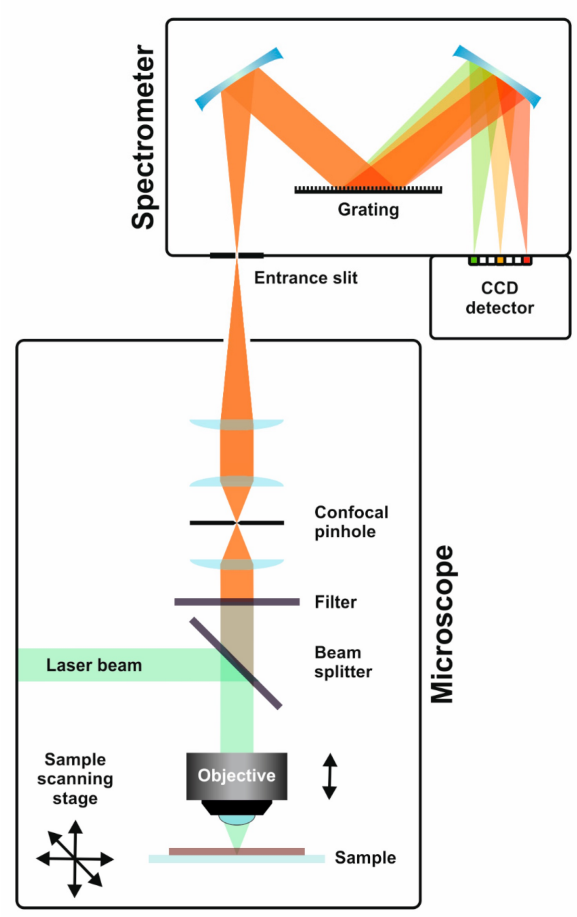


Figure 2.1: Schematic of confocal Raman microscope: Laser beam induces Raman-scattered light, which is filtered and passed through a confocal pinhole. The light passes to the spectrometer onto the grating, which disperses the signal to the CCD detector. Adapted with permission under the Creative Commons Attribution 4.0 International License from Ref. [3]

The instrument used in this project was the Renishaw InVia Reflex confocal Raman spectrometer, which was equipped with a near-IR 785 nm diode laser, a 1800 gr/mm grating and CCD detector.

2.2 Electrochemical Techniques

2.2.1 Electrochemical Impedance Spectroscopy

Electrochemical Impedance Spectroscopy (EIS) is an experimental technique that allows one to gain insight into time-dependent electrochemical processes. EIS measures the impedance (Z) of a system, with Z defined as the ratio between voltage and current in the *frequency* domain:[6, 7]

$$Z = \frac{\widetilde{V}(\omega)}{\widetilde{I}(\omega)} \tag{2.4}$$

Where Z is the impedance, V is the voltage, I is the current and ω is the frequency.

Z includes any process that might inhibit current flow, like resistance (R), capacitance (C) and inductance (L), with each of these elements having a different relationship with time:[8, 9]

$$V(t) = L\frac{dI}{dt} + RI + C^{-1}\int Idt \tag{2.5}$$

By performing a Fourier Transform and thus putting voltage into the frequency domain, one can calculate Z:

$$\frac{\widetilde{V}(\omega)}{\widetilde{I}} = (i\omega L + R + (i\omega C)^{-1}) = \widetilde{Z}(\omega) \tag{2.6}$$

Experimentally one measures Z by applying an AC sinusoidal voltage signal (potentiostatic) of sweeping frequency and measuring the current response signal. By measuring a sinusoidal current response, one can perform a Fourier Transform to put the response in the frequency domain, and therefore measure the impedance of the system. As one notes from equation 2.6, both capacitance and inductance have imaginary number i associated with their terms after Fourier Transform.

A type of parametric plot called a "Nyquist plot" is the most popular form to display Z data (see Figure 2.3). The x-axis displays the positive real element and the y-axis displays the negative imaginary element. Additionally, one often fits this

data by using "equivalent circuits", where processes within the electrochemical systems are approximated by the described elements like resistors and capacitors. A common example is measuring the impedance at the interface of electrochemical cells. At the interface there is impedance from the capacitance of the double layer and from the resistance of charge-transfer. Charge-transfer happens in parallel with charging of the double layer, resulting in an equivalent circuit below.

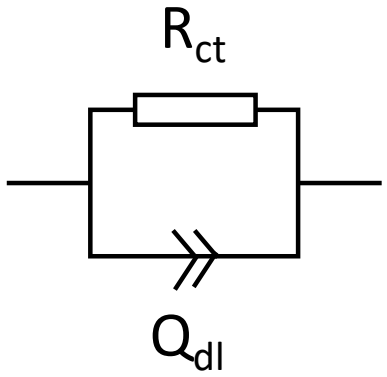


Figure 2.2: Equivalent circuit of non-blocking electrode, showing R_{ct} and Q_{dl}

By adding each element in parallel, and rearranging:[8]

$$Z = \left(\frac{1}{R} + \frac{1}{(i\omega C)^{-1}}\right) = \frac{R}{1+(\omega RC)^2} - i\left(\frac{\omega R^2 C}{1+(\omega RC)^2}\right) \tag{2.7}$$

Rearranging and separating the real and imaginary parts of Z allows one to illustrate the data in a Nyquist plot. Classically, a parallel RC circuit results in a semi-circle in a Nyquist plot as one scans the frequency. Due to the complex nature of electrochemical systems, the described impedance elements are often too simplistic. For example, equation used to describe a capacitor is often altered to be a constant phase element (CPE) (Q). Q accounts for imperfection when measuring the capacitance of electrochemical systems, by incorporating α into the equation. For example, the capacitance in a double-layer is not perfect due to surface inhomogeneities or to a continously distributed set of time constants during charge-transfer.[10]

$$Z_Q = \frac{1}{(i\omega)^{\alpha} Q} \tag{2.8}$$

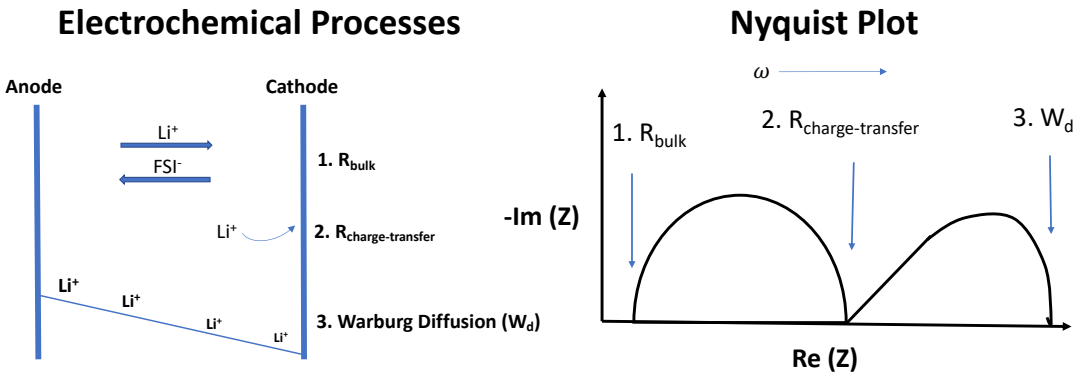


Figure 2.3: Common electrochemical processes and corresponding EIS Nyquist plot, including resistance of the bulk (R_{bulk}), resistance of charge-transfer (R_{ct}) and Warburg diffusion resistance (W_d)

The inclusion of a CPE within the fitting equations allows for the depression of the semi-circle, depending on the value of α. The equivalent circuit that describes the interface is often extended to include resistance of the electrolyte bulk (R_{bulk}) and diffusional resistance termed the Warburg impedance (Z_w), when describing a full or symmetric cell. R_{bulk} is simply the ohmic resistance, which is the sum of current collector, wires and electrolyte resistance. Often researchers deem current collector and wire resistance as negligible so use R_{bulk} to calculate the electrolyte resistance and therefore its ionic conductivity, κ. Warburg resistance is characterised by its 45^o angle in a Nyquist plot, at low frequencies. The equation that describes it includes a real and imaginary element:[11]

$$Z_W = \sigma\omega^{-1/2} - i\sigma\omega^{-1/2} \tag{2.9}$$

Where σ is the Warburg coefficient. With both the real and imaginary elements in the equation 2.9 being equivalent, as one scans the frequency, the W_d element is indeed at 45^o on a Nyquist plot. Z_w increases with decreasing frequency. Equation 2.9 describes so-called "semi-infinite" Warburg diffusion, which covers diffusion prior to steady-state conditions. As a system reaches steady-state, diffusional impedance can either be described as finite-length (FLW) or finite-space Warburg (FSW) impedances. For FLW, at low frequencies, Z_w approaches a pure resistive value as a concentration gradient along the length

of the interelectrode space hits steady state. One sees this Warburg-type in symmetric cells with plating "non-blocking" electrodes as a concentration gradient forms and reaches steady state. It is described by:[12]

$$Z_{FLW} = \frac{Z_0}{\sqrt{i\omega\tau_0}} \tanh(\sqrt{i\omega\tau_0}) \tag{2.10}$$

Where Z_0 is the FLW Warburg coefficient:

$$Z_0 = \frac{RTl}{z^2F^2AC_{eq}D_{app}}\chi_M \tag{2.11}$$

and τ_0 is the time constant:

$$\tau_0 = \frac{l^2}{D_{app}} \tag{2.12}$$

Therefore by fitting with a FLW element one can calculate critical transport parameters described above.

For FSW, at low frequencies, Z_w tends toward a complete capacitative element often associated with a blocking boundary. This is usually seen when using "blocking" outer interfaces, such as a porous electrode. Once the porous layer becomes flooded, it acts like capacitor.

Each of these resistive processes (i.e. R_{bulk}, R_{ct} and W_d) have a different time constant associated with them. This means that they are relatively easy to deconvolute on a Nyquist plot. However, due to the complexity of the multiple processes occurring in batteries, overlapping processes or semi-circles are likely to occur. Most notably, employing reactive electrodes within a cell, an SEI forms either spontaneously or during cycling. Depending on the thickness, morphology and composition of the SEI, an associated impedance is measured, which often overlaps with the interfacial charge-transfer.[13] Equating distinctly separate processes can lead to misleading conclusions, so wariness is urged when assigning electrochemical processes.

Moreover, for the EIS measurements to be valid there are two main requirements: linearity and stability.[6] Linearity shows that Z is independent of the voltage amplitude (V_a) of the AC signal applied. To remain linear, V_a

needs to be small, usually <100mV. Indeed, one needs to balance linearity with spectral resolution, as lower voltages lead to poorer resolution. If performing measurements to very low frequencies, the electrochemical system needs to be chemically stable because low frequency measurements can require a substantial amount of time to run. If unstable, there can be "drifting" of the measurement, which can lead to inaccurate conclusions. Indeed, if both of these requirements are met one can assume the measurement to be both valid and non-destructive, as the EIS measurement has not affected the system.

This project extensively uses EIS to characterise symmetric cells to gain an understanding of bulk electrolyte and interfacial properties.

2.2.2 Chronopotentiometry

Chronopotentiometry is an experiment where one applies a controlled current between working and counter electrode with a power source. The potential is then recorded between the working and counter/reference if using a two-electrode setup. When applying a current to a symmetric, 2-electrode system, the voltage recorded is a result of the various resistances or "overpotentials" (η) present in the system; otherwise the voltage would be zero. Equivalent to the resistive processes described in the above section, common overpotentials includes ohmic (η_{ohmic}), activation (η_{act}) and concentration (η_{conc}). η_{ohmic} is due to the resistance of the electrolyte, η_{act} is a result of resistance of charge-transfer and η_{conc} stems from concentration gradient formation in the electrolyte. Each overpotential is realised over a different time frame, with η_{ohmic} acting first, then η_{act} and η_{conc}. η_{conc}, or concentration gradient formation, is often the limiting step for the voltage to reach a steady-state.

2.3 References

1. Rhodes, W. T. *et al. Springer Series in Optical Sciences - Confocal Raman Microscopy* 300 (2010).

2. Opilik, L. *et al.* Modern raman imaging: Vibrational spectroscopy on the micrometer and nanometer scales. *Annual Review of Analytical Chemistry* **6,** 379–398 (2013).
3. Schmid, T. *et al.* Raman Microspectroscopic Imaging of Binder Remnants in Historical Mortars Reveals Processing Conditions. *Heritage* **2,** 1662–1683 (2019).
4. Smith, D. G. *Modern Raman Spectroscopy: A Practical Approach* 1st (Wiley, 2005).
5. Larkin, P. J. *Instrumentation and Sampling Methods* 29–61 (2018).
6. AMT, A. *Electrochemistry - Electrochemical Impedance Spectroscopy (EIS) Theory* Youtube. https://www.youtube.com/watch?v=I3uvugRXHG8.
7. Macdonald, J. R. Theory of space-charge polarization and electrode-discharge effects. *J. Chem. Phys.* **58,** 4982–5001 (1973).
8. Cooper, S. *Introduction to Electrochemical Impedance Spectroscopy (EIS: Maths and Theory)* Youtube. https://www.https://www.youtube.com/watch?v=5puDQjCl2pk.
9. Andre, D. *et al.* Characterization of high-power lithium-ion batteries by electrochemical impedance spectroscopy. I. Experimental investigation. *Journal of Power Sources* **196,** 5334–5341 (2011).
10. Orazem, M. E. *et al. Electrochemical Impedance Spectroscopy* 1–211 (John Wiley and Sons Inc., Hoboken, New Jersey, 2008).
11. *Electrochemical Impedance Spectroscopy* http://lacey.se/science/eis/. [Online; accessed 23-May-2021].
12. Boukamp, B. A. Derivation of a Distribution Function of Relaxation Times for the (fractal) Finite Length Warburg. *Electrochim. Acta* **252,** 154–163 (2017).
13. Single, F. *et al.* Theory of Impedance Spectroscopy for Lithium Batteries. *Journal of Physical Chemistry C.* arXiv: 1908.00962 (2019).

3 | Characterising Binary Electrolytes via Operando Raman Microspectroscopy

Contents

3.1 Abstract 65
3.2 Introduction 66
3.3 Results & Discussion 69
3.3.1 Densitometry & Partial Molar Volumes 69
3.3.2 Raman Calibration 70
3.3.3 Cell Design & Concentration Visualisation 73
3.3.4 Measuring Transport & Thermodynamic Properties . . . 77
3.3.5 Effect of Concentration 86
3.3.6 Stefan-Maxwell Measurements 94
3.3.7 Transport using PEIS 96
3.3.8 COMSOL Modelling 99
3.4 Conclusions & Future Work 102
3.5 Experimental Detail 105
3.6 References 108

3.1 Abstract

In this chapter, a novel method for fully characterising electrolyte systems was presented. The method involved monitoring electrolyte concentration gradients over time via operando Raman microspectroscopy, while in tandem with potentiostatic electrochemical impedance spectroscopy. Using the single experimental setup, concentration-dependent properties including the Fickian "apparent" diffusion coefficient, transference number, thermodynamic factor, ionic conductivity and resistance of charge-transfer of LiFSI in G4 were quantified. The study described a method for visualising electrolyte concentration gradient; a procedure for determining the described electrolyte properties, and a necessary technique for correlating bulk intermolecular electrolyte structure with the described transport and thermodynamic properties. Furthermore, full cell simulations using the

measured electrolyte properties were provided, and a comparison with other characterisation methods was discussed.

3.2 Introduction

As mentioned in section 1.1, to keep up with the increasing need for high-energy storage solutions, innovative technologies that go beyond Li-ion batteries (LIBs) are required, with many researchers aiming to improve on LIBs' energy density by 2-3 times. The ultimate success of high energy alternatives depends on the development of new electrolytes. To understand an electrolyte's suitability, a full characterisation of its mass transport, thermodynamic and interfacial properties is paramount. Few researchers fully characterise novel electrolyte formulations presumably due to the time and resource intensive nature of each characterisation method (see Section 1.5).

As was also mentioned, a full characterisation of electrolyte properties requires both transport and thermodynamic information. Indeed, the interaction of the electrolyte at the electrode interface is also an important metric for understanding battery performance, so its isolation is also valuable. In this Chapter, a full characterisation of a binary electrolyte, namely LiFSI in tetraethylene glycol dimethyl ether (tetraglyme – G4), is presented using operando Raman microspectroscopy and potentiostatic electrochemical impedance spectroscopy (PEIS). Extending the technique that Rey et al. introduced, the diffusion coefficient (D_{app}), transference number (t^0_{Li+}), thermodynamic factor (χ_M), ionic conductivity (κ) and resistance of charge transfer (R_{ct}) were determined within one experimental setup. This is the first time full concentration gradients have been observed using operando Raman microspectroscopy, and the first time all key electrolyte parameters have been determined using one technique. This is especially true for χ_M because this value has never been determined in such a dynamic setup. The schematic in Figure 3.1 illustrates the method that was developed to extract these key electrolyte properties.

Specifically the chapter will cover:

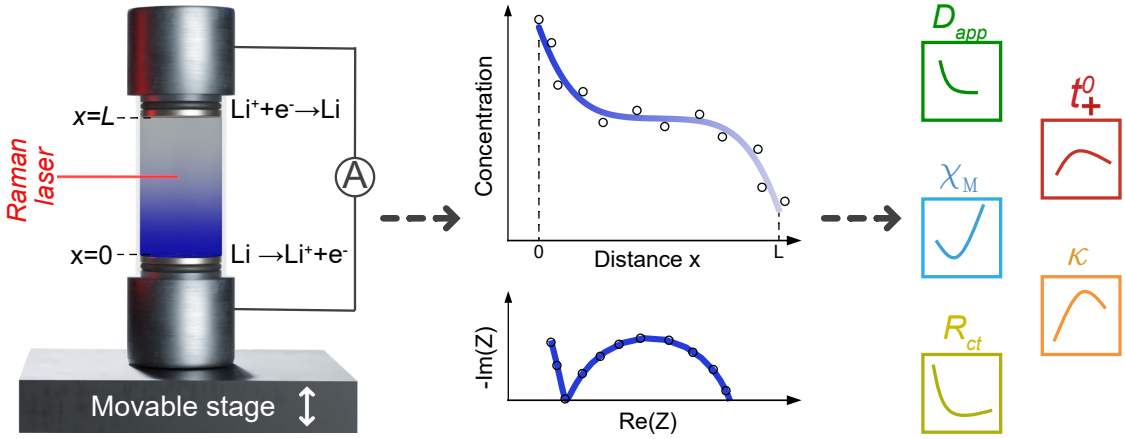


Figure 3.1: Schematic of method to measure key electrolyte properties. Li^+ concentration (c_s) gradient formation in an optical Li/Li symmetric cell, while current is passed. Using a scanning confocal Raman microspectrometer, a time-series of one-dimensional line scans was performed to obtain a progression of concentration gradients; measured with the stage moving in the z-direction. The cell was placed vertically on the stage to avoid natural convection. Potentiostatic electrochemical impedance spectroscopy (PEIS) was also performed prior to passing current to quantify ionic conductivity (κ) and resistance of charge-transfer (R_{ct}), and between line scans to obtain an accurate concentration overpotential (η_c). Using the diffusion length (L_d), interfacial gradient ($dc_s/dz|_{z=0,L}$) and η_c from each concentration profile, the Fickian "apparent" diffusion coefficient (D_{app}), cation transference number (t_+^0), and molar thermodynamic factor (χ_M), were calculated.

- The precise **experimental method** for gathering concentration gradients using operando Raman microspectroscopy.
- **Calibration** of Raman spectral information and Li^+ concentration.
- Description of the **concentration gradients** formed at different current densities.
- **Fitting** of the concentration gradients, and the subsequent extraction of electrolyte transport and thermodynamic properties.
- **Effect of bulk concentration** on gradient formation and subsequent electrolyte property comparison.
- **COMSOL modelling** for full-cell simulations.
- **Comparison** of isolated properties with conventional methods.

All the work in this chapter was performed by myself, under the supervision of Prof. Mauro Pasta. I did all the experiments, cell designs, simulations and analysis. The work has been published in *Nature Communications*, authored

by Jack Fawdon, Dr. Johannes Ihli, Prof. Fabio La Mantia and Prof. Mauro Pasta. Adapted with permission under the Creative Commons Attribution 4.0 International License from Ref.[1] Dr. Ihli assisted in the initial operando Raman measurements using the "prototype capillary cell" (see Figure 3.6) and Prof. La Mantia provided useful discussion regarding the electrochemical data.

3.3 Results & Discussion

3.3.1 Densitometry & Partial Molar Volumes

Densitometry. Each electrolyte concentration was prepared using molalities (mol kg^{-1} (of solvent)) and converted to molarity (mol dm^{-3} (of solution)). Preparing concentrations on a gravimetric scale is more accurate than volumetric, as one uses an analytical balance instead of relying on the accuracy a volumetric flask. The density curve is presented in Figure 3.2, fitted with a 2nd order polynomial. The concentration in molality was converted to molarity with equation 3.1 below:

$$c_{molarity} = \frac{n_{mols}\rho}{m_{total}} \tag{3.1}$$

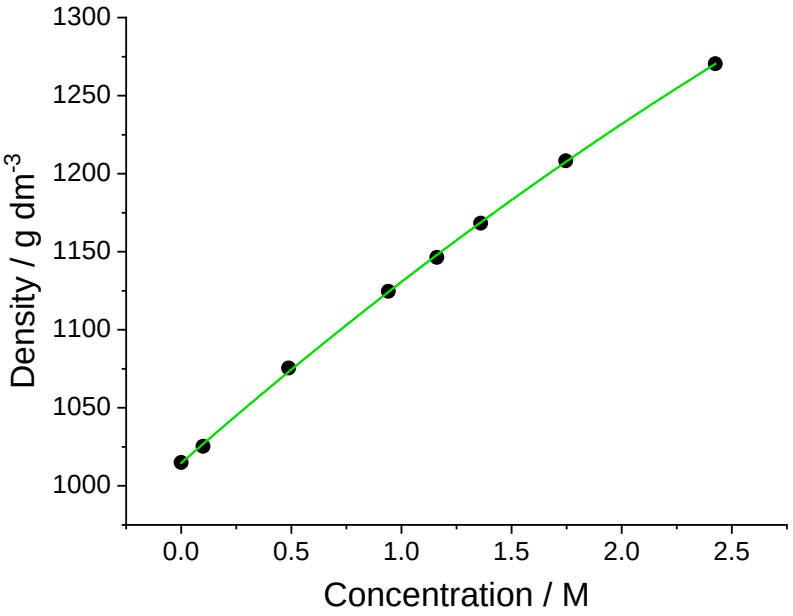


Figure 3.2: LiFSI in G4 density vs. concentration

Partial Molar Volumes. The partial molar volumes of the salt (V_s) and the solvent (V_0) were calculated from the density and equations 1.25 and 1.24.[2] The non-linearity of density with concentration implied that V_0 was changing is concentration.

Using the density curve data fitting (ρ_0 = 1014.64, ρ_1 = 123.48, ρ_2 = -7.45), V_s and V_0 were calculated and plotted:

$$V_s = \frac{M_s - \rho_1 - 2\rho_2 c}{\rho_0 - \rho_2 c^2} \tag{3.2}$$

$$V_0 = \frac{M_0}{\rho_0 - \rho_2 c^2} \tag{3.3}$$

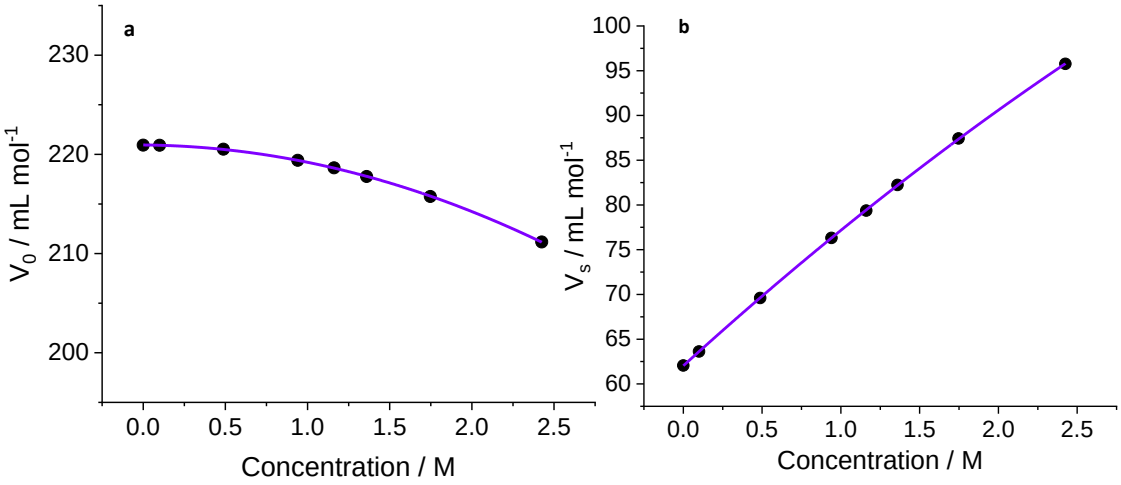


Figure 3.3: Partial Molar Volumes of a) Solvent (G4) b) Salt (LiFSI)

Figures 3.3 illustrates the relationship between partial molar volumes and concentration of LiFSI in G4. One should note the drop V_0 as it occupies a smaller volume fraction with increasing concentration. Whereas the salt molar volume increased with higher electrolyte content, perhaps due to more solvation by G4 or larger aggregates forming.

3.3.2 Raman Calibration

To visualise Li-ion concentration using Raman spectroscopy, one requires an isolated and concentration-sensitive Raman band. Then a set of standard solutions of known Li^+ concentration can be prepared to understand specifically how this Raman band changes with c_{Li+}. Li^+ has no Raman active bands being monatomic, but due to electroneutrality defined by Poisson's Equation below, a concentration-dependent FSI^- peak can be used to equate c_{Li+}.[2]

$$\nabla^2\Phi = \frac{-F(c_+ + c_-)}{\varepsilon_r \varepsilon_0} = -1.40 \times 10^6 (c_+ + c_-)(V \cdot \mu m^{-2}) \tag{3.4}$$

Where Φ is the electrode potential, ε_r is the relative permittivity, ε_0 is the vacuum permittivity (F m^{-1}) and c_+ and c_- are the concentrations of the cation

and anion respectively. Figure 3.4 shows the Raman spectrum of 2 m LiFSI in G4 normalised to peak intensity at 1471 cm^{-1}. Labelled are the key bands that were used to both calibrate c_{Li+} and understand intermolecular changes that occurred with increasing c_{Li+}. The anion peak at 717 cm^{-1}, corresponding to the S-N-S vibration, was used to correlate peak area with c_{Li+}.[3] Peak area and intensity is directly proportional with species concentration, as is described by the equation 2.1. Also included is n, the refractive index, which was likely to change marginally with concentration, but did not affect the line scan values because the calibration standards took this effect into account. The solvent peak at 1471 cm^{-1} represents the -CH_2 bending/scissoring mode, and was used to normalise the line scan spectra. A set of calibration standards of LiFSI in G4 were prepared, and scanned using the Raman setup and parameters described in Experimental Detail. Each spectrum was normalised against the solvent peak, and the 717 cm^{-1} peak was integrated. Each of the normalised spectra isolating the 717 cm^{-1} peak is plotted in Figure 3.5a, along with the resulting calibration curve plotted in Figure 3.5b. The error bars represent the propagated standard error from the balance and density measurements (x-axis), and the area calculation from the separate Raman acquisition (y-axis). As was expected, Figure 3.5b shows the linear dependence of anion peak area with concentration.

The spectra used to construct the calibration curve were analysed to understand how concentration affected the microscopic structure in each solution. Firstly, as concentration increased shoulder peaks at higher wavenumbers to the 717 cm^{-1} began to emerge, indicating the formation of contact ion pairs (CIPs) then aggregates (AGGs). Indeed, monitoring "X at Max Height" the peak began to shift to higher wavenumbers at $\sim$1 m, which suggested CIPs and AGGs began to dominate at this concentration, see Figure 3.23c. Also labelled in Figure 3.4 is the peak at 868 cm^{-1}, identified as the $[Li(G4)]^+$ crown ether-like breathing mode. With increasing salt concentration, this peak became more prominent indicating Li^+ was being solvated by G4 forming stable $[Li(G4)]^+$ structures. The accumulation of this information suggested competing association in the salt, and

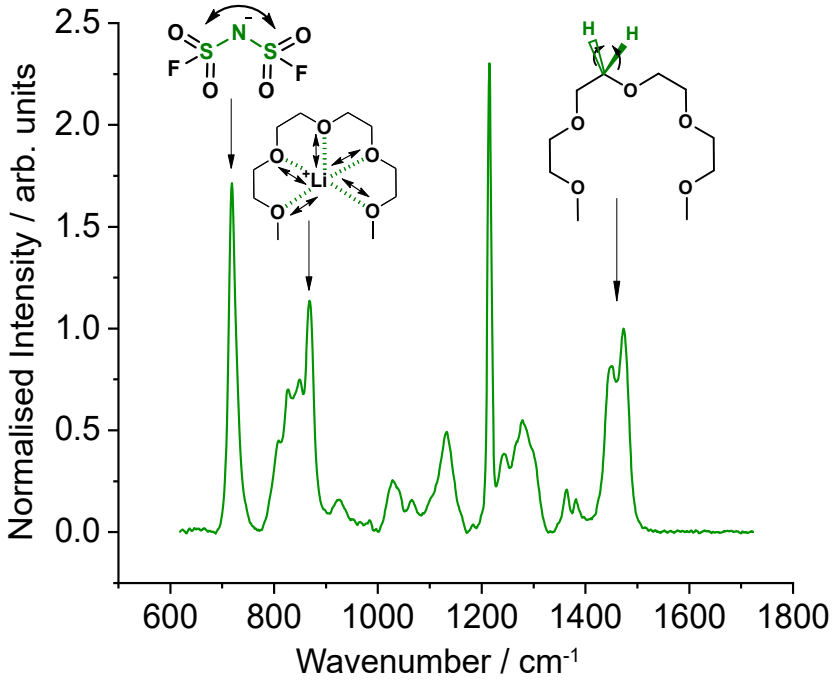


Figure 3.4: 2 m LiFSI in G4 Raman Spectrum normalised to peak intensity at 1471 cm^{-1}; identifying the 717 cm^{-1} FSI^- S-N-S bending mode peak, 868 cm^{-1} $[Li(G4)]^+$ crown ether-like breathing mode peak, 1471 cm^{-1} -CH_2 bending/scissoring mode peak.

solvation by the solvent. The analysis of these peaks proved important for the explanation of macroscopic transport and thermodynamic trends described later.

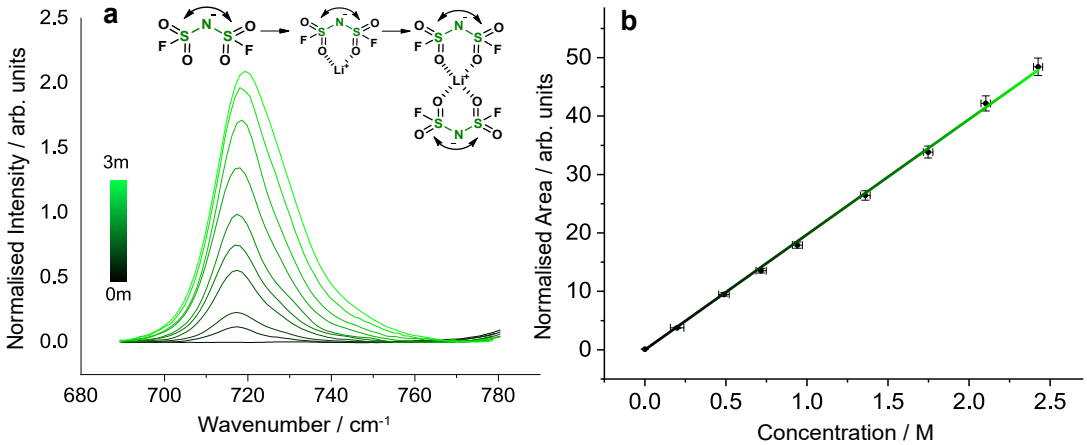


Figure 3.5: Calibration Data. a) Normalised 717 cm^{-1} peak, showing broadening of the peak with concentration, indicating the evolution of CIPs and AGGs, as illustrated. b) Calibration curve equating normalised 717 cm^{-1} peak area to concentration, which was used to determine the concentration gradient via operando Raman microspectroscopy 1D line scans. Error bars represent the propagated standard error from the balance and density measurements (x-axis) and area calculation from three separate Raman acquisitions (y-axis).

3.3.3 Cell Design & Concentration Visualisation

The extraction and visualisation of concentration profiles required a custom-designed cell that was 1) transparent so the Raman laser would penetrate the cell, and 2) linear so that the concentration gradient that formed would be geometrically uniform. There were multiple iterations of design, from a prototype cell that used a capillary tube, to a PEEK-based cell that had a quartz window, and finally a cell that used a wider quartz tube and two stainless steel (SS) pistons (Figure 3.6). Specifically, this final cell consisted of two stainless steel pistons that were designed to fit inside a quartz glass tube of 20 mm in length. Each piston had an inner diameter (ID) of 8 mm and outer diameter (OD) of 10 mm. An interelectrode distance of 15 mm was chosen because it was sufficiently large to detect a concentration gradient with good spectral resolution and also meant the diffusion layer did not progress too quickly into the centre of the cell, which would make the fitting equation invalid. If it were longer the diffusion layer would not progress quickly enough, and the measurement would take substantially longer than 36 hours. Also, two perfluoroelastomer FFKM O-rings were required to seal the cell, with the more common Nitrile or Viton-based O-rings not compatible with our chosen ether-based electrolyte – using these O-rings led to the cracking of the quartz tube due to the large swelling of the O-rings. The lithium metal foil (99.9%, 750 µm thickness, Alfa-Aesar) acting as electrodes for the symmetric cell, was prepared by scraping off the native oxide layer of the foils and calendaring to 300 µm in thickness. From here, circular lithium discs were prepared with a diameter of 8 mm and placed onto each of the stainless steel pistons. One piston was then placed inside the quartz tube, $\sim$1 mL of electrolyte was added, and then the second piston was introduced on the opposite side, sealing the cell. Care was taken not to introduce any gas bubbles into the system. Before any tests were run, the cell was set up inside the Raman microscope and connected to a Biologic SP150 potentiostat (Figure 3.7).

For each sample concentration, a constant current was applied to the operando cell for 24-48 hours, allowing for a sufficient gradient to form. 100 μA cm^{-2} was

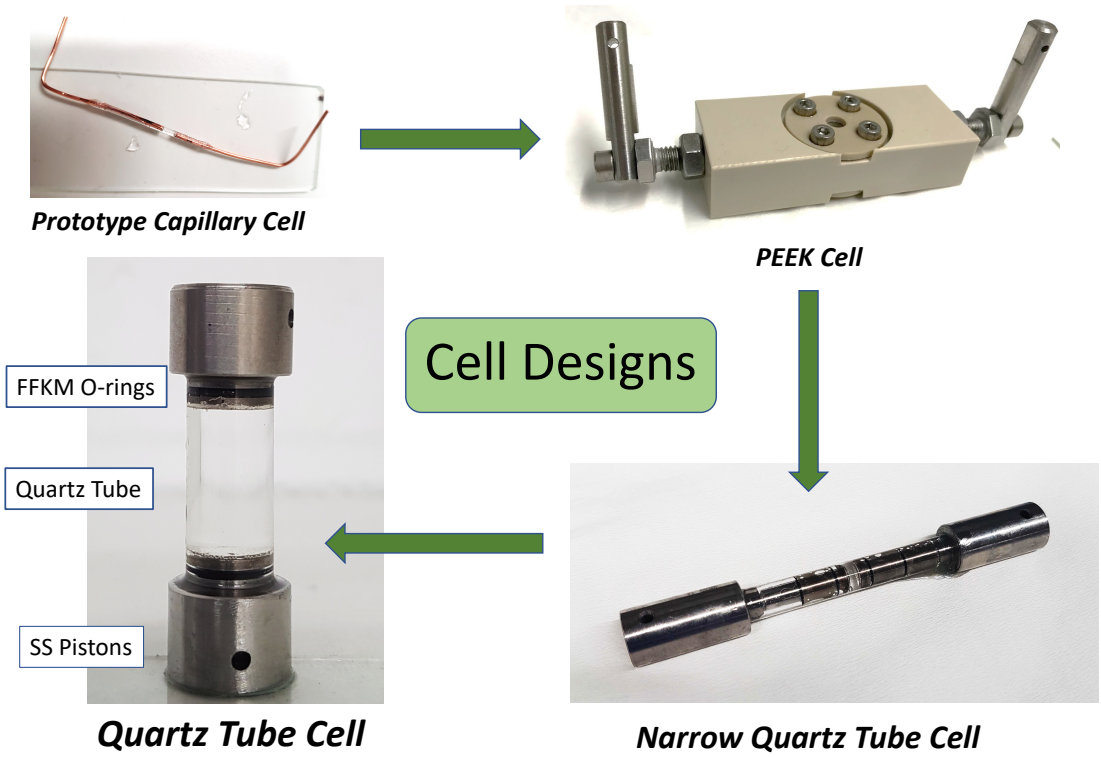


Figure 3.6: Cell Designs: Progression of cell design used for operando Raman experiments; namely, a prototype cell that used a capillary tube for optical measurements; a cell housed in a PEEK shell, utilising a quartz window; a narrow quartz tube cell, and finally a long, wider quartz tube cell used for all described operando Raman experiments in this work.

chosen as the operating current (J) to avoid dendrite formation, and also to allow a concentration gradient of sufficient magnitude to form. Both visually, and there being no drop in R_{ct} with time, provided evidence that there was no dendrite growth at 100 μA cm^{-2}. (see Figures 3.10a and 3.15b)

To measure each gradient, a point-by-point 1D line scan was performed, taking 50 points between each electrode, using the same laser settings as the calibration curve as described in Experimental Detail. A laser power of 5% was deemed optimal as it provided good spectral resolution, whilst showing no evidence of thermal heating nor oxidation of the solvent. This is illustrated in Figure 3.8, which shows no change in the solvent peak with time showing no evidence of decomposition products. Moreover, there was no emergence of additional peaks in the spectra after repeated line scans. Also, there was no decrease in the overpotential with time, which indicated there was no thermal heating.

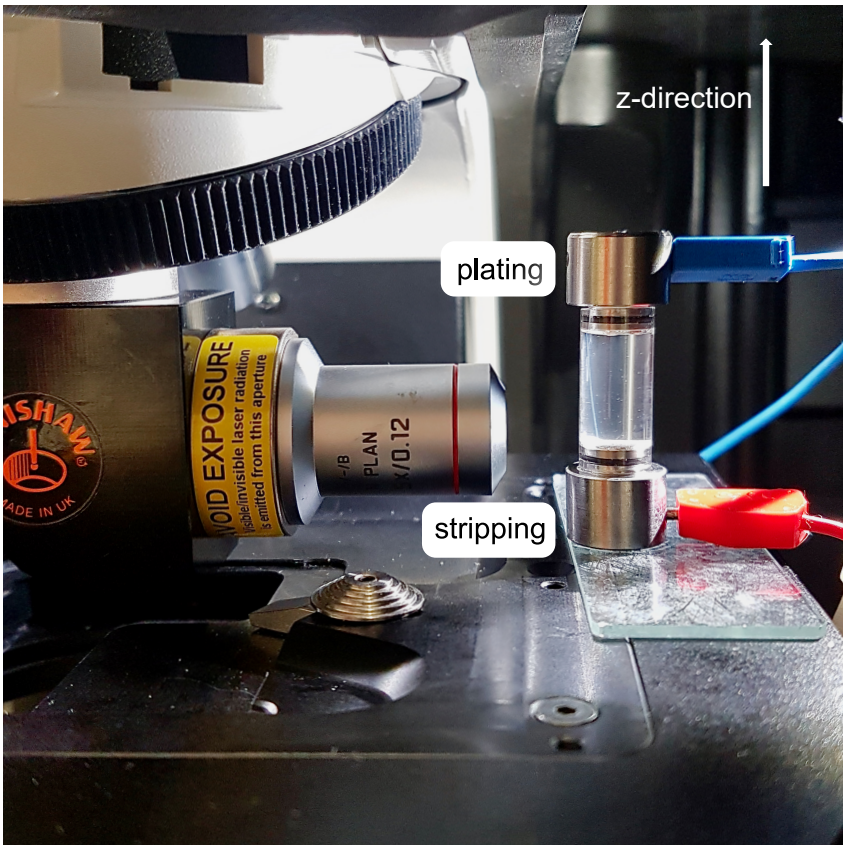


Figure 3.7: Experimental Setup for Raman Line Scan. Quartz tube optical cell equipped with two lithium electrodes, stripping occurs at the bottom of the cell and plating at the top to avoid natural convection.The cell was scanned "side-on" by using a 90° mirror and the stage moving in the z-direction. A 5x objective was used, with a spot size of $\sim$4.8 μm

For the starting point of each line scan, the laser was focused as close to the electrode surface as possible, at a defined depth. As described in section 2.1, confocal microscopy uses a pinhole aperture to block out-of-focus light, measuring spectra in a precise plane of focus. This meant spectra were gathered at defined depths (centre point of the cell) with an accurate spot size. The gradient evolution during a line scan acquisition, under the selected operational conditions of the cell, was determined to be within the signal-to-noise error for the acquired Raman spectra. Using Renishaw's WiRE5.5 software, each spectra had its background removed, then using a Python script each spectra was compared to the calibration curve to extract the electrolyte concentration at each point along each line scan. The Python script is presented in Appendix 1 (also available

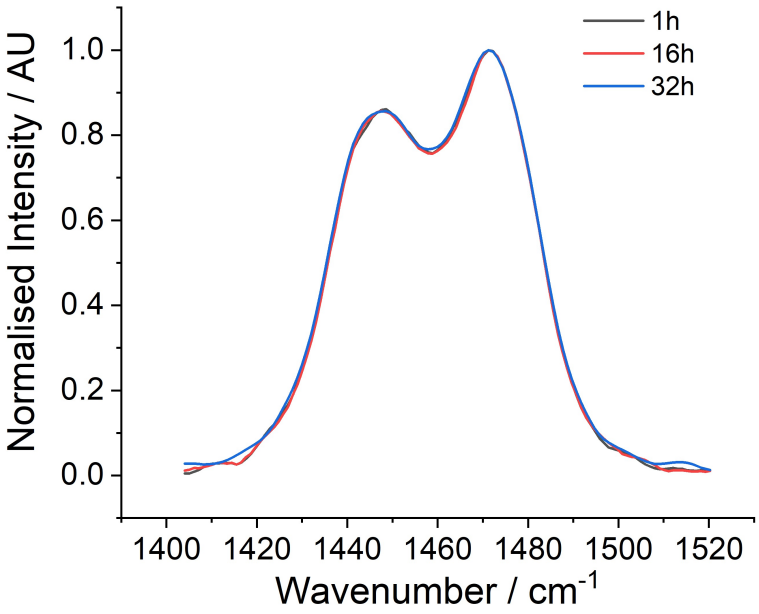


Figure 3.8: Raman spectra of 1471 cm^{-1} peak, illustrating the -CH_2 bending/scissoring not shifting over each line scan, indicating the lack of solvent decomposition.

at GitHub), and specifically normalises each spectra; truncates the spectra to only include the 717 cm^{-1} peak; integrates the peak to find the area, and then converts it to a lithium-ion concentration using the calibration curve.

PEIS measurements were taken intermittently, every 4 hours, to track R_{ct} and other impedance elements. This allowed the tracking of changes in R_{ct}, which provided evidence of potential dendrite growth, and also allowed for an accurate determination of the concentration overpotential (η_c), which was required for the isolation of χ_M. To check the PEIS measurements, and therefore the pause on the passing of current was not affecting the concentration gradient, experiments were repeated with and without the PEIS measurements. Further details of PEIS experimental parameters are described in Experimental Detail.

Effect of Orientation. An extremely important feature of the experimental setup was the cell being placed vertically on the sample stage (as seen in Figure 3.7). If placed horizontally, no gradient would form due to natural convection when the current was passed, as shown in Figure 3.9a. Density gradients that occur perpendicular to the current flow induce bulk flow as illustrated in Figure 3.9b. This level of convection would not occur in commercial cell formats due to

the presence of a separator, which prevents convective effects. To scan vertically (z-direction) required the implementation of a 90^o mirror.

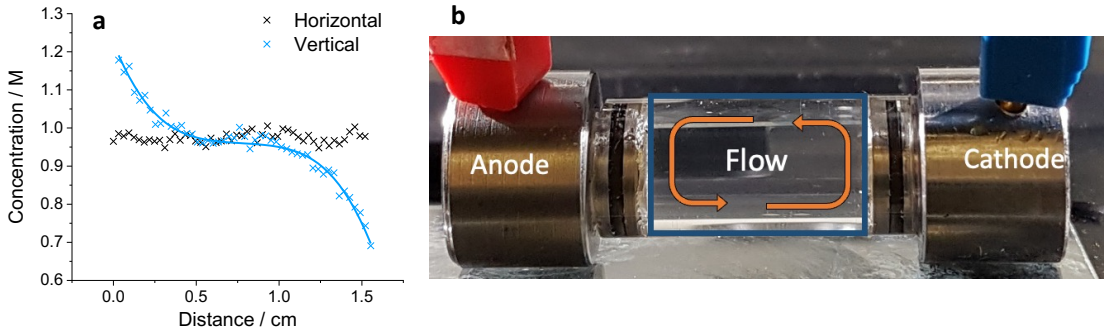


Figure 3.9: Natural Convection. a) Concentration gradient comparison between the cells placed vertically and horizontally, after current was applied for 12 h at 100 µA cm^{-2}. If placed horizontal, the gradient suffers from natural convection due to the density gradient. b) Diagram showing annular flow of the electrolyte if the cell was placed horizontally during the experiment. Density gradients that occur perpendicular to the concentration gradient induce natural convection.

Effect of Current Density. Figure 3.10a shows concentration gradients of 1 m LiFSI in G4 at three different values of current densities, namely 100, 200 and 400 μA cm^{-2}, for 8 hours. The figure shows a clear drop in concentration on the plating side of the cell, and an equally noteworthy concentration increase on the stripping side. At the two higher currents, mossy dendrites began to form (Figure 3.10)b, which blocked the Raman signal, leading to a loss of resolution closer to the electrodes. In Figure 3.10a, the points close to the electrode have been excluded due to poor spectral resolution. In fact, the blocking of the Raman laser allowed for a good estimation of when dendrites were growing, which could be a promising method for dendrite detection in future studies. As was expected, there are proportionally larger gradients with increasing J.

3.3.4 Measuring Transport & Thermodynamic Properties

Using the concentration profiles and PEIS spectra, electrolyte transport and thermodynamic were extracted. 1 m LiFSI in G4 was used as a model system to demonstrate this process. Each gradient was fitted using non-linear least-

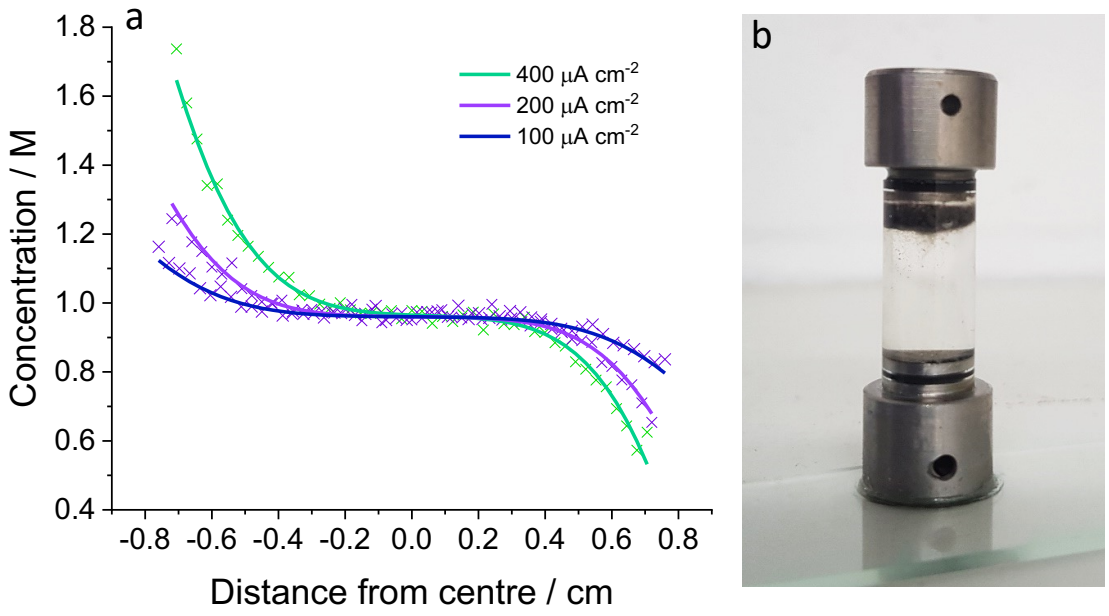


Figure 3.10: Effect of Current Density. a) Concentration gradient comparison after an applied 100, 200 and 400 μA cm^{-2} current rfor 8 hours. b) Example of mossy dendrite growth at the top of cell (plating) after an applied 400 μA cm^{-2} current over 36 hours.

squares minimisation with equation 3.16. The derivation of this equation is described below.

Equation 3.16 is a solution to Fick's diffusion equation. First, one starts with Fick's 2nd law of diffusion [4]:

$$\frac{\partial c_s(z,t)}{\partial t} = D_{app}\frac{\partial^2 c_s(z,t)}{\partial z^2} \tag{3.5}$$

The boundary conditions used are:

$$c_s(z,0) = c_s^* \tag{3.6}$$

$$\lim_{z\to+\infty} c_s(z,t) = c_s^* \tag{3.7}$$

$$D_{app}\left(1-\frac{\partial \ln c_0}{\partial \ln c_s}\right)\left[\frac{\partial c_s(z,t)}{\partial z}\right]_{z=0} = \frac{J(1-t_+^0)}{nF} \tag{3.8}$$

Where c_s is the concentration of the electrolyte or salt, s, t is time, z is distance between the electrodes, c_s^* is the initial concentration, D_{app} is the "apparent" Fickian diffusion coefficient, J is the applied current density I/A, n is the number

of moles, and the factor in rounded parentheses represents how solvent concentration is changing with respect to salt concentration at the interface, which we termed the "solvent velocity factor". Its inclusion is particularly important in measuring t_+^0 as described later. Equation 3.6 states the concentration before the experiment is run. Equation 3.7states the concentration will equal the initial concentration at increasing distances from the electrode surface. Equation 3.8 is derived from the constitutive law for cation flux:

$$N_+(t,z) = -D_{app}\left(1-\frac{\partial \ln c_0}{\partial \ln c_s}\right)\left[\frac{\partial c_s(z,t)}{\partial z}\right] + \frac{J(z)(t_+^0)}{nF} \tag{3.9}$$

Where $N_+(t,z)$ is the cation flux. Using Laplace transform:

$$\bar{c_s}(z,s) = \frac{c_s^*}{s} + A(s)e^{-\sqrt{\frac{s}{D_{app}}}z} \tag{3.10}$$

Where:

$$A = \frac{J(1-t_+^0)}{nFD_{app}^{\frac{1}{2}}s^{\frac{1}{2}}}\left(1-\frac{\partial \ln c_0}{\partial \ln c_s}\right)^{-1} \tag{3.11}$$

And:

$$\bar{c_s}(z,s) = L\{c_s(z,t)\} \tag{3.12}$$

Inversion then leads to the equation that describes the concentration at the plating side of the cell:

$$c_s(z,t) = c_s^* + \frac{J(1-t_+^0)}{nFD_{app}}\left(1-\frac{\partial \ln c_0}{\partial \ln c_s}\right)^{-1}\left\{2\left(\frac{D_{app}t}{\pi}\right)^{\frac{1}{2}}\exp\left(-\frac{z}{2(D_{app}t)^{\frac{1}{2}}}\right)^2 - z\,\mathrm{erfc}\left(\frac{z}{2(D_{app}t)^{\frac{1}{2}}}\right)\right\} \tag{3.13}$$

Adapting 3.13 to measure the concentration at the opposite electrode:

$$c_s(z,t) = c_s^* + \frac{J(1-t_+^0)}{nFD_{app}}\left(1-\frac{\partial \ln c_0}{\partial \ln c_s}\right)^{-1}\left\{2\left(\frac{D_{app}t}{\pi}\right)^{\frac{1}{2}}\exp\left(-\frac{-z+L}{2(D_{app}t)^{\frac{1}{2}}}\right)^2 + (-z+L)\,\mathrm{erfc}\left(\frac{-z+L}{2(D_{app}t)^{\frac{1}{2}}}\right)\right\} \tag{3.14}$$

Where L is the distance between the electrodes. Combining the two equations allows one to look at the concentration at both sides of the cell:

$$c_s(z,t) = c_s^* + \frac{J(1-t_+^0)}{nFD_{app}}\left(1-\frac{\partial \ln c_0}{\partial \ln c_s}\right)^{-1}\left\{2\left(\frac{D_{app}t}{\pi}\right)^{\frac{1}{2}}\exp\left(-\frac{z}{2(D_{app}t)^{\frac{1}{2}}}\right)^2 - z\,\mathrm{erfc}\left(\frac{z}{2(D_{app}t)^{\frac{1}{2}}}\right) - 2\left(\frac{D_{app}t}{\pi}\right)^{\frac{1}{2}}\exp\left(-\frac{-z+L}{2(D_{app}t)^{\frac{1}{2}}}\right)^2 + (-z+L)\,\mathrm{erfc}\left(\frac{-z+L}{2(D_{app}t)^{\frac{1}{2}}}\right)\right\} \tag{3.15}$$

Equation 3.15 can be simplified so that only two parameters are included, a and b:

$$c_s(z,t) = c_s^* + a\left\{\left(\frac{b}{\pi^{\frac{1}{2}}}\right)\exp\left(-\frac{z}{b}\right)^2 - z\,\mathrm{erfc}\left(\frac{z}{b}\right) - \left(\frac{b}{\pi^{\frac{1}{2}}}\right)\exp\left(-\frac{-z+L}{b}\right)^2 + (-z+L)\,\mathrm{erfc}\left(\frac{-z+L}{b}\right)\right\} \tag{3.16}$$

Where:

$$a = \frac{J(1-t_+^0)}{nFD_{app}}\left(1-\frac{\partial \ln c_0}{\partial \ln c_s}\right)^{-1} \tag{3.17}$$

$$b = 2(D_{app}t)^{\frac{1}{2}} \tag{3.18}$$

For equation 3.16 to remain valid, $2(D_{app}t)^{\frac{1}{2}} < \frac{L}{2}$. In other words, the diffusion layer cannot extend into the centre of the cell for equation 3.15 to remain valid. Due to the large L that was used experimentally, the Equation still held for our experiments.

By including the solvent velocity factor in equations 3.17, as derived from Equation 3.9, the cationic transference number is labelled t_+^0 (in Equation 3.17) because it is referenced against the solvent velocity. This is required for a rigorous understanding of t_+^0, as one should always note what transference is referenced against. Figure 3.11 illustrates how this factor changed with concentration, showing that its inclusion became increasingly important at high concentrations. It was calculated by finding c_0 at each concentration, which is equal to $(1-V_s c_s)/V_0$, where V_s and V_0 are the partial molar volumes of the

salt and solvent respectively.[2] The measurement of V_0 and V_s were described in Section 3.3.1. Figure 3.11a also shows how the c_0 gradient compared to the c_s gradient.

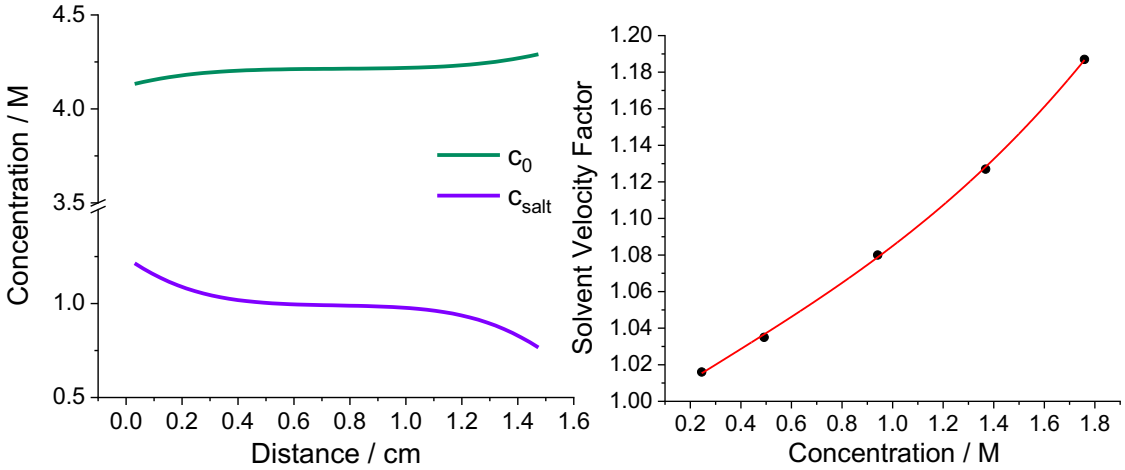


Figure 3.11: Solvent Reference Velocity a) Concentration gradient fittings of the salt and solvent after current was applied for 12h at 100 µA cm^{-1}. b) Solvent velocity factor plotted as a function of electrolyte concentration.

Figure 3.12a shows an example of a fitted concentration profile using 1 m LiFSI in G4 at 100 μA cm^{-2} after 12 hours. With the fitting, two parameters, a and b were identified along with their standard error. a was the interfacial concentration gradient, $dc_s/dz|_{z=0,L}$, and b was the diffusion length, L_d. Figure 3.12b illustrates how the concentration profile progressed over 8 hour gaps between line scans. As predicted $dc_s/dz|_{z=0,L}$ stayed constant, and L_d extended increasingly into the centre of the cell with time.

Diffusion Coefficient. D_{app} is the proportionality constant of L_d progressing with time. Figure 3.13a shows how L_d moved with $t^{1/2}$, with the error parts representing the standard error of the from Equation 3.16 fitting. Note the linearity of the fitting; with the magnitude of the gradient indicating how large D_{app} was. From the weighted gradient fitting, D_{app} was calculated as $7.2 \pm 0.6 \times 10^{-11}$ m^2 s^{-1}. To compare with a more conventional method for measuring D_{app}, a restricted-diffusion measurement was performed using the same cell setup, (as described in section 1.5.2 but with a smaller interelectrode distance (L) to allow for a faster OCV relaxation. Using equation 1.28, with L equal to 6.58 mm, which

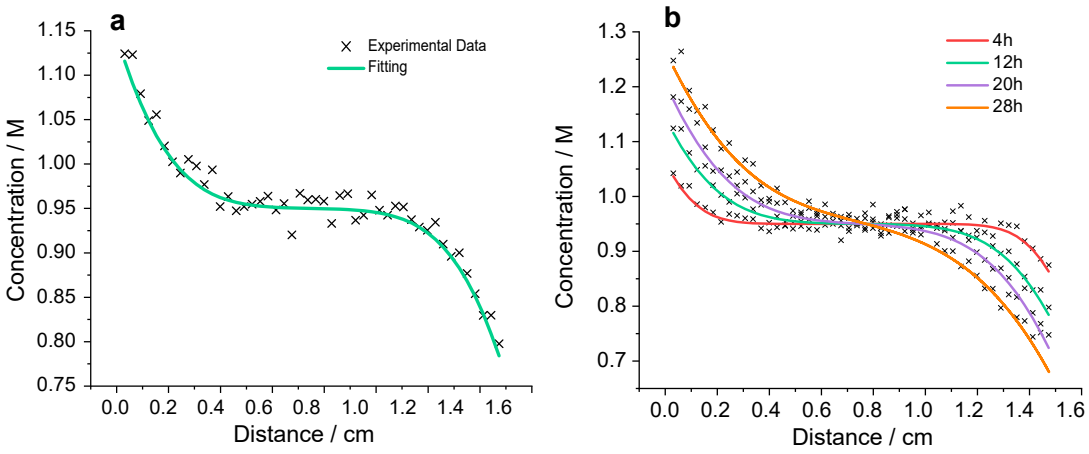


Figure 3.12: Model system 1 m LiFSI in G4, gradients. a) The Li^+ concentration profile in 1m LiFSI in G4 electrolyte after applying 100 µA cm^{-2} of current for 12 h, with fitting (equation 3.15). b) Progression of concentration gradient in 1m electrolyte, after 4 h, 12 h, 20 h, 28 h.

was accurately measured with the optical microscope, D_{app} was calculated to be 6.98×10^{-11} m^2 s^{-1}. The $\ln OCV$ vs $time$ curve is shown in Figure 3.13b, noting its linearity. To my knowledge, there are specifically no restricted-diffusion values of 1 m LiFSI in G4 measured in the current literature, but Grundy et al. measured LiTFSI in G4 and Saito et al. provided pfg-NMR information on LiFSI in G4. [5, 6] Using Saito's pfg-NMR D_i values and calculating the harmonic-mean, as described by Equation 1.29, D_{app} was estimated. Using their values, D_{app} for 1 M LiFSI in G4 was estimated as 8.27×10^{-11} m^2 s^{-1}, which compared well to the concentration profile calculation considering their were run at a 10 ^{o}C higher temperature. Grundy measured a value of $\sim 5 \times 10^{-11} m^2$ s^{-1}, but using a more viscous electrolyte, LiTFSI in G4, this lower value was to be expected.

Transference Number. There were two methods for calculating t_+^0 from the analysis of the concentration profiles. One involved the isolation and calculation from $dc_s/dz|_{z=0,L}$, using D_{app} from the previous examination of L_d, and the solvent velocity factor calculation. Because $dc_s/dz|_{z=0,L}$ remained constant over the measured time frame, t_+^0 was quantified from each measured gradient and averaged along with its standard error. Due to the concentration differences on each side of the cell, the solvent velocity factor was slightly different at

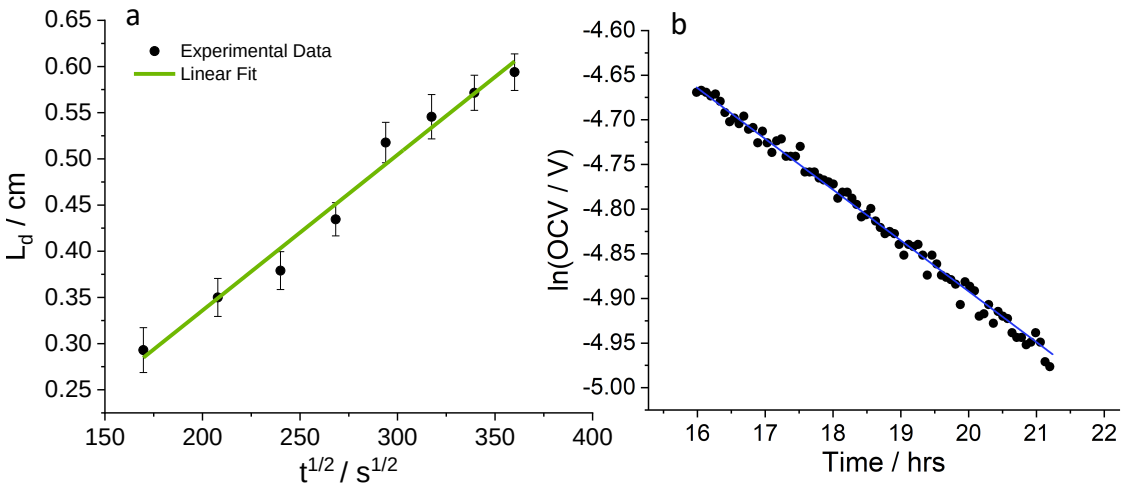


Figure 3.13: Measuring Diffusion Coefficient. a) Movement of Li^+ diffusion length (L_d) with time$^{1/2}$, showing linear behaviour for the D_{app} calculation. D_{app} = 7.2 $\pm$ 0.6 $\times$ 10^{-11} m^2 s^{-1}. b) ln(OCV) vs. time for D_{app} calculation using a restricted-diffusion setup.

each interface, leading to somewhat different t_+^0 values throughout the cell. Nevertheless, due to the error from the fitting, this difference was deemed negligible for the calculation. As shown in Figure 3.11b, the solvent velocity factor was shown to be 1.08 for 1 m, leading to a t_+^0 value of 0.35 $\pm$ 0.06. This value compared well to other Li-ion binary electrolytes, with Li^+ often moving poorly compared to its counterion. Secondly, t_+^0 could be calculated from a Hittorf-style analysis by integrating the concentration profiles and measuring the concentration molar changes at each half of the cell with time, as noted by equation 1.34, and illustrated by Figure 3.14. t_+^0 using this method was calculated as 0.392 $\pm$ 0.006. Again, these values compared well to the pfg-NMR values provided by Seito et al.. For their 1 M LiFSI in G4 electrolyte, they calculated a t_+ value of 0.44.[5] This method is not directly comparable to restricted-diffusion nor concentration profile analysis, but an analysis of all these method proves conclusively that Li^+ is moving less freely than FSI^-.

Thermodynamic Factor. Using the fitted profiles, and the intermittent PEIS data, χ_M was calculated from equation 4.13, similar to equation 1.18 described earlier.

$$\chi_M = 1 + \frac{d \ln f_\pm}{d \ln c} = \frac{F}{2RT(1-t_+^0)} \frac{d\eta_c}{d \ln \frac{c_{s,z=L}}{c_{s,z=0}}} \tag{3.19}$$

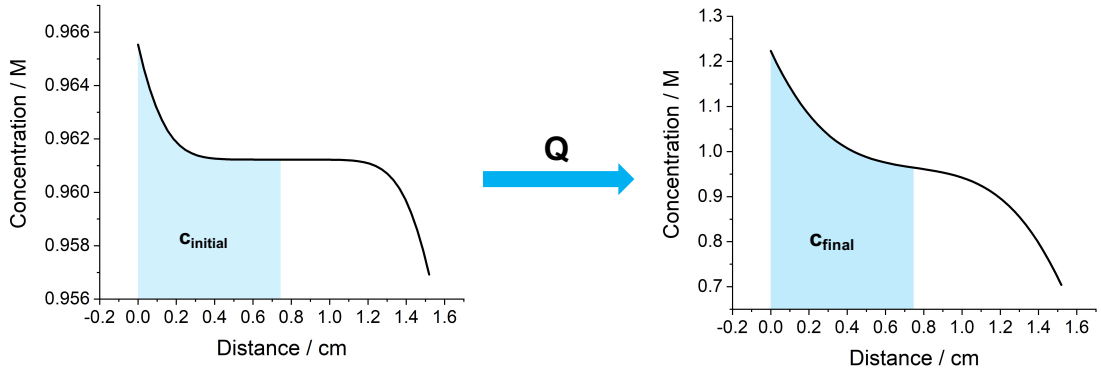


Figure 3.14: Calculating concentration differences for Hittorf-style transference number measurement, when measuring concentration gradients over time.

To repeat, this was the first time χ_M had been measured in such a dynamic setup, inducing a concentration difference from the passing of current, as opposed to manually changing concentrations in a concentration cell. χ_M was extracted from the gradient of $\frac{Fd\eta_c}{2RT(1-t_+^0)}$ vs. $d\ln\frac{c_{s,z=L}}{c_{s,z=0}}$ from Figure 4.15. The error bars represent uncertainty in the interfacial concentrations from the fitted profiles on the x-axis, and error in the t_+^0 calculation in the y-axis. To calculate η_c, PEIS Nyquist plot data had to be fitted to understand the charge-transfer and bulk resistances contribution to the overall overpotential (η_{total}). η_c was subsequently calculated: $\eta_c = \eta_{total} - I(R_{bulk} + R_{ct})$. $\eta total$ was measured from the chronopotentiometry data, i.e. the voltage vs. time curve. Because no dendritic structures were forming on the Li metal surface during plating, and the SEI that was formed was stable, there was little change in R_{ct} with time. This is illustrated in Figure 3.15b. Also, R_{bulk} remained stable throughout the duration of the experiment. The voltage vs. time curve is shown in Figure 3.15a, illustrating a steady increase with time. This is due to the increasing difference in concentration on each side of the cell.

χ_M was calculated as 1.4 ± 0.3, which implied a higher "effective concentration" than the measured concentration. It was due to the depletion in the free solvent to stabilise the Li-ion, increasing its chemical potential. The extent of solvation by G4 was illustrated by the emergence of the peak at 868 cm^{-1} as shown in Figure 3.4.

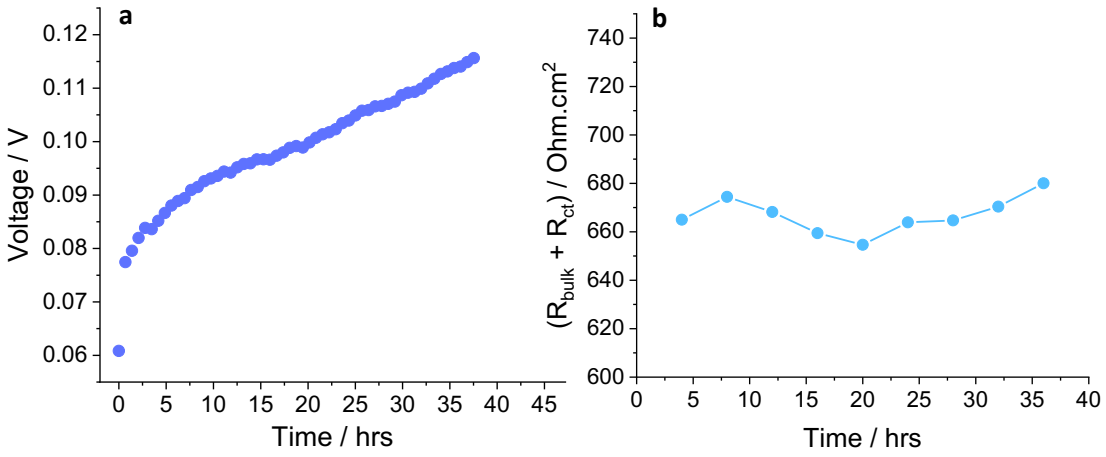


Figure 3.15: a) Voltage of *operando* cell with 1m electrolyte, while passing 100 µA cm^{-2}. The increase in voltage is due to the increasing magnitude of the electrolyte concentration gradient. b) R_{bulk} + R_{ct} over time, showing a stable interface with no side reactions

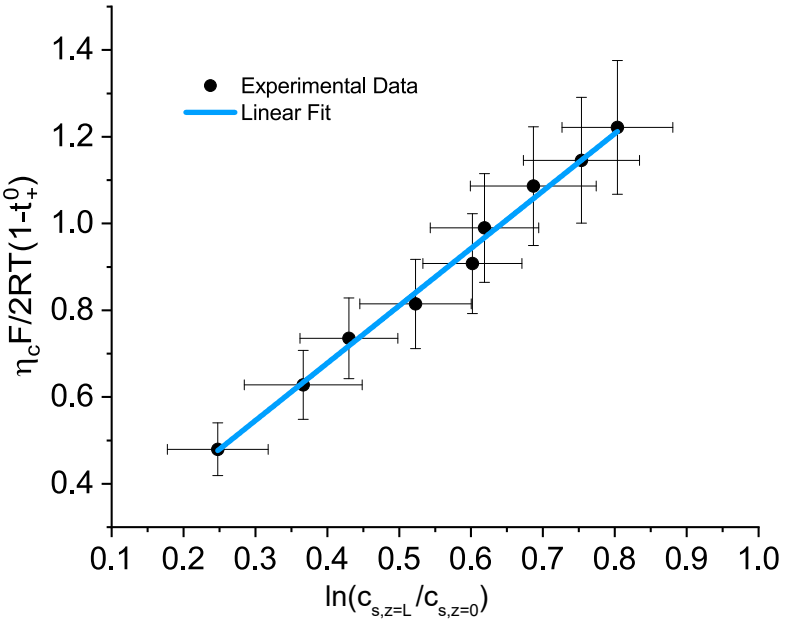


Figure 3.16: Measuring Thermodynamic Factor Plotting equation 4.13, illustrating how the η_c function changes linearly with respect to the natural log of concentration ratio of each cell extreme, to measure χ_M. χ_M = 1.4 $\pm$ 0.3.

PEIS. While the cell rested for 4 hours prior to the application of current, PEIS measurements were taken every 1 hour. This allowed for an accurate understanding of R_{ct} and κ before current potentially affected these values. κ was calculated with equation 3.20:

$$\kappa = \frac{L}{R_{bulk} A} \tag{3.20}$$

Where A is the electrode area. The optical microscope allowed for an accurate measurement of L, which can be a problem sometimes in a closed-cell system (i.e. coin cell). For 1 m, κ = 2.70 $\pm$ 0.03 mS cm^{-1} and R_{ct} = 90 $\pm$ 10 $\Omega{\cdot}cm^2$. R_{ct} was assumed to be a combination of classical-transfer and SEI resistance. Indeed, the deconvolution of these processes is of especial difficulty and could be of extreme value in future work.

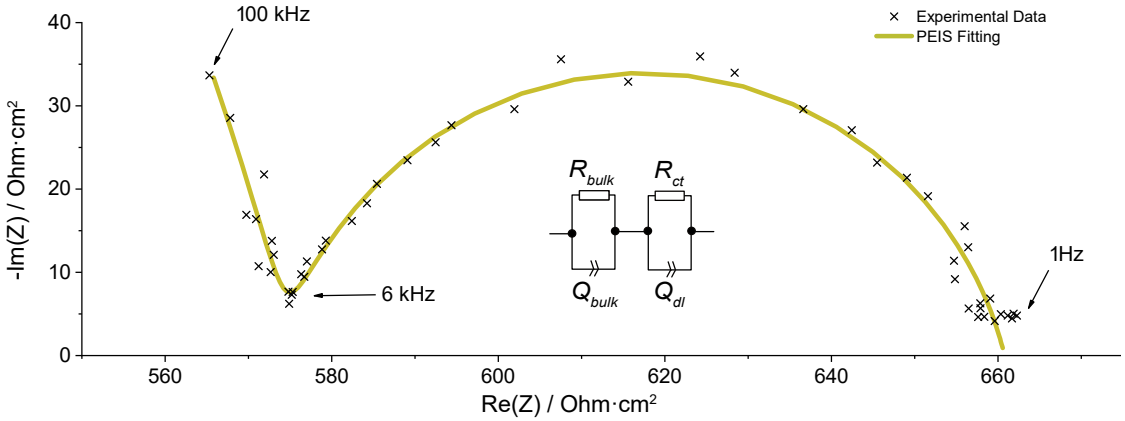


Figure 3.17: Measuring Ionic Conductivity and Resistance of Charge-Transfer PEIS Nyquist plot, with equivalent circuit, of 1 m electrolyte, prior to current being passed, after 4h rest, equating to κ = 2.70 $\pm$ 0.03 mS cm^{-1} and R_{ct} = 90 $\pm$ 10 $\Omega{\cdot}cm^2$.

This section has provided an example for the extraction of key transport and thermodynamic parameters of Li-ion electrolytes using concentration visualisation and PEIS data. For a broad understanding of an electrolyte system however, an analysis of multiple concentrations is required to identify which electrolyte composition may perform best in full electrochemical cells. The next section will cover this aspect of the study.

3.3.5 Effect of Concentration

Along with 1 m, concentrations of 0.25 m, 0.5 m, 1.5 m and 2 m were analysed like that described in the previous section. Repeat runs were taken at each concentration, both with and without PEIS between each line scan to check the PEIS measurement was not affecting the gradient measurement.

Ionic Conductivity & Resistance of Charge-Transfer. Figure 3.18 shows a Nyquist plot, illustrating how LiFSI concentration affected the resistances in the cell.

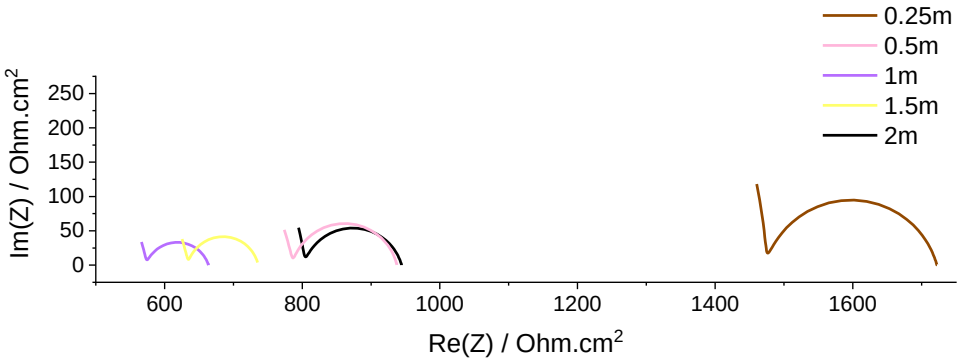


Figure 3.18: Nyquist Plots PEIS fittings of each concentration, after 4h rest, used to measure κ and R_{ct}

Each spectrum was taken after the 4 hour rest period. Using Equation 3.20, κ was calculated and plotted in Figure 3.19a. It was fitted with the function proposed by Casteel and Amis, see equation 3.21 below.

$$\kappa(c) = \kappa_{max}\left(\frac{c}{c_{max}}\right)^{x_1}\exp\left(x_2(c-c_{max})^2 - \frac{x_1}{c_{max}}(c-c_{max})\right) \tag{3.21}$$

Where x_1 and x_2 are constants, c_{max} is the concentration at the maximum ionic conductivity, κ_{max}. κ_{max} was calculated as 2.67 mS cm^{-1} at a c_{max} of 0.99 M. This value is lower than most conventional electrolytes like LP30, due to the increased viscosity of G4. Indeed, κ is a function of the ionic concentration (number of ions in solution), and so its low value could be due to the presence of many ion pairs. Intriguingly, most non-aqueous binary electrolytes have a c_{max} value of $\sim$1 M. Indeed, this could be reason for the wide use of $\sim$1 M electrolytes for commercial applications. Different κ values lead to differing ohmic overpotentials, which can affect the overall energy of the battery. Its influence of cell performance is analysed in a section 3.3.8, describing full-cell simulations.

As illustrated in Figure 3.19b, there was an evident decrease in R_{ct} going from 0.25 m to 1 m, but a flattening as one moved to a high concentrations. One could maybe argue there was a slight increase in R_{ct} moving to very high

concentrations, but this was not statistically significant as highlighted by the 95% confidence band. R_{ct} is influenced by electrolyte composition and solvation, SEI composition and substrate chemistry. The complexity of multiple contributions and its difficulty to deconvolute, makes it tough to explain R_{ct} trends. Chapter 5 below expands this idea by providing SEI compositional analysis through XPS, to understand these trends further and provide a theory to understand trends in non-uniform lithium plating. Broadly, however, the initial decrease in R_{ct} is due to the dependence of concentration on interfacial kinetics (through exchange current density in the Butler-Volmer equation) and the slight increase is due to a change in the SEI composition because of different solvation structures forming at high concentrations.

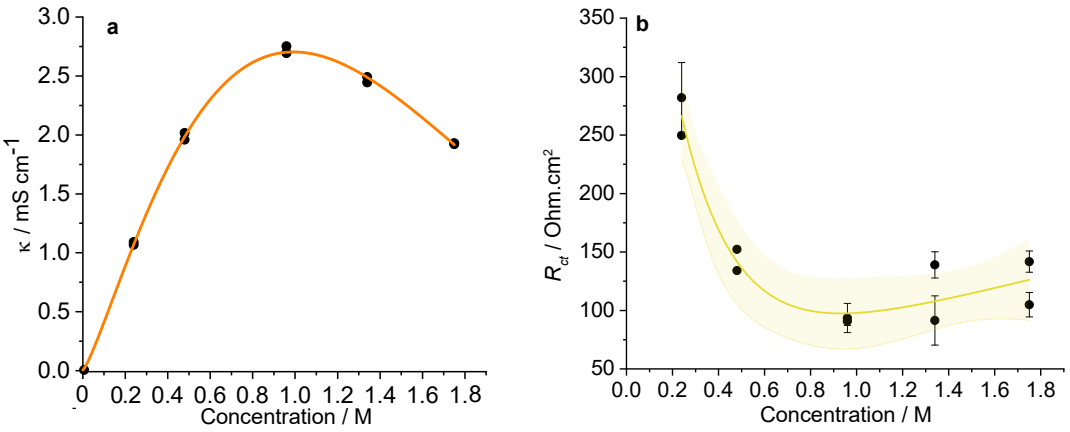


Figure 3.19: LiFSI in G4 concentration-dependent κ and R_{ct} values a) κ, fitted with the Casteel-Amis equation, κ_{max} was calculated as 2.67 mS cm^{-1} and c_{max} as 0.99 M. b) R_{ct}, showing an initial drop with concentration, then a stabilising at 100-125 Ω·cm^2.

Diffusion Coefficient. Figure 3.20a shows how D_{app} magnitude was affected by changes in LiFSI concentration. Generally a decrease in D_{app} with concentration was observed, which is common for electrolyte solutions. D_{app} is directly affected by the viscosity of solutions as noted by Stokes-Einstein relation.[2] These D_{app} values were compared to literature values. The absolute values compared well to Grundy's findings, although due to the use of LiTFSI salt, their D_{app} values were expected to be slightly lower.[6] Compared to other Li-ion electrolytes, D_{app} was quite low, with 1 M PC and EMC-based electrolyte

exhibiting values of 2-6 times higher. An increasing viscosity, and so therefore a decreasing D_{app} value is due to increased association of the salt and solvation of Li^+ with G4; an increasing frictional interaction between ions and solvent, as described by Stefan and Maxwell (see Section 3.3.6 below). Increased solvation and association can be seen from the calibration curve Raman peaks described in previous section.

Transference Number. Figure 3.20b shows how t_+^0 was affected by concentration. As explicitly stated by Bazak et al. to measure t_+^0 with accuracy a very precise measurement of local interfacial concentration gradients is required, due to the high sensitivity of t_+^0 with small changes in $dc_s/dz|_{z=0,L}$.[7] Also, as seen in Figure 3.5b, the absolute error in measuring the area of the peak at 717 cm^{-1} increases with concentration. This translates into larger error in measuring $dc_s/dz|_{z=0,L}$ at high concentrations. This, along with error propagation from calculating D_{app}, could lead to poor reliability and large error, explaining the range of error in Figure 3.20b, especially at high concentrations. The low concentrations have t_+^0 error as low as ± 0.01, whereas at high concentrations it was as high as ± 0.12. However, even with the error there was a clear trend in t_+^0 with increasing concentration. There was a general increase in t_+^0 with concentration, with a plateauing at moderate concentrations. One should note that if the solvent velocity factor was not included (i.e. calculating t_+), an even more pronounced trend of increasing t_+^0 would be observed. This underlines the importance of including this factor in transference number calculations. Within this concentration range Grundy noticed a similar t_+^0 trend. However, they used an adapted Bruce-Vincent method measurement to calculate t_+^0, as described by Balsara.[8, 9] A physical explanation for trend's shape remains contentious. A potential explanation could be that at low concentrations Li^+ is solvated more strongly than FSI^- so therefore FSI^- moves more freely. With increasing concentration FSI^- becomes partially solvated or involved in extended aggregates, lowering its ability to move, increasing t_+^0.

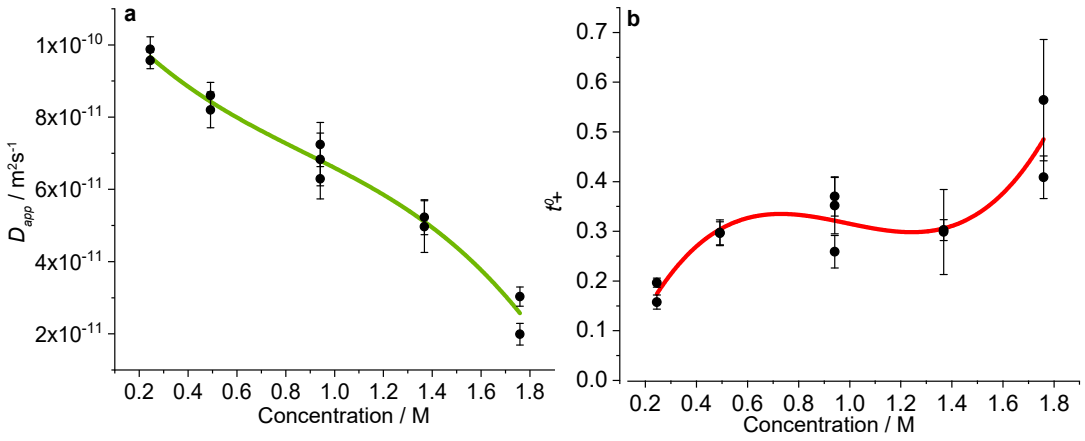


Figure 3.20: LiFSI in G4 concentration-dependent D_{app} and t_+^0 a) D_{app}, observable was a decrease in D_{app} with concentration. b) t_+^0, showing an increase at low concentrations, then generally plateauing, and increasing again at 2 m.

Interfacial Concentration Gradient. Not mentioned in the literature due to its difficulty to measure, $dc_s/dz|_{z=0,L}$ is arguably the most important factor to emerge from the measurement. There was a recent study suggesting that this factor likely influenced the plating morphology of Li, but they only simulated the $dc_s/dz|_{z=0,L}$ from individual characterisation experiments they performed to isolate t_+^0 and D_{app} (i.e. Hittorf and restricted-diffusion).[10] Furthermore it is directly related to η_c, affecting the performance of LIBs too. As shown in equation 3.17, it is a function of D_{app}, t_+^0 and J. Figure 3.21 shows how $dc_s/dz|_{z=0,L}$ changed with concentration. It shows that it stayed constant at low concentrations but increased dramatically at high concentrations. With a constant current applied to all concentrations this change was due only to changes in D_{app} and t_+^0. With a 5-fold drop in D_{app} over the concentration range, the large increase in $dc_s/dz|_{z=0,L}$ at high concentrations was due to a drop in D_{app}. An increase in t_+^0, as shown in the LiFSI in G4 system, has the opposite effect on $dc_s/dz|_{z=0,L}$. This suggests that to improve cell performance and lower $dc_s/dz|_{z=0,L}$ researchers should focus on increasing D_{app} of the electrolyte as opposed to t_0^+.

Thermodynamic Factor. Using Equation 4.13, χ_M for each concentration was isolated. Figure 3.22a shows $\frac{Fd\eta_c}{2RT(1-t_+^0}$ vs. $d\ln\frac{c_{s,z=L}}{c_{s,z=0}}$, with the gradient equal to χ_M. Note the change slope with increasing concentration. Shown in Figure

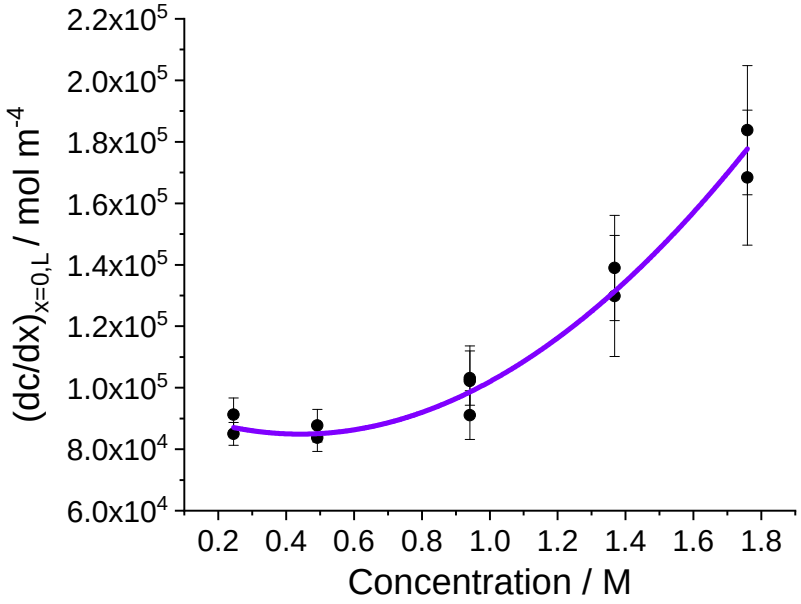


Figure 3.21: LiFSI in G4 concentration-dependent $dc_s/dz|_{z=0,L}$, which was quite constant at low concentrations but increased rapidly after 1 m. This was concluded to be a result of a dramatic decrease in D_{app} with concentration.

3.22b is how χ_M changed with the square-root of concentration. It shows the electrolyte behaved according to extended Debye-Hückel theory described in the Introduction Section 3.22. It was fitted with an extended Debye-Hückel Guggenheim equation,[11] i.e. a $x^{1/2}$ power series. The following equation led to the best-fit of the data:

$$\chi_M = 1 + 2.88x^{7/2} - 2.32x + 0.37x^{1/2} \tag{3.22}$$

The shape was akin to those of other organic-based electrolytes at low concentrations; at low concentrations $\chi_M < 1$, meaning long-range (SSIPs) or short-range (CIPs) association dominates the electrolyte thermodynamics, but at high concentrations $\chi_M > 1$, indicating the depletion of solvation by G4 dominates this value. In other words, with increasing concentration, the solvent becomes increasingly bound, which decreases the vapour pressure, leading to an increase in salt activity and therefore χ_M.

The extent of whether association dominates χ_M values is highly influenced by the physicochemical properties of the solvent, like the relative dielectric

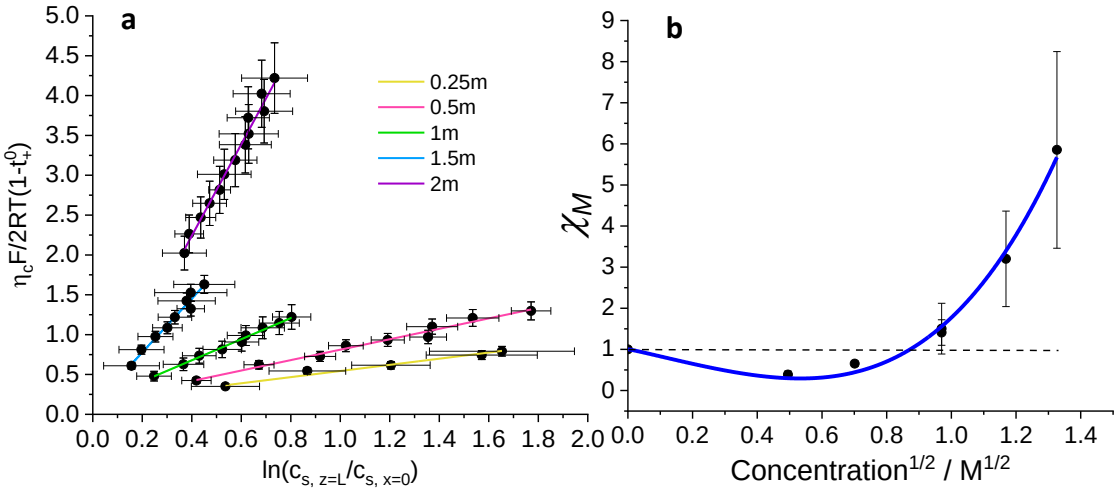


Figure 3.22: LiFSI in G4 concentration-dependent χ_M a) Plotting equation 4 (main text) of each electrolyte concentration, illustrating each gradient and ultimately how χ_M is varying with concentration. b) χ_M change with concentration, below 1 at low concentrations as ion-pair association dominates, then at $\sim$1 M, there is a large increase in χ_M as more solvation occurs, lowering G4's ability to stabilise Li^+.

constant (ε_r). For instance, a high ε_r will allow for more salt dissociation, as the solvent stabilises isolated ions and therefore the effect of association does not appear. Wang et al. showed this by comparing a PC-based and EMC-based electrolyte.[12] G4 has a ε_r that lies between PC and EMC (7.91 vs. 64.92 and 2.96 respectively), and its χ_M dependence on concentration agreed with this. The concentration at which the curve crosses $\chi_M = 1$ is indicative of when ion-solvent effects out-compete ion-ion effects. For EMC and PC it was 1.01 M and 0.12 M respectively, and for this system it was $\sim$0.72 M.

Using the Raman calibration spectra, the extent of the associated species can be illustrated from the shifting of 717 cm^{-1} peak. Shoulder peaks start to emerge, demonstrating increased Li^+-FSI^- interaction. Bockris suggests triple-ion formation occurs when $\varepsilon_r < 15$, indicating triplets and perhaps larger clusters are likely to be forming in G4.[13] Figure 3.23c shows the 717 cm^{-1} peak position change with concentration, indicating at $\sim$0.5 m, free FSI^- becomes a minor species and an associated/aggregated species becomes increasingly prevalent. This evidence suggested a decrease in χ_M with concentration.

Table 3.1: Ratio of free:bound solvent, with solvation number

Concentration$_{molality}$	**Concentration**$_{molarity}$	**[G4]**$_{bound}$	**[G4]**$_{free}$	**Solvation Number**
4.44	3.17	3.171	0.000	1.000
4	3	3.227	0.143	1.076
3	2.44	2.668	0.998	1.093
2	1.75	2.196	1.765	1.255
1	0.95	1.257	3.011	1.323
0.5	0.49	0.659	3.771	1.318

However, the decreasing number of free solvent molecules available to bind and stabilise Li^+, shown in Figure 3.23a, leads to an increase in ion-solvent interaction and therefore an increase in χ_M. The emergence and increasing intensity of the 868 cm^{-1} peak correlates with increasing χ_M. For an understanding of the free:bound solvent ratio, at each concentration, a fitting of the solvent peak 780-900 cm^{-1} was performed, shown in Figure 3.23b, illustrating 4 distinct environments. Like Terada et al. we notice at $c_{Li}/c_{G4} = 1$, which is 3.17 M or 4.44 m, the peak area at 868 cm^{-1} is constant.[3] This suggested all solvent molecules were bound from this concentration onwards, meaning there are no free solvent molecules. Like Kottam et al. and Tatara et al., one can normalise this peak, extract the bound solvent and free solvent concentrations, and calculate the solvation number.[14] Table 3.1 shows how the solvation number changed with concentration. Clearly, as concentration increased the solvation number decreased due to the availability of solvent molecules with increasing concentration. The increasing amount of bound solvent would lead to an increase in χ_M.

In summary, the introduction of solvent structures like $[Li(G4)]^+$ and the formation of SSIPs, CIPs and AGGs have competing effects on the observed χ_M value. The fairly low G4 ε_r leads to SSIPs and CIPs at low concentrations resulting in a decrease in χ_M; with increasing concentration more $[Li(G4)]^+$-like solvent structures form, resulting in an increase in χ_M.

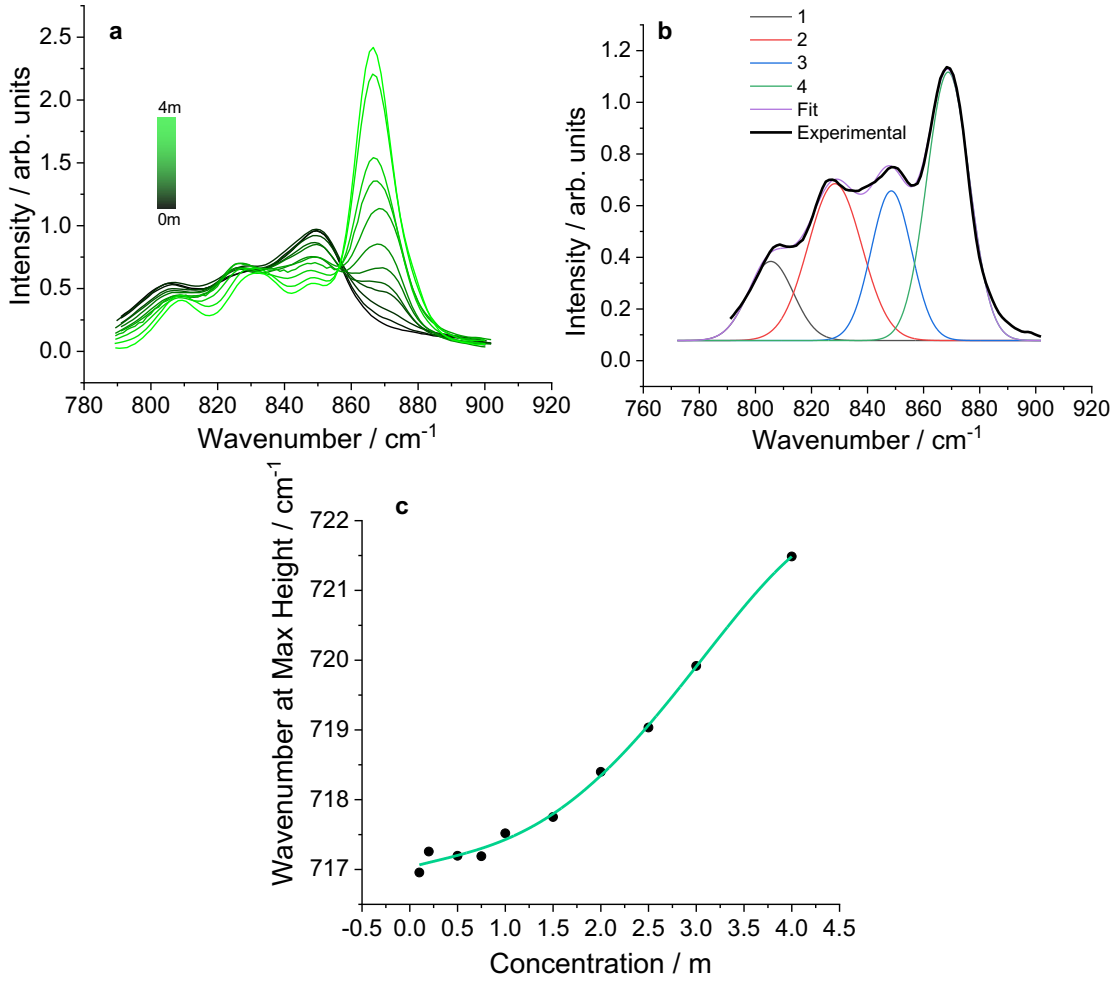


Figure 3.23: a) Evolution of 868 cm^{-1} peak with concentration b) Fitting of 2m 780-900 cm^{-1} peak, showing 4 distinct environments c) Wavenumber at max height of 717 cm^{-1}, showing a dramatic shift from $\sim$1 m

3.3.6 Stefan-Maxwell Measurements

For a more in-depth understanding of diffusional behaviour of each individual species and their interactions with the other species in solution, the Stefan-Maxwell coefficients were calculated.[2] As mentioned previously, Stefan-Maxwell diffusion theory provides information on ion-solvent and ion-ion frictional interactions, which is an important consideration when describing diffusion in multi-component systems. Using Equations 1.19$-$1.23, Stefan-Maxwell coefficients were calculated.

$\mathfrak{D}$ followed an exponential decay with concentration, see Figure 3.24a. $\mathfrak{D}_{0+}$ and $\mathfrak{D}_{0-}$ were very large at low concentrations, with $\mathfrak{D}_{0-}$ generally higher than

$\mathfrak{D}_{0+}$. This is a result of increased movement of FSI^- due to weaker interaction with the solvent compared to Li^+, which is known to bind to G4 strongly, as evidenced by $t_+^0 < 0.5$. The general decreasing trend of both $\mathfrak{D}_{0+}$ and $\mathfrak{D}_{0-}$ is due to the increasing drag on the solvated complexes. $\mathfrak{D}_{+-}$ was the lowest of each of the Stefan-Maxwell coefficients at low concentrations because of the poor movement of paired species. Interestingly at 2 m, each of the coefficients were of similar magnitude, within error. As free solvent is depleted, aggregates and/or even domains of ions begin to form, and it is speculated that the mechanism of transport begins to transition from vehicular movement to ion-hopping. Imide-based salts in G4 are sometimes described as "solvate" ionic liquids at high concentrations.[3, 15] The strong $[Li(G4)]^+$ complexes forming and their weak interaction with FSI^- the solution could be described as a "quasi" ionic liquid. As solvent molecules begin to deplete in solution, this description becomes apt.

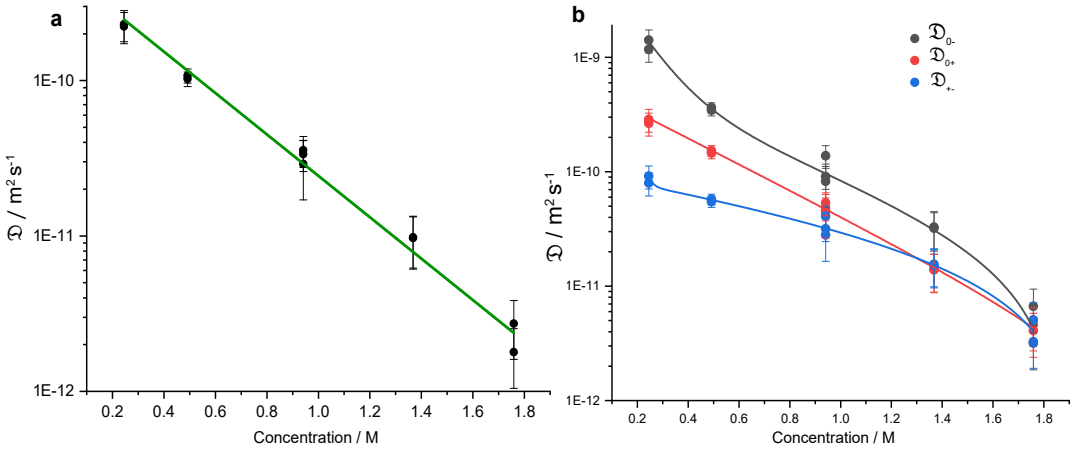


Figure 3.24: Stefan-Maxwell analysis. a) Exponential decay of LiFSI thermodynamic diffusion coefficient ($\mathfrak{D}$) with concentration. b) Stefan-Maxwell coefficients $\mathfrak{D}_{0+}$, $\mathfrak{D}_{0-}$ and $\mathfrak{D}_{+-}$, all decreasing with concentration. $\mathfrak{D}_{0-}$ was generally the highest value across concentrations, indicating FSI^- had the least frictional interaction with G4, while FSI^-'s frictional interaction Li^+ was high. At 2 m, each Stefan-Maxwell coefficient was very similar, within error, which could illustrate a change in transport mechanism, from vehicular to ion-hopping. The error bars in a) and b) represent the standard error and propagation from previous calculations

3.3.7 Transport using PEIS

It is important to understand various methods for determining t_+, especially those that are common in the literature. Very few are critical of the calculated value when using a steady-state method of measuring t_+. In this section I will present the EIS method for determining t_+, providing an evaluative analysis on this method. To reiterate, I will exclusively use the EIS method, not the BV method, due to it being easier to determine its validity. This is primarily by using EIS's unique ability to separate different impedances within the cell, and specifically W_d having its distinct shape.

Before the ideality assumption is addressed (see section 1.5.3), a valid EIS measurement of a symmetric Li|Li cell was required. A commonly used cell format for this analysis is a coin-cell, using a glass fibre separator (Whatman – GF/F). Figure 3.25a shows a EIS spectrum of a coin-cell that, scanning from 100 kHz to 200 μHz appeared to have four distinct regions: namely, the x-intercept representing ohmic resistance, the interfacial impedance for charge-transfer and double layer capacitance and two other processes at lower frequencies. The second semi-circle has been seen before in the literature and is sometimes attributed to the SEI layer resistance; but with a capacitance of 10^{-3} F, either the surface area would be very large, or the thickness would be on a picometre-scale. From this analysis, it is fairly easy to discount this as SEI impedance. Also, as is shown in Figure 3.17, this semi-circle is not present in that Nyquist plot when using the optical cell for the operando Raman experiments. During the investigation it was noted that if the separator's diameter was reduced, the semi-circle also reduced in size. Furthermore, if the separator was exactly the same size as the lithium electrodes and stacked directly on top of each other, the semi-circle almost disappeared completely. It appeared therefore, there was an additional diffusive process emerging from lateral transport. A coin-cell is often flooded with electrolyte, so it is difficult to completely remove the additional diffusion from the sides.

To rectify this, a cell was designed that included two stainless steel pistons and a PEEK piece in between to separate the pistons. Each stainless steel piston was fitted with an FFKM O-ring to make sure the cell was air-tight. To allow for the pressure to be released easily during cell fabrication, a hole was placed at the side of the PEEK separator, with an additional piece to plug it once the cell made. The cell had a 20 mm diameter, and was geometrically stacked so each component was aligned, leading to linear diffusion lines. See Figures 3.26a and b for the cell drawing and photo respectively. Figure 3.25b shows the Nyquist plot of this cell, showing a clear reduction in the medium frequency semi-circle, although during the fitting procedure it was included because its presence could not completely be discounted. The slight depression in W_d was likely due to the inhomogeneities present on the electrode surface as described in section 2.2.1. A low V_a was run to maintain linearity, and a PEIS measurement to medium frequencies was run directly after the VLF-PEIS measurement to check if any drift was occurring. See Experimental Detail for further information. By using equation 1.38, t_+ was calculated as 0.25, similar to the value measured via operando Raman above. R_{bulk} = 16.8 $\Omega{\cdot}cm^2$ and W_d = 51.1 $\Omega{\cdot}cm^2$.

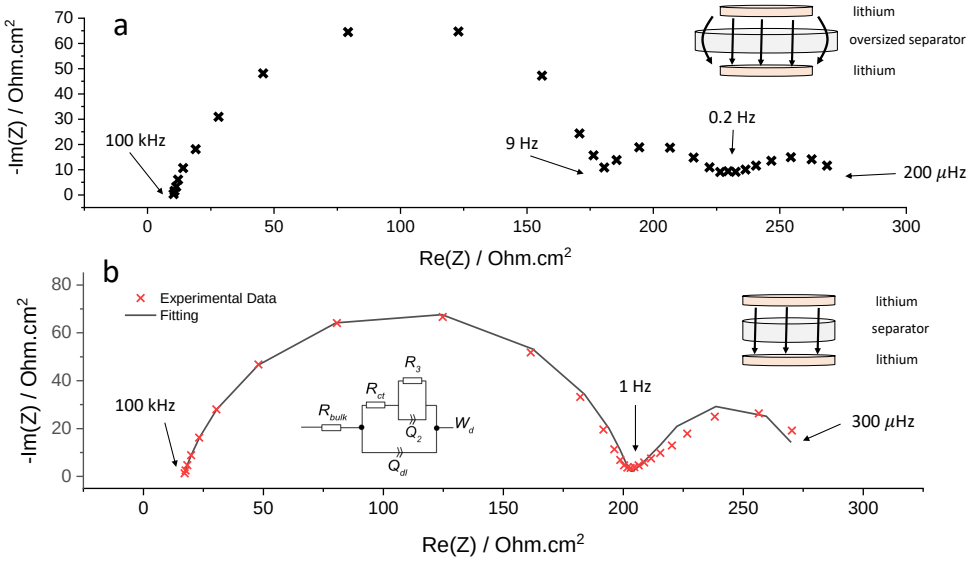


Figure 3.25: a) Nyquist plot of Li|Li coin cell, with 1 m LiFSI in G4 electrolyte and oversized separator, illustrating a separate semi-circle between 9 Hz and 0.2 Hz, a result of lateral diffusion. b) Nyquist plot of Li|Li custom-designed cell, with 1 m LiFSI in G4 and aligned stack so no lateral diffusion was present. t_+ was calculated as 0.25.

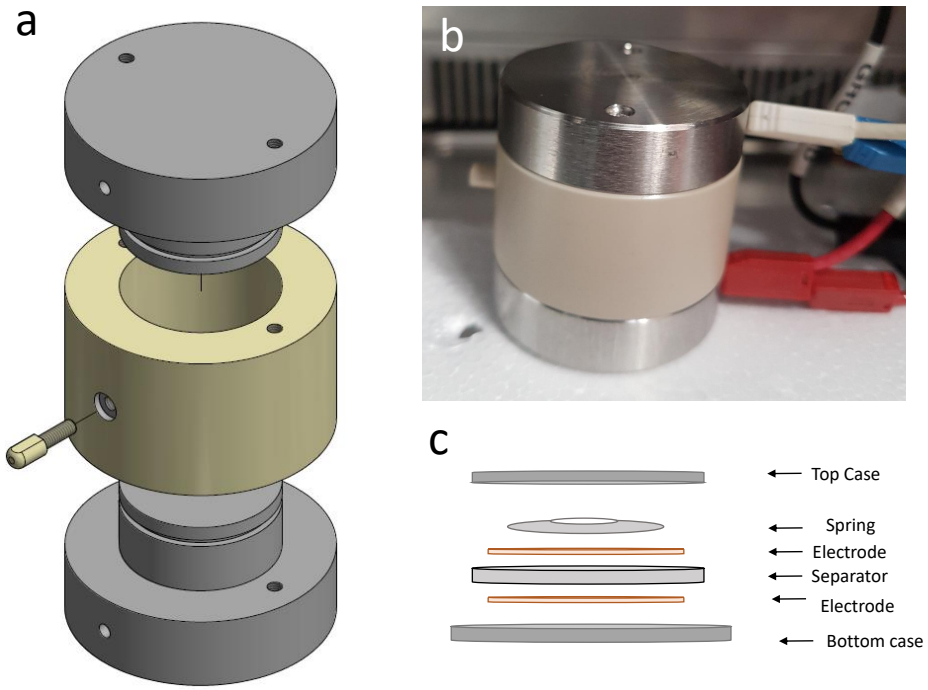


Figure 3.26: Cells for PEIS. a) Cell design for PEIS of symmetric Li|Li cell to allow of aligned cell setup for linear diffusion. b) Photo of assembled cell described in a). c) Exploded view of a coin cell with each labelled part.

When using steady-state methods for understanding t_+ almost no researchers acknowledge a critical assumption made by Sørenson and Jacobsen: the electrolyte is infinitely dilute i.e. $\chi_M = 1$. Depending on the electrolyte used, this is especially problematic at low concentrations when χ_M is often <1, and high concentrations when χ_M increases steeply. Although experimentally I have not seen others implement χ_M, one can adjust equation 1.38 to include χ_M, leading to the adjusted equation [16]:

$$t_+ = \frac{R_{bulk}}{R_{bulk} + W_d \chi_M} \tag{3.23}$$

Including χ_M from the operando Raman measurement, t_+ was calculated as 0.19. The discrepancy from the value measured via operando Raman is likely due difficulty in isolating W_d and separating it from the other interfacial processes occurring in the cell. A solution to this could be the design of a 4-electrode cell, which would discount the interfacial kinetic element of the Nyquist plot. However, this is beyond the scope of this study but would prove useful for further work.

3.3.8 COMSOL Modelling

By measuring parameters κ, D_{app}, t_+^0 and χ_M one can implement the values into a Doyle-Fuller-Newman (DFN) model and simulate symmetric and full cell performance. The DFN model was mentioned in the Introduction, and details of the equations used are presented in Appendix B. These simulations were performed using the Batteries and Fuel Cells Module in COMSOL Multiphysics 5.5. In the module, various parameters are inputted for modelling porous electrodes and CST electrolytes. The parameters used are shown in Table 3.2.

Firstly, a 1 m LiFSI in G4 concentration gradient in symmetric cell was modelled at 15 µm, 50 µm and 100 µm, at 5 mA cm^{-2}, with the results illustrated in Figures 3.27a-c. To repeat, the measured parameters in the operando Raman study were independent of current density and interelectrode distance, but it illustrates the extent and speed of concentration gradient formation at more realistic LMB geometries. For example, at a 100 µm distance, the gradient reached steady-state in 60 seconds, but at 15 µm, it takes only 3 seconds. Also, the final concentration at each cell extreme were very different depending on cell distance. For 15 µm there was only a difference of 0.04 M between the cell extreme and middle, and for 100 µm it was 0.25 M difference. Experimentally, a characterisation technique with increased temporal and spatial resolution would allow for analysis at these interelectrode distances and current densities.

Then, LIB full cells were simulated using the experimentally isolated electrolyte properties. A full LIB cell geometry was used using porous graphite and porous lithium manganese oxide (LMO) as the negative and positive electrode respectively. Full cell parameters are described in the Table 3.2 below. Figure 3.27e shows a galvanostatic discharge curve at a 1C C-rate, illustrating how electrolyte concentration, transport and thermodynamic properties can influence the shape of the curve, and ultimately overall cell performance. Interestingly, it was 1 m and 0.5 m that performed best, showing the least overpotential. Figure 3.27d shows how the concentration gradient of the electrolyte progresses over 1 h. Figure 3.27f highlights even further how electrolyte composition can influence cell performance,

Table 3.2: COMSOL Simulation Parameters

Parameter	Value
Temperature	298.15 K
Electrolyte thickness	50 μm
Graphite thickness	100 μm
LMO thickness	185 μm
Positive electrode LMO volume fraction	0.273
Positive electrode electrolyte volume fraction	0.654
Negative electrode graphite volume fraction	0.471
Negative electrode electrolyte volume fraction	0.503
Anodic/cathodic rate coefficients for each electrode	0.5
Reference exchange current density	100 A/m^2
Electric conductivity graphite	100 S/m
Electric conductivity LMO	3.8 S/m
Initial lithium concentration in graphite	17644 mol/m^3
Initial lithium concentration in LMO	3886 mol/m^3
Radius of graphite particles	12.5E-6 m
Radius of LMO particles	8E-6 m
Diffusion of lithium in graphite	3.10E-14 m^2/s
Diffusion of lithium in LMO	1.05E-14 m^2/s

when increasing the C-rate to 4C. The biggest influencer on final state-of-charge (SOC) is the bulk concentration, with 0.25 m and 0.5 m performing particularly poorly. Figures 3.28a and b show the difference in electrolyte concentration distribution for the 0.5 m electrolyte discharged at 1 C and 4 C respectively. Due to the low initial concentration throughout the cell and a high C-rate causing large concentration gradients, the concentration in the cathode drops to zero in much of the electrode. This leads to a low final average SOC at a 3 V cut-off. Again it is the 1 m composition that achieved the best results, showing the least overpotential and highest final capacity at a 3 V cut-off. Performance here was dictated by the transport through the porous electrode, underlining further the importance of understanding electrolyte properties to improve LIB performance. Indeed, it also highlights the importance of understanding electrolyte performance through porous media, which is not always considered.

Finally, full LMB cells were simulated using an LMO cathode and 1 m electrolyte separator, using same dimensions as the LIB simulation. The lithium electrode was modelled simply as an electrode surface whose kinetics were dic-

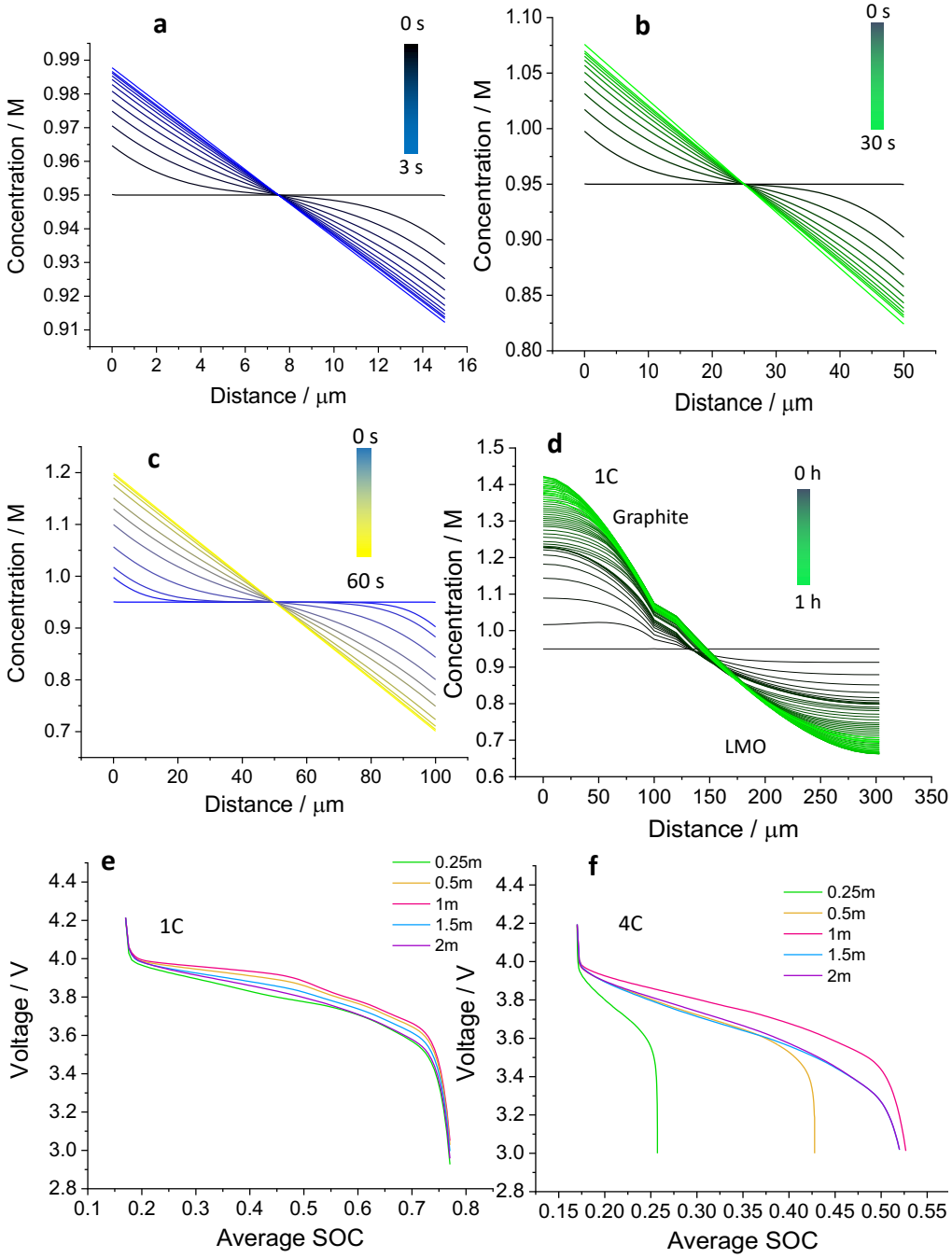


Figure 3.27: COMSOL Simulations. a-c) Simulation of the 1 m LiFSI in G4 electrolyte concentration gradient forming in a lithium symmetric cell at a) 15 µm b) 50 µm c) 100 µm, at 5 mA cm^{-2}. d-f) Simulation of a full LIB cell, with porous graphite and porous LMO as the negative and positive electrodes respectively. d) Discharge curve simulation at 1C, illustrating that the 1m concentration performed with the least overpotential. e) Discharge curve simulation at 4C, showing cell performance with a high dependence on concentration with 0.25 m and 0.5 m performing poorly. 1 m performed at the least overpotential and highest final SOC at 3 V cut-off. f) Electrolyte concentration profile at 1C of 1m initial concentration.

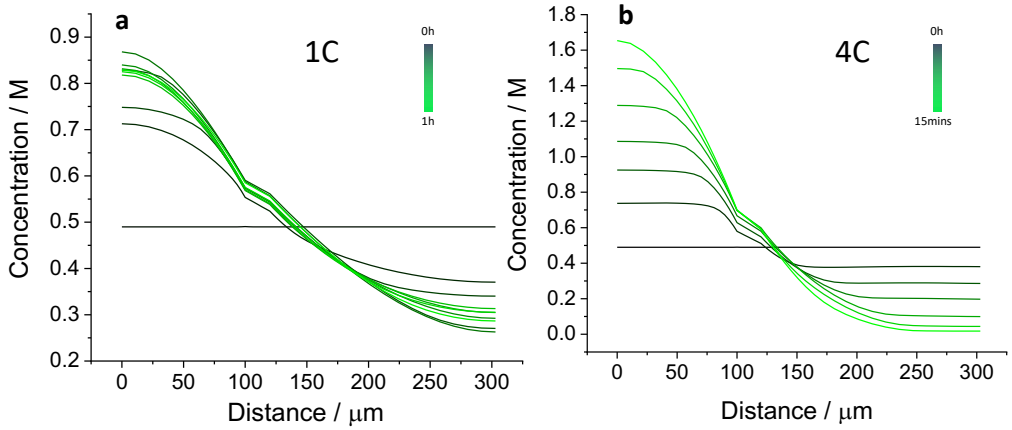


Figure 3.28: a) Electrolyte concentration profile at 1 C with 0.5 m initial concentration. b) Electrolyte concentration profile at 4 C with 0.5 m initial concentration.

tated by the Butler-Volmer equation. For LMBs, one is especially interested in the concentration profile during charge due to the plating morphology's dependence on concentration. Indeed, as mentioned in the Introduction, if the concentration drops to zero fractal dendrites could grow and penetrate the separator. Figures 3.29a-c shows the charge-discharge voltage curve and concentration profiles at 1 C and d-f show the same but at 4 C. Due to the thickness of the cathode and the relatively poor transport properties of 1 m LiFSI in G4, the concentration drops significantly at the lithium metal surface at high currents, to 0.05 M. Although these simulations do not include the affect of the SEI and the resulting plating morphology, the concentration drop is likely to have a large affect on the structural shape of the deposits.

3.4 Conclusions & Future Work

This chapter has presented a novel method for the full characterisation of Li-ion electrolytes, utilising operando Raman microspectroscopy in tandem with PEIS. Each of the key concentration-dependent transport and thermodynamic electrolyte properties, diffusion coefficient, lithium transference number, thermodynamic factor, ionic conductivity and resistance of charge transfer have been presented. Furthermore, the Stefan-Maxwell coefficients were calculated showing

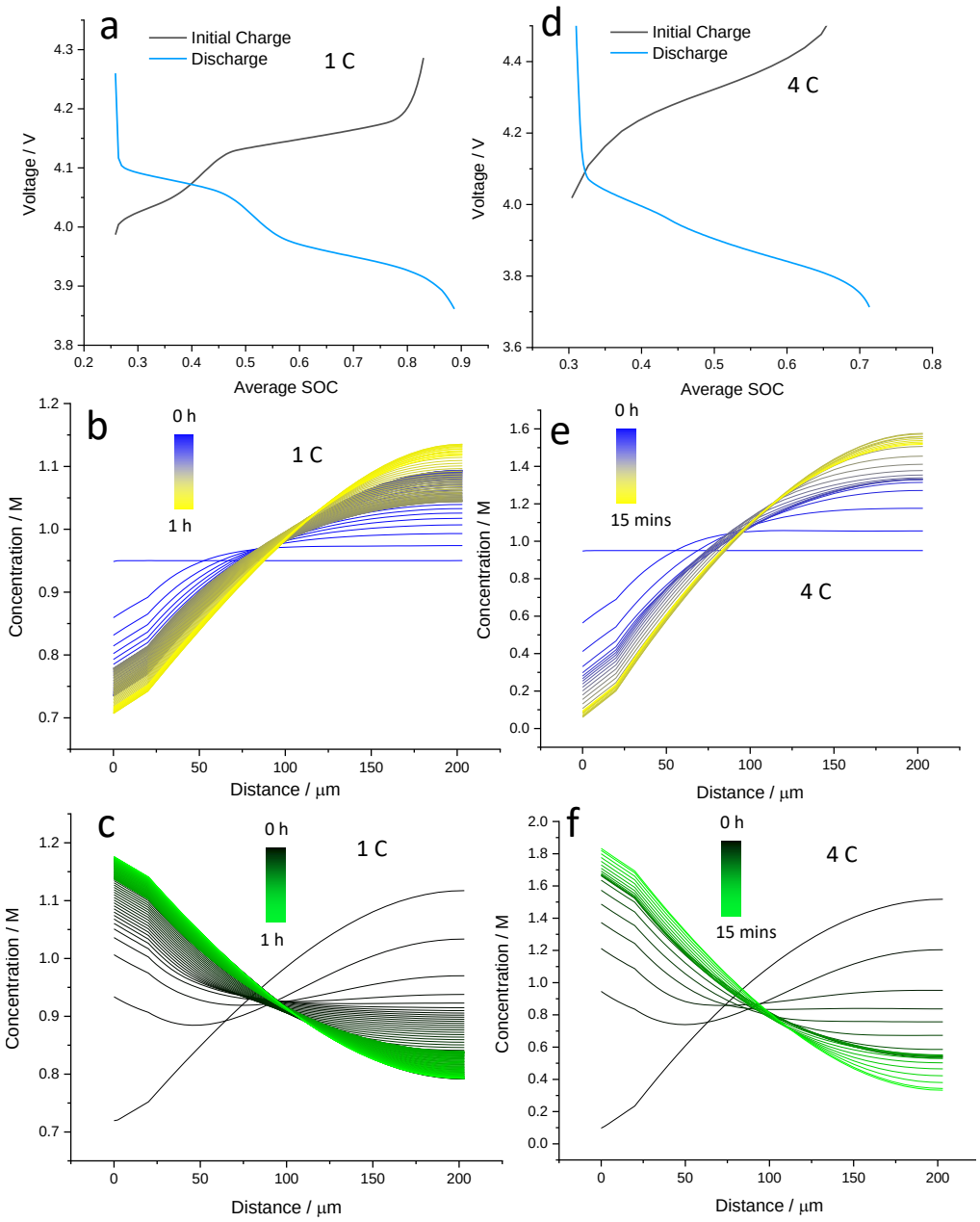


Figure 3.29: Simulation of 1 m LiFSI in G4 in full LMB, with Li metal anode and porous LMO electrode: a-c) Charge and discharge at 1C a) Voltage curve b) Initial charge concentration profile, showing a drop in concentration at the Li metal electrode c) Subsequent discharge concentration profile. d-f) Charge and discharge at 4C d) Voltage curve. e) Initial charge concentration profile, showing a drop in concentration nearly to 0 M f) Subsequent discharge concentration profile.

the method's compatibility with CST. A range of concentrations were tested to understand how the bulk concentration affected each of these properties. The Raman spectra used for calibration provided useful insight into how microscopic

electrolyte structural features were influencing the macroscopic electrolyte parameters. A full description meant one can pinpoint the potential shortcomings of the electrolyte system. Here, for LiFSI in G4 it was noted that $dc_s/dz|_{z=0,L}$ increased with concentration dramatically after 1 m due to a decrease in D_{app}. Therefore, it is recommended, to improve η_c, one should prioritise an increase in D_{app} over t_+^0. By isolating each parameter, it provided the basis for theoretical modelling of electrolyte systems in symmetric and full cells, using COMSOL Multiphysics. Also, a cell was designed to perform steady-state EIS measurements to measure t_{Li+}, comparing value against those gather via operando Raman.

There are many fruitful avenues one can take for further work using the described methodology. As mentioned previously, to successfully measure concentration gradients with Raman microspectroscopy, an isolatable and concentration-sensitive Raman band is required. Furthermore, if the required Raman band(s) are present, the presented method could be extended to electrolyte systems with multiple ions. Evidence from the few other studies that have used Raman spectroscopy to monitor electrolyte concentration differences shows that many commonly used salts (e.g. $LiClO_4$ [17], LiBOB[18], LiTFSI [19]) and solvents (e.g. DMC [17] and G4 [18]) can successfully be studied via the presented method. The most popular salt for use in LIBs, $LiPF_6$, has been studied using Raman for structural analysis, although not been studied to test concentration changes in solution. Although $LiPF_6$ has been shown to induce a fluorescence background in Raman spectroscopy experiments, its strong PF_6^- Raman-active band would make it an ideal candidate for further studies.[20] This thesis will utilise this chapter's method in Chapter 4, when analysis ILE transport and structure.

To increase viability of the presented method further, more advanced Raman techniques such as stimulated Raman scattering (SRS) spectroscopy could be employed. Its utilisation would increase the sensitvity of the method and reduce the acquisition time per spectrum. [21] Although, it would lose a major advantage of using the described method, namely its ease-of-access with many laboratories housing a Raman spectroscopy instrument.

Further work could also involve analysing the effect of temperature on each of these properties. This was performed by Bazak et al. using MRI, to see how temperature affected the concentration gradient and therefore t_+^0 and D_{app}.[7] There have been no studies, to my knowledge, that looked at the effect of temperature on χ_M. This would be especially important to understand how the electrolyte's thermodynamic state at different temperatures affect the SEI composition. This would require a re-design of the cell, by including a temperature chamber around it, while also allowing optical access for the laser. If we are to progress electrolyte design for lithium metal batteries, this would be of primary importance.

The next chapter will look a study of ionic liquid electrolyte concentration gradients, providing insight into the transport and structure of these complex electrolyte systems.

3.5 Experimental Detail

Electrolyte Description. Lithium bis(fluorosulfonyl)imide (LiFSI) (Battery Grade – 99%) was purchased from Fluorochem Ltd. Tetraethylene glycol dimethyl ether (G4) (anhydrous, 99%+) was purchased from Sigma Aldrich. Handling of LiFSI and G4 was always performed in an argon-filled glovebox (MBraun) with low H_2O content ($<$1 ppm) and low O_2 content ($<$1 ppm). LiFSI was dried further under high vacuum at 70 ^{o}C for 48 hours. G4 was dried over 3 Å molecular sieves, which were washed and then dried for one week. All glassware was dried at 80 ^{o}C under vacuum before being used and brought into the glovebox. The H_2O content of the electrolyte solutions was determined by Karl Fischer titration, also performed in an argon-filled glovebox, and recorded to be below 15 ppm of H_2O.

Density. For density measurements were taken using an Anton Paar DMA 4100, high precision 5-digit density meter, located in an Argon-filled glovebox. Each measurement was temperature controlled at 20 ^{o}C. The density was rinsed with isopropanol (>=99.9%, HPLC grade, Fisher Chemical) at least three times and dried in ambient argon between measurements.

Raman Spectroscopy Experimental. A Renishaw inVia Reflex laser confocal Raman microscope equipped with a near-IR 785 nm laser, a 5x magnification objective (Leica, 0.12 NA, 14 mm WD), providing a 4.8 µm spot size, and a 90º mirror was used to collect Raman spectra of the prepared calibration solutions. Specifically spectra were recorded with a centre at 1200 cm^{-1}, at 5% laser power, with a one second exposure time for each calibration sample. Measurements were repeated 20 times. For both the point-by-point line scan and calibration measurements the same method was followed.

PEIS. For the PEIS prior to current application and the intermittent PEIS measurements, the same setup was used, with a Biologic SP-150 potentiostat. A voltage amplitude (V_a) of 100 mV and frequencies from 100 kHz to 1 Hz was used. The large voltage amplitude was chosen for a reasonable signal-to-noise ratio. Linearity was still maintained. 10 points were measured per decade, with each point being an average of 2 collected points. The ionic conductivity (κ), from R_{bulk}, and resistance of charge transfer (R_{ct}) were collected after 4 hours. The data was then fitted using Biologic EC-lab V11.26 software with the equivalent circuit (Q_{bulk}/R_{bulk})+(Q_{dl}/R_{ct}), with R_{bulk} and R_{ct} representing the bulk resistance of the electrolyte and charge transfer respectively, and Q_{bulk} and Q_{dl} are the constant phase element of electrolyte and double layer respectively.

For the very-low frequency PEIS measurements for steady-state t_+ measurement, the custom-designed and coin cell in Figure 3.26 was used. Measurements were taken with a Biologic VMP3, V_a of 2 mV, frequencies from 100 kHz to 300 μHz, and 3 points per decade, with an average of 2 collected points. The data was fitted using Biologic EC-lab V11.26 software with the equivalent circuit (R_{bulk})+$(Q_{dl}/(R_{ct}+(R_3/Q_2))+W_d)$, with W_d representing the Warburg diffusion resistance, and R_3 and Q_2 indicative of the resistance and capacitance associated with the lateral diffusion process.

Chronoamperometry Using a Biologic SP-150 potentiostat, 100 μA cm^{-2} was applied for 3 hours 59 minutes and 30 seconds between PEIS measurements, because each PEIS measurement took 30 minutes. This allowed for an

overall PEIS + CA measurement time of 4 hours. The voltage was recorded every 5 seconds

Error Estimation. For most of the calculations when propagating error the multiplication/division propagation equation 3.24 was used. It is noted in the text if an alternative estimation method was used.

$$\sigma_x = x\sqrt{\left(\frac{\sigma_p}{p}\right)^2+\left(\frac{\sigma_q}{q}\right)^2+\left(\frac{\sigma_r}{r}\right)^2} \tag{3.24}$$

Specifically, D_{app} was calculated using the weighted gradient of L_d vs. $t^{1/2}$, with L_d standard error from the fitting with equation 3.16.

t_+^0 was determined from equation 3.17 using the average of $dc_s/dz|_{z=0,L}$ from each fitting. t_+^0 error was propagated from the $dc_s/dz|_{z=0,L}$ standard error along with the error from the previous D_{app} calculation.

χ_M was deduced from equation 4.13, by plotting $\frac{F}{2RT(1-t_+^0)\eta_c}$ vs. $\ln\frac{c_{s,z=L}}{c_{s,z=0}}$. The y-axis error was calculated with t_+^0 and the x-axis error was due to the uncertainty in measuring c_s at each cell extreme. The error in $\ln\frac{c_{s,z=L}}{c_{s,z=0}}$ (σ_x) was determined from the average interfacial concentration ratio ($c_{s,z=L}c_{s,z=0}$), which was calculated from fitting equation 3.16, and its standard error (σ_c). This allowed the use of the error propagation equation when using natural log:

$$\sigma_x = \frac{\sigma_c}{c_{s,z=L}/c_{s,z=0}} \tag{3.25}$$

χ_M was subsequently calculated from linearly fitting $\frac{F}{2RT(1-t_+^0)\eta_c}$ vs. $\ln\frac{c_{s,z=L}}{c_{s,z=0}}$, weighted by x- and y-error.

κ and R_{ct} error were calculated from the standard deviation of four R_{bulk} measurements prior to cell polarisation. With the distance and area known very accurately, σ_κ is very small.

For the Stefan-Maxwell diffusion coefficients ($\mathfrak{D}$, $\mathfrak{D}_{0+}$, $\mathfrak{D}_{0-}$, $\mathfrak{D}_{-+}$), error was calculated by propagating χ_M and D_{app} error.

3.6 References

1. Fawdon, J. *et al.* Characterising lithium-ion electrolytes via operando Raman microspectroscopy. *Nat. Commun.,* 13–15 (2021).
2. Newman, J. *et al. Electrochemical Systems* 3rd (Wiley & Sons, 2004).
3. Terada, S. *et al.* Liquid structures and transport properties of lithium bis(fluorosulfonyl)amide/glyme solvate ionic liquids for lithium batteries. *Aust. J. Chem.* **72,** 70–80 (2019).
4. Bard, A. J. *et al. Electrochemical Methods* 2nd ed. (Wiley & Sons, 2001).
5. Saito, M. *et al.* Factors influencing fast ion transport in glyme-based electrolytes for rechargeable lithium-air batteries. *RSC Adv.* **7,** 49031–49040 (2017).
6. Grundy, L. S. *et al.* Impact of Frictional Interactions on Conductivity , Diffusion , and Transference Number in Ether- and Perfluoroether-Based Electrolytes. *J. Electrochem. Soc.* **167,** 120540 (2020).
7. Bazak, J. D. *et al.* Mapping of Lithium-Ion Battery Electrolyte Transport Properties and Limiting Currents with In Situ MRI Mapping of Lithium-Ion Battery Electrolyte Transport Properties and Limiting Currents with In Situ MRI. *J. Electrochem. Soc.* **167,** 140518 (2020).
8. Shah, D. B. *et al.* Comparing Measurements of Limiting Current of Electrolytes with Theoretical Predictions up to the Solubility Limit. *J. Phys. Chem. C* **123,** 23872–23881 (2019).
9. Balsara, N. P. *et al.* Relationship between Steady-State Current in Symmetric Cells and Transference Number of Electrolytes Comprising Univalent and Multivalent Ions. *J. Electrochem. Soc.* **162,** A2720–A2722 (2015).
10. Frenck, L. *et al.* Effect of salt concentration profiles on protrusion growth in lithium-polymer-lithium cells. *Solid State Ionics* **358,** 115517 (2020).
11. Guggenheim, E. *Thermodynamics: An Advanced Treatment for Chemists and Physicists* 5th (North-Holland Publishing Company, 1950).
12. Wang, A. A. *et al.* Shifting-reference concentration cells to refine composition-dependent transport characterization of binary lithium-ion electrolytes. *Electrochim. Acta* **358,** 136688 (2020).
13. Bockris, J. O. *et al. Modern Electrochemistry Volume 1 Ionics* 2nd (Kluwer Academic Publishers, 2002).
14. Kottam, P. K. *et al.* Effect of salt concentration, solvent donor number and coordination structure on the variation of the Li/Li+ potential in aprotic electrolytes. *Energies* **13** (2020).
15. Ueno, K. *et al.* Glyme-lithium salt equimolar molten mixtures: Concentrated solutions or solvate ionic liquids? *J. Phys. Chem. B* **116,** 11323–11331 (2012).
16. Boukamp, B. A. Derivation of a Distribution Function of Relaxation Times for the (fractal) Finite Length Warburg. *Electrochim. Acta* **252,** 154–163 (2017).
17. Forster, J. D. *et al.* Mapping Li+ concentration and transport via in situ confocal Raman microscopy. *J. Phys. Chem. Lett.* **5,** 2007–2011 (2014).

18. Cheng, Q. *et al.* Operando and three-dimensional visualization of anion depletion and lithium growth by stimulated Raman scattering microscopy. *Nat. Commun.* **9,** 1–10 (2018).

19. Georén, P. *et al.* Concentration Polarization of a Polymer Electrolyte. *J. Electrochem. Soc.* **149,** A1015 (2002).

20. Cabo-Fernandez, L. *et al.* Kerr gated Raman spectroscopy of LiPF₆ salt and LiPF₆ -based organic carbonate electrolyte for Li-ion batteries. *Phys. Chem. Chem. Phys.* **21,** 23833–23842 (2019).

21. Prince, R. C. *et al.* Stimulated Raman scattering: From bulk to nano. *Chem. Rev.* **117,** 5070–5094 (2017).

4 | Insights into Ionic Liquid Electrolyte Transport and Structure

Contents

4.1 Abstract 111
4.2 Introduction 111
4.3 Results & Discussion 114
4.3.1 Concentration Gradient Visualisation 114
4.3.2 Asymmetry and Structural Implications 118
4.3.3 Li^+ Transport Properties 123
4.3.4 Dependence on Concentration 131
4.3.5 Plating at Low Concentrations 133
4.4 Conclusions & Future Work 135
4.5 Experimental Detail 137
4.6 References 139

4.1 Abstract

Ionic liquid electrolytes (ILEs) have become popular in various advanced Li-ion battery chemistries because of their high electrochemical and thermal stability, and low volatility. However, due to their relatively high viscosity and poor Li^+ diffusion, it is thought large concentration gradients form, reducing their rate capability. This chapter looks to visualise lithium-ion concentration gradients in a common ILE, and subsequently understanding its key transport and thermodynamic properties. In doing so, unique revelations regarding ILE bulk structure will be described.

4.2 Introduction

For next-generation battery technologies, such as those that utilise lithium metal anodes,[1] high-voltage cathodes[2] or conversion cathodes[3], conventional electrolyte solutions such as LP30 have been deemed unsuitable. This has been primarily due to either the electrochemical instability of common organic electrolytes, and also the undesirable decomposition product that form the SEI

or CEI.[4] Conversely, ionic liquid electrolytes (ILEs) have shown promising performance in such setups due to their (electro)chemical and thermal stability, and preferable SEI/CEI composition.[5–7] As was mentioned in Section 1.6 however, with multiple ions in solution and an often high viscosity, ILEs have shown to exhibit particularly poor transport properties.[8, 9] This limits their rate performance, as ohmic resistance and concentration gradient formation lead to increasing overpotential with increasing current density. Furthermore, in lithium metal batteries (LMBs), the depletion of Li^+ at the lithium metal surface has shown to induce lithium dendrite growth and short-circuiting.[10]

Common ILEs used for battery applications contain 3 or 4 ions, and due to D_{Li+} often being the lowest D_i value, the transference number of Li^+ (t_{Li+}) has been shown to be very low.[11] With ILEs showing poor diffusion and transference, it has been proposed that ILEs exhibit large concentration gradients through the cell. In section 1.6, the most common methods for measuring t_{Li+} of ILEs were presented, including (electrophoretic) pfg-NMR, or a steady-state method such as Bruce-Vincent or EIS.[12–15] There were studies a few decades ago that used the Hittorf method for measuring t_i of "ionic melts", but to the best of my knowledge this method has not been extended to room-temperature ILEs. So, although these methods have shed light on the complexities and intracies of ILE transport, there is yet to be a complete experimental study that monitors both D_{app}, t_{Li+} and an added thermodynamic understanding through χ_M for room-temperature ILEs.

The purpose of this chapter is to visualise the concentration gradient of Li^+ in a common room-temperature ILE, LiFSI in $Pyr_{1,3}FSI$ at different concentrations, for the first time. The visualisation will lead to the isolation of the key transport and thermodynamic properties, D_{app}, t_{Li+}, χ_M, κ and R_{ct}. Visualising c_{Li+} provided the unique opportunity to see how ILE structure was affecting the gradient, see Figure 4.1.

Specifically the chapter will cover:

- Presentation of **calibration methods** for isolating the Li^+ concentration gradient in ILEs.

- **Fitting** of the concentration gradients, and the subsequent extraction of electrolyte transport and thermodynamic properties.
- Description of gradient prior to application of current, and **structural implications**.
- **Effect of bulk concentration** on gradient formation and subsequent electrolyte property comparison.
- **Comparison** with values gathered from pfg-NMR measurements.
- Present data on **plating behaviour** at low concentrations.

All the work in this chapter was performed by myself, under the supervision of Prof. Mauro Pasta. I performed all the experiments and analysis, apart from pfg-NMR measurements, which were measured by Dr. Gregory J. Rees. The work from Sections 4.3.1-4.3.4 has been submitted for publication, authored by Jack Fawdon, Dr. Gregory J. Rees, Prof. Fabio La Mantia and Prof. Mauro Pasta.

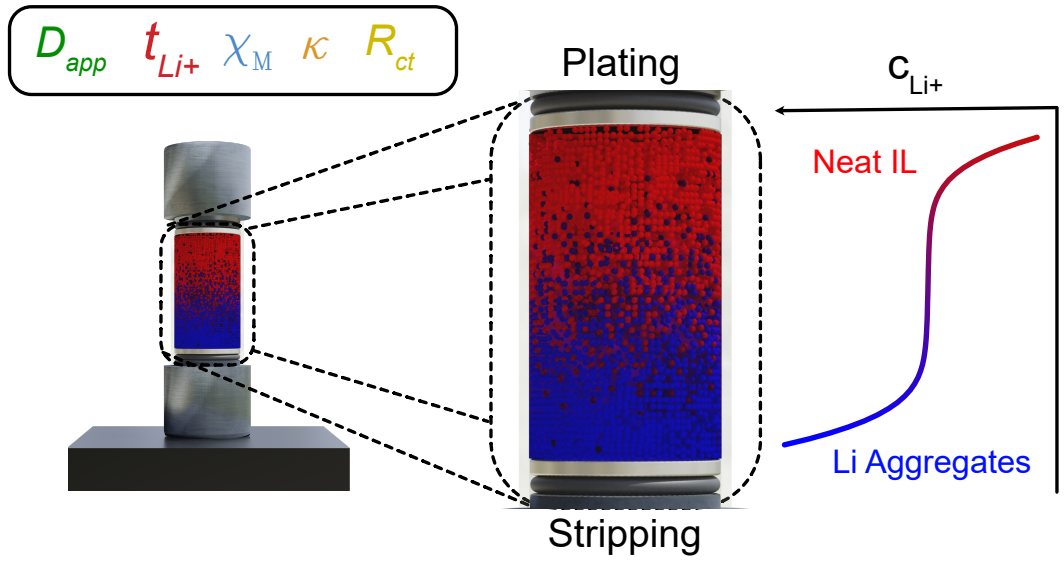


Figure 4.1: Schematic of Li^+ concentration gradient in ILE, gathering each fundamental electrolyte transport and thermodynamic property, D_{app}, t_{Li+}, χ_M, κ and R_{ct}. There is an aymmetry to the gradient, hypothesised to be due to the formation of large Li-based aggregates.

4.3 Results & Discussion

4.3.1 Concentration Gradient Visualisation

The general method for concentration gradient visualisation using operando Raman microspectroscopy was illustrated in the previous chapter; specifically a time-series of one-dimensional (1D) Raman scans across a custom-built optical Li|Li symmetric cell while current is passed. Importantly, the cell was placed vertically on the stage, with stripping occurring at the bottom and plating at the top, to avoid natural convection from density differences of the bulk concentration. The line-scan was performed every 4 hours for 36 hours. Electrolyte solutions were prepared as molalities to increase the reliability and accuracy of preparation. The molarity was calculated using equation 3.1, and Figure 4.2 shows the dependency of density on concentration, with a linear fit.

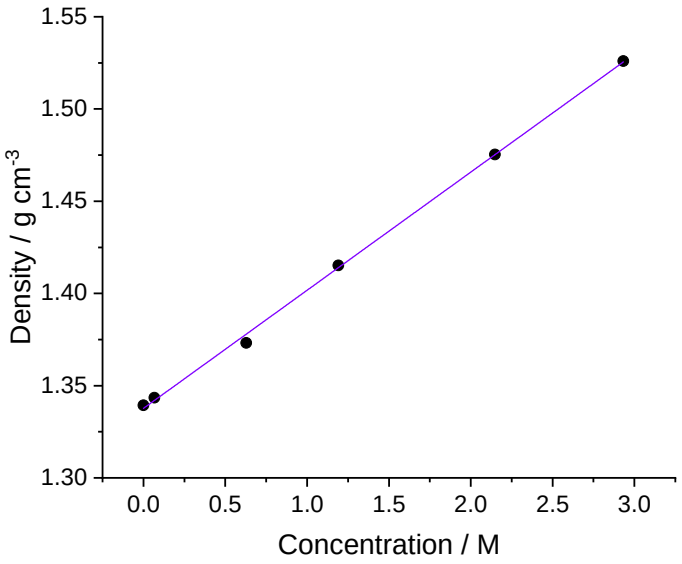


Figure 4.2: LiFSI in $Pyr_{1,3}FSI$ density vs. concentration

Figure 4.3 shows a Raman spectrum of 1 m LiFSI in $Pyr_{1,3}FSI$, with the arrows pointing to the peaks associated with FSI^-. The other peaks are $Pyr^+_{1,3}$.[16]

Due to there being no solvent peak to normalise FSI^- and $Pyr^+_{1,3}$ peak area to, for calibration we looked at two methods to equate each point scan to c_{Li+}.

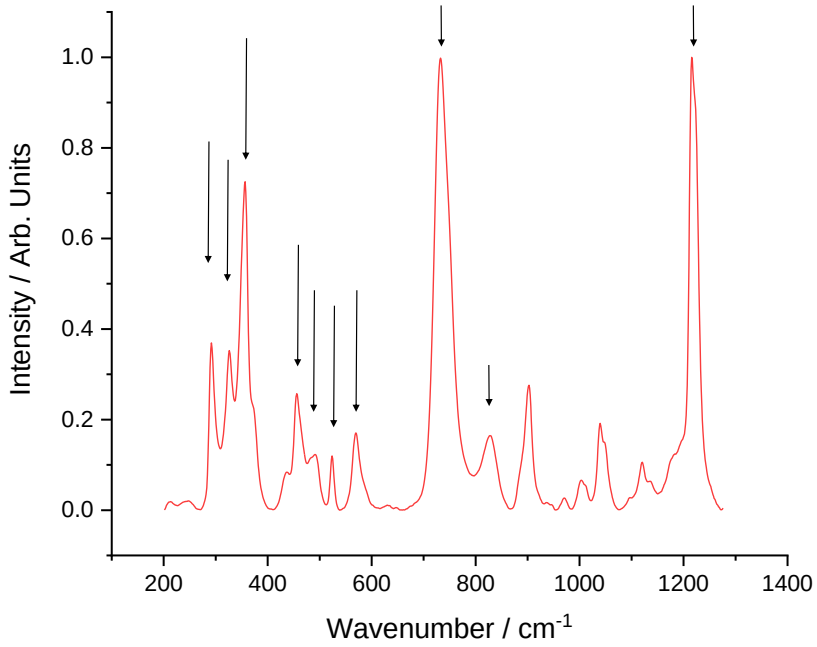


Figure 4.3: Raman spectrum of 1 m LiFSI in $Pyr_{1,3}FSI$, with centre of 800 cm^{-1}, 5% laser power, 20 accumulations, 1 second exposure.

First, c_{Li^+} was correlated to the 730 cm^{-1} FSI^- peak shift. Representing the the S-N-S bending mode,[17] the 730 cm^{-1} peak shifts to higher wavenumbers monotonically with increasing c_{Li^+} due to the continuing formation of high-energy bonding in $Li(FSI)_2^-$ structures.[18] Specifically this peak was fitted with a exponentially modified Gaussian (EMG) function because it was slightly skewed due to the emerging shoulder peak (see equation 4.1). A python script was used, as illustrated in Appendix A (also available at GitHub). Figure 4.4a shows an example of the fitting.

$$y = y_0 + \frac{A}{t_0} * \exp\left(0.5 * \left(\frac{w}{t_0}\right)^{\frac{2-(x-x_c)}{t0}}\right) * \left(\operatorname{erf}\left(\frac{z}{\sqrt{2}}\right) + 1\right)/2; \tag{4.1}$$

Where y_0 is the y-offset, A is the area, t_0 is a constant, w is the width and x_c is the X and maximum height (in y-axis). Figure 4.4b shows how the 700 peak shifted to higher wavenumbers with increasing concentration. x_c was isolated and plotted in Figure 4.5a, illustrating the non-linearity of wavenumber increase with c_{Li^+} as LiFSI concentration approaches saturation.

Secondly, the area ratio of the FSI^- 730 cm^{-1} and $Pyr_{1,3}^+$ 900 cm^{-1} peaks was calculated and the dependence on c_{Li^+} was analysed. One should note again the

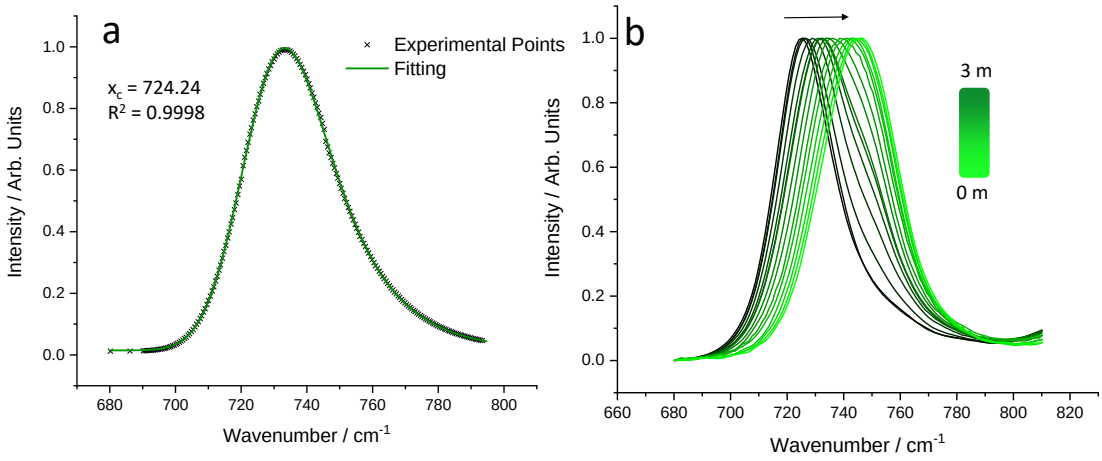


Figure 4.4: Raman spectrum of 1 m LiFSI in $Pyr_{1,3}FSI$, with centre of 800 cm^{-1}, 5% laser power, 20 accumulations, 1 second exposure.

non-linear relationship of area ratio with c_{Li+}, which suggests a structural change is occurring (Figure 4.5b). On both curves, at around 1-2 m (see discussion below), there was an especial change in gradient, but for ease we fitted both curves to a 2nd-order polynomial. Another potential strategy to correlate operando Raman spectra with c_{Li+} was using an internal standard. However, this was deemed unfeasible in our presented system due the standard's requirement of remaining at a constant concentration throughout the cell while in operation. A potential internal standard was benzonitrile (PhCN) due to its strongly active Raman bands and solubility in ILEs, but after attempting its use, it moved in response to a current. It was concluded this was likely to occur for any potentially suitable internal standard.

An example illustrating each calibration method on a line-scan of a 1 m electrolyte, using a 100 μA cm^{-2} current density after 12 h, is shown in Figure 4.6. The shape was the same but using the "area ratio method" led to a much more noisy concentration profile and problems with accuracy of concentration determination from the calibration curve. This was due to the influence the glass-background had on the analysis and mossy-dendrite growth close to the plating surface. For better spectral resolution, one could employ stimulated Raman scattering microscopy (SRS), though this is beyond the scope of this work. So although peak area is usually used as the best correlate of ion

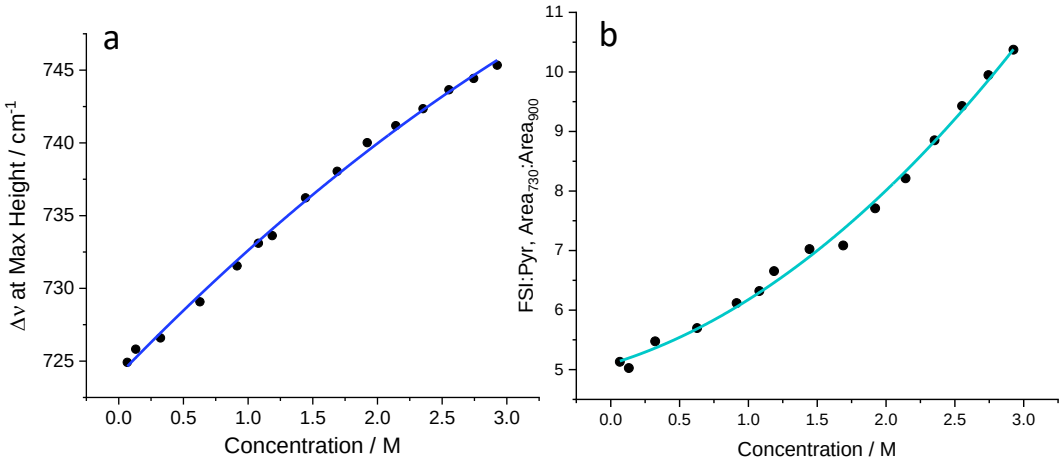


Figure 4.5: Raman spectrum of 1 m LiFSI in $Pyr_{1,3}FSI$, with centre of 800 cm^{-1}, 5% laser power, 20 accumulations, 1 second exposure.

concentration, the 730 cm^{-1} peak shift was chosen to progress this study for analysis. Using this calibration method the mass-balance of the system was checked by integrating each concentration profile over the 36 hour experiment, and noted no change with each integral being within 1.2 % of the highest and lowest profile integral. It was concluded therefore that this was a valid method for calibrating concentration in ILEs.

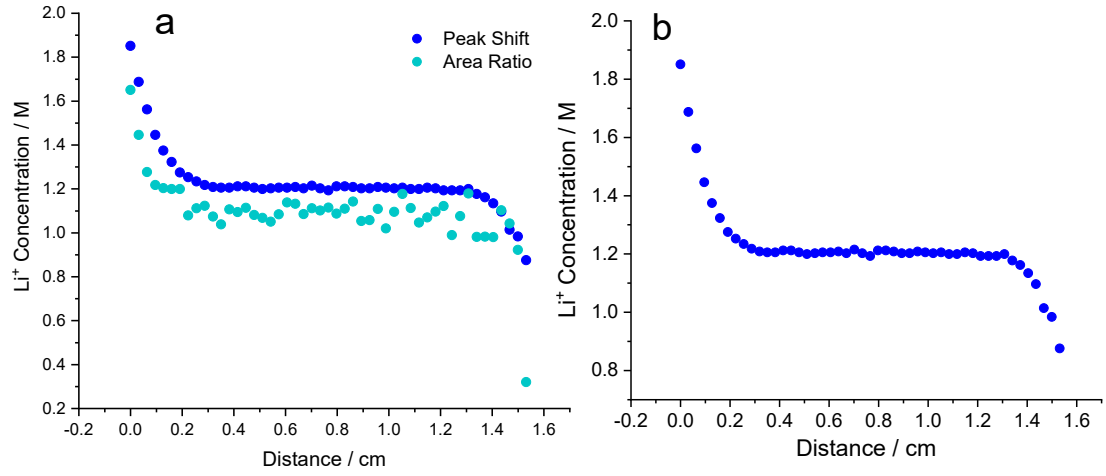


Figure 4.6: Comparison of gradients with different methods of calibration: a) Gradients showing either the "peak shift" method and "area ratio" method of calibration, with "peak shift" showing better resolution. b) Li^+ concentration gradient of 1 m LiFSI in $Pyr_{1,3}FSI$ at 100 μA cm^{-2}, after 12 hours, noting its asymmetry.

4.3.2 Asymmetry and Structural Implications

Figure 4.6b shows a concentration profile of Li^+ in 1 m LiFSI in $Pyr_{1,3}FSI$ at 100 μA cm^{-2} after 12 hours. Surprisingly, the profile appeared to be asymmetric, with both the bulk concentration change and dc/dz to be larger on the stripping side compared to the plating side. This seemed unique to an ILE systems, with LiFSI in tetraglyme (G4) from chapter 3 not showing this phenomenon.

Prior to applying current, the cell was left to rest for 4 hours and a Raman line-scan was recorded. There was an increase in Li^+ concentration at the bottom of the cell, which indicated an accumulation of Li^+ before any current was applied, see Figure 4.7a. This accumulation suggested distinct Li^+ species of higher density were falling due to gravity. To investigate this further, the open circuit voltage (OCV) of the cell was measured while changing the cell's orientation. As described in the Nernst equation, cell potential depends on electrolyte interfacial concentration, so if there was a difference in concentration one will see a change in OCV. Figure 4.7b shows how OCV changed with time, labelled with the orientation of the cell. It was clear that the OCV was dependent on the orientation of cell, with it rising from 0 V to $\sim$4 mV after the first few hours and dropping to $\sim$-5 mV when the cell was inverted. The cell was then placed horizontally, which led to the OCV reverting back to 0 V. Using 4 mV as OCV, the thermodynamic activity ratio calculated from the Nernst equation was 1.16, in good agreement with the 1.11 measured by Raman (Figure 4.7a).

To check the accumulation was independent of the electrode used, the Li^+ profile of the cell with stainless-steel blocking electrodes was studied (Figure 4.8). Although there was some Li^+ accumulation it was noticeably less than using reactive Li-metal electrodes, with an increase at the electrode surface of only $\sim$0.04 M vs. $\sim$0.12 M when using Li-metal electrodes. So although the data suggests the presence of large aggregates, using reactive electrodes increased the movement of these species further. Monitoring R_{ct} via EIS suggested Li metal was reacting with the ILE. As has been described by Nyman and Liu, volume changes caused by interfacial reactions can induce bulk flow.[19, 20] If the partial

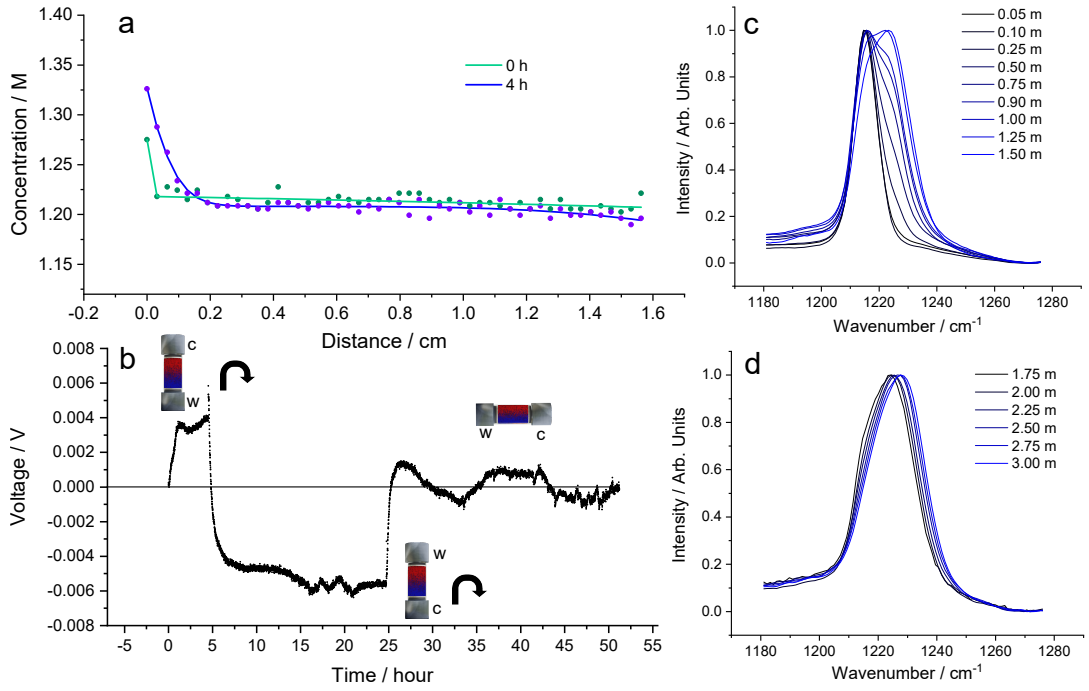


Figure 4.7: Asymmetric Concentration Gradients: a) Formation of concentration differences over 4 h, 0 cm is the bottom of the cell b) OCV vs. time while no current is passed, showing how orientation affects OCV c) Raman spectra of 0.05 m to 1.5 m showing two distinct FSI^- Raman bands, representing "free" and "bound" FSI d) Raman spectra from 1.75 m to 3 m showing a peak shift. At ~1.1 m $[FSI^-]<[Li(FSI)_2]^-$.

molar volume change of the reacting species is large, this could explain increased bulk flow against reactive vs. non-reactive electrodes.

Several molecular dynamic (MD) studies have proposed the formation of long-range ordered structures in ILEs, with some suggesting mesoscopic aggregate formation[21, 22] and others offering theories on percolating network formation.[23] Past experimental studies using small angle X-ray scattering (SAXS) experiments have also predicted the formation of mesoscopic aggregates or domains in neat ILs, and with lithium salt in IL solutions.[24–26] SAXS showed that the addition of lithium salt to ILs results in a reorganisation of polar group around Li^+. The structure of self-segregated heterogeneities appeared to be highly dependent on the alkyl side-chain on the cation in the IL. However, there is little consensus on the overall size and structure of the aggregates present in IL and Li-salt solutions.

To estimate the size of the Li^+ species forming, the Stokes' law was used,[27] measuring the sedimentation time for the OCV vs. time graph in Figure 4.7b.

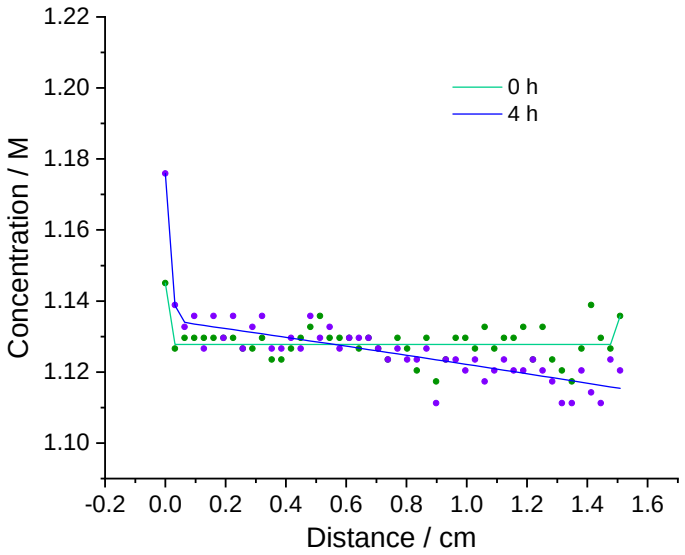


Figure 4.8: Lithium concentration gradient between two stainless steel pistons prior to application of current. A smaller gradient forms compared to using lithium metal electrodes.

$$v = \frac{2}{9}(\rho_p - \rho_l)\frac{gr^2}{\eta} \tag{4.2}$$

Where v is the velocity (v = height/sedimentation time), ρ_p is particle density, ρ_l is the viscosity of the liquid, g is the gravitational acceleration (= 9.81 m/s^2), η is the dynamic viscosity and r is the particle radius. A range was estimated for particle size. The density difference in aggregate and surrounding liquid was estimated, with an upper limit of ρ_{LiFSI} for ρ_p and ρ_l was used as the neat IL. η of the neat IL was measured as 40.7 cP. h was estimated was used as half the distance between the electrodes (7.5 mm). The calculated aggregate size was 3-8 μm. Although the density differences and between neat IL and aggregate, and velocity, were estimated, it can be assumed that the particles are on a micron-scale.

The Raman spectra required for c_{Li+} calibration provided information on electrolyte structural changes with increasing LiFSI content. The peak at 1200-1240 cm^{-1} represents the S=O stretching mode of FSI$^-$. In the neat IL there is a single peak at 1215 cm^{-1} and with increasing LiFSI addition a new, defined peak

appears at 1225 cm^{-1}(Figure 4.7c). The 1215 cm^{-1} peak is commonly seen in LiFSI in organic-electrolytes (e.g. LiFSI in G4[28]), but a defined 1225 cm^{-1} peak is unique to ILEs. This suggested the ILEs have distinctive structures or domains present that are not in organic-based electrolytes. As has been mentioned in other works, the 1215 cm^{-1} peak was speculated to be free FSI^- and 1225 cm^{-1} was thought to be a bound Li-FSI_n species. The solvation number (n) of the Li^+ can be estimated by calculating the fraction of bound FSI species present using the areas of the fitted 1215 cm^{-1} and 1225 cm^{-1} peaks:[18]

$$a = \frac{A_b}{A_f + A_b} \tag{4.3}$$

Where A_b and A_f are the areas of the bound and free peak, respectively. Also, the fraction of c_{Li+}/[FSI^-] was calculated to understand how much Li^+ there was vs. FSI^-.

$$b = \frac{[Li^+]}{[FSI^-]} \tag{4.4}$$

If one assumes Li^+ is solvated:

$$SolvationNo. = \frac{a}{b} \tag{4.5}$$

From the fitting of the 1215 cm^{-1} and 1225 cm^{-1} peaks, with a full width at half maximum (FWHM) of 10, the estimated solvation number of Li^+ was $\sim$2, independent of concentration (see Table 4.1). The deviation at low concentrations was attributed as an error in the fitting of a small bound-FSI peak.

Table 4.1: Solvation Number of Li^+

Concentration$_{molality}$	**Concentration**$_{molarity}$	**Area**$_{boundFSI}$	**Area**$_{freeFSI}$	**Solvation Number**
0.05	0.066	0.19	9.90	1.25
0.10	0.13	0.69	8.91	2.41
0.25	0.32	1.68	9.87	2.03
0.50	0.63	3.60	9.47	2.06
0.75	0.91	5.60	9.38	1.99
0.90	1.08	6.81	9.12	1.97
1.00	1.19	7.26	9.17	1.88
1.25	1.44	8.16	8.82	1.87

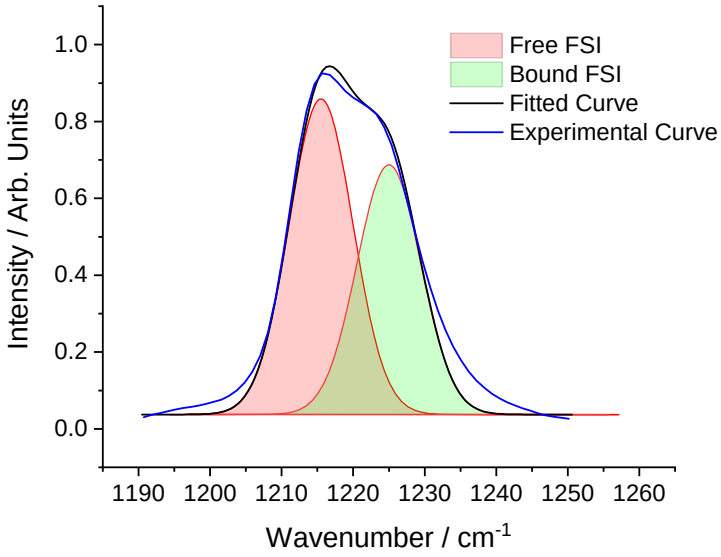


Figure 4.9: Example fitting of 1220 cm^{-1} peak of 1 m LiFSI in $Pyr_{1,3}FSI$, representing bound and free FSI. The peak at 1220 cm^{-1} is indicative of the S=O stretch.

It was concluded that *n* remained constant at 2 (i.e. Li^+ is solvated by two FSI^-, ($[Li(FSI)_2]^-$). With FSI^- experiencing two separate environments, it is at $\sim$1.1 m that $[FSI^-]<[Li(FSI)_2]^-$. Indeed, as the concentration increases past 1.25 m, the 1225 cm^{-1} peak becomes less defined and more broad (Figure 4.7d), which was speculated to be due to the fusing of the $[Li(FSI)_2]^-$-derived aggregates forming a homogeneous, percolating network. Indeed, McEldrew et al. predicted when using MD simulations a "critical threshold" or gelation point where these extended networks form. I propose that both the finite aggregates and percolating network are of a higher density than the IL medium that surrounds them.

Although a more homogeneous environment moving from 1 m to 2 m is being proposed, as illustrated by the spectroscopic data, there still appears to be the accumulation of Li^+ at the bottom of the cell in the 2 m too. As suggested above, this could be due to the percolating network falling in on itself due to the density differences. For this to happen the pores within the network would likely have to be very large. More work is required to fully characterise these aggregates and networks experimentally.

4.3.3 Li^+ Transport Properties

The presence of the described secondary environments no doubt influences the transport of the Li^+ through the electrolyte. The 1 m electrolyte was used as a model system, like in chapter 3, to describe the process of fitting and transport property isolation. Using the same derivation as chapter 3, equation 4.6 is a solution to the diffusion equation in a symmetric cell setup, using the interfacial concentration gradient as a spatial boundary condition. Each gradient was fitted to this equation, elucidating information on the transport properties of the electrolytes. Due to the gradients' asymmetry, each side of the cell was fitted separately with different diffusion length and interfacial gradient values:

$$\begin{aligned} c_{Li+}(z,t) = c^*_{Li+} + a(s)\left\{\left(\frac{b(s)}{\pi^{\frac{1}{2}}}\right)\exp\left(-\frac{z}{b}\right)^2 - z\,\mathrm{erfc}\left(\frac{z}{b(s)}\right)\right\} - \\ c(p)\left\{\left(\frac{d(p)}{\pi^{\frac{1}{2}}}\right)\exp\left(-\frac{(-z+L)}{d(p)}\right)^2 + (-z+L)\,\mathrm{erfc}\left(\frac{-z+L}{d(p)}\right)\right\} \end{aligned} \tag{4.6}$$

$$a, c\left(= c_{Li+}z\Big|_{z=0,L}\right) = \frac{J(1-t_{Li+})}{nFD_{app}} \tag{4.7}$$

$$b, d(= L_d) = 2(D_{app(s,p)}t)^{\frac{1}{2}} \tag{4.8}$$

The Li^+ concentration gradient is illustrated in Figure 4.10 at 100 μA cm^{-2} over 36 hours with an 8 hour gap between each spectrum.

As expected, the gradients were large across the electrolyte, with the stripping electrode showing a significant interfacial concentration ($dc/dz_{z=0}$) at 100 gradient μA cm^{-2} of 5.3 $\pm$ 0.2 $\times 10^6$ mol m^{-4}. The measurement was also performed at 50 μA cm^{-2} showing $dc/dz_{z=0}$ as 2.8 $\pm 0.1 \times 10^6$ mol m^{-4}. As was expected, $dc/dz_{z=0}$ was directly proportional to the current applied, with $dc/dz_{z=0}$ being almost exactly double when a 100 μA cm^{-2} compared to 50 μA cm^{-2}. The plating interfacial gradient ($dc/dz_{z=L}$) at 100 μA cm^{-2} was lower at 3.5 $\pm$ 0.6 $\times 10^6$ mol m^{-4}; presumably due to the accumulated aggregates at the bottom of the cell. For comparison, 1 m LiFSI in tetraglyme (G4) in the previous chapter showed an $dc/dz_{z=0,L}$ as $\sim 1 \times 10^6$ mol m^{-4} at 100 μA cm^{-2}.

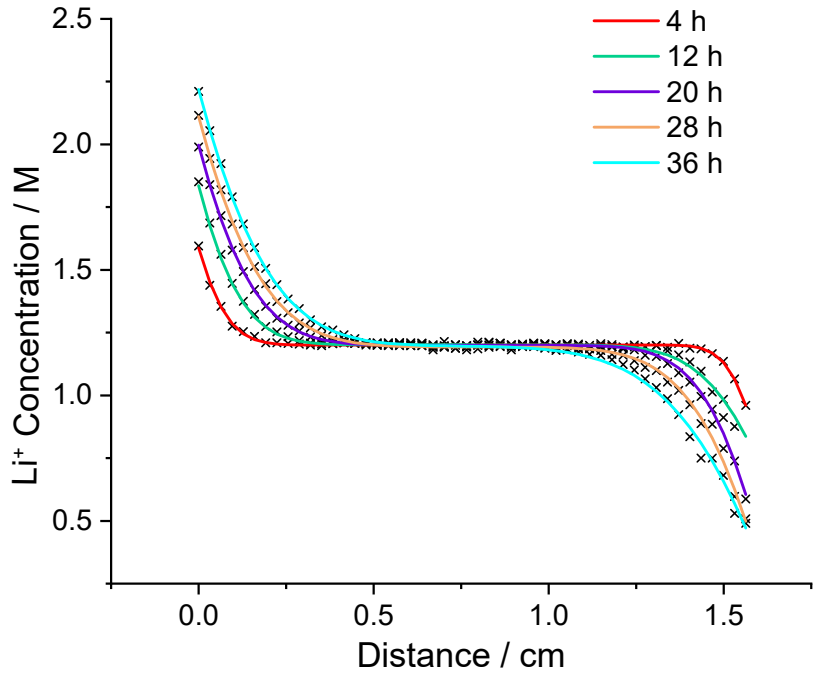


Figure 4.10: Fitted Li^+ concentration gradient formation over time, using Equation 4.6, up to 36 hours with 8 hours gaps.

Diffusion. By monitoring the diffusion length (b and d) over time, one can calculate the "apparent" diffusion coefficient (D_{app}) on both sides of the cell. Figure 4.11 shows b and d vs. time$^{1/2}$, with the slope being proportional to the D_{app}. Also plotted is the 95% confidence band, which highlights the uncertainty especially on the plating side of the cell. The fitting on the stripping side was much tighter, which was reflected in the error of the D_{app} calculation. On the stripping side, $D_{app} = 1.77 \pm 0.06 \times 10^{-11}$ m^2 s^{-1}, and on the plating side $D_{app} = 2.5 \pm 0.5 \times 10^{-11}$ m^2 s^{-1}, with a inverse-variance weighted average of 1.78 $\pm$ 0.09×10^{-11} m^2 s^{-1} . pfg-NMR measurements were performed to compare against these values, using the harmonic mean; D_{app} was calculated:

$$D_{app} = \frac{c_T}{\frac{c_{Li^+}}{D_{Li^+}} + \frac{c_{FSI^-}}{D_{FSI^-}} + \frac{c_{Pyr^+}}{D_{Pyr^+}}} \tag{4.9}$$

Where c_T is the concentration total, $D_{Li^+} = 1.42 \times 10^{-11}$, $D_{FSI^-} = 1.88 \times 10^{-11}$, $D_{Pyr^+} = 1.76 \times 10^{-11}$ m^2 s^{-1}. D_{app} was calculated as 1.77×10^{-11} m^2 s^{-1}, identical to the stripping D_{Li^+} calculated with concentration visualisation.

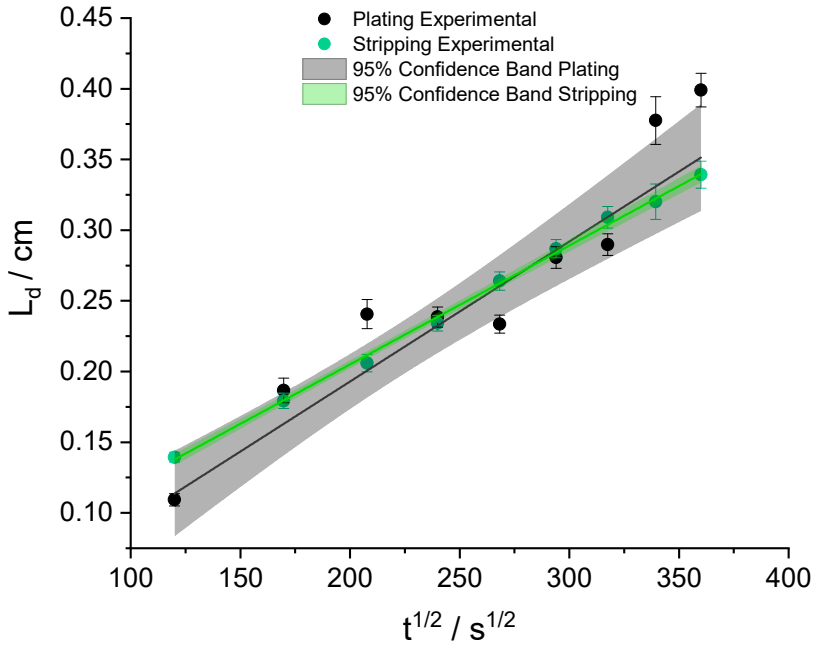


Figure 4.11: Evolution of the diffusion layer on the stripping side (green) and the plating side (grey), noting the wider confidence band from fitting the plating side, perhaps due to the side effects of dendrite growth.

Transference Number. The transference number of Li^+ (t_{Li^+}) was also calculated from the fitted concentration gradient. Using the Hittorf method is particularly straight-forward when utilising concentration gradient visualisation, as one can monitor the concentration on each side of the cell by integrating under the concentration curve. To the best of my knowledge, the Hittorf method has not been utilised for studying t_{Li^+} in lithium-ion room temperatures ILEs, with the majority of groups using pfg-NMR or eNMR. Others have used the Bruce-Vincent or EIS methods. As stated in the Introduction, a few decades ago there were numerous studies measuring the transference number of ions in "ionic melt" (molten salt) mixtures utilising the Hittorf method.[29–33] Although Richter often measured t_{Li^+} internally, as Gouverneur et al. mention in their work, there is a loss of information if one were to reference t_{Li^+} internally.[12] Therefore, it was decided an external laboratory frame to reference ionic movement was most suitable. t_{Li^+} was calculated (similar to equation 1.32 from Section 1):

$$t_{Li^+} = 1 - \frac{\Delta n_{Li^+}}{n_{charge}} = \frac{A \cdot F(\Delta \int_0^{z_{cell}/2} c_{Li^+} dz)}{Q} \tag{4.10}$$

$$\Delta c_{Li^+} = c_{Li^+}^{0h} - c_{Li^+}^{t} \tag{4.11}$$

Where n_{charge} is the number of moles of charge passed, Δn_{Li^+} is the molar difference between the two sides of the cell before and after time, t, Q is the charge passed over time, and A is the area of the electrode.

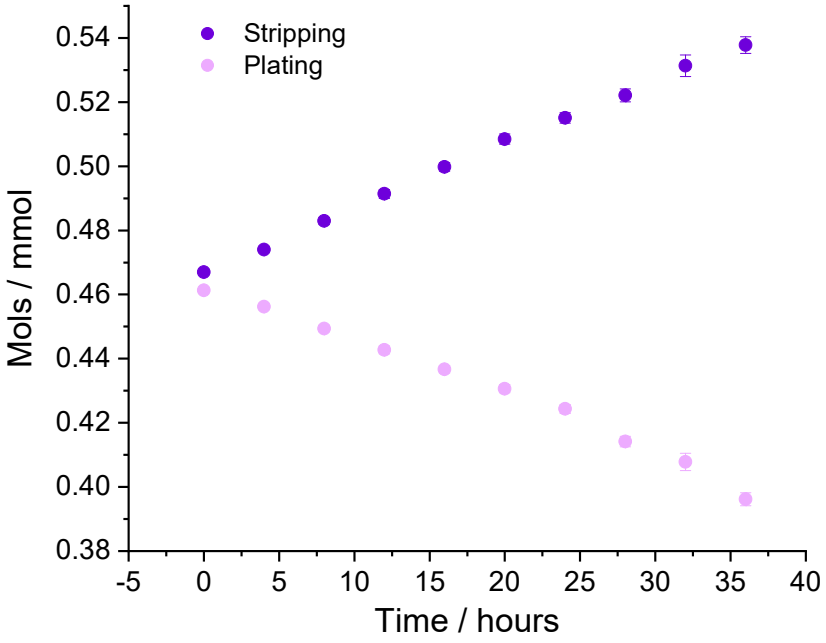


Figure 4.12: Change in the molar content on the stripping and plating side of the cell with time.

Figure 4.12 shows how the molar amount changed for the stripping and plating side; note the change in area is linear indicating the movement of the aggregated structures remained constant, and so does t_{Li^+}. Using the initial concentration profile prior to application of current, t_{Li^+} was calculated for each scan over time, and the average t_{Li^+} was calculated from the inverse-variance weighted mean. On the stripping side t_{Li^+} was calculated as -0.09 ± 0.02 and on the plating side, 0.11 ± 0.06, with a weighted average of -0.06 ± 0.07. Again, the lower value on the stripping side was likely due the accumulation of higher density aggregates on oxidation of Li.

As noted above, prior eNMR measurements have shown negative t_{Li^+} value due to the formation of $[Li(FSI)_2]^-$ species. The negative t_{Li^+} we measured was speculated either to be a result of migration due to the presence of $[Li(FSI)_2]^-$-type species or due the continued formation of large aggregates that fall due to gravity. To test this hypothesis we performed a separate measurement that visualised the concentration gradient using blocking electrodes (SS). We applied 2.5 V to the cell, which was low enough not to allow SS corrosion, but was a large enough voltage to detect changes in concentration due only to migration. If t_{Li^+} was negative due to migration there would be gradient formation; a positive t_{Li^+} would lead to no gradient forming. Gouverneur et al. used blocking electrodes to detect negative t_{Li^+} values, over a short-time frame. Over a larger time-frame in this measurement, there was no gradient forming purely due to polarisation in the cell, indicating there was no long-term movement of Li^+ in the "wrong direction". This is important for applications that involve longer-term transport using ILEs.

By using the pfg-NMR diffusivities and measured concentrations, t_{Li^+} via pfg-NMR was 0.094. See Table 4.3 for full details.

Very-low-frequency PEIS was performed to measure t_{Li+} and compare. To confirm Sørenson and Jacobsen's theory was appropriate for a three-ion system, a simulation was run using COMSOL Multiphysics 5.5 analysing if the below equation holds true:

$$\frac{c_{Li+}D_{Li+}}{c_{Li+}D_{Li+} + c_{FSI-}D_{FSI-} + c_{Pyr+}D_{Pyr+}} = \frac{R_{bulk}}{R_{bulk} + W_d} \tag{4.12}$$

The equations used in the simulation are presented in Appendix 3; PEIS theory used to derive equation 1.38 is not based on CST theory so the Battery Module could not be used like in Chapter 3. Instead, three charged species were simulated in a neutral solvent, using fundamental flux and charge-balance equations. Specifically, individual flux equations were included for each species, and the overall Poisson equation was used to maintain charge-balance. Each species was treated as an unassociated ion, with interaction or accumulation between them; in other words, the solution was treated as "ideal". The rate of

Table 4.2: Simulated PEIS fittings of ILE at 0.5 M, 1 M and 2 M

Concentration / M	**0.5**	**1**	**2**
R_{bulk} / x10^{-5} Ohm.m^2	6.61	5.75	4.57
W_d / x10^{-5} Ohm.m^2	127	61.0	28.8
$t_{Li+}^{D_i}$	0.050	0.085	0.137
t_{Li+}^{PEIS}	0.050	0.085	0.137

accumulation at the boundaries was defined by the Butler-Volmer equation. Using a MATLAB script written by Prof. La Mantia and implemented by myself, a PEIS Nyquist plot was simulated and fitted, see Figure 4.13. Table 4.2 shows that equation 4.12 did hold for three-ion systems, as $t_{Li+}^{D_i}$ and t_{Li+}^{PEIS} were the same. This confirms, the experimentally measured VLF-PEIS measurements were a valid approach for comparing transference number values.

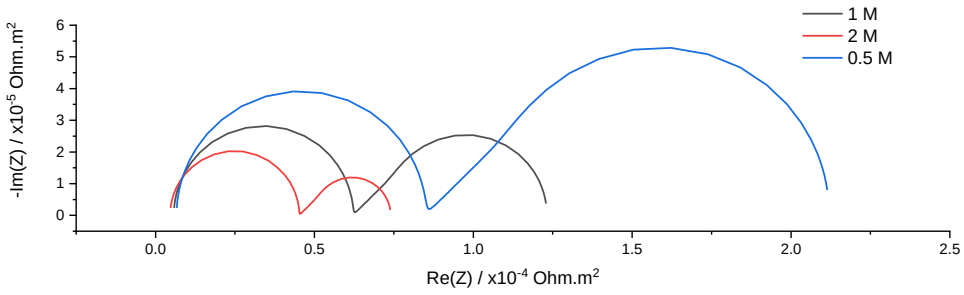


Figure 4.13: PEIS Simulation of Ionic Liquid-based electrolyte, with three ions present, looking at a salt concentration of 0.5 M, 1 M and 2 M.

For experimental measurements, using the custom-built cell described in the previous chapter, the frequency was scanned to 25 μHz with a voltage amplitude of 20 mV (see Experimental Detail). A PEIS measurement was taken after this one to check minimal drift was occurring. After fitting the PEIS spectrum with an appropriate equivalent circuit t_{Li^+} was calculated, see Figure 4.14. The same cell was used as described in section 3.3.7. The medium-frequency semi-circle was assumed to include the impedance of charge-transfer and SEI, and the low-frequency was assumed to be exclusively finite-length Warburg diffusion. An additional process was included in the medium frequency range, which was

included in Chapter 3 also, speculated to be a result of lateral diffusion. As a ball-park understanding on the most resistive element of the cell, one can notice how large W_d is, indicating the large concentration gradient that has formed. In other words, this is the element that will cause the most overpotential in the cell, compared to the SEI, charge-transfer or ohmic resistances. Using equation 1.38, the t_{Li+} was calculated as 0.0858. Indeed, by introducing χ_M (see "Thermodynamic Factor" below) into the formula, the value increases slightly to 0.0940. Intriguingly, this was very similar to the value calculated via pfg-NMR. The "transport number", which as shown in equation 4.12, is not directly equivalent to the "transference number", although it is a good estimate. For instance, the transport number would never be calculated as negative, like the transference number measurement via Hittorf.

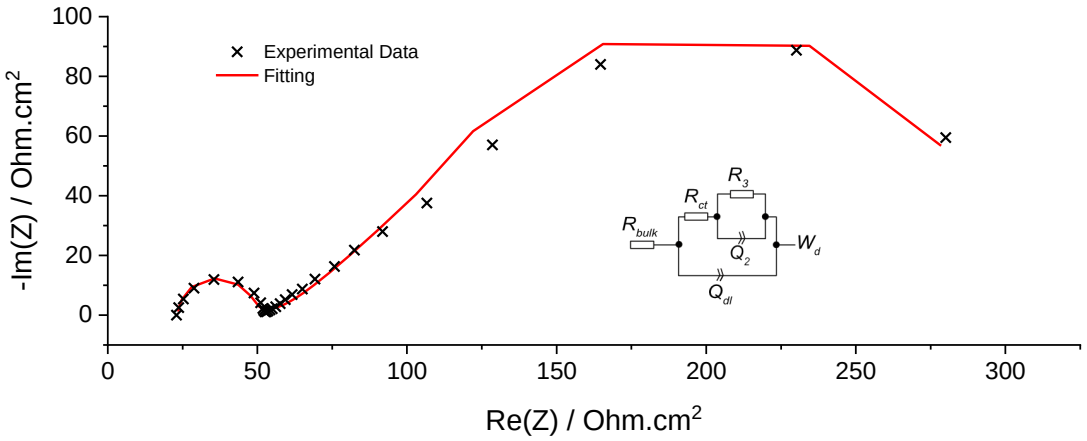


Figure 4.14: VLF-EIS Nyquist plot, with equivalent circuit, for calculation of t_{Li^+}, noting the large W_d and small R_{ct}.

Thermodynamic Factor To my knowledge, no room-temperature Li-ion ILE's χ_M has been measured, but the activity of various $LiNO_3$-$AgNO_3$ melt compositions has been measured by Richter, as described in the Introduction, to compare. χ_M was calculated:

$$\chi_M = 1 + \frac{\ln f_{\pm}}{\ln c} = \frac{F}{2RT(1-t_{Li+})} \frac{d\eta_c}{d\ln \frac{c_{Li^+,z=L}}{c_{Li^+,z=0}}} \tag{4.13}$$

Using the PEIS data prior to each line scan, η_c was calculated like the previous chapter via the chronopotentiometry and PEIS data. By measuring c_{Li^+} at the extremes of the cell and using t_{Li^+} from the previous Hittorf calculation, χ_M was isolated from the weighted gradient in Figure 4.15. χ_M was measured as 0.91 $\pm$ 0.06, which is reasonable if one were to compare against Richter's findings.

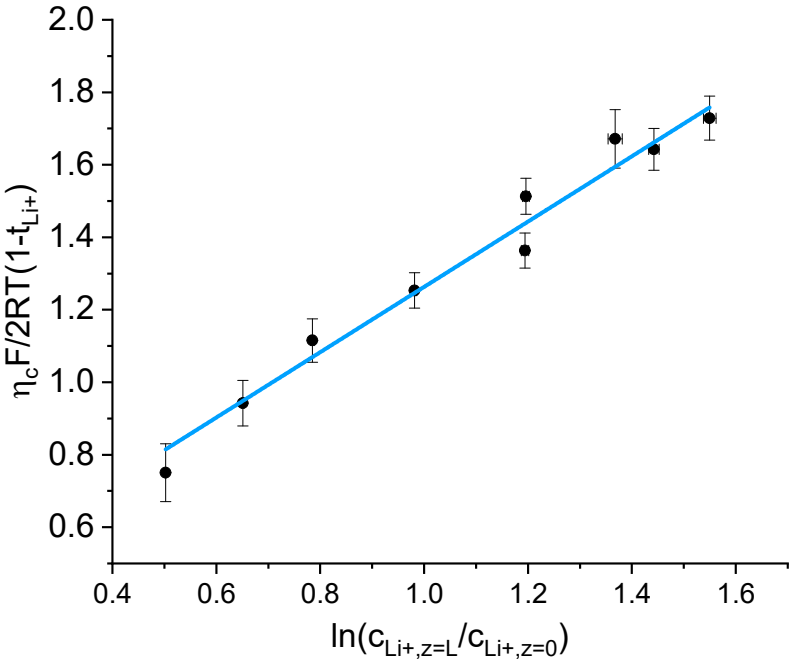


Figure 4.15: Plotting equation 4.12, illustrating how the η_c function changes linearly with respect to the natural log of concentration ratio of each cell extreme. χ_M was calculated as 0.91 $\pm$ 0.06.

Ionic Conductivity and Resistance of Charge-Transfer. From PEIS prior to current being passed κ and R_{ct} were measured (Figure 4.16). κ was calculated as 3.52 $\pm$ 0.01 mS cm^{-1}, which agreed well with previous literature values. Using the pfg-NMR data the Haven ratio was calculated as 0.520, showing a significant amount of ion-ion correlation. R_{ct} was calculated as 44 $\pm$ 4 $\Omega\cdot$ cm^2, and assumed to be a combination of classical charge-transfer and SEI resistance. ILEs containing FSI$^-$ in particular have shown to have fast charge-transfer kinetics illustrated by the low R_{ct} value.[34, 35]

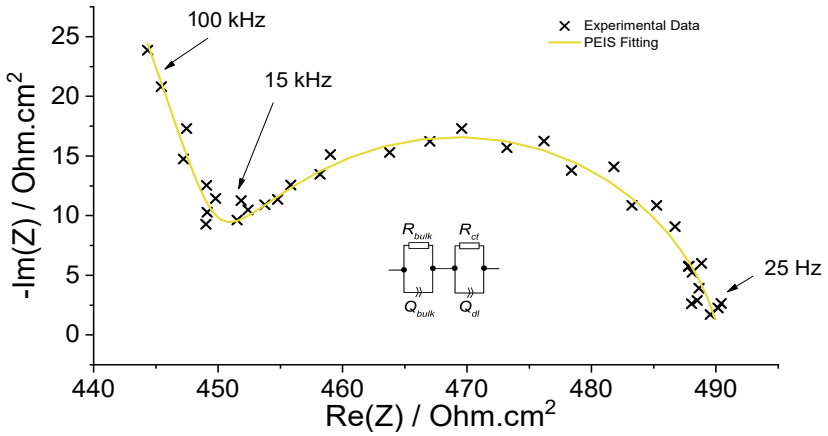


Figure 4.16: PEIS of electrolyte prior to application of current, indicating a low R_{ct}

4.3.4 Dependence on Concentration

To understand transport changes with a varying amount of Li^+ present, operando Raman experiments were performed on two additional ILE concentrations, namely 0.5 m and 2 m. Like the measurements performed with the 1 m electrolyte, 100 μA cm^{-2} was applied. With 0.5 m, a 50 μA cm^{-2} measurement was also performed because at the higher current c_{Li+} dropped very quickly at the plating side.

Figure 4.17 shows how electrolyte transport and thermodynamic properties were affected by concentration. D_{app}, t_{Li+} and $dc/dz_{z=0,L}$ were taken from the inverse-variance weighted average of the stripping and plating side. Most strikingly, 0.5 m ILE showed many similar transport and thermodynamic values to 1 m. For instance, 0.5 m showed $dc/dz_{z=0,L}$ equal to $\sim 5.5 \times 10^6$ mol m^{-4} like 1 m. t_{Li^+} for both these concentrations is very low, although due to the error involved it is not possible to report whether the values are negative or positive. Values of χ_M were lower than 1 for both 0.5 m and 1 m, indicating their activity was lower than their concentration due to a high amount of association, and a surplus of neat IL that surrounds it.

For 2 m, there was a noticeable change in many of the transport and thermodynamic properties. For example, there was a marginal increase in $dc/dz_{z=0,L}$ from $\sim$5.5 to $\sim$ mol m^{-4}, due to changes in D_{app}. There was a drop in D_{app} vs. 1 m and 0.5 m. Most certainly there was an increase in t_{Li^+}, which indicated a structural

Table 4.3: pfg-NMR diffusivities and transference in 0.5 m, 1 m and 2 m at 25 ^{o}C

$\mathbf{c}_{Li^+}$ / M	$\mathbf{c}_{FSI^-}$ / M	$\mathbf{c}_{Pyr^+}$ / M	$\mathbf{D}_{Li+}$ x 10^{-11} m^2s^{-1}	$\mathbf{D}_{FSI-}$ x 10^{-11} m^2s^{-1}	$\mathbf{D}_{Pyr+}$ x 10^{-11} m^2s^{-1}	$\mathbf{D}_{app}$ x 10^{-11} m^2s^{-1}	$\mathbf{t}_{Li+}$
0.62	4.38	4.08	2.04	2.79	2.47	2.58	0.053
1.19	5.06	3.87	1.42	1.88	1.76	1.77	0.094
2.14	5.63	3.46	0.81	0.97	0.92	0.92	0.169

Table 4.4: Transference number measured via PEIS for 0.5 m, 1 m and 2 m at 25 ^{o}C.

$\mathbf{c}_{Li^+}$ / m	t_{Li+}
0.5	0.063
1	0.086
2	0.182

change; perhaps correlated to the broadening of the 1200-1240 cm^{-1} peak. An increase χ_M at high concentrations is common amongst electrolyte solutions and is noticeable here too. Furthermore, results from Richter showed similar behaviour. It was speculated that as more LiFSI was added there were fewer free FSI^- to stabilise Li^+ via extended $[Li(FSI)_2]^-$ structures; χ_M then began to rise.

D_{app} and t_{Li+} values collected via pfg-NMR are presented in Table 4.3. The D_{app} values compared well to D_{app} measured via operando Raman. Although the trend was the same for t_{Li+} in both experimental methods, it appeared the values obtained via operando Raman were lower that those via pfg-NMR. This could be because pfg-NMR measures self-diffusivities on a short time-scale, whereas the operando Raman measurements were seeing falling aggregates over a longer time-scale, decreasing t_{Li+}.

The reported data suggested there was a transport mechanism change moving from 1 m to 2 m. Between these concentrations it's speculated there was a structural change too, illustrated by the Raman data. Perhaps as $[Li(FSI)_2]^-$ $>$ $(FSI)^-$, ordered networks form, increasing t_{Li^+}.

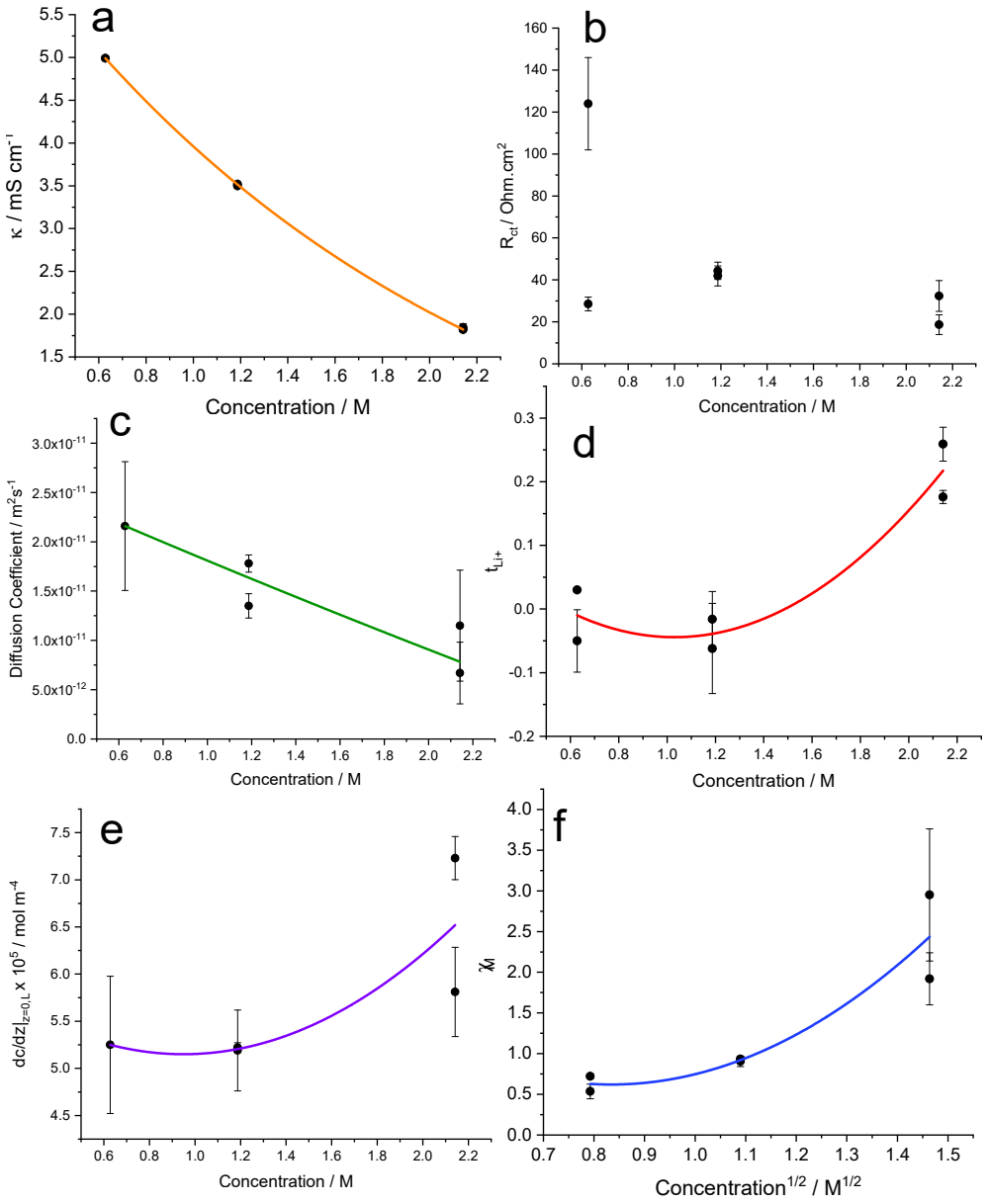


Figure 4.17: Electrolyte Properties of Varying Concentrations of LiFSI in $Pyr_{1,3}$FSI: a) Ionic conductivity (κ), fitted by exponential decay. b) Resistance of charge transfer (R_{ct}) showing a marginal increase at 1 m, then a decrease again at 2 m. c) Fickian diffusion coefficient (D_{app}), show a change moving from 1 m to 2 m d) Transference number of lithium (t_{Li^+}), initially very low but showing a marked increase from 1 m to 2 m. e) $(dc/dz)_{z=0}$ at 100 μA cm^{-2}, which was initially constant but showed an increasing moving to 2 m. f) χ_M showing values below 1 for concentrations below 1 m, but increased to $\sim$ 2.5 at 2 m. Values below 1 indicate increased association between Li^+ and FSI^- and values above 1 indicate the decreasing amount of free FSI^- present and so an increase in "effective concentration" of Li^+.

4.3.5 Plating at Low Concentrations

Conventionally if c_{Li+} drops to zero at the electrode, the voltage increases substantially due to the lack of reactants at the interface. In the setup with LiFSI in

G4 this was true, as seen in Figure 4.19a and b. However, using 0.5 m of the ILE at 100 μA cm^{-2} the concentration would seemingly not drop to zero. Evidence of this was in the voltage, which plateaued with small "spikes" throughout (Figure 4.18b stage 2), where in binary organic electrolytes it would usually fully-"spike" until the cell failed (Figure 4.19b). When analysing the concentration profile, the concentration was not dropping to zero as the voltage profile predicted. Instead it would plateau at ∼0.1 M, and extend into the cell.

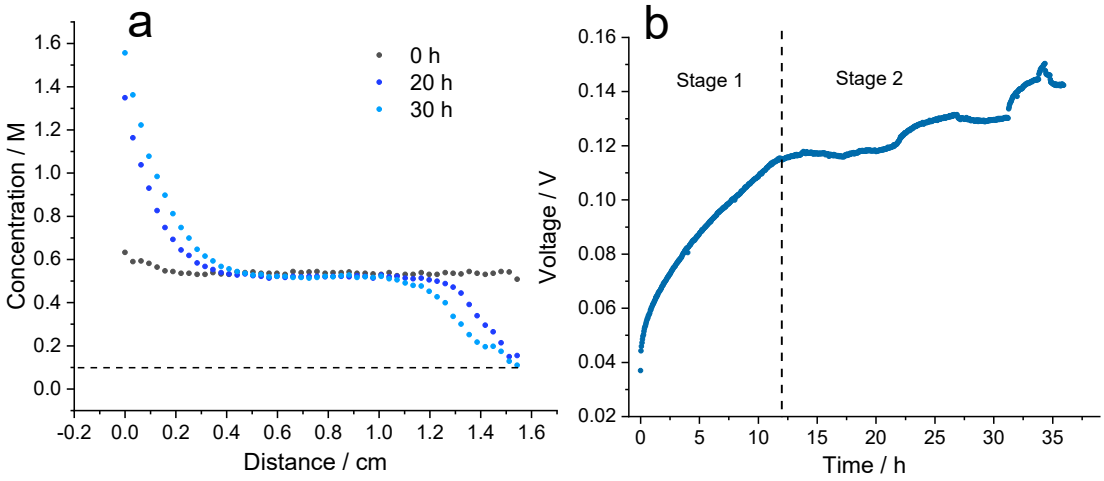


Figure 4.18: Behaviour of plating for 0.5 m LiFSI in Pyr$_{1,3}$FSI a) Concentration gradients of the bulk 0.5 m electrolyte, showing a drop in concentration at the plating side to only ∼0.1 M. b) Voltage vs. time curve of the 0.5 m electrolyte symmetric cell, with stage 1 showing behaviour prior to plating dropping to ∼0.1 M, and stage 2 showing instability after as Li^+ concentration remained constant, not dropping to zero.

To test this further the current density was increased to 500 μA cm^{-2}. At a 5-fold higher current, c_{Li+} did indeed drop to zero as is illustrated by the voltage curve (Figure 4.19d). The concentration profile was especially odd, with the zero-concentration extending into the centre of the cell before the voltage spiked. Again this behaviour was not seen in the binary electrolyte case. 0.25 m ILE was also tested, at a lower current of 50 μA cm^{-2}. This behaved similarly to the 0.5 m ILE at 100 μA cm^{-2} in that it also did not "spike".

These tests indicated competing steps in the reduction of Li^+: namely, diffusion, desolvation (dissociation), and reduction at the lithium interface. In an ion-hopping mechanism of diffusion, like in ILEs, Li^+ moves via dissociation then

subsequent association usually through an anionic matrix. For the voltage to spike, the rate of Li^+ reduction has to be higher than the diffusion step (mass-transport limited). From χ_M values and Raman data at low concentrations, association of Li^+ to $[Li(FSI_2)]^-$ is thermodynamically favourable. When Li^+ is depleted to zero at the interface, the equilibrium could move significantly to accommodate the loss of Li^+, which might be the reason for c_{Li+} not dropping so readily to zero. In other words, the rate of dissociation to association is faster than the rate of Li^+ reduction at low Li^+ ILE concentrations. Indeed, this could have far-reaching consequences for electrolytes that exhibit an ion-hopping mechanism of transport as opposed to a vehicular mechanism. It is likely to be unique to ILEs at low concentrations however, with conventional electrolytes at low concentrations displaying a vehicular transport mechanism. This could have favourable repercussions when using ILEs for lithium metal plating, encouraging uniform plating.

More studies are required to test this theory fully, including modelling work.

4.4 Conclusions & Future Work

The full characterisation of transport and thermodynamic properties of a popular ionic liquid electrolyte, LiFSI in $Pyr_{1,3}FSI$, has been presented for the first time. Additionally by utilising concentration gradient visualisation the unique bulk structure was speculated, which led to an asymmetry of the respective gradient.

Also from Raman calibration measurements a change in bulk molecular structure was observed, moving from 1 m to 2 m, which was reflected in the isolated transport properties. This was seen especially in t_{Li+}, which showed a notable increase as the concentration moved from 1 m to 2 m, which was speculated to be due to the formation of a homogeneous ordered structure that slows the movement of FSI^-, increasing the proportional current carried by Li^+ . The $dc/dz_{z=0,L}$ values at all concentrations were large compared to an organic-based electrolyte illustrated in the previous chapter, showing a $\sim$5-fold increase. This confirmed the speculated problem when using ILEs: large

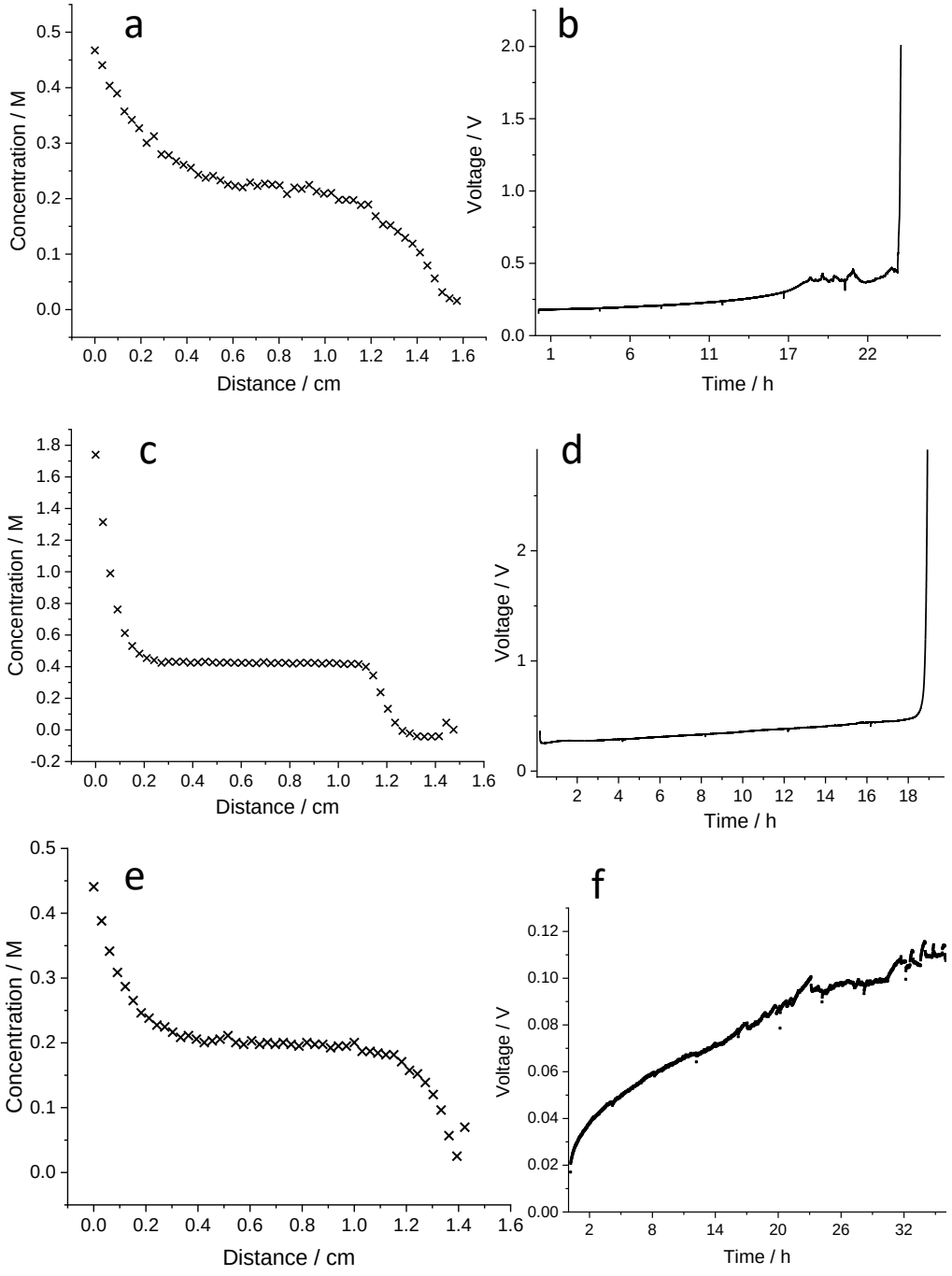


Figure 4.19: Examples of plating behaviour as Li^+ concentration drops to zero in ILE and binary electrolytes. a)c)e) Concentration profiles and b)d)f) Voltage profiles of a)b) 0.25 m LiFSI in G4 at 100 μA cm^{-2} at 20 hours c)d) 0.5 m LiFSI in $Pyr_{1,3}FSI$ at 500 μA cm^{-2} at 8 hours e)f) 0.25 m LiFSI in $Pyr_{1,3}FSI$ at 50 μA cm^{-2} at 28 hours.

concentration gradient formation. Similar to the previous findings, to reduce the gradient formation one should primarily target increasing D_{app}, perhaps by

lowering the viscosity. Indeed, this has been a popular topic of research, with some groups blending ILEs with less viscous organic solvents to increase κ. Less frequently reported is the benefit ILE-organic blends will have on the reduction in the steepness of concentration gradients. Of course, this may reduce the benefits that ILEs bring, namely the electrochemical and thermal stability, and desirable SEI composition.

In summary, by combining spectroscopic and electrochemical techniques with concentration visualisation particularly valuable findings were presented, not yet reported in the ILE literature. With ILEs' main weakness being their transport properties, understanding fully the origin of this is paramount for their continuing development.

4.5 Experimental Detail

Electrolyte Description. Lithium bis(fluorosulfonyl)imide (LiFSI) (Battery Grade – 99%) was purchased from Fluorochem Ltd. N-Propyl-N-methylpyrrolidinium bis(fluorosulfonyl)imide ($Pyr_{1,3}FSI$) (99.9%) was purchased from Solvionic. Handling of LiFSI and $Pyr_{1,3}FSI$ was always performed in an argon-filled glovebox (MBraun) with low H_2O content ($<$1 ppm) and low O_2 content ($<$ 1ppm).LiFSI was dried further under high vacuum at 70 ^oC for 48 hours. $Pyr_{1,3}FSI$ was dried under high vacuum at 70 ^oC for 24 hours, with a stirrer bar. The H_2O content of the electrolyte solutions was determined by Karl Fischer titration, also performed in an argon-filled glovebox, and recorded to be below 15 ppm of H_2O.

Calibration, Cell Construction, Line Scan and PEIS. Using a Renishaw inVia Reflex laser confocal Raman microscope equipped with a near-IR 785 nm laser, the same setting parameters, cell construction, PEIS settings were used in this study as the previous chapter.

pfg-NMR. All pulsed field gradient (PFG) nuclear magnetic resonance (NMR) measurements were completed at 9.45 T ($_0(^1H)$ = 400.20, $_0(^{19}F)$ = 376.58, and $_0(^7Li)$ = 155.53 MHz) on Bruker Avance III HD spectrometer using a 5 mm single-axis diffusion probe with exchangeable ^1H, ^{19}F and ^7Li ceramic heads.

A stimulated echo pulse sequence was utilized with an effective gradient pulse duration () of between 1-2 ms, a diffusion time () of 43-46 ms, with the gradient amplitude varied between 0.1 and 5 T/m. All samples were sealed in a J-Young valve NMR tube, temperature stabilized at 298.1 K, and a 5 second recycle delay was used throughout.

PEIS. For t_{Li+} measurements, the frequency was scanned from 100 kHz to 25 μHz at a 10 mV V_a, 3 points per decade with an average of 1 point. Measurements were taken using a Biologic VMP3 potentiostat, using the custom-built cell described above in section 3.3.7, in an oven at 20 ^{o}C. The data was fitted using Biologic EC-lab V11.26 software, with the equivalent illustrated in Figure 4.14.

Error Estimation. Error estimations were the same as Chapter 4, apart from specific cases. Due to the asymmetry the inverse-variance weighted average of $dc/dz_{z=0}$ and $dc/dz_{z=L}$ was calculated using:

$$\bar{x}_{wtd} = \frac{\sum_{i=0}^{n} w_i x_i}{\sum_{i=0}^{n} w_i} \tag{4.14}$$

Where $\bar{x}_{wtd}$ is the weighted average of x_i and weight, w_i:

$$w_i = \frac{1}{\sigma_i^2} \tag{4.15}$$

The standard deviation of the weight-average ($(\sigma_{\bar{x}})_{wtd}$) begins with the weighted variance ($Var(s)_{wtd}$):

$$Var(s)_{wtd} = (\sigma_x^2)_{wtd} = \frac{\sum_{i=0}^{n} w_i (x_i - \bar{x}_{wtd})^2}{\sum_{i=0}^{n} w_i} \tag{4.16}$$

Then:

$$(\sigma_{\bar{x}})_{wtd} = \sqrt{\frac{(\sigma_x^2)_{wtd}}{n}} \tag{4.17}$$

t_{Li+} through the Hittorf method and D_{app} were also averaged using a weighting of inverse-variance.

4.6 References

1. Yoon, H. *et al.* Fast Charge/Discharge of Li Metal Batteries Using an Ionic Liquid Electrolyte. *J. Electrochem. Soc.* **160,** A1629–A1637 (2013).
2. Li, W. *et al.* High-voltage positive electrode materials for lithium-ion batteries. *Chem. Soc. Rev.* **46,** 3006–3059 (2017).
3. Wu, F. *et al.* Conversion cathodes for rechargeable lithium and lithium-ion batteries. *Energy Environ. Sci.* **10,** 435–459 (2017).
4. Li, M. *et al.* New Concepts in Electrolytes. *Chem. Rev.* **120,** 6783–6819 (2020).
5. Lee, H. J. *et al.* Ordered LiNi0.5Mn1.5O4 Cathode in Bis(fluorosulfonyl)imide-Based Ionic Liquid Electrolyte: Importance of the Cathode-Electrolyte Interphase. *Chem. Mater.* **33,** 1238–1248 (2021).
6. Xiao, A. W. *et al.* Understanding the conversion mechanism and performance of monodisperse FeF2 nanocrystal cathodes. *Nat. Mater.* **19,** 644–654 (2020).
7. Basile, A. *et al.* Stabilizing lithium metal using ionic liquids for long-lived batteries. *Nat. Commun.* **7,** 11794 (2016).
8. Watanabe, M. *et al.* Application of Ionic Liquids to Energy Storage and Conversion Materials and Devices. *Chem. Rev.* **117,** 7190–7239 (2017).
9. Macfarlane, D. R. *et al.* Energy applications of ionic liquids. *Energy Environ. Sci.* **7,** 232–250 (2014).
10. Zheng, J. *et al.* Regulating electrodeposition morphology of lithium: towards commercially relevant secondary Li metal batteries. *Chem. Soc. Rev.* **49,** 2701–2750 (2020).
11. Liu, K. *et al.* Ionic liquids for high performance lithium metal batteries. *J. Energy Chem.* **59,** 320–333 (2021).
12. Gouverneur, M. *et al.* Negative effective Li transference numbers in Li salt/ionic liquid mixtures: does Li drift in the “Wrong” direction? *Phys. Chem. Chem. Phys.* **20,** 7470–7478 (2018).
13. Schönhoff, M. *et al.* Reply to the ’Comment on "negative effective Li transference numbers in Li salt/ionic liquid mixtures: Does Li drift in the "wrong" direction?"’ by M. Gouverneur, F. Schmidt and M. Schönhoff,: Phys. Chem. Chem. Phys., 2018, 20, 7470. *Phys. Chem. Chem. Phys.* **20,** 30041–30045 (2018).
14. Wohde, F. *et al.* Li ⁺ Transference Numbers in Liquid Electrolytes Obtained by Very-Low-Frequency Impedance Spectroscopy at Variable Electrode Distances. *J. Electrochem. Soc.* **163,** A714–A721 (2016).
15. Ravn Sørensen, P. *et al.* Conductivity, charge transfer and transport number-an ac-investigation of the polymer electrolyte LiSCN-poly(ethyleneoxide). *Electrochim. Acta* **27,** 1671–1675 (1982).
16. Fujii, K. *et al.* Liquid structure and conformation of a low-viscosity ionic liquid, N-methyl-N-propyl-pyrrolidinium bis(fluorosulfonyl) imide studied by high-energy X-ray scattering. *J. Mol. Liq.* **143,** 64–69 (2008).

17. Umebayashi, Y. *et al.* Liquid structure of and Li+ ion solvation in bis(trifluoromethanesulfonyl)amide based ionic liquids composed of 1-ethyl-3-methylimidazolium and N -methyl- N -propylpyrrolidinium cations. *J. Phys. Chem. B* **115,** 12179–12191 (2011).
18. Fujii, K. *et al.* Unusual Li ⁺ Ion Solvation Structure in Bis(fluorosulfonyl)amide Based Ionic Liquid. *J. Phys. Chem. C* **117,** 19314–19324 (2013).
19. Liu, J. *et al.* Solute-volume effects in electrolyte transport. *Electrochim. Acta* **135,** 447–460 (2014).
20. Nyman, A. *et al.* Electrochemical characterisation and modelling of the mass transport phenomena in LiPF₆ -EC-EMC electrolyte. *Electrochim. Acta* **53,** 6356–6365 (2008).
21. Aguilera, L. *et al.* The effect of lithium salt doping on the nanostructure of ionic liquids. *Phys. Chem. Chem. Phys.* **17,** 27082–27087 (2015).
22. Judeinstein, P. *et al.* Interplay of structure and dynamics in Lithium/Ionic liquid electrolytes: Experiment and molecular simulation. *J. Phys. Chem. B* **125,** 1618–1631 (2021).
23. McEldrew, M. *et al.* Theory of ion aggregation and gelation in super-concentrated electrolytes. *J. Chem. Phys.* **152,** 1–19. arXiv: 2002.11825 (2020).
24. Russina, O. *et al.* Mesoscopic structural organization in triphilic room temperature ionic liquids. *Faraday Discuss.* **167,** 499–513 (2013).
25. Pontoni, D. *et al.* Self-segregated nanostructure in room temperature ionic liquids. *Soft Matter* **13,** 6947–6955 (2017).
26. Hayes, R. *et al.* Structure and Nanostructure in Ionic Liquids. *Chem. Rev.* **115,** 6357–6426 (2015).
27. Lamb, H. *Hydrodynamics* 4th (Cambridge University Press, 1916).
28. Fawdon, J. *et al.* Characterising lithium-ion electrolytes via operando Raman microspectroscopy. *Nat. Commun.,* 13–15 (2021).
29. Richter, J. *et al.* On the Migration of Ions in Alkali Nitrate-Silver Nitrate Melts. *Zeitschrift fur Naturforsch. - Sect. A J. Phys. Sci.* **27,** 280–287 (1972).
30. Richter, J. *et al.* Transport numbers and ionic mobilities in nitrate melts by EMF-measurements on concentration cells with transference. *Electrochim. Acta* **23,** 1165–1172 (1978).
31. Hussey, C. L. *et al.* Aluminum Bromide-1-Methyl-3-Ethylimidazolium Bromide Ionic Liquids: *J. Electrochem. Soc.* **134,** 1977 (1987).
32. Ratkje, S. K. *et al.* Transference coefficients and transference numbers in salt mixtures relevant for the aluminium electrolysis. *Electrochim. Acta* **38,** 415–423 (1993).
33. Haase, R. Internal and External Transport Numbers in Ionic Melts. *Zeitschrift fur Phys. Chemie* **87,** 77–87 (1991).
34. Matsumoto, H. *et al.* Fast cycling of Li/LiCoO2 cell with low-viscosity ionic liquids based on bis(fluorosulfonyl)imide [FSI]-. *J. Power Sources* **160,** 1308–1313 (2006).

35. Bayley, P. M. *et al.* Transport properties and phase behaviour in binary and ternary ionic liquid electrolyte systems of interest in lithium batteries. *ChemPhysChem* **12,** 823–827 (2011).

5 Effect of Electrolyte Transport and Thermodynamics on Lithium Metal Plating Morphology

Contents

5.1 Abstract 143
5.2 Introduction 143
5.3 Results & Discussion 145
5.3.1 Rate of Roughening 145
5.3.2 Interfacial Concentration Gradients 146
5.3.3 SEI Transport 147
5.4 Conclusions & Future Work 161
5.5 Experimental Detail 162
5.6 References 163

5.1 Abstract

For secondary lithium metal batteries to be commercially realised, a solution to their poor coulombic efficiency, stemming from a non-uniform plating morphology, has to be achieved. By using transport and thermodynamic property data of the electrolytes LiFSI in G4 and LiFSI in $Pyr_{1,3}FSI$, plus an understanding of SEI chemistry gathered via X-ray photoelectron spectroscopy (XPS) and PEIS, a correlation between electrolyte and filament nucleation tendency was observed. An SEI that was both thicker and had a higher LiF content led to an increased likelihood of high-surface area Li growth.

5.2 Introduction

It is well understood that electrolytes play a significant role in the plating morphology of lithium in LMBs. However, there is no universal theory as to how electrolytes shape filament growth. This section looks to contribute toward the catalogue of literature that correlates electrolyte composition and transport with non-uniform plating morphology.[1]

As explained in the Introduction, there are two distinct morphologies that are recognised in the current literature: diffusion-limited fractal dendrites and reaction-limited moss-like filaments.[2] Moss-like growth has primarily been attributed to SEI formation and the continuous (electro)chemical reaction with lithium metal. Although less of a safety hazard than needle-like diffusion-limited growth, moss-like growth leads to poor CE in LMBs; a major hurdle in the commercialisation of LMBs. [3]

Formulating a comprehensive theory on how the SEI influences non-uniform plating nucleation is difficult due to the complexity of its composition and structure. Its heterogeneous nature leads to a complex grain structure with differing transport, physical and mechanical properties that facilitate differing Li^+ mobility.[4] Nonetheless, it is the electrolyte composition and chemistry that ultimately determines the microstructure, highlighting the importance of electrolyte choice for stable deposition. Most studies report electrolyte mixtures that improve plating morphology, without concocting convincing theories as to *why* the electrolyte leads to favourable plating.[5] Some general conclusions include carbonate-based electrolytes perform poorly because the resulting polymer outer-layer is mechanically weak; high concentrations of fluoride salt lead to more lithium fluoride (LiF) in the inner layer, which is seen as favourable due to its high mechanical strength and low electronic conductivity; and ether-based electrolytes are chemically stable against lithium, leading to a thin SEI for fast transport.[3]

Furthermore, the distinction between nucleation and propagation behaviour of dendritic structures is rarely discussed. Most studies measure growth at current densities well above the nucleation point of non-uniform growth. Therefore, researchers are often only investigating the propagation morphology of these structures.[6, 7] Here, I will look to correlate electrolyte composition with SEI formation and why this leads to variation in the initiation of non-uniform growth.

As has been repeatedly stated in this thesis, very few studies fully characterise electrolytes by understanding their transport, thermodynamics and molecular structure. Those that do, do not link these properties to LMB performance. Here,

by using data from the previous sections plus additional surface characterisation using X-ray photoelectron spectroscopy (XPS), conclusions and trends are determined on how electrolyte properties may be affecting the plating morphology.

Specifically the chapter will cover:

- A presentation of which **electrolyte compositions lead to poor plating morphology**, using an understanding of their roughening rate.
- An understanding of whether **transport properties are influencing the nucleation** of dendritic structures.
- Use of **PEIS and XPS techniques to understand the composition and thickness** of the SEI.
- A discussion on whether **SEI composition and thickness influences the nucleation** of non-uniform growth.

All the work in this chapter was performed by myself, under the supervision of Prof. Mauro Pasta, unless otherwise stated. I performed all the sample preparation, experiments and analysis, apart from XPS measurements, which were conducted by Dr. Sudarshan Narayanan.

5.3 Results & Discussion

5.3.1 Rate of Roughening

An indirect but sensitive method for detecting non-uniform growth and surface roughening is utilising PEIS, specifically monitoring the R_{ct} as current is applied. R_{ct} is highly sensitive to changes in electrode surface area, so can measure when non-uniform growth initiates (surface roughening) and propagates. As is noted in Method Fundamentals, the impedance is proportional to current (I) after a constant voltage (V) is applied. The amount of I passed is a function of the surface area. As the surface area increases, R_{ct} decreases proportionally, due to an increase in I. Indeed, R_{ct} can also change due to SEI compositional changes so variation in R_{ct} cannot be purely attributed to surface-area changes. So one still requires to be wary when using R_{ct} measurements to analyse changes in

electrode surface area. A related method is monitoring the overpotential,[8] η, to determine if there is a drop to show an increase in surface area. This is less reliable as it measures the total overpotential including the concentration overpotential, which will rise with an increasing concentration gradient. The power of PEIS is de-coupling the various processes involved in the cell, as is described in Method Fundamentals.

The previous sections noted that mossy lithium growth occurred in the LiFSI in G4 electrolyte at 200 μA cm^{-2} and in the LiFSI in Pyr$_{1,3}$FSI electrolyte at 100 μA cm^{-2}. Not mentioned in prior sections, but relevant here, is that mossy lithium grew in highly concentrated 3 m LiFSI in G4 at 100 μA cm^{-2}. Therefore, one should ask why mossy growth initiated at lower current densities in highly concentrated electrolytes, including ILEs, but not lower concentrated G4 electrolytes?

First, a plot of R_{ct} versus $time^{1/2}$, using 3 m LiFSI in G4 at 100 μA cm^{-2}, showed a linear decrease, as shown in Figure 5.1a. A recent collaboration with Wang et al. also showed a linear dependence of i_0 versus $time^{1/2}$, using a $LiPF_6$ in EMC electrolyte.[9] Both of these findings suggest a square-root time dependency in surface area change, signifying that mossy Li growth was diffusion-controlled. But as mentioned earlier, growth occurred prior to [Li$^+$] = 0 (Sands' Time) at the interface, so the growth was not a result of diffusional behaviour in the electrolyte bulk. After a certain length of time, R_{ct} stabilised, which was potentially due to the growth of new SEI balancing the surface area growth. This occurred more quickly in both the ILE at 100 μA cm^{-2} and 1 m LiFSI in G4 at 200 μA cm^{-2}, but it was less clear whether these were also diffusion-limited, as shown in Figure 5.1b and c, respectively.

5.3.2 Interfacial Concentration Gradients

Very few researchers report $dc/dz|_{z=0,L}$, so there is no theory as to how it may affect the plating morphology of mossy lithium. To the best of my knowledge, there has only been one study that suggested its potential influence on filament growth.

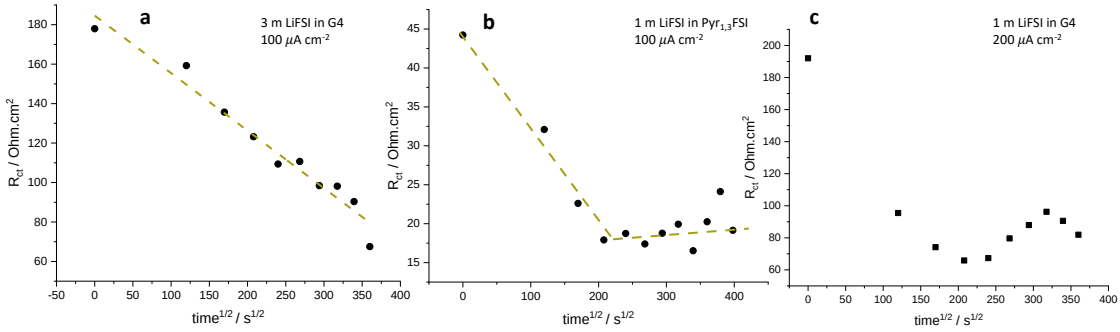


Figure 5.1: Change in R_{ct} with time$^{1/2}$: a) 3 m LiFSI in G4 at 100 μA cm^{-2} b) 1 m LiFSI in Pyr$1,3$FSI at 100 μA cm^{-2} c) 1 m LiFSI in G4 at 200 μA cm^{-2}

Frenck et al. detected a direct correlation between $dc/dz|_{z=0,L}$ and protrusion growth in their LiTFSI in block co-polymer, PS-b-PEO.[10] After measuring each fundamental electrolyte property individually, they simulated the concentration gradient through their electrolyte to isolate $dc/dz|_{z=0,L}$ values. The higher concentrations showed higher $dc/dz|_{z=0,L}$ values. Figure 5.2 shows $dc/dz|_{z=0,L}$ for each of the electrolytes measured from chapter 3 and 4, in one plot. Indeed, like Frenck, these results show increasing $dc/dz|_{z=0,L}$ led to a greater tendency for mossy Li growth. While this correlation supports the conclusions of Frenck, the variability in the onset of mossy growth with $dc/dz|_{z=0,L}$ suggests there are other factors which are also affecting non-uniform growth. For example, 1 m LiFSI in G4 at 200 μA cm^{-2} and 2 m LiFSI in G4 at 100 μA cm^{-2} had very similar $dc/dz|_{z=0,L}$ values, but the former showed non-uniform growth and the latter did not. That being said, all samples that exhibited gradients above 3×10^5 mol m$^{-}4$ did lead to non-uniform growth. So, although there were other factors affecting growth, further investigation is required to test whether there is a gradient magnitude at which these other factors begin to dominate.

5.3.3 SEI Transport

Another theory, provided by Maraschcky et al., posits that Li mossy growth occurs when c_{Li+} drops to zero, as in Sands' Time, but at the Li-SEI interface, not in the bulk.[11] Lithium will form a passivating layer if in contact with the electrolyte (corrosion),[12] forming an SEI prior to any current being passed, therefore

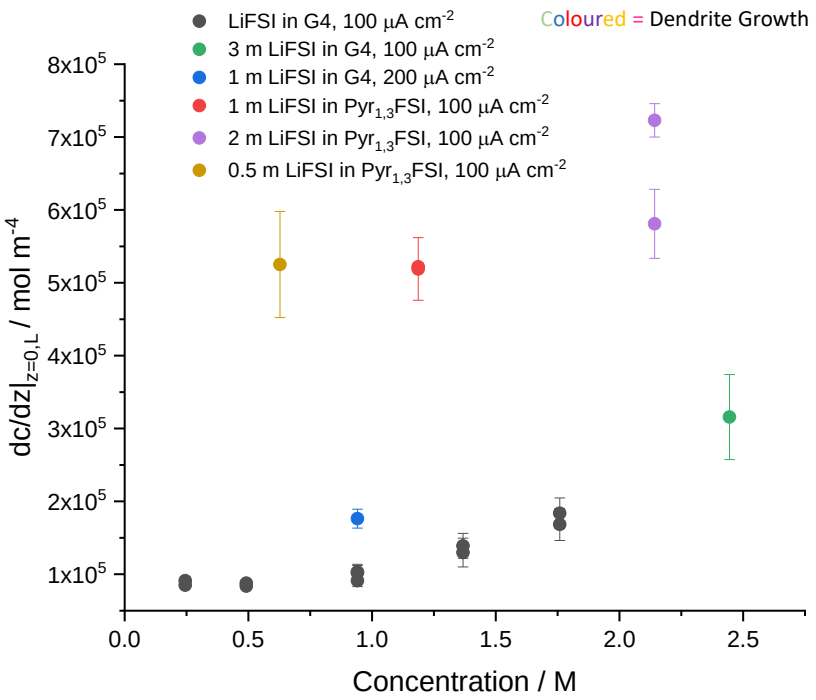


Figure 5.2: Interfacial concentration gradient of all concentrations studied in the thesis, comparing those that plated uniformly and those that did not.

influencing the nucleation of non-uniform plating. Marashcky speculated about the SEI thickness and composition based on common assumptions from the literature. Due to SEI layers often only being several nanometres thick, it was impossible to detect a gradient in the SEI using the operando Raman technique described in the previous chapters. This work furthers Marashcky's theory by measuring SEI thickness and composition via XPS and PEIS.

To understand if Maraschsky's claim is true, further information was required about the extent of the gradient through the SEI. As Maraschky stated:[11]

$$C_e = C_0 - \frac{IL}{nFD_{SEI}} \tag{5.1}$$

Where C_e is the concentration at the Li-SEI interface, C_0 is the concentration at the SEI-electrolyte interface, I is the current density, L is the SEI thickness and D_{SEI} is the average diffusion coefficient through the SEI. Both L and D_{SEI} were required to test this theory; neither were trivial to isolate.

PEIS. For a qualitative understanding of how diffusion through the SEI was affected by increasing concentration of LiFSI in G4, one can take a closer look at

R_{ct}. A plot of R_{ct} with concentrations up to 3 m is shown in Figure 5.3.

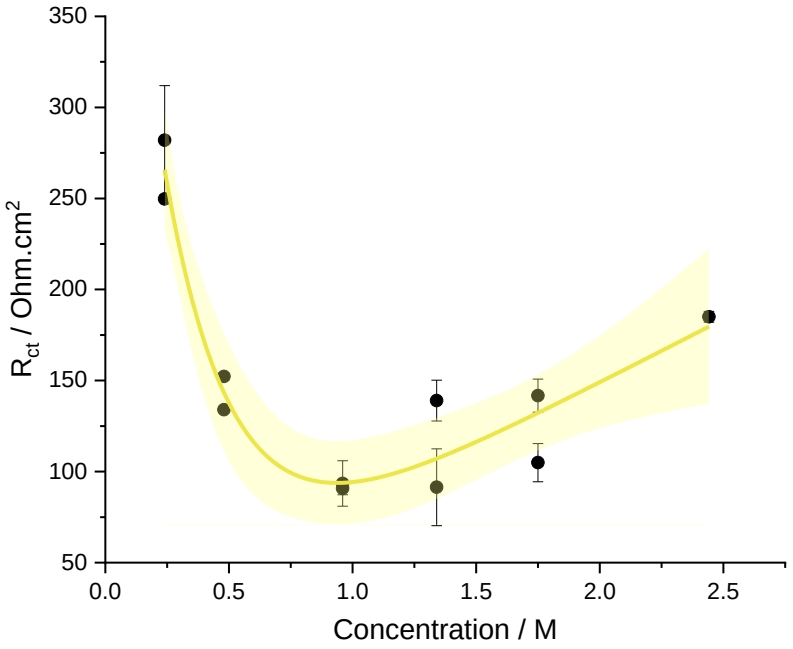


Figure 5.3: R_{ct} of LiFSI in G4 at various concentrations, showing an decrease, then an increase at higher concentrations.

As noted above, there were three summing effects on R_{ct}, firstly the resistance of the SEI layer, which depends on the layer's composition, secondly the resistance of (de)solvation, and finally the kinetics directly at the interface. The solvation energy in LiFSI in G4 is high compared to smaller glymes, and so is a primary component of R_{ct}. Interfacial kinetics is described by the Butler-Volmer equation as illustrated by equation B.4, and shown to be dependent on the exchange current density, which in turn is influenced by the concentration (or specifically, the activity) of the electrolyte. The higher the concentration of the salt, the faster the kinetics, and therefore the lower the resistance of electron-transfer. This is why R_{ct} decreased from 0.25 m to 1 m. However, with increasing concentration R_{ct} began to increase, as was confirmed by the inclusion of 3 m. This suggested a thicker SEI or lower D_{SEI} (so a change in SEI composition) was present, as this effect began to dominate. XPS data will confirm this in subsequent sections. As seen in Figure 4.17b, R_{ct} of the ILE was much lower than that of the LiFSI in G4 solutions. However, this was likely due to stronger Li^+

solvation in G4 versus the ILE. FSI-based ILEs are known for their fast interfacial kinetics, and therefore low R_{ct} values.

PEIS can also be used to estimate the thickness of the SEI; again this is only an estimate due to the problem of deconvoluting the charge-transfer semi-circle. By isolating the capacitance from fitting the Nyquist plot, one can detect trends in SEI thickness from Equation 5.2 below [13]:

$$C = K\varepsilon_0 \frac{A}{l} \tag{5.2}$$

Where C is the capacitance of the SEI, ε_0 is the dielectric constant in vacuum, K is the dielectric constant for compositional components of SEI, A is the electrode area, and l is the SEI thickness. From the Nyquist plot fittings, C was calculated [13]:

$$C = R_{SEI}^{(1-\alpha)/\alpha} Y^{1/\alpha} \tag{5.3}$$

Where Y is the pseudocapacitance and α describes the ideality of the C. C is plotted vs. concentration in Figure 5.4. Due to the difficulty in deconvoluting the charge-transfer semi-circle, the capacitance is a sum of the double-layer, SEI and the capacitance associated with (de)solvation. This makes it difficult to calculate the thickness of the SEI, but if the double-layer and (de)solvation capacitances were assumed to be constant, one can observe a trend in SEI thickness between electrolytes. Figure 5.4 shows that capacitance decreases with increased ILE concentration, predicting a thicker SEI. Also, the thickness of the SEI formed by LiFSI in G4 was fairly constant apart from 3 m, which was thicker. This agreed with the XPS results described below.

XPS. X-ray photoelectron spectroscopy (XPS) measurements with Ar^+ beam etching were run to gain a compositional understanding and further thickness estimate of the SEI layer prior to current flow. The Li-metal electrodes were submerged in each electrolyte for 24 hours (see Experimental Detail) to form the passivation layer. Etching experiments were run to determine the compositional dependence on SEI depth.

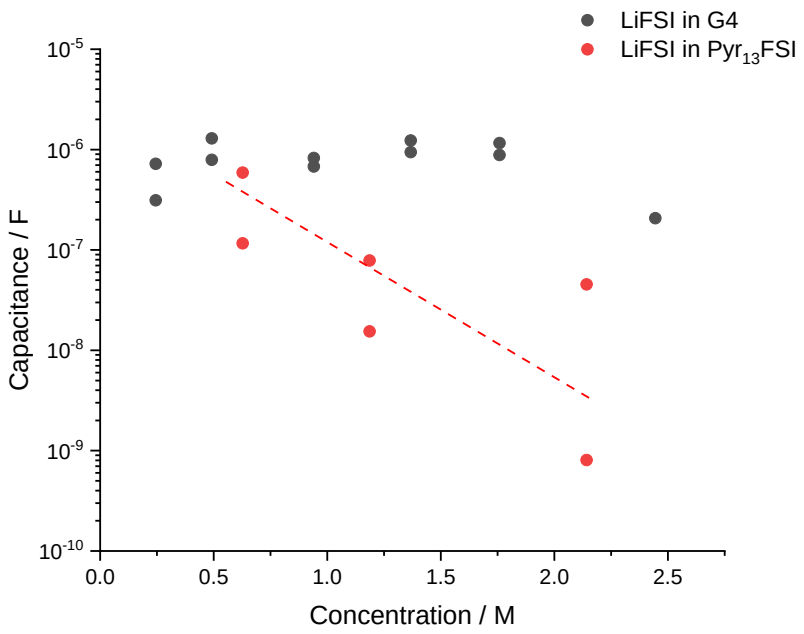


Figure 5.4: Capacitance from fitting of PEIS charge-transfer semi-circle, showing a general decrease with in LiFSI in $Pyr_{1,3}FSI$, and at high concentrations of LiFSI in G4.

Two sample sets were taken for the experiment. Although the procedure was identical, a pristine Li metal control was required for each set as a comparison. Before exposure to the electrolyte, Li metal is covered in a native layer that is difficult to control – this is a major reason for difficulty in studying lithium metal surfaces. In other words, the "starting point" for each sample set was slightly different. In an argon-filled glovebox, it was attempted to scrape the native layer off (as described in Experimental Detail), but the layer would reform quickly, with varying composition. Methods have been formulated to mitigate this variability in lithium metal surface composition including polymer or carbon coatings; various mechanical modifications; and sputter coatings, using atomic layer deposition (ALD), for examples.[14] However, this goes beyond the scope of this chapter.

Figures 5.5 and 5.6 show 1s Li spectra of two experimental sets of LiFSI in G4, along with a pristine sample, with each legend number representing the etching time in seconds. Using a 2 kV Ar^+ ion beam, the etching rate was estimated to be 1 Å/s. One should note this is a very rough estimate, as the rate is dependent on the phases present in the SEI, but is generally accepted in the literature.[15]

The peak with a binding energy (B.E.) of 52.5 eV was characterised as Li metal (Li^0), the middle peak at 54 eV was labelled as Li_2O and at 56 eV was combined LiOH and Li_2CO_3.[16, 17] SEI thickness was estimated by observing when the 52.5 eV peak and broad plasmon loss feature at 58-60 eV began to emerge, as this indicated that the Li metal had been reached. Firstly, it was interesting to note the pristine lithium sample had a thicker native layer than the Li exposed to the electrolyte. Two other control experiments were run: one using pure G4, and another where the pristine Li was washed with DME to check if these solvents were dissolving the native surface of Li. Exposing Li to neat DME or G4 did not appear to change the surface noticeably, see Figure 5.7. This suggested the electrolyte salt (LiFSI) was the primary component that reacted with the native Li layer. Broadly, concentration did not affect the thickness of the SEI layer much; however, in the first set, the 3 m SEI was thicker, with the 52.5 eV peak emerging later. This matched with the C measurement above. Figure 5.8 shows the difference in Li composition for the ILEs. It was clear that compared to the pristine lithium, the ILE SEI layer was noticeably thicker, with thickness increasing with concentration too. Using the estimated etching rate above, the G4-based electrolyte SEI was 30-100 nm, and ILE electrolyte SEI was 100-350 nm.

Next, the primary components within the SEI were analysed. Tables 5.1 and 5.2 present an allocation of each species present in the SEI.[16, 17] Labelled in bold were the major components present from XPS analysis. Figure 5.9a, b and c shows the atomic percent of each component within the LiFSI in G4 SEI for 0.25 m, 1 m and 3 m LiFSI in G4 (see Appendix 4 for 0.5 m, 1.5 m and 2 m). Largely, the 0.25 m to 2 m LiFSI in G4 were similar, with the primary components being oxide species, beginning with LiOH/Li_2CO_3, and then Li_2O. Figure 5.11 shows the atomic %F present in the SEI of each G4-electrolyte, as a function of etch time. With increasing concentration, there was an increasing amount of fluoride present, but below 3 m, this mostly appeared at the surface of the SEI. Oddly, there appeared to be more fluoride in 1.5 m than 2 m, but it was concluded that this was an anomaly, perhaps due to analysing a part of the 2 m electrode

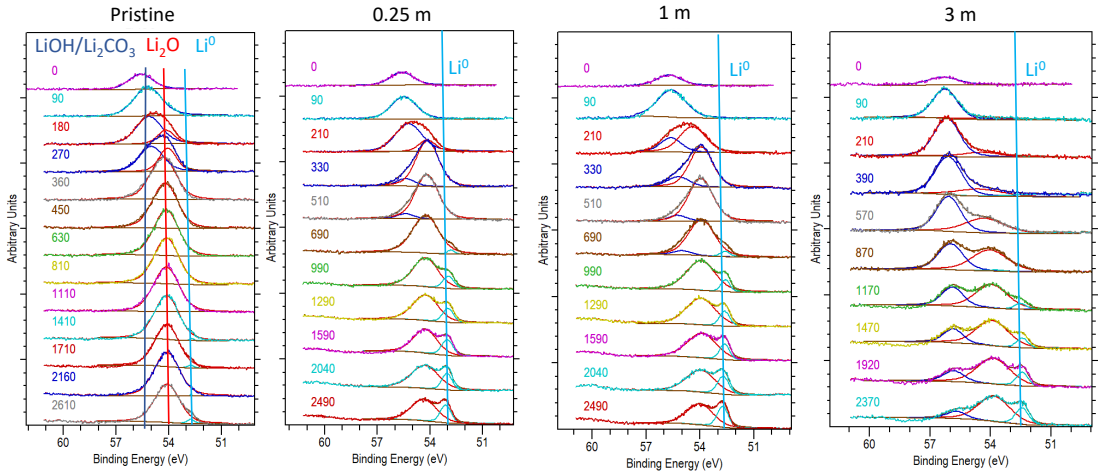


Figure 5.5: Li 1s XPS Spectra 1st Data Set with G4 electrolyte: Pristine, 0.25 m, 1 m and 3 m LiFSI in G4 at different etch times shown on the left of each spectrum, in seconds. The emergence of the Li^0 peak at 52.5 allows one to understand SEI thickness, with the highest concentration (3 m) showing the thickest SEI here. Cyan line = 52.5 eV (Li^0), red line = 54 eV (Li_2O) and dark blue line = 56 eV (LiOH and Li_2CO_3). To allow for easier viewing, the two higher BE lines have been omitted for the final three concentrations.[16]

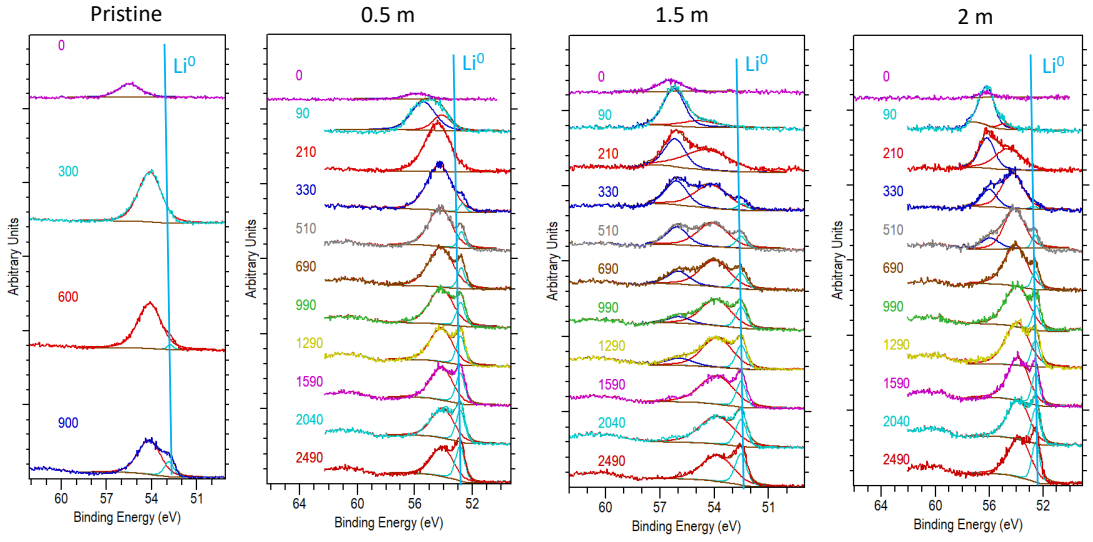


Figure 5.6: Li 1s XPS Spectra 2nd Data Set with G4 electrolyte: Pristine, 0.5 m, 1.5 m and 2 m LiFSI in G4 at different etch times, shown on the left of each spectrum, in seconds. Fewer etch depths were taken on the pristine compared to the previous set due to limited time. The peaks at 54 eV and 56 eV were the same as Figure 5.5, with the cyan line = 52.5 eV (Li^0).[16]

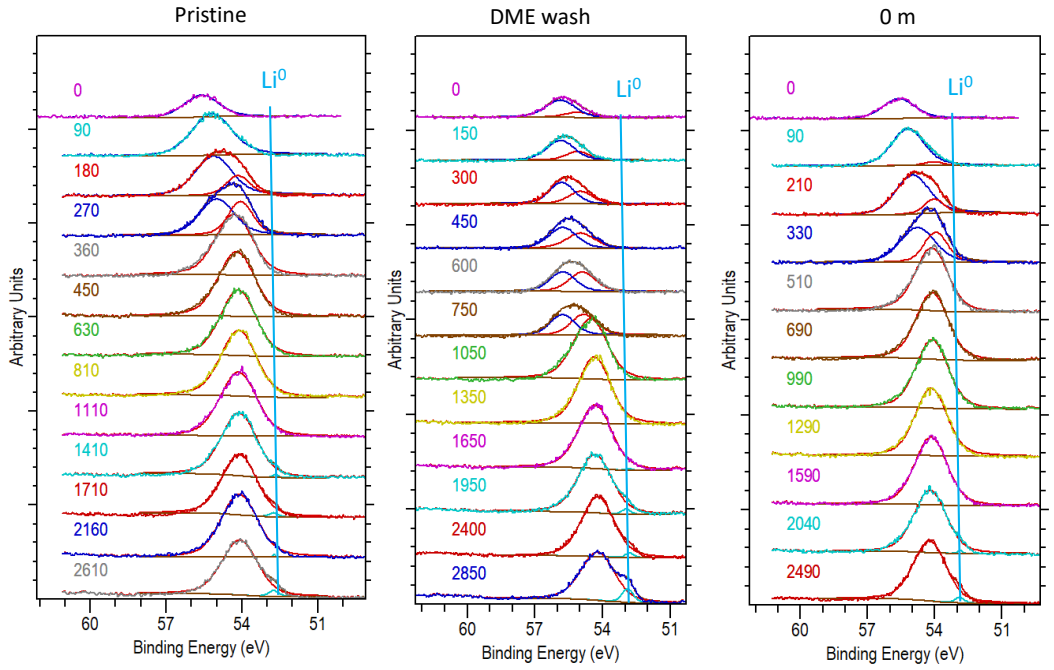


Figure 5.7: Li 1s XPS Spectra Control Washes: Pristine, DME wash and pure G4 exposure (0 m) at different etch times, shown on the left of each spectrum, in seconds. The cyan line = 52.5 eV, and peaks 54 eV and 56 eV were the same as Figure 5.5. Exposure to DME and G4 had no noticeable difference to the Li composition, indicating the chemical stability against Li metal.[16]

which had been damaged due to handling when performing the experiment. Due to time constraints, a repeat run was not achieved, but would be required for conclusive evidence on this anomaly. In 3 m LiFSI in G4, the LiF extended into the inner layer of the SEI, becoming its major component. It is clear the 3 m has a large amount of fluoride present, and as shown in Figure 5.12 the vast majority is LiF. Therefore, one can state that the 3 m electrolyte has both a thicker and more LiF-rich SEI. For ILEs, LiF was a major component throughout the SEI with the higher LiFSI concentrations generally showing more LiF, see Figure 5.11d. Additionally, more carbon species were present, attributed to C-C, C-H and C-N^+ based hydrocarbons. This illustrates the instability of $Pyr^+_{1,3}$ compared to G4 as a source of carbon. Furthermore, there was less oxygen compared to G4 electrolytes, with most appearing as LiOH/Li_2CO_3 close to the surface. Sulfur was more prevalent with the ILEs, but both showed existence of some amount

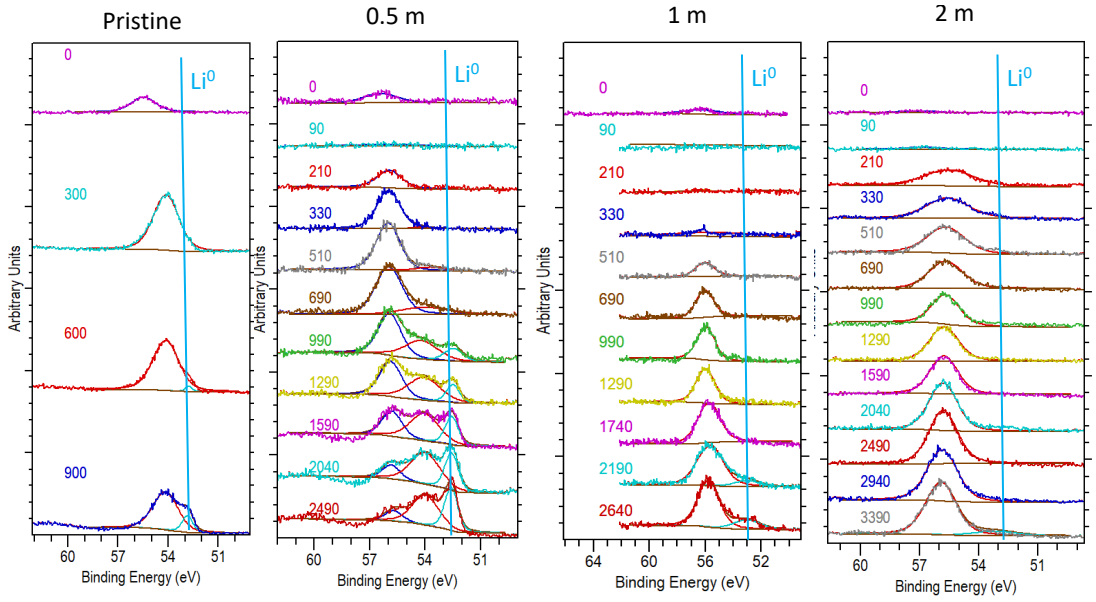


Figure 5.8: Li 1s XPS Spectra of ILE: Pristine, 0.5 m, 1 m and 2 m LiFSI in $Pyr_{1,3}FSI$ at different etch times, shown on the left of each spectrum, in seconds. The cyan line = 52.5 eV, and peaks 54 eV and 56 eV were the same as Figure 5.5. 0.5 m had the most thin SEI, with 1 m and 2 m showing a noticeably thicker SEI, with Li^0 taking longer to emerge.[16]

on the surface likely as $(N^-)SO_2F$ and some Li_2S closer to the Li.

Table 5.1: Summary of components in SEI of lithium metal treated with LiFSI in G4, obtained by XPS. Values presented are binding energies in eV. In **bold** are the major components.

Component	Li 1s	O 1s	C 1s	F 1s	N 1s	S 2p
Li^0	52.5					
LiOH	56.3	531.9				
Li_2CO_3	56.3	533.7	289.5			
Li_2O	54.0	528.4				
LiF				685.5		
Li_2S						160.3
$LiSO_2F$				688.3		170.3
C-O		531.9	287.1			
C-C, C-H			285.2	688.3		
NSO^-					399.2	
$LiNSO_2F$					400.4	
SO_x						167.5

Broadly, the low LiFSI in G4 electrolyte concentrations had similar SEIs to the pristine Li, indicating that few reactions occurred between the electrolyte and Li metal. This made sense as G4 is known for its chemical stability against Li

Table 5.2: Summary of components in SEI of lithium metal treated with LiFSI in $Pyr_{1,3}FSI$, obtained by XPS. Values presented are binding energies in eV. In **bold** are the major components.

Component	Li 1s	O 1s	C 1s	F 1s	N 1s	S 2p
Li^0	52.5					
LiOH	56.3	531.9				
Li_2CO_3	56.3	533.7	289.5			
Li_2O	54.0	528.4				
LiF				685.5		
Li_2S						160.3
$LiSO_2F$				688.3		170.3
C-O		531.9	287.1			
C-C, C-H			285.2			
NSO^-					399.2	
$LiNSO_2F$					400.4	
SO_x						164.2
$C\text{-}N^+$					403.1	

metal.[18] At 3 m LiFSI, it appeared that FSI^- decomposed from the reaction with Li metal, forming multiple phases in the SEI. With increasing concentration of FSI^- and high χ_M values, the likelihood of decomposition increased. It has been proposed that FSI^- decomposes via single-electron reduction:[16, 19, 20]

$$Li(NSO_2F)_2{}^- + e^- \longrightarrow LiF + SO_2NSO_2F^{-\bullet}$$

This suggests the cleavage of the S-F bond is favourable. The radical $SO_2NSO_2F^{-\bullet}$ forms, with LiF as a by-product. The radical has been shown to be highly stable in a popular EPR study by Shkrob et al.[20] Its persistence leads to:

$$SO_2NSO_2F^{-\bullet} + Li^0 + e^- \longrightarrow LiNSO_2F^- + NSO_2{}^-$$

$NSO_2{}^-$ is further reduced to Li_2O:

$$NSO_2{}^- + 2\,Li \longrightarrow Li_2O + NSO^-$$

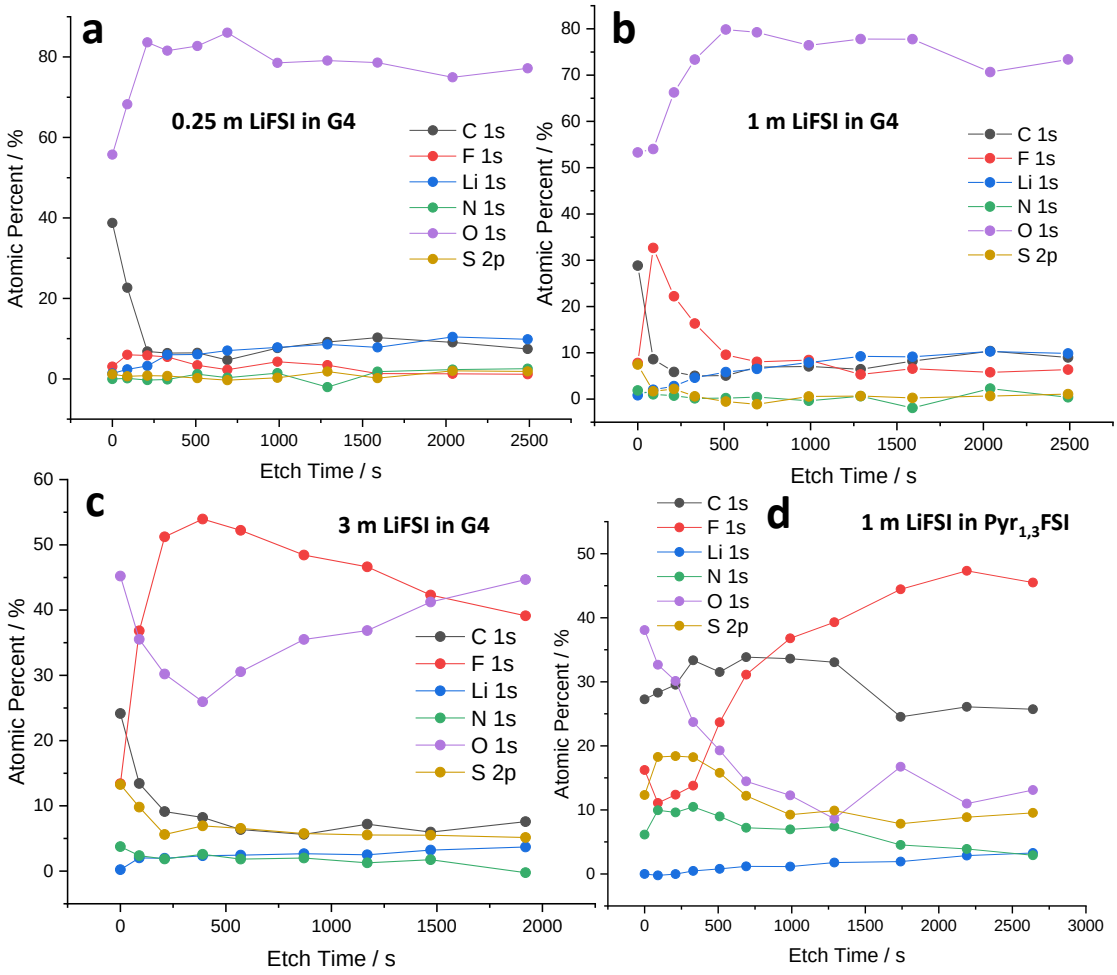


Figure 5.9: Atomic Percent of different SEI components: a) 0.25 m LiFSI in G4 b) 1 m LiFSI in G4 c) 3 m LiFSI in G4 d) 1 m LiFSI in $Pyr_{1,3}FSI$.

This highlights the mechanism of Li_2O formation.

The mechanism illustrated thus far suggests the cleavage of the S-F bond is most favourable. However, Howlett et al. has proposed the cleavage of N-S bond is also possible, albeit for $TFSI^-$ instead of FSI^-.[15] After the single-electron reduction of FSI^-:[19]

$$N(SO_2F)_2^{2\bullet -} + e^- \longrightarrow NSO_2F^{-\bullet} + SO_2F^-$$

The resulting compounds can decompose further:

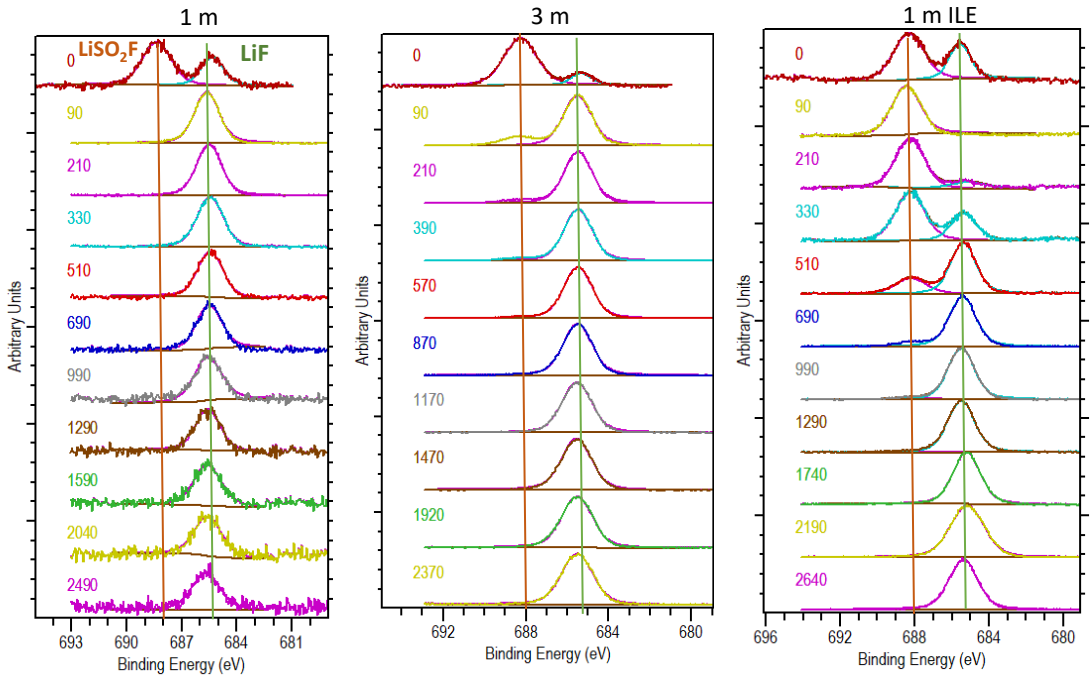


Figure 5.10: 1s Fluorine XPS Spectra: 1m LiFSI in G4, 3 m LiFSI in G4 and 1 m LiFSI in $PyrFSI_{1,3}FSI$ at different etch times, shown to the left of each spectrum, in seconds. The green line indicates the LiF peak and orange is tentatively assigned as $LiSO_2F$.

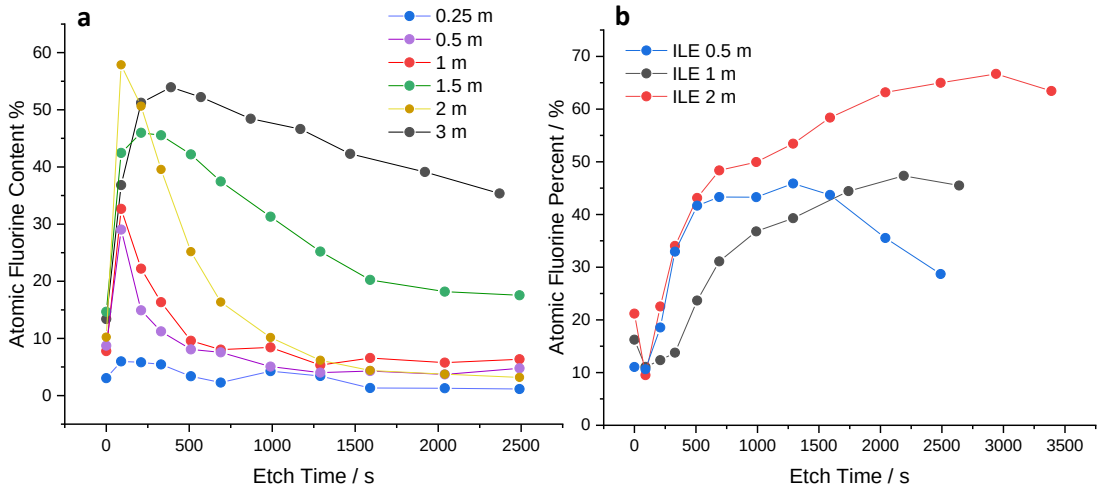


Figure 5.11: Atomic Percent of fluorine in SEI: a) 0.25 m LiFSI in G4 b) 1 m LiFSI in G4 c) 3 m LiFSI in G4 d) 1 m LiFSI in $Pyr_{1,3}FSI$.

$$SO_2F^- + Li \longrightarrow LiF + SO_2{}^-$$

Which introduces a further mechanism for LiF formation.

Camacho-Forero et al. used ab initio MD to simulate the decomposition

of LiFSI, concluding that it is highly efficient at LiF formation.[21] DFT calculations showed the above reactions were extremely thermodynamically favourable (negative ΔE, where E is the interaction energy). They saw that S-F and N-S bonds are most likely to cleave, with S-F being the most favoured (-2.93 eV). They also mentioned FSI^- had a conformational change when moving to higher concentrations, from a *trans* to *cis* structure. This may also influence the SEI decomposition products as the ΔE of each bond changes.

In the ILEs, FSI^- concentrations were consistently high and increased with salt concentration as the density increased, as shown in Table 5.3. As the XPS results showed, both FSI^- and $Pyr^+_{1,3}$ decomposed to form various SEI components, including primarily LiF from the fluoride spectra. FSI^- decomposition is likely to be similar to those mechanisms mentioned above, and $Pyr^+_{1,3}$ has been proposed to form methylpyrrolidine and propylpyrrolidine, via reduction of the $Pyr^+_{1,3}$ to form the neutral species and methyl or propyl radical. Basile et al. further proposed a mechanism that promoted the formation of propylene and methylpyrrolidine via Hoffman β elimination.[16] Although not mentioned by them, the formation of propylene could lead to polymeric structures, likely as an outer layer in the SEI.

Table 5.3: Molar concentrations of each ion in LiFSI in $Pyr_{1,3}FSI$

Concentration / m	**Li^+**	**FSI^-**	**$Pyr^+_{1,3}$**
0.5	0.63	4.08	4.70
1	1.19	5.06	3.87
2	2.15	5.63	3.49

Both the thicker SEIs and higher LiF content of the 3 m LiFSI in G4 and ILEs appeared to result in the nucleation and growth of Li filaments at lower current densities. Using equation 5.1, c_{Li+} drops to zero through the SEI if D_{SEI} is low and L is thick. There is little consensus on absolute values of Li^+ diffusivity through LiF and Li_2O.[22] However, Yildirim et al. used DFT calculations to estimate Li-transport through LiF, stating that it was three orders of magnitude lower than Li_2O and Li_2CO_3.[23] In that study, using DFT, they found diffusion coefficients of Li^+ in LiF as low as 10^{-26}-10^{-20} m^2s^{-1}. Another study using MD found it

to be 3.7×10^{-16} m^2 s^{-1}, illustrating the vast differences in values reported.[24] Furthermore, He et al. artificially formed a 50 nm thick LiF layer and noted how poor it was at preventing non-uniform growth, discounting the possibility that LiF was mechanically strong enough to prevent filament penetration. They concluded that the poor diffusivity through LiF resulted in the initiation of non-uniform growth. For the 3 m electrolyte, by estimating an SEI thickness of ∼100 nm, with LiF as a primary component, the diffusivity of the SEI would be 3.5×10^{-16} m^2 s^{-1} for the c_{Li+} to drop to zero at 100 μA cm^{-2}, very close to an estimation above. Indeed, some studies suggest Li_2O is not too dissimilar to LiF for Li^+ diffusivity, with some also estimating a diffusivity as high as 10^{-16} m^2 s^{-1}.[25] So although LiF appeared to be detrimental for Li^+ diffusivity, Li_2O was also poor for Li^+ transport.

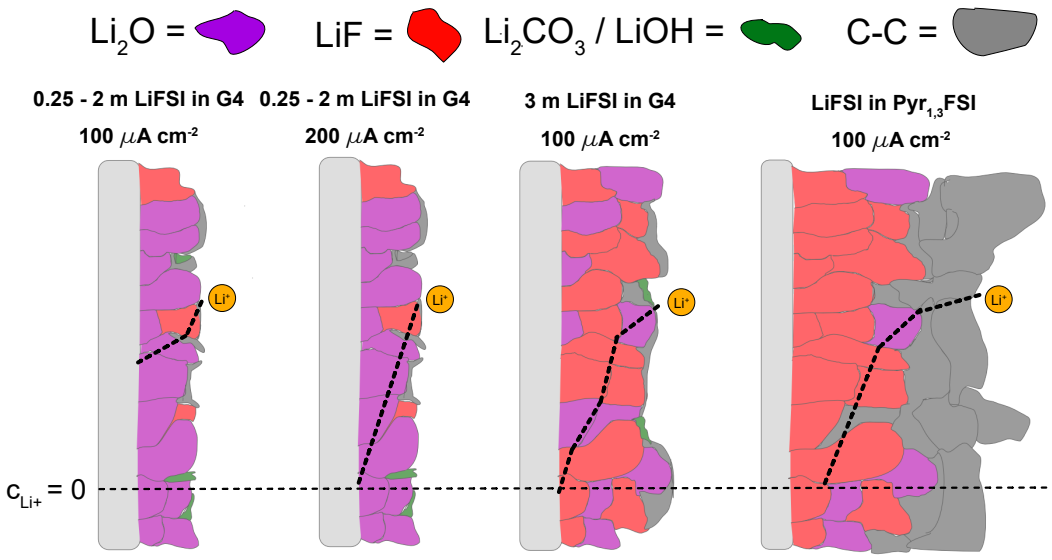


Figure 5.12: Schematic illustrating Li^+ concentration gradient formation through SEI in each electrolyte system. The G4-based electrolytes generally had a thinner SEI with less carbon species present. At higher current densities, the gradient is steeper. The 3 m LiFSI in G4 electrolyte had a higher LiF concentration, which has poor Li^+ diffusivity, lead to large concentration gradients and c_{Li+} dropping to zero. The ILE-based electrolyte has a thicker SEI with a carbon-based outer layer and highly LiF concentrated inner layer in the SEI. The high concentration of LiF leads to a large gradient through the SEI.

5.4 Conclusions & Future Work

This chapter aimed to understand how the electrolyte systems discussed in the previous chapters influenced the plating morphology of Li^+ on lithium metal. Progress was made toward this goal by analysing the transport and thermodynamic data of each electrolyte as well as studying the Li surface chemistry to understand the SEI's influence. Although a correlation was made regarding the interfacial concentration gradient and non-uniform plating, this was largely discounted as the primary reason for the poor plating morphology. By analysing the composition and thickness of the SEI, it was concluded the systems that more readily led to filament growth had thicker SEIs with more LiF content. This was proposed to be due to the gradient that formed within the interphase, due to poor Li^+ diffusion in LiF.

Both the results presented here and discussed by He et al. question the common consensus that LiF is a beneficial component of the SEI.[7] Firstly, one should note the difference between the results measured here, and those that are most commonly reported: namely, this work looks at one half-cycle as opposed to multiple cycles usually measured. It therefore looks at when dendrites nucleate, not a study on overall CE during cycling. From various studies, it appears that at commercially viable current densities (>1 mA cm^{-2}), it is almost impossible to prevent non-uniform growth of some kind due to the presence of varying concentrations of inorganic phases, which generally possess poor Li^+ transport. Due to this inevitability, it is inherently difficult to have very high CEs ($>$99.9%) required for LMBs with high cycle lives (>500). He et al., citing another study, mentions fluorinated solvents have low-energy lowest unoccupied molecular orbitals (LUMOs), so therefore a higher potential vs. lithium. Added to this argument is the high thermodynamic activity of salt anion in highly concentrated electrolytes, likely increasing the kinetics of electrolyte decomposition to form LiF. The faster kinetics for LiF formation is hypothesised to lead to smoother Li deposits due to quick passivation and less fractal growth. Furthermore, they

mention an outer layer, primarily composed of amorphous carbon could buffer the inner inorganic layer, allowing for better passivation. This could be why ILEs perform well for LMBs,[16, 26] as they show a high carbon content in the XPS results. Due to its very low electronic conductivity, LiF can passivate very effectively, increasing CE. If LiF can passivate quickly, forming a very thin layer for adequate Li^+ diffusion, this could be the explanation for its success in the literature. However, LiF, and ultimately fluorinated electrolytes, should not be unique in this capacity, and could explain why $LiNO_3$ is a common additive in electrolytes too.

Further work could include more cell cycles and analysing the morphology of the filaments. This may parse the difference between how electrolytes influence the likelihood of dendrite nucleation, and the morphology of filaments when cycling. Furthermore, morphology is also known to be influenced by the microstructure of the substrate, namely lithium metal. The understanding of how the interplay between SEI composition and substrate microstructure influence deposit morphology will provide a more universal theory of propagation structure.

The ultimate goal is to prevent dendrite nucleation from occurring at all, which looks unlikely when using a fluorinated electrolyte. Therefore, a new paradigm in electrolyte exploration and understanding is required if even higher CEs are to be recognised.

5.5 Experimental Detail

PEIS and dc/dz$|_{z=0,L}$. See Experimental Detail sections of Chapter 3 and 4.

XPS. Electrolytes and lithium metal were prepared in an argon-filled glovebox (low H_2O content ($<$1 ppm) and low O_2 content ($<$1 ppm)) like in Chapter 3 and 4. Lithium metal was cut, stuck on a stainless-steel spacer and submerged into each electrolyte, in a vial, and capped for 24 hours. Each lithium metal sample was subsequently washed with 2 mL of anhydrous (99.5%) 1,2-dimethoxyethane (DME) (purchased from Sigma-Aldrich), which had been further dried over 3 Åmolecular sieves for 1 week. Each sample was dried in a heated antechamber

at 60 ^{o}C for 1 hour and placed on an XPS sample stage, transferred under inert atmosphere.

XPS data was gathered using a PHI VersaProbe III XPS system, generating monochromatic X-rays at 1486 eV, using an Al anode. For survey and high resolution scans a pass energy of 224 eV and 55 eV were used respectively. The lithium metal surface was etched using a monochromatic Ar^{+} ion beam accerlerated at 2 kV or 3 kV and rastered of a 3 x 3 mm^2 area. Etch times are specified in the main text. Data processing and analysis was performed using CasaXPS software and Origin Pro. Each spectrum was charge corrected using the 1s F peak representing LiF at 685.5 eV.[17] This was due to LiF being present in all samples. A Shirley background subtraction was used, with an asymmetric Lorentzian line shape used to fit individual components within peak regions.

5.6 References

1. Horstmann, B. *et al.* Strategies towards enabling lithium metal in batteries: interphases and electrodes. *Energy Environ. Sci.* (2021).
2. Bai, P. *et al.* Transition of lithium growth mechanisms in liquid electrolytes. *Energy Environ. Sci.* **9,** 3221–3229 (2016).
3. Zheng, J. *et al.* Regulating electrodeposition morphology of lithium: towards commercially relevant secondary Li metal batteries. *Chem. Soc. Rev.* **49,** 2701–2750 (2020).
4. Peled, E. *et al.* Review—SEI: Past, Present and Future. *J. Electrochem. Soc.* **164,** A1703–A1719 (2017).
5. Yu, Z. *et al.* Molecular design for electrolyte solvents enabling energy-dense and long-cycling lithium metal batteries. *Nat. Energy* **5,** 526–533 (2020).
6. Liu, J. *et al.* Pathways for practical high-energy long-cycling lithium metal batteries. *Nat. Energy* **4,** 180–186 (2019).
7. He, M. *et al.* The intrinsic behavior of lithium fluoride in solid electrolyte interphases on lithium. *Proc. Natl. Acad. Sci.* **117** (2020).
8. Wood, K. N. *et al.* Dendrites and pits: Untangling the complex behavior of lithium metal anodes through operando video microscopy. *ACS Cent. Sci.* **2,** 790–801 (2016).
9. Wang, A. A. *et al.* Potentiometric MRI of a Superconcentrated Lithium Electrolyte: Testing the Irreversible Thermodynamics Approach. *ACS Energy Lett.,* 3086–3095 (2021).

10. Frenck, L. *et al.* Effect of salt concentration profiles on protrusion growth in lithium-polymer-lithium cells. *Solid State Ionics* **358,** 115517 (2020).

11. Maraschky, A. *et al.* Mechanism Explaining the Onset Time of Dendritic Lithium Electrodeposition via Considerations of the Li + Transport within the Solid Electrolyte Interphase. *J. Electrochem. Soc.* **165,** D696–D703 (2018).

12. He, X. *et al.* The passivity of lithium electrodes in liquid electrolyte for secondary batteries. *Nat. Rev. Mater.* **0123456789** (2021).

13. Bouchet, R. *et al.* An EIS Study of the Anode Li/PEO-LiTFSI of a Li Polymer Battery. *J. Electrochem. Soc.* **150,** A1385 (2003).

14. Delaporte, N. *et al.* Pre-treatments of Lithium Foil Surface for Improving the Cycling Life of Li Metal Batteries. *Front. Mater.* **6** (2019).

15. Howlett, P. C. *et al.* Characterization of the Lithium Surface in N-Methyl-N-alkylpyrrolidinium Bis(trifluoromethanesulfonyl)amide Room-Temperature Ionic Liquid Electrolytes. *J. Electrochem. Soc.* **153,** A595 (2006).

16. Basile, A. *et al.* Stabilizing lithium metal using ionic liquids for long-lived batteries. *Nat. Commun.* **7,** 11794 (2016).

17. *XPS Simplified* `https://xpssimplified.com/_whatisxps.php`. [Online; accessed 01-Sep-2021].

18. Horwitz, G. *et al.* Electrochemical stability of glyme-based electrolytes for Li-O2batteries studied by: In situ infrared spectroscopy. *Phys. Chem. Chem. Phys.* **22,** 16615–16623 (2020).

19. Basile, A. *Identifying the Solid-Electrolyte Interphase formed on Lithium Metal Electrodes using Room Temperature Ionic Liquid based Electrolytes* PhD thesis (RMIT University, 2014), 304.

20. Shkrob, I. A. *et al.* Why Bis(fluorosulfonyl)imide is a “Magic Anion” for Electrochemistry? *J. Phys. Chem. C* **118,** 19661–19671 (2014).

21. Camacho-Forero, L. E. *et al.* Effects of high and low salt concentration in electrolytes at lithium-metal anode surfaces. *J. Phys. Chem. C* **121,** 182–194 (2017).

22. Ramasubramanian, A. *et al.* Lithium Diffusion Mechanism through Solid Electrolyte Interphase in Rechargeable Lithium Batteries. *J. Phys. Chem. C* **123,** 10237 (2019).

23. Yildirim, H. *et al.* First-Principles Analysis of Defect Thermodynamics and Ion Transport in Inorganic SEI Compounds: LiF and NaF. *ACS Appl. Mater. Interfaces* **7,** 18985–18996 (2015).

24. Guan, P. *et al.* Simulation and Experiment on Solid Electrolyte Interphase (SEI) Morphology Evolution and Lithium-Ion Diffusion. *J. Electrochem. Soc.* **162,** A1798–A1808 (2015).

25. Benitez, L. *et al.* Ion Diffusivity through the Solid Electrolyte Interphase in Lithium-Ion Batteries Ion Diffusivity through the Solid Electrolyte Interphase in. *J. Electrochem. Soc.* **164,** E3159 (2017).

26. Liu, K. *et al.* Ionic liquids for high performance lithium metal batteries. *J. Energy Chem.* **59,** 320–333 (2021).

6 | Conclusion and Future Work

6.1 Conclusion

The electrolyte is a critical component in the further development of LIB and LMBs. Improving electrolyte transport properties, D_{app} and t_{Li+}, reduces concentration overpotential, and higher κ and χ_M values lead to reduced ohmic and activation overpotentials respectively, resulting in higher operational potentials and faster charging rates. The accurate measurement of the described properties is paramount for knowledge in how they correlate with electrolyte chemistry. This allows for informed development of high-performing electrolytes and ultimately improved battery performance. Specifically in LMBs, a universal theory for how and why non-uniform Li growth initiates and propagates is yet to be realised. It is proven that electrolyte chemistry is an influential component in whether dendrite nucleate and the morphology of subsequent growth, through their transport properties and in-situ SEI formation. Overall, a full understanding of electrolyte chemistry, transport and thermodynamics allows for a closer understanding of electrolytes' influence on LMB and LIB performance. A summary of key findings in each chapter is presented.

In Chapter 3, a novel method for measuring key electrolyte properties D_{app}, t_{Li+}, χ_M, κ and R_{ct} was presented. The technique combined operando Raman microspectroscopy with PEIS, visualising concentration gradients while monitoring potential differences in the cell. The analysis utilised concentrated solution theory to obtain each concentration-dependent property of the binary electrolyte LiFSI in G4. The parameters were inputted into a DFN model to simulate LIB and LMB performance. This was the first time the isolation of each property was measured in one experimental setup, presenting key trends for a full understanding of the electrolyte system.

In Chapter 4, the technique presented in Chapter 3 was extended to an ionic liquid electrolyte system, LiFSI in $Pyr_{1,3}FSI$. Using concentration visualisation,

an asymmetric gradient was detected, hypothesised to be due to large, ordered aggregates in the ILE. A full transport and thermodynamic characterisation of the ILE was presented for the first time for room-temperature ILEs.
Chapter 5 presented a discussion on how the electrolytes presented in Chapter 3 and Chapter 4 were influencing dendrite nucleation during plating in LMBs. Although there was correlation between electrolyte transport, it was concluded the SEI had more influence on whether dendrite nucleated. Using XPS, it was deduced that a thicker SEI with higher LiF content was more likely to lead to non-uniform plating.

6.2 Suggested Further Work

The aim of this thesis has been to present a methodology for characterising binary and complex ionic liquid electrolytes, while also highlighting their importance in current and next-generation LIB technologies. From this work, there are many promising avenues one can take to investigate electrolytes further:

- Many electrolytes could be tested using the described tandem operando Raman microspectroscopy with PEIS technique. Most interestingly, one could measure the transport and thermodynamics of multi-solvent systems. Utilising concentration visualisation will highlight the intricacies of these electrolyte systems, illustrating the role each solvent plays.
- Further cell design that allows for changes in temperature for monitoring concentration profiles. This may mean using a calibrated heating mat, or a specially designed temperature chamber.
- For increased spatial and temporal resolution, stimulated Raman microspectroscopy could be used to measure electrolyte concentration gradients. Using this technique could allow for a smaller cell, which will decrease the time required for the concentration gradient to form, and also allow for high resolution gradients nearer the surface.

- Further work is required to understand the size and structure of the aggregates forming in ILEs. Dynamic light scattering (DLS) allows for accurate determination of particle size distribution. Intriguingly, this analysis has not been performed to date. Further analysis of the ILE structure could be achieved via through-space 2-D NMR techniques (Nuclear Overhauser Effect Spectroscopy (NOESY)) to understand the long-range ordering clearer.
- Design a working 4-electrode cell to measure steady-state t_{Li+} without the interfacial kinetic influence.
- An investigation into the unusual Li^+ plating behaviour in ILEs would be of interest. Understanding the mechanism that allows this behaviour to occur, and the potential consequences it has on plating morphology would be vital information for ILEs' use in LMBs.
- Implementation of a three-ion system into a CST framework to simulate LIB performance using ILE characterisation data.
- A clearer understanding on the correlation between χ_M and Li metal SEI composition and reaction kinetics. Very little work has implemented an understanding of how electrolyte thermodynamics influences the performance. A systematic study of various electrolytes would be of major interest.
- Understanding how electrolyte transport and thermodynamics influences the propagation behaviour of Li filament growth and comparing it to its influence on nucleation behaviour.

The success of next-generation battery technologies will be highly influenced by the invention of novel electrolyte systems. Answering questions related to their fundamental problems allows for a framework of new discovery, perhaps leading to a shift outside of the current paradigm.

Appendices

A | Python Scripts

Each script is available on GitHub. The concentration visualisation scripts are in the repository `https://github.com/JFawd/Raman-to-Concentration-Gradients` and fitting scripts are in the repository `https://github.com/JFawd/Fitting-Concentration-Gradients`.

A.1 Concentration Visualisation – Binary Electrolyte

```
"""
File:          concentration_plot2.py
Author:         Jack Fawdon & Kevin Hurlbutt
Date:         2020-03-31
-----------------------
This program converts a series of Raman spectra into a concentration
 ↪  vs. time spectrum, concentration gradient.
"""
import os
import numpy as np
import matplotlib.pyplot as plt
from tkinter import Tcl
from scipy import integrate

class Peak():
        """         class: Peak
                -----------------
                This is the heart of the function. It takes in the
 ↪  path to a text file
                containing the spectroscopic data and writes a file
 ↪  containing a normalized
                700 cm-1 peak and converted that peak's area into a
 ↪  resulting concentration
        """
        def __init__(self, path_to_input, dst_dir):
                self.filename = path_to_input
                self.dst_dir = dst_dir
                self.wavenumber = []
                self.intensity = []
                self.normalized = []
                self.truncated = []
                self.wavenumber2 = []
                self.concentration_m = []
                return
```

```
31
32          def run(self):
33                  self.parse()
34                  self.normalize()
35                  self.truncate()
36                  self.write_results()
37                  self.plotting()
38                  self.area()
39                  return
40
41
42          #This parses a two-column text file into wavenumber and
            ↪  intensity data.
43
44          def parse(self):
45                  with open(self.filename, encoding="utf8",
                    ↪  errors="ignore") as f:
46                          for line in f:
47                                  if line.startswith('#'):
48                                          continue
49                                  parts = line.split()
50                                  w = float(parts[0])
51                                  i = float(parts[1])
52                                  self.wavenumber.append(w)
53                                  self.intensity.append(i)
54                  return
55
56          #Normalise the data against the highest peak above 1400
            ↪  wavenumbers.
57
58          def normalize(self):
59                  index = 0
60                  for ind, val in enumerate(self.wavenumber):
61                          if val > 1400:
62                                  index = ind
63                  m = max(self.intensity[:index])
64                  for i in self.intensity:
65                          self.normalized.append(i/m)
66                  return
67
68          #Truncate the spectrum so it only includes the the 717 cm-1
            ↪  peak.
69
70          def truncate(self):
71                  index1 = 0
72                  index2 = 0
73                  for ind1, val1 in enumerate(self.wavenumber):
```

```
74                          if val1 < 762 and val1 > 758:
75                                  index1 = ind1
76                          if val1 < 682 and val1 > 678:
77                                  index2 = ind1
78                          self.truncated =
                             ↪  self.normalized[index1:index2]
79                          self.wavenumber2 =
                             ↪  self.wavenumber[index1:index2]
80                  return
81
82          #Calculate the area of the peak and convert to a
             ↪  concentration from the calibration curve data already
             ↪  gathered. Add each spectra's concentration into a
             ↪  list.
83
84          def area(self):
85
86                          area_peak = integrate.simps(self.truncated,
                             ↪  self.wavenumber2)
87
88                          a = -20.46985
89                          b = -0.6228
90
91                          self.concentration_m = (area_peak-b)/a
92
93                          return
94
95
96          #Plot data if desired
97
98          def plotting(self):
99                  plt.plot(self.wavenumber2, self.truncated)
100                 plt.fill_between(self.wavenumber2, self.truncated,
                     ↪  color = "grey",alpha = 0.3, hatch = '|')
101                 plt.show()
102                 return
103
104         #Write normalised 717 cm-1 peak into a .txt file if desired.
105
106         def write_results(self):
107                 with
                     ↪  open(self.dst_dir+'/'+self.filename[self.filename.rfind('/'):-
                     ↪  'w', encoding="utf8", errors="ignore") as f:
108                         for i in range(len(self.truncated)):
109                                 f.write(str(self.wavenumber2[i]))
110                                 f.write('\t')
111                                 f.write(str(self.truncated[i]))
```

```
                                f.write('\n')
                return


def main():

        src_dir = input("Please type the full path to the input directory or input file : ").strip()
        dst_dir = input("Please type the full path to the output directory: ").strip() + '/'
        distance = input("How many steps?").strip()
        step_size = input("What was the step size?").strip()


        conctotal=[]
        distance_list = []

        x = 0
        y = 0
        while x < int(distance):
                s = int(step_size)*y
                distance_list.append(s)
                x = x+1
                y = y+1


        #Write .txt file with concentration vs. distance, obtaining a concentration gradient file.

        if os.path.isdir(src_dir):
                for filename in Tcl().call('lsort', '-dict', os.listdir(src_dir)):
                        if filename.endswith(".txt") and "700PEAK" not in filename and "NORMALIZED" not in filename:
                                print(filename)
                                n = Peak(src_dir+'/'+filename, dst_dir)
                                n.run()
                                conctotal.append(n.concentration_m)
                with open(src_dir+'/'+"_NORMALIZED_conctotal.txt", 'w', encoding="utf8", errors="ignore") as f:
                        for i in range(len(conctotal)):
                                f.write(str(distance_list[i]))
                                f.write('\t')
                                f.write(str(conctotal[i]))
                                f.write('\n')
```

```
151
152         else:
153                 n = Peak(path_to_input=src_dir, dst_dir=dst_dir)
154                 n.run()
155
156         print(conctotal)
157         print(distance_list)
158
159         plt.plot(distance_list, conctotal, 'o')
160         plt.xlabel('Distance / um')
161         plt.ylabel('Concentration / M')
162         plt.show()
163
164 if __name__ == '__main__':
165         main()
```

A.2 Symmetric Concentration Gradient Fitting

```
1  """
2  File:          conc_fit_full.py
3  Author:         Jack Fawdon
4  Date:         2021-07-12
5  ----------------------
6  This program fits a symmetric concentration gradient,
7  """
8
9
10 import os
11 import matplotlib.pyplot as plt
12 import matplotlib.pyplot as mpl
13 import matplotlib.cm as cm
14 import matplotlib as mpl
15 from collections import OrderedDict
16 from lmfit import Model, Parameters, minimize, fit_report
17 import numpy as np
18 import math
19 from scipy import integrate, special
20 from cycler import cycler
21
22 cmaps = OrderedDict()
23
24
25 # distance between electrodes
26 c = 15631
27
28 # initial concentration
```

```
d = 1115


def func(x, a, b):
        return (a)*((b/(3.1415)**0.5)*np.exp(-((((-x+c)/1e6)/b)**2))-((((-x+c)/1e6))*speci


src_dir = input("Please type the full path to the input directory or input file : ").strip()


#bunch of lists to populate
report_list = []
max_list = []
min_list = []
a_list = []
b_list = []
a_list_err = []
b_list_err = []
area_plate_list = []
area_strip_list = []
area_plate_err_list = []
area_strip_err_list = []
A = ['4h', '12h', '20h', '28h', '36h']



#import file
k = 0
all_txt_files = sorted(os.listdir(src_dir))
for txt in all_txt_files:
        if txt.endswith(".txt") and "fit" not in txt and "max" not in txt:
                data = np.loadtxt(src_dir+'/'+txt)
                x=data[:,0]
                ydata=data[:,1]

                #lmfit function described above
                gmodel = Model(func)
                params = Parameters()
                params.add('a', value=184000, vary=True) #min=100000, max=300000)
                params.add('b', value=0.004, vary=True, min=1e-6, max=1e-1)
                result = gmodel.fit(ydata, params, x=x, weights=np.sqrt(1.0/ydata))
```

```
70                  color = cm.winter(np.linspace(0,1,5))
71                  plt.rc('axes', prop_cycle=(cycler('color', color)))
72
73
74                  #taking the max and minimum concentration from the
                     ↪  fitting and adding to the list above (used for
                     ↪  TDF calculation)
75                  m = max((result.best_fit))
76                  mi = min((result.best_fit))
77                  max_list.append(m)
78                  min_list.append(mi)
79
80                  #plotting the data + fit
81                  plt.plot(x, ydata, 'o')
82                  plt.plot(x, result.best_fit, label = "Fitted Curve")
83                  plt.xlabel('Distance / um')
84                  plt.ylabel('Concentration / $moldm^-3$')
85
86                  #dely = result.eval_uncertainty(sigma=1)
87                  #plt.fill_between(x, result.best_fit-dely,
                     ↪  result.best_fit+dely, color="#ABABAB",
                     ↪  label='3-$sigma$ uncertainty band')
88
89                  #print(result.fit_report())
90
91                  #writing the fitted data into a txt file
92                  newfilename = 'fit'+str(txt)
93                  with open(src_dir+'/'+newfilename,'w') as p:
94                          for j in range(len(x)):
95                                  p.write(str(x[j]))
96                                  p.write('\t')
97                                  p.write(str(result.best_fit[j]))
98                                  p.write('\n')
99                                  j+1
100
101
102                 #adding the 'a' (interfacial conc gradient) and
                     ↪  'b'        (diffusion length) and associated
                     ↪  errors to the list above
103                 a_list.append(result.params['a'].value)
104                 b_list.append(result.params['b'].value)
105                 a_list_err.append(result.params['a'].stderr)
106                 b_list_err.append(result.params['b'].stderr)
107
108                 #finding the area under the curve for the plating
                     ↪  and stripping side
109                 y_eval = gmodel.eval(result.params, x=x)
```

```
110
111                 y_eval_plate = y_eval[25:]
112                 x_plate = x[25:]
113
114                 y_eval_strip = y_eval[:25]
115                 x_strip = x[:25]
116
117                 area_plate = integrate.simps(y_eval_plate, x_plate)
118                 area_strip = integrate.simps(y_eval_strip, x_strip)
119
120                 area_plate_list.append(area_plate)
121                 area_strip_list.append(area_strip)
122
123                 #the uncertainty band for the fitting and using this
                    ↪  integrl as the error
124                 dely = result.eval_uncertainty(sigma=1)
125
126                 area_plate_err = integrate.simps(dely[25:], x_plate)
127                 area_strip_err = integrate.simps(dely[:25], x_strip)
128
129                 area_plate_err_list.append(area_plate_err)
130                 area_strip_err_list.append(area_strip_err)
131
132                 k+1
133
134 #writing to txt files: max conc; the fitting parameters + error; the
    ↪  areas + error
135 with open(src_dir+"/max_min.txt", 'w') as f:
136         for i in range(len(max_list)):
137                 f.write(str(max_list[i]))
138                 f.write('\t')
139                 i+1
140         for i in range(len(max_list)):
141                 f.write(str(min_list[i]))
142                 f.write('\n')
143                 i+1
144
145
146 with open(src_dir+"/fitting_parameters.txt", 'w') as f:
147         for i in range(len(a_list)):
148                 f.write(str(a_list[i]))
149                 f.write('\t')
150                 f.write(str(b_list[i]))
151                 f.write('\t')
152                 f.write(str(a_list_err[i]))
153                 f.write('\t')
154                 f.write(str(b_list_err[i]))
```

```
                f.write('\n')
                i+1

with open(src_dir+"/areas.txt", 'w') as f:
        for i in range(len(area_plate_list)):
                f.write(str(area_plate_list[i]))
                f.write('\t')
                f.write(str(area_strip_list[i]))
                f.write('\t')
                f.write(str(area_plate_err_list[i]))
                f.write('\t')
                f.write(str(area_strip_err_list[i]))
                f.write('\n')
                i+1


plt.legend(A)

plt.show()
```

A.3 Concentration Visualisation – Ionic Liquid Electrolyte

```
"""
File:          ILarea.py
Author:         Jack Fawdon
Date:         2021-06-01
----------------------
This program truncates and subtracts the baseline Raman spectra.
"""

import matplotlib.pyplot as plt
import numpy as np
from numpy import linspace
import os
from scipy import integrate, special
from lmfit import Model, Parameters, minimize, fit_report
import matplotlib.cm as cm
from cycler import cycler
import operator
from natsort import natsorted
import itertools

#exponentially modified gaussian function

```

```
def gaussmod(x, y0, A, t0, w, xc):
    return y0 + A/t0 *
     ↪  np.exp(0.5*(w/t0)**2-(x-xc)/t0)*(special.erf(((x-xc)/w -
     ↪  w/t0)/np.sqrt(2))+1)/2

src_dir = input("Please type the full path to the input directory or
 ↪  input file : ").strip()
distance = input("How many steps?").strip()
step_size = input("What was the step size?").strip()


#lists of the concentration values and distance after fitting

conc_values = []
distance_list = []


x = 0
y = 0
while x < int(distance):
        s = int(step_size)*y
        distance_list.append(s)
        x = x+1
        y = y+1


#importing data

i = 0
all_txt_files = natsorted(os.listdir(src_dir))
for txt in all_txt_files:
        if txt.endswith(".txt") and "conc_gradient" not in txt:
                data = np.loadtxt(src_dir+'/'+txt)
                xdata=data[:,0]
                ydata=data[:,1]

                #truncate spectra

                index=[]
                for ind, val in enumerate(xdata):
                        if 680 <= val <= 800:
                                index.append(ind)

                        ydata_trunc = ydata[index]
                        xdata_trunc = xdata[index]

                #fitting of truncated data
```

```
67
68                  gmodel = Model(gaussmod)
69
70                  params = Parameters()
71                  params.add('y0', value=10000, vary=True) #min=100000,
                     ↪  max=300000)
72                  params.add('A', value=36e5, vary=True)
73                  params.add('t0', value=11.2, vary=True)
74                  params.add('w', value=11.5, vary=True)
75                  params.add('xc', value=732, vary=True)
76                  result = gmodel.fit(ydata_trunc, params,
                     ↪  x=xdata_trunc, weights=np.sqrt(1.0/ydata_trunc))
77                  color = cm.winter(np.linspace(0,1,5))
78                  plt.rc('axes', prop_cycle=(cycler('color', color)))
79
80
81                  #plt.plot(xdata_trunc, ydata_trunc, 'o')
82                  ##plt.plot(xdata_trunc, result.best_fit, 'o', label
                     ↪  = "Fitted Curve")
83                  plt.xlabel('Distance / um')
84                  plt.ylabel('Concentration / $moldm^-3$')
85
86
87                  #specifying the fitted function
88
89                  x_eval = linspace(680, 800, 5000)
90                  y_eval = gmodel.eval(result.params, x=x_eval)
91                  """plt.plot(x_eval, y_eval)
92                  plt.show()"""
93
94                  #find the x at max height of the fitted function
95
96                  max_value = np.max(y_eval)
97                  max_index = np.where(y_eval == max_value)
98                  max_wavenumber = x_eval[max_index]
99
100                 #convert to concentration using calibration curve
                     ↪  values
101
102                 a = -0.6078
103                 b = 9.17847
104                 c = 724.034
105
106                 concentration =
                     ↪  (-b+(np.sqrt(b**2-(4*a*(c-max_wavenumber)))))/(a*2)
107                 concentration1 = concentration.tolist()
108                 conc_values.append(concentration1)
```

```
                i+1


#convert list of lists into a list

conc_values1 = list(itertools.chain(*conc_values))

plt.plot(distance_list, conc_values1)

print(conc_values1)

plt.show()

#write file into a .txt file of concentrations and distance

newfilename = 'conc_gradient.txt'
with open(src_dir+'/'+newfilename,'w') as p:
        for j in range(len(distance_list)):
                p.write(str(distance_list[j]))
                p.write('\t')
                p.write(str(conc_values1[j]))
                p.write('\n')
```

A.4 Asymmetric Concentration Gradient Fitting

```
"""
File:          conc_fit_full_IL.py
Author:         Jack Fawdon
Date:         2021-05-01
-----------------------
This program fits an asymmetric concentration gradient and writes
 ↪  the fitted parameters to .txt files.
"""
import os
import matplotlib.pyplot as plt
import matplotlib.pyplot as mpl
import matplotlib.cm as cm
import matplotlib as mpl
from collections import OrderedDict
from lmfit import Model, Parameters, minimize, fit_report
import numpy as np
import math
from scipy import integrate, special
from cycler import cycler

cmaps = OrderedDict()
```

```
e = 15631
#f = 2075

#fitting equation
def func(x, a, b, c, d, f):
        return (a)*((b/(3.1415)**0.5)*np.exp(-((((-x+e)/1e6)/b)**2))-((((-x+e)/1e6))*

src_dir = input("Please type the full path to the input directory or input file : ").strip()

#lists used in the script
report_list = []
max_list = []
min_list = []
list_dely_plate = []
list_dely_strip = []
a_list = []
b_list = []
c_list = []
d_list = []
f_list = []
a_list_err = []
b_list_err = []
c_list_err = []
d_list_err = []
f_list_err = []
area_plate_list = []
area_strip_list = []
area_plate_err_list = []
area_strip_err_list = []

A = ['4h', '20h', '36h']

#loads .txt file
k = 0
all_txt_files = sorted(os.listdir(src_dir))
for txt in all_txt_files:
        print(txt)
        if txt.endswith(".txt") and "max" not in txt and "fit" not in txt and "area" not in txt:
                data = np.loadtxt(src_dir+'/'+txt)
                x=data[:,0]
                ydata=data[:,1]

                #lmfit model
                gmodel = Model(func)
```

```
65                  params = Parameters()
66                  params.add('a', value=200, vary=True) #min=100000,
                     ↪  max=300000)
67                  params.add('b', value=0.004, vary=True) #min=1e-3,
                     ↪  max=1e-1)
68                  params.add('c', value=0.004, vary=True, min=1e-6,
                     ↪  max=1e-1)
69                  params.add('d', value=200, vary=True) #min=13000,
                     ↪  max=17000)
70                  params.add('f', value=1000, vary=True)# min=0.9,
                     ↪  max=1)
71                  result = gmodel.fit(ydata, params, x=x,
                     ↪  weights=np.sqrt(1.0/ydata))
72                  color = cm.winter(np.linspace(0,1,5))
73                  plt.rc('axes', prop_cycle=(cycler('color', color)))
74                  dely = result.eval_uncertainty(sigma=1)
75
76                  m = max((result.best_fit))
77                  mi = min((result.best_fit))
78                  max_list.append(m)
79                  min_list.append(mi)
80
81
82                  #plot data
83                  plt.plot(x, ydata, 'o')
84                  plt.plot(x, result.best_fit, label = "Fitted Curve")
85                  plt.xlabel('Distance / um')
86                  plt.ylabel('Concentration / $moldm^-3$')
87
88                  #write best fit to a .txt file
89                  newfilename = "fit_"+str(txt)
90                  with open(src_dir+'/'+newfilename,'w') as p:
91                          for j in range(len(x)):
92                                  p.write(str(x[j]))
93                                  p.write('\t')
94                                  p.write(str(result.best_fit[j]))
95                                  p.write('\n')
96                                  j+1
97
98                  #create lists for all the fitted parameters
99                  a_list.append(result.params['a'].value)
100                 b_list.append(result.params['b'].value)
101                 c_list.append(result.params['c'].value)
102                 d_list.append(result.params['d'].value)
103                 f_list.append(result.params['f'].value)
104                 a_list_err.append(result.params['a'].stderr)
105                 b_list_err.append(result.params['b'].stderr)
```

```
106                 c_list_err.append(result.params['c'].stderr)
107                 d_list_err.append(result.params['d'].stderr)
108                 f_list_err.append(result.params['f'].stderr)
109
110
111
112                 y_eval = gmodel.eval(result.params, x=x)
113
114                 #plating side is the second half of the gradient
115                 y_eval_plate = y_eval[24:]
116                 x_plate = x[24:]
117
118                 #stripping side is the first half od the gradent
119                 y_eval_strip = y_eval[:24]
120                 x_strip = x[:24]
121
122
123                 #find area of each side of the gradient
124                 area_plate = integrate.simps(y_eval_plate, x_plate)
125                 area_strip = integrate.simps(y_eval_strip, x_strip)
126
127                 area_plate_list.append(area_plate)
128                 area_strip_list.append(area_strip)
129
130
131                 #find uncertainty of the fitting
132                 dely = result.eval_uncertainty(sigma=1)
133
134
135                 #find area of the uncertainty
136                 area_plate_err = integrate.simps(dely[24:], x_plate)
137                 area_strip_err = integrate.simps(dely[:24], x_strip)
138
139                 area_plate_err_list.append(area_plate_err)
140                 area_strip_err_list.append(area_strip_err)
141
142                 plt.fill_between(x, result.best_fit-dely,
                    ↪  result.best_fit+dely, color="#ABABAB",
                    ↪  label='3-$sigma$ uncertainty band')
143
144                 m_dely_plate = dely[47]
145                 m_dely_strip = dely[0]
146                 list_dely_plate.append(m_dely_plate)
147                 list_dely_strip.append(m_dely_strip)
148
149                 k+1
150
```

```
#write lists for all of the fitting parameters and the fitted
↪  gradients

with open(src_dir+"/max_min.txt", 'w') as f:
        for i in range(len(max_list)):
                f.write(str(max_list[i]))
                f.write('\t')
                f.write(str(min_list[i]))
                f.write('\t')
                f.write(str(list_dely_plate[i]))
                f.write('\t')
                f.write(str(list_dely_strip[i]))
                f.write('\n')
                i+1

with open(src_dir+"/fitting_parameters.txt", 'w') as f:
        for i in range(len(a_list)):
                f.write(str(a_list[i]))
                f.write('\t')
                f.write(str(b_list[i]))
                f.write('\t')
                f.write(str(c_list[i]))
                f.write('\t')
                f.write(str(d_list[i]))
                f.write('\t')
                f.write(str(f_list[i]))
                f.write('\t')
                f.write(str(a_list_err[i]))
                f.write('\t')
                f.write(str(b_list_err[i]))
                f.write('\t')
                f.write(str(c_list_err[i]))
                f.write('\t')
                f.write(str(d_list_err[i]))
                f.write('\t')
                f.write(str(f_list_err[i]))
                f.write('\n')
                i+1

with open(src_dir+"/areas.txt", 'w') as f:
        for i in range(len(area_plate_list)):
                f.write(str(area_plate_list[i]))
                f.write('\t')
                f.write(str(area_strip_list[i]))
                f.write('\t')
                f.write(str(area_plate_err_list[i]))
                f.write('\t')
```

```
                f.write(str(area_strip_err_list[i]))
                f.write('\n')
                i+1


#ax=plt.gca()
#ax.spines['top'].set_visible(False)
#ax.spines['right'].set_visible(False)

plt.legend(A)

plt.show()
```

B | Doyle-Fuller-Newman Equations

The DFN model combines concentrated solution theory to account for electrolyte flux in non-ideal solutions, and porous electrode theory to understand behaviour in porous microstructures.

Molar flux in a binary electrolyte is governed by:

$$N_i = -D_{app}\nabla c_i + \frac{i_i t_+^0}{F} \tag{B.1}$$

Where N_i is the molar flux of i, F is the Faraday constant and i_i is the current density of i and c_i. To know current density, one needs to understand how electrolyte potential is varying in solution:

$$i_i = -\kappa\nabla\Phi_i + \frac{2\kappa RT}{F}\chi_M(1-t_+^0)\nabla\ln c_i \tag{B.2}$$

Where Φ_i is measured with a lithium reference electrode, T is the temperature, R is the ideal gas constant.

In short, equations B.1 and B.3 describe how electrolyte potential and concentration vary in an electrolyte. Then, one needs to set the boundary conditions. At one boundary (x=0), the potential is set to zero, and the other (x=L) includes the flux of lithium ions:

$$N_+ = \frac{I}{F} \tag{B.3}$$

To measure how current at the interface influences surface overpotential, the Butler-Volmer equation was used:

$$i_{loc} = i_0\left(\exp\frac{\alpha_a F\eta}{RT} - \exp\frac{\alpha_c F\eta}{RT}\right) \tag{B.4}$$

i_{loc} is the local current density at the interface, η is the local activation overpotential, α_i is the anodic and cathodic transfer coefficients and i_0 is the exchange current density. i_0 was assumed to be 1 A/m^2.

Full Cell

Li-ion full cell simulations utilised the equations above to describe electrolyte concentration and potential, and reaction kinetics at the interface. Additionally, porous electrode theory was used.

For Li-ion full cell simulations the porous electrode consisted of spherical active material particles and LiFSI in G4 electrolyte in the void space. The electric current in the active material particles was defined by Ohm's Law:

$$i = -\sigma_s \nabla \Phi_s \tag{B.5}$$

Where σ_s is the electric conductivity of the material.

With the full cell consisting of insertion electrodes, Li^+ diffusion was defined by Fick's Law:

$$N_s = -D_s \nabla c_s \tag{B.6}$$

$$\frac{\partial c_s}{\partial t} = \nabla(D_s \nabla c_s) \tag{B.7}$$

Where D_s is the diffusion coefficient of Li^+ in the material, and c_s is the concentration of lithium in the solid phase.

The interfacial kinetics were again defined by equation B.4 with i_0 defined as:

$$i_0 = Fk(c_s^{max} - c_s)^{\alpha_a}(c_s)^{\alpha_c}(c_l)^{\alpha_a} \tag{B.8}$$

Where k is the rate constant and c_s is the solid phase lithium concentration.

The current density was specified at the cathode/current collector interface.

Electrolyte flux and potential were defined by equations B.1 and B.3. Measured values of D_{app}, t_+^0, κ and χ_M were used in the simulations.

For Li-metal full cell performance, the lithium metal surface was modelled as an electrode surface via the Butler-Volmer B.4.

C | ILE Simulation Equations

The below equations describe the model used to validate the EIS method for determining t_{Li^+} for ILEs. COMSOL Multiphysics 5.5 was used for perform the simulations, along with a MATLAB script for simulating Nyquist Plots, written by Prof. Fabio La Mantia.

The mass balance equation is used for each species, Li^+, FSI^- and $Pyr^+_{1,3}$:

$$\frac{\partial c}{\partial t} = \nabla.(-D_i \nabla c_i - \frac{z_i D_i F}{RT}.c_i \nabla \Phi) \tag{C.1}$$

Where D_i and c_i are the diffusion coefficient and concentration of each species, i, R is the gas constant, T is the temperature, and $\nabla\Phi$ is potential difference. This meant a total of 3 mass balance equations were used. The boundary condition describes the rate of accumulation of Li^+, based on the Butler-Volmer equation (see Appendix 2). The rate of accumulation of FSI^- and $Pyr^+_{1,3}$ was 0, as these were inactive ions at the interface.

The charge balance equation was described by Poisson's Equation:

$$\nabla^2 \Phi = -\frac{F}{\varepsilon_0 \varepsilon} \sum_i c_i z_i \tag{C.2}$$

Where ε_0 and ε are dielectric constants in vacuum and solution (assumed as 72-times ε_0) respectively. The equation relates the charge density to the Laplacian of the electric potential. Neumann boundary conditions were used at each interface:

$$\varepsilon_0 \nabla^2 \Phi = \frac{\varepsilon}{d_H}(\Phi_H - \Phi_0) \tag{C.3}$$

$$\varepsilon_0 \nabla^2 \Phi = \frac{\varepsilon}{d_H}(\Phi_H + \Phi_{CE}) \tag{C.4}$$

Where d_H is the thickness of the double layer (assumed as 5×10^{-10} m, Φ_{CE} is the potential at the counter electrode, and Φ_0 at the centre of the cell, Φ_H is the potential at the outer double layer.

The measured current is combination of the Faradaic current, defined by the rate of reaction, r, and double layer charging:

$$I_{tot} = nFr + C_{dl}\frac{d\eta_s}{dt} \tag{C.5}$$

Where C_{dl} is the capacitance of the double layer, η_s is the overpotential caused by double layer charging. A sinusoidal voltage (V) was applied (for EIS):

$$V = V_1 \sin(\omega t) \tag{C.6}$$

Where V_1, is the voltage amplitude, and ω is defined:

$$\omega = 2\pi f \tag{C.7}$$

Where f is the frequency of oscillation.

D | Further XPS Data

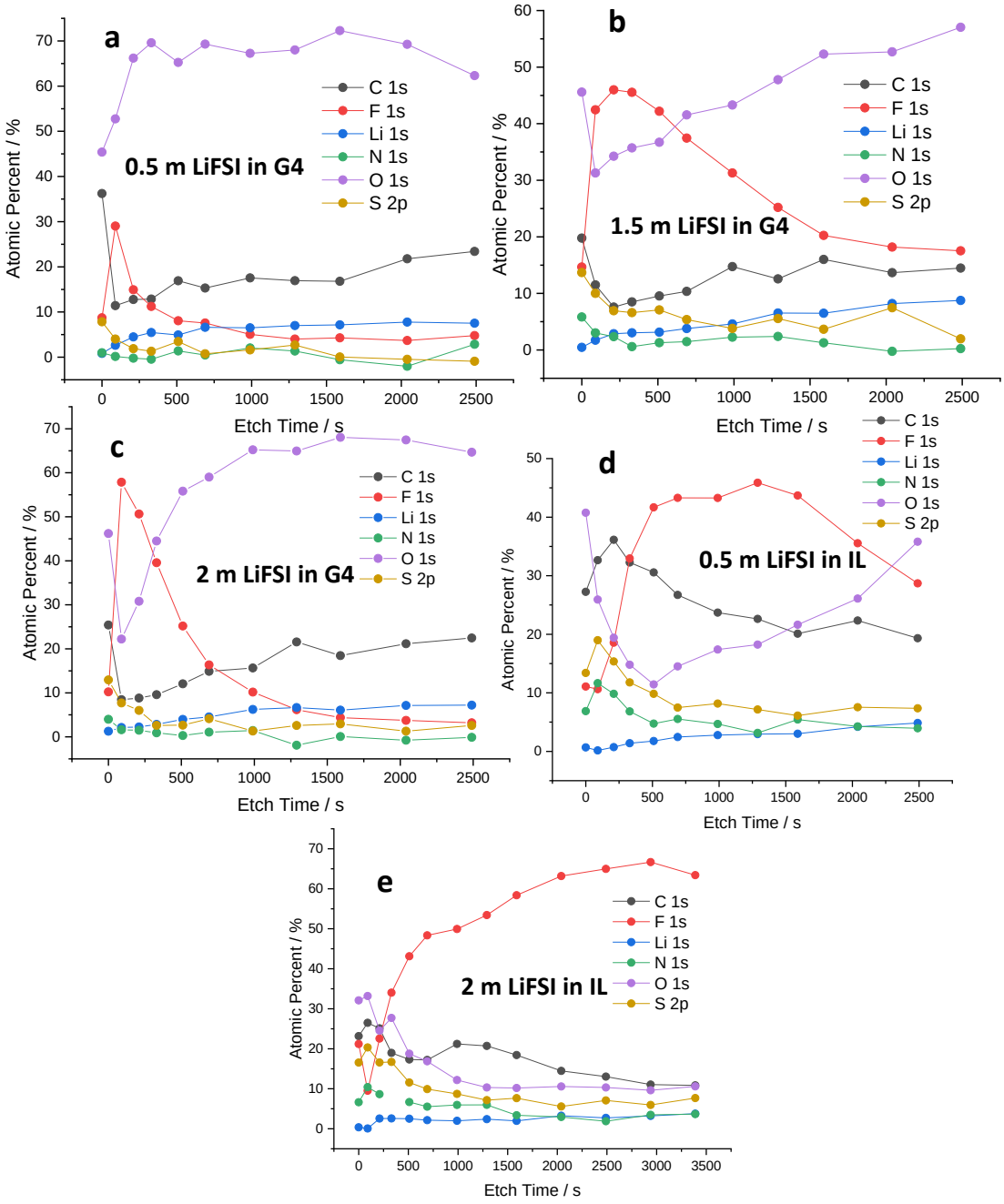


Figure D.1: Atomic Percent of different SEI components: a) 0.5 m LiFSI in G4 b) 1.5 m LiFSI in G4 c) 2 m LiFSI in G4 d) 0.5 m LiFSI in $Pyr_{1,3}FSI$ e) 2 m LiFSI in $Pyr_{1,3}FSI$.